MOL.19970724.0005

University of California
Lawrence Livermore National Laboratory

UCRL-LR-124998

MOL.19970515.0072

INFORMATION ONLY

Volume II: Near-Field and Altered-Zone Environment Report

Introduction and Chapter 1

Dale G. Wilder

August 23, 1996

102.2 - Part 1

Volume II:
Near-Field and Altered-Zone Environment Report

Dale G. Wilder
Scientific Editor

August 1996

DISCLAIMER

Prepared by Yucca Mountain Site Characterization Project (YMP) participants as part of the Civilian Radioactive Waste Management Program. The YMP is managed by the Yucca Mountain Site Characterization Project Office of the U.S. Department of Energy, Las Vegas, Nevada.

Contents

Acronyms and Abbreviations

ACD	advanced conceptual design
APD	areal power density
ASTM	American Society for Testing and Materials
bfs	blast furnace slag
BHW	borehole wall
CEC	cation exchange capacity
CHnv	Calico Hills, nonwelded, vitric
CHnz	Calico Hills, nonwelded, zeolitized
DFM	discrete fracture model
DHLW	defense high-level waste
DOE	U.S. Department of Energy
DST	drift scale test
EBS	engineered barrier system
EBSFT	engineered barrier system field tests
ECM	equivalent continuum model
ERT	electrical resistivity tomography
ESF	Exploratory Studies Facility
ESFTT	ESF thermal tests
FMM	fracture-matrix model
GTUF	G-Tunnel Underground Facility
GWTT	groundwater travel time
HLW	high-level waste
LA	license application
LAD	license application design
LBT	large block tests
LLNL	Lawrence Livermore National Laboratory
LSLDT	large-scale long-duration tests
MPBX	multiple borehole extensometer
NF	near field
NFE	near-field environment
NFER	*Near-Field Environment Report*
NTS	Nevada Test Site
NWTRB	Nuclear Waste Technical Review Board
PEBSFT	prototype engineered barrier system field test
PPw	Prow Pass, welded
PTn	Paintbrush, nonwelded
QA	quality assurance
REKA	rapid estimation of K (thermal conductivity) and alpha (diffusivity)
RIB	*Reference Information Base* (DOE, 1990)
RMR	rock-mass rating
RTD	resistance temperature device
SCP	*Site Characterization Plan* (DOE, 1988)
SCPCDR	Site Characterization Plan Conceptual Design Report
SCSSS	Standard Canadian Shield Saline Solution
SEAMIST	Science Engineering Associate Mambrane Insitu Sampling Technology
SEM	scanning electron microscopy
SF	spent fuel
SHT	single-heater tests
SIMS	secondary ion mass spectrometry
SP	spontaneous electrical potentials
TCw	Tiva Canyon, welded
TMHC	thermal-mechanical-hydrological-chemical

Acronyms and Abbreviations (continued)

Tpt	Topopah Spring Member of the Paintbrush tuff
TSw1	Topopah Spring, welded, lithophysae-rich
TSw2	Topopah Spring, welded, lithophysae-poor
TSw3	Topopah Spring, welded, vitric
UNE	underground nuclear explosion
WP	waste package
WPP	*Waste Package Plan* (Harrison-Giesler et al., 1991)
XRD	x-ray diffraction
YM	Yucca Mountain
YMP	Yucca Mountain Site Characterization Project
YMPO	Yucca Mountain Site Characterization Project Office

(ACD) for the repository, and there have been decisions made regarding the emplacement mode and the Waste Package Design. Therefore, this report is now entitled *The Near-Field and Altered Zone Environment Report.*

Volume I "Technical Basis for EBS Design" will provide technical information on the NFE needed for repository design decisions and performance analyses; Vol. II documents the scientific and engineering data, models, and approaches that were used to gather that information, thus enabling scientists and engineers to determine the validity of the information to be provided in Vol. I. This is of particular importance since there is only limited data and experience with these types of engineered systems, especially in unsaturated rock masses, and very little data or understanding of engineering system performance at the temperatures that will likely result from waste emplacement. It is important, therefore, to have an understanding of the physical processes (mechanistic understanding) in addition to the statistical distributions of the environmental conditions.

Volume II consists of 11 chapters. For convenience to the readers, chapters 1–9 are in the same order as the PNFER (Wilder, 1993); chapters 10 and 11 are new. The topics covered are as follows:

- Chapters 1–8 are divided into technical disciplines or studies.
- Chapter 9 is a discussion of field testing, which covers all technical disciplines. It summarizes the results of field tests performed at G-Tunnel at the Nevada Test Site (NTS) near Yucca Mountain (YM) and field and laboratory studies associated with the Large Block Test performed at Fran Ridge (ridge just east of YM) in the same geologic unit as that of the repository. It also covers pre-test analyses of ESF tests that support test designs for ESF.
- Chapter 10 discusses the Altered Zone where coupled processes will be dominant. As such, it is an integration of technical disciplines to reflect the coupled processes that will determine the environment within YM.
- Chapter 11 deals with Thermodynamic data for radionuclides.

Within each chapter, we discuss ambient conditions in the potential repository and those processes that cause perturbations. Although the individual chapters do not include a complete discussion of all that is known in any particular area, we include the findings of related studies and provide references to other sources of information to be as comprehensive as possible. The technical findings presented will be updated as more information is available, in accordance with the YM Project's long-range plan. For previous comprehensive sources of information on the NFE, refer to the *Site Characterization Plan (SCP)* (MacDougall et al., 1987), the

Yucca Mountain Project Reference Information Base (RIB) (DOE, 1995), the *Reference Waste Package Environment Report* (Glassley, 1986), and the *Preliminary Near-Field Environment Report* (Wilder, 1993).

The Yucca Mountain Site Characterization Project Office (YMPO) of the Department of Energy's (DOE's) Office of Civilian Radioactive Waste Management Program is conducting a broad range of studies to determine the suitability of Yucca Mountain, Nevada as the site for a potential nuclear-waste repository. The site is located about 120 km northwest of Las Vegas, Nevada, in an area of uninhabited desert (Fig. 1). The potential repository horizon is in the unsaturated zone, well above the saturated rock units. The major advantages of unsaturated conditions are that container corrosion, waste-form leaching, and radionuclide transport mechanisms are minimized due to reduced contact between liquid water and the waste package (WP), and recent studies indicate that the response to emplacement may minimize the relative humidity, which will also minimize corrosion and waste-form leaching. The design and performance of the WP and the EBS will be dependent on the geomechanical, hydrologic, and geochemical conditions over time in the rock forming the NFE.

Geologic/Hydrologic Setting

YM consists of a series of variably fractured, nonwelded to densely welded tuff units with an eastward tilt of about 5 to 30° (Montazer and Wilson, 1984). The potential repository is located in the Topopah Spring Member of the Paintbrush tuff (Tpt), within the unsaturated zone, lying approximately 350 m below the ground surface and 225 m above the water table (Klavetter and Peters, 1988). The Tpt is a formal stratigraphic unit and has been subdivided into more specific thermal/mechanical units, which are particularly useful for hydrologic analyses. These units are identified in Chapter 1 (section 1.12) of the *Yucca Mountain Project Reference Information Base (RIB)* (DOE, 1995). The units, as summarized in Fig. 2, are consistent with the listings in the *RIB* (see Table 1), but because the reference from the RIB is not yet available, we extracted a like-figure from Nimick and Schwartz (1987) for illustration. A current discussion of units may be found in Buesch et. al 1996 (as referenced in the *RIB*). The hydrostratigraphic units at YM generally fall into two categories: (1) welded tuffs of very low permeability and low porosity (TCw, TSw1, TSw2, and TSw3); and (2) nonwelded vitric tuffs of high permeability and high porosity (PTn and CHnv). The zeolitized nonwelded CHnz

has low permeability and intermediate porosity, and the welded PPw has intermediate permeability and porosity. The permeabilities of the nonwelded vitric tuffs are 4 to 5 orders of magnitude greater than those of the welded tuffs and the zeolitized nonwelded CHnz.

The potential repository horizon is in the thermal/mechanical TSw2 unit (Ortiz et al., 1985). TSw2 is a devitrified, welded, rhyolitic tuff that is moderately to densely welded, and appears to consist of a mass of intact blocks separated by planar fractures. Results of tunnel mapping in the access drift (Barr, et. al, 1996) indicate that the fracture system consists of predominately vertical fractures (two sets: the most dominate of which has a roughly NW strike and the second with a NE strike), and a low-angle set with a NW strike. These orientations are not corrected for orientation bias introduced by the roughly N–S drift orientation, and therefore may under-represent fractures with strikes that are within 15^0 of the drift's orientation, as will be discussed further in Chapter 1.9. The repository horizon rock is more fractured than the overlying units, with an overall fracture density of about 4 fractures/m in the ESF tunnel interval from station 27+00 to 56+30 and local average densities in any 400 to 500 m segment ranging from about 2 to 6 fractures/m. Price et al. (1987) report that the majority of the rock has a fine-grained matrix and contains gray-colored regions of vapor-phase-altered material. These altered regions vary in size and are quite common. In addition to these main components, the rock contains small (open and closed) lithophysal and healed fractures filled with quartz or calcite. The porosities of the matrix and vapor-phase-altered regions are 0.08 and 0.49, respectively (Price et al., 1985, 1987). The *RIB* gives a value of 0.12 but does not distinguish between the matrix and vapor-phase altered regions. Based on samples taken from surface coring, the TSw2 is expected to have 65% saturation (±19%) and a porosity of 15% (Montazer and Wilson, 1984).

Petrographic analysis shows that the repository horizon tuff consists of primary minerals, such as sanidine, plagioclase, quartz, biotite, iron-titanium oxides, allanite, and zircon that formed at temperatures in excess of 600°C in a magma chamber prior to eruption of the tuff; and secondary minerals, such as cristobalite, quartz, alkali feldspars, and smectite clays, that formed during cooling and later alteration of the tuff at temperatures less than 500°C (Lipman et al., 1966; Bish et al., 1981, 1982; Broxton et al., 1982; Vaniman et al., 1984; Warren et al., 1984; Broxton, 1987; Bish, 1989; and Bish and Chipera, 1986, 1989; Chipera et al., 1995). A mineralogy–petrology summary is in preparation that will contain details about the make-up of the rock (Bish et. al., 1996).

Distinguished from the primary and secondary minerals are those that formed on fracture surfaces [e.g., calcite, smectite, quartz, cristobalite, alkali feldspar, and the zeolites mordenite, chabazite, clinoptilolite, and heulandite (Carlos, 1985, 1989; and Lin and Daily, 1989)]. These minerals form layers which possess physical properties distinct from those minerals in the rock matrix and are estimated to comprise a maximum of 5% of the total rock mass. The mineral assemblage along a fracture surface varies from one location to another, and appears to reflect, at least in part, the previous location of the saturated zone (Carlos, 1989). Based on x-ray diffraction (XRD) analyses, the mineral assemblage of a typical fracture surface within the repository horizon might consist of 7% smectite, 7% cristobalite, 12% quartz, 29% clinoptilolite, and 45% alkali feldspar (Carlos, 1985, 1987; Carlos et al., 1995 a,b,c). These references also discuss the mineralogy and frequency of fracture coatings, which will be important to coupled thermo-hydrology-chemistry of the NFE. Since the mineralogy is dominated by secondary minerals, discussion of geochemical processes in the Altered Zone will consider these or similar minerals.

Evaluations of the expected NFE are based on currently available data on properties, parameters, analyses, and assumptions, as well as the ACD of repository designs, and on prototype or scoping tests and analyses.

Advanced Conceptual Design (ACD)

The engineering design of the EBS and repository, as well as operational considerations (e.g., sequence of emplacement, ventilation rates, age and mix of waste), can have a significant effect on the EBS's interaction with the environment and thus the performance of the overall system. We use the ACD (CRWMS M&O, 1996) for the repository and operations and a conceptual EBS to evaluate the environment. At the present time, the design is based on emplacing waste in large cylindrical multi-assembly packages (MPCs or similar) that contain approximately 21 PWR or 40 BWR spent-fuel assemblies, and then horizontally emplacing these containers directly into the emplacement drifts. The waste containers will contain a variety of waste that varies from young, very hot spent fuel from Pressure Water Reactors (PWRs) to the relatively low thermal output Defense High Level Waste (DHLW) containers filled with reprocessed, glass immobilized waste. Older PWR spent fuel and Boiling Water Reactor spent fuel will tend to have intermediate thermal output. The studies discussed in this report focus on spent fuel, because temperatures are a factor in many of the environmental issues.

The ACD emplacement concept provides for somewhat even spacing of waste packages and drifts, as illustrated in Chapter 1 (Fig. 1.10.1-1). Because the WPs are separated by considerable distances, they become essentially thermally isolated from neighbors so that each WP has its own individual environmental conditions. Thus, for the ACD there are a large number of potential environments (almost as many as there are individual WPs) which must be assessed to make design decisions and to make performance assessments. This can result in such highly variable emplacement environments (see Chapter 1.10.5) that it will be practically impossible to determine the environment and would possibly be a greater issue than the natural heterogeneity of the system.

References

Barr, D. L., T. C. Moyer, W. L. Singleton, A. L. Albin, R. C. Lung, S. C. Beason, A. C. Lee, and G. L. W. Eatman (1996), *Geology of the North Ramp–Station 4+00 to 28+00, Exploratory Studies Facility, Yucca Mountain Project,* Yucca Mountain, Nevada, Bureau of Reclamation and U. S. Geological Survey, Prepared in cooperation with the Nevada Field Office, U.S. Department of Energy (DE-A108-92NV10874).

Bish, D. L. (1989), *Evaluation of Past and Future Alterations in Tuff at Yucca Mountain, Nevada, Based on the Clay Mineralogy of Drill Cores USW G-1, G-2, and G-3,* Los Alamos National Laboratory, Los Alamos, NM, LA-10667-MS.

Bish, D. L., F. A. Caporuscio, J. F. Copp, B. M. Crowe, J. D. Purson, J. R. Smyth, and R. G. Warren (1981), Los Alamos National Laboratory, Los Alamos, NM, LA-8840-MS.

Bish, D. L., and S. J. Chipera (1986), *Mineralogy of Drill Holes J-13, UE-25A#1, and USW G-1 at Yucca Mountain, Nevada,* Los Alamos National Laboratory, Los Alamos, NM, LA-10764-MS.

Bish, D. L., and S. J. Chipera (1989), *Revised Mineralogic Summary of Yucca Mountain, Nevada,* Los Alamos National Laboratory, Los Alamos, NM, Report LA-11497.

Bish, D. L., D. T. Vaniman, F. M. Byers, Jr., and D. E. Broxton (1982), *Summary of the Mineralogy-Petrology of Tuffs of Yucca Mountain and the Secondary Phase Thermal Stability in Tuffs,* Los Alamos National Laboratory, Los Alamos, NM, LA-9321-MS.

Broxton, D. E. (1987), "Clinoptilolite Compositions in Diagenetically-Altered Tuffs at a Potential Nuclear Waste Repository, Yucca Mountain, Nevada," *The Technology of High-Level Nuclear Waste Disposal,* P. L. Hofmann, Ed., vol. 3, pp. 179–194.

Broxton, D., D. F. Vaniman, B. Arney Caporuscio, and G. Heiken (1982), *Detailed Patrographic Descriptions and Microprobe Data for Drill Holes USW-G2 and UE25b-1H, Yucca Mountain, Nevada,* Los Alamos National Laboratory, Los Alamos, NM, LA-9324-MS.

Buesch, D. C., R. W> Spengler, T. C. Moyer, J. K. Geslin, Proposed Stratigraphic Nomenclature and Macroscopic Identification of Lithostratigraphic Units of the Paintbrush Group Exposed at Yucca Mountain, Nevada, U.S. Geological Survey, Open-File Rep 94-469.

Carlos, B. A. (1985), Minerals in Fractures of the Unsaturated Zone from Drill Core USW-G4, Yucca Mountain, Nye County, Nevada, Los Alamos National Laboratory, Los Alamos, NM, LA-10415-MS.

Carlos, B. A. (1987), Minerals in Fractures of the Saturated Zone from Drill Core USW G-4, Yucca Mountain, Nye County, Nevada, Los Alamos National Laboratory Report, LA-10927-MS, 32 pp.

Carlos, B. A (1989), Fracture-Coating Minerals in the Topopah Spring Member and Upper Tuff of Calico Hills from Drill Hole J-13, Los Alamos National Laboratory, Los Alamos, NM, LA-11504-MS.

Carlos, B. A., S. J. Chipera, D. L. Bish, and R. Raymond (1995a), "Distribution and Chemistry of Fracture Lining Zeolites at Yucca Mountain, Nevada," Natural Zeolites '93: Occurrence, Properties, Use, D. W. Ming and F. A. Mumpton, eds., pp. 547–563.

Carlos, B. A., S. J. Chipera, and D. L. Bish (1995b), Distribution and Chemistry of Fracture-Lining Zeolites at Yucca Mountain, Nevada, Los Alamos National Laboratory Report, LA-12977-MS, 92 pp.

Carlos, B. A., S. J. Chipera, and M. G. Snow (1995c), "Multiple Episodes of Zeolite Deposition in Fractured Silicic Tuff," Proceedings of the 8th International Symposium on Water–Rock Interaction, WRI-8, Y. K. Kharaka and O. V. Chudaev, eds., pp. 67–71.

Chipera, S. J., D. T. Vaniman, B. A. Carlos, and D. L. Bish, (1995), Mineralogic Variation in Drill Core UE-25 UZ #16, Yucca Mountain, Nevada, Los Alamos National Laboratory Report, LA-12810-MS, 39 pp.

CRWMS M&O (1996) (Civilian Radioactive Waste Management System Management and Operating Contractor). Mined Geologic Disposal System Advanced Conceptual Design Report, B00000000-01717-5705-00027, Rev 00, four volumes, TRW Environmental Safety Systems Inc., Las Vegas, Nevada.

DOE (U.S. Department of Energy) (1990), Yucca Mountain Project Reference Information Base, Version 4, Yucca Mountain Site Characterization Project Office, Las Vegas, NV, YMP/CC-0002. (NNA 890330.0077)

Glassley, W. E. (1986), Reference Waste Package Environment Report, Lawrence Livermore National Laboratory, Livermore, CA, UCRL-53726.

Klavetter, E. A., and R. R. Peters (1988), "A Continuum Model for Water Movement in an Unsaturated Fracture Rock Mass," Water Resources Research 24, 416–430.

Lin, W., and W. D. Daily (1989), "Laboratory Study of Fracture Healing in Topopah Spring Tuff—Implications for Near Field Hydrology," Proc. of the ANS Topical Mtg. on Nuclear Waste Isolation in an Unsaturated Zone, Focus '89 (American Nuclear Society, La Grange Park, IL), p. 443.

Lipman, P. W., R. L. Christiansen, and J. T. O'Connor (1966), A Compositionally Zoned Ash-Flow Sheet in Southern Nevada, U. S. Geological Survey, Prof. Pap. 524-F.

MacDougall, H. R., L. W. Scully, and J. R. Tillerson, (Compilers) (1987), Site Characterization Plan Conceptual Design Report, Sandia National Laboratories, Albuquerque, NM, SAND84-2641.

Montazer, P., and W. E. Wilson (1984), Conceptual Hydrologic Model of Flow in the Unsaturated Zone, Yucca Mountain, Nevada, U. S. Geological Survey, Lakewood CO, Water Resources Investigation Report 84-4345.

Nimick, F. B., R. G. Van Buskirk, and A. F. McFarland (1987), Uniaxial and Triaxial Compression Test Series on Topopah Spring Member from USW G-2, Yucca Mountain, Nevada, Sandia National Laboratories, Albuquerque, NM, SAND85-0703.

Nimick, F. G., and B. M. Schwartz (1987), Bulk, Thermal, and Mechanical Properties of the Topopah Spring Member of the Paintbrush Tuff, Yucca Mountain, Nevada, Sandia National Laboratories, Albuquerque, NM, SAND85-0762.

Office of Civilian Radioactive Waste Management (1988), Site Characterization Report 2(A), Chp. 3, 139.

Ortiz, T. S., R. L. Williams, F. B. Nimick, B. C. Whittet, and D. L. South (1985), A Three-Dimensional Model of Reference Thermal/Mechanical and Hydrologic Stratigraphy at Yucca Mountain, Southern Nevada, Sandia National Laboratories, Albuquerque, NM, SAND84-1076.

Price, R. H., J. R. Connolly, and K. Keil (1987), Petrologic and Mechanical Properties of Outcrop Samples of the Welded, Devitrified Topopah Spring Member of the Paintbrush Tuff, Sandia National Laboratories, Albuquerque, NM, SAND86-1131.

Price, R. H., F. B. Nimick, J. R. Connolly, K. Keil, B. M. Schwartz, and S. J. Spense (1985), Preliminary Characterization of the Petrologic, Bulk, and Mechanical Properties of a Lithophysal Zone Within the Topopah Spring Member of the Paintbrush Tuff, Sandia National Laboratories, Albuquerque, NM, SAND84-0860.

Vaniman, D., D. Bish, D. Broxton, F. Byers, G. Heiken, B. Carlos, E. Semarge, F. Caporuscio, and R. Gooley (1984), Variations in Authigenic Mineralogy and Sorptive Zeolite Abundance at Yucca Mountain, Nevada, Based on Studies of Drill Cores USW GU-3 and G-3, Los Alamos National Laboratory, Los Alamos, NM, LA-9707.

Warren, R. G., F. M. Byers, Jr., and F. A. Caporuscio (1984), Petrography and Mineral Chemistry of Units of the Topopah Spring, Calico Hills, and Crater Flat tuffs, and Older Volcanic Units, with Emphasis on Samples from Drill Hole USW G-1, Yucca Mountain, Nevada Test Site, Los Alamos National Laboratory, Los Alamos, NM, LA-10003-MS.

Wilder, D. G. (1993), Preliminary Near-Field Environment Report Volume II: Scientific Overview of Near-Field Environment and Phenomena, Lawrence Livermore National Laboratory, Livermore, CA, UCRL-LR-107476.

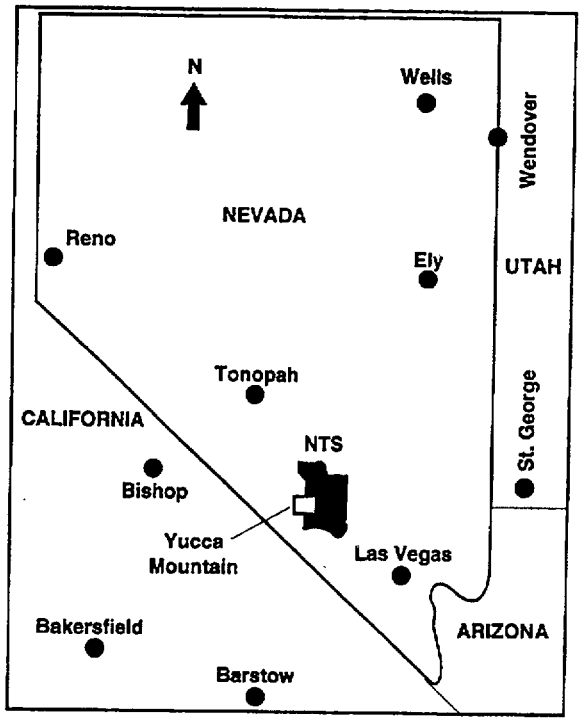

Figure 1. Location of Yucca Mountain, Nevada.

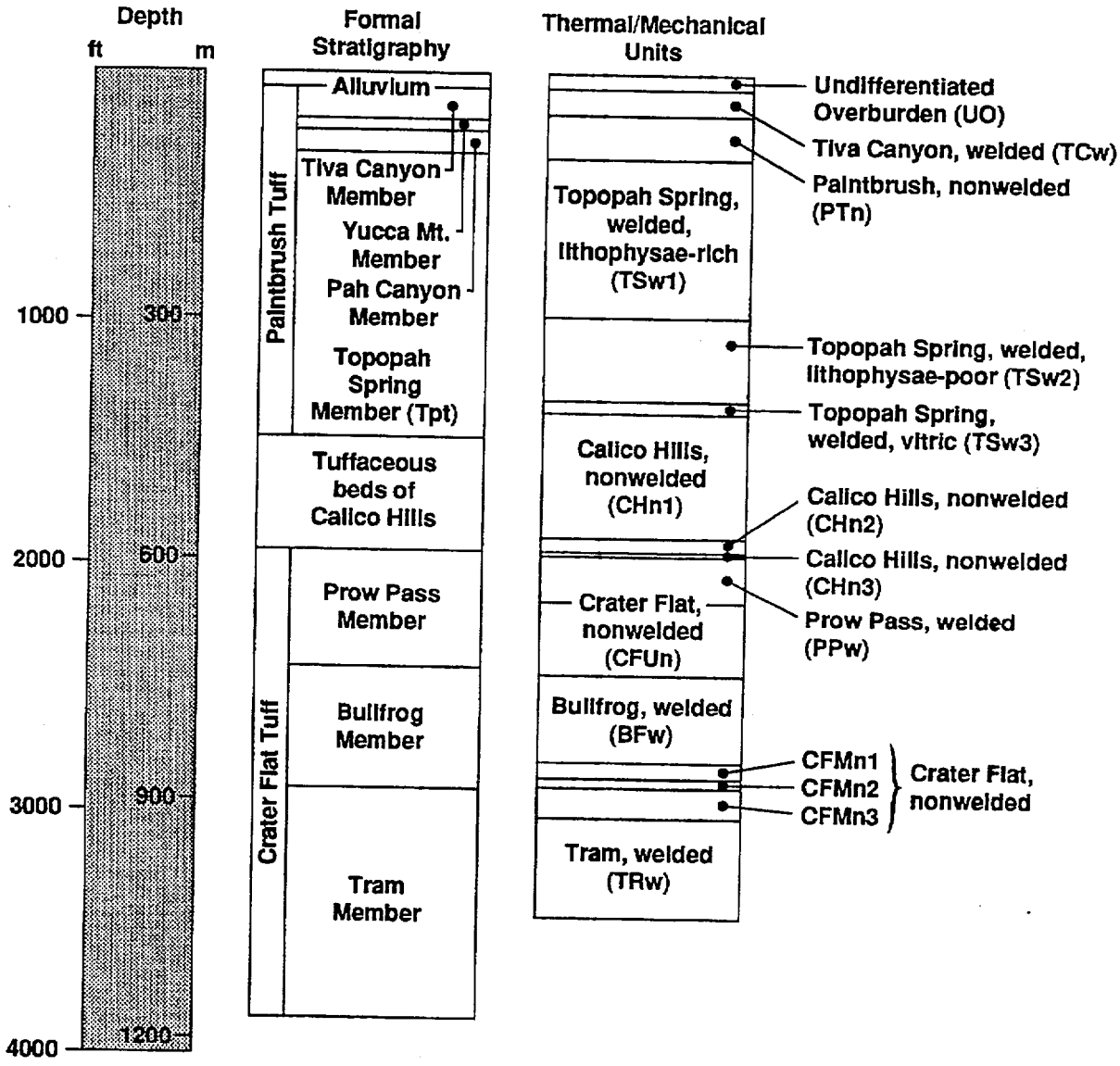

Figure 2. Relationship of formal stratigraphy and thermal/mechanical units. Adapted from Nimick and Schwartz (1987).

Table 1. Correlation of lithologic, thermal-mechanical, and hydrogeologic units on the basis of the revised lithostratigraphy (Buesch et al., 1996).

Lithologic units (from: Buesch et al., 1996)	Thermal-mechanical units (Ortiz et al., 1985)	Hydrogeologic units (Office of Civilian Radioactive Waste Management, 1988)
Paintbrush Group		
Rhyolite of Comb Peak (Tpk)		
includes tuff unit "x" (Tpki)		
Rhyolite of Vent Pass (Tpv)	Undifferentiated overburden[1] (UO)	Unconsolidated surficial materials (UO)
Post-Tpc bedded tuff (Tpbt5)		
Tiva Canyon Tuff (Tpc)		
Crystal-rich		
Vitric		
Nonwelded (rv3: v3n, v3p)		
Moderately welded (rv2)		
Densely welded (rv1: v1c, v1v)		
Nonlithophysal (rn: n4, n3, n2, n1)		
Lithophsal (rl: l2, l1)		
Crystal-poor	Tiva Canyon welded unit (TCw)	Tiva Canyon welded hydrogeologic unit (TCw)
Upper lithophysal (pul)		
Middle nonlithophysal (pmn: mn3, mn2, mn1)		
Lower lithophysal (pll)		
Hackly-fractured (pllh)		
Lower nonlithophysal (pln)		
Hackly (plnh)		
Columnar (plnc: c3, c2, c1)		
Vitric (pv)		
Densely welded (pv3: v3v, v3c)[2]		
Moderately welded (pv2)		
Nonwelded (pv1: v1p, v1n)		
Pre-Tpc bedded tuff (Tpbt4)		
Yucca Mountain Tuff (Tpy)	Upper Paintbrush nonwelded unit (PTn)	Paintbrush nonwelded hydrogeologic unit (PTn)
Pre-Tpy bedded tuff (Tpbt3)		
Pah Canyon Tuff (Tpp)		
Pre-Tpp bedded tuff (Tpbt2)		
Topopah Spring Tuff (Tpt)		
Crystal-rich		
Vitric		
Nonwelded (rv3: v3n, v3p)		
Moderately welded (rv2)		
Densely welded (rv1: v1c, v1v)		
Nonlithophysal (rn: n3, n2, n1)	Topopah Spring welded unit lithophysae-rich (TSw1)[3]	
Lithophysal (rl: l2, l1)		
Crystal-poor		
Upper lithophysal (pul: ulc, uls)		

Table 1. (continued)

Lithologic units (from: Buesch et al., 1996)	Thermal-mechanical units (Ortiz et al., 1985)	Hydrogeologic units (Office of Civilian Radioactive Waste Management, 1988)
Middle nonlithophsal (pmn: mn3, mn2, mn1) Lower lithophysal (pll) Hackly-fractured (pllh) Lower nonlithophysal (pln) Hackly fractured (plnh) Columnar (plnc: c3, c2, c1)	Topopah Spring welded unit lithophysae-poor (TSw2)	Topopah Spring welded hydrogeologic unit (TSw)
Vitric Densely welded (pv3: v3v, v3c)	Topopah Spring welded unit vitrophyre (TSw3)	
Moderately welded (pv2) Nonwelded (pv1: v1p, v1n) Pre-Tpt bedded tuff (Tpbt1) CALICO HILLS FORMATION	Calico Hills and Lower Paintbrush nonwelded unit (CHn1)	Calico Hills nonwelded hydrogeologic unit (CHn)

[1] Thermal-mechanical unit UO of Ortiz et al. (1985, p. 11) includes "alluvium; colluvium; nonwelded vitric ashflow tuff of the Tiva Canyon Member of the Paintbrush Tuff; and any other tuff units that stratigraphically overlie the welded, devitrified Tiva Canyon Member."

[2] Where preserved, the base of the densely welded subzone forms the base of the TCw thermal-mechanical and hydrogeologic units.

[3] The TSw1-TSw2 contact is where the amount of lithophysae changes from greater than to less than 10 percent of the total rock volume (Ortiz et al., 1985). This change in the amount of lithophysae occurs up to 30 meters above the upper lithopyhsal-middle nonlithophysal zone contact as identified by multiple criteria.

Contents

1.0 Hydrothermal Modeling

Tom Buscheck

1.1 Introduction

1.1.1 Organization of This Chapter

Several hydrological and thermal-hydrological (T-H) issues must be considered in evaluating the viability of the Yucca Mountain site as a potential nuclear-waste repository. Chapter 1 and Sections 10.1 and 10.2 of Chapter 10 describe these issues and the modeling and testing that have been performed (and are being planned) to address them. The major hydrological and T-H topics are:

The nominal pre-emplacement hydrological system: The major pre-emplacement attributes of the ambient hydrological system in the unsaturated zone (UZ) and saturated zone (SZ) include:

The distribution of fracture and matrix properties: These properties affect both the small-scale and large-scale flow of water vapor and liquid water in the UZ and the large-scale flow of liquid water in the SZ. Section 1.2.1 describes the available data on these properties.

Fracture-matrix flow interaction: This interaction can range from matrix-dominated flow (which occurs when the matrix imbibition flux is comparable to liquid-phase flux in the fracture) to nonequilibrium fracture-dominated flow (which occurs when the liquid-phase flux in the fracture is greater than the capacity of the rock matrix to imbibe it). The key factors are (1) the spatial distribution of fracture flow (spatially heterogeneous versus uniform flow) and (2) the temporal distribution of fracture flow (episodic versus steady flow). Section 1.3 describes the processes involved with fracture-matrix flow interaction and how these processes are likely to play out in the major hydrostratigraphic units in the UZ at Yucca Mountain.

Preferential flow pathways: Features such as fault zones and zones of high fracture permeability may facilitate the preferential flow of water vapor and liquid water at the mountain scale. Of particular interest is focused flow, primarily occurring in the vertical direction. Features such as those resulting from a high contrast in matrix and fracture properties at hydrostratigraphic boundaries may facilitate preferential lateral movement of water vapor and liquid water. Preferential flow will affect the potential for water to enter emplacement drifts and contact WPs and will also affect the drift-scale and mountain-scale transport of radionuclides. Section 1.4 addresses preferential flow pathways.

Ambient percolation flux distribution: This is the distribution of liquid-phase flux in the host rock (the TSw2 unit), which is the net result of infiltration and exfiltration in the alluvium and TCw unit and lateral flow in the PTn. Section 1.5 describes the available information on ambient percolation flux.

The post-emplacement thermal-hydrological (T-H) system: The major post-emplacement attributes of the thermal-hydrological system in the Engineered Barrier System (EBS), UZ and SZ include:

The impact of repository construction/operational activities: The important effects of repository activities include (1) changes to near-field distribution of fracture permeability and connectivity that result from mining-induced mechanical stresses, (2) dryout of the near-field rock as a result of mine ventilation, (3) introduction of water from mining and drilling activities, and (4) introduction of man-made materials, such as cement grout and concrete. Section 1.6 discusses the potential impact of repository activities on waste isolation.

Thermal-hydrological (T-H) flow processes in the UZ: Decay heat from WPs will significantly mobilize vapor and condensate flow (at least) as long as boiling conditions persist. Depending on the degree to which condensate builds up above the repository, these T-H effects will persist (resulting in decay-heat-enhanced liquid-phase flow) for some time after boiling ceases. If the bulk permeability k_b is large enough (>1–10 darcy) and the fractures well enough connected to allow buoyant gas-phase convection to dominate moisture transport, then decay-heat-altered vapor and liquid-phase flow can persist for up to 100,000 yr. If vapor diffusion is significantly enhanced as suggested by Pruess et al.[1993], then decay heat will continue to significantly mobilize vapor and liquid-phase flow long after boiling has ceased. The intercoupling of T-H processes with geomechanical and geochemical processes (called coupled T-H-M-C processes) may also affect decay-heat-driven T-H flow; these coupled processes may significantly alter flow and transport properties in the near field and altered zone, thereby continuing to influence radionuclide transport well after decay heat stops mobilizing gas-phase and liquid-phase flow in the UZ. Section 1.7 discusses the decay-heat-driven T-H processes.

Thermal-hydrological-geomechanical-geochemical (T-H-M-C) processes: The geochemical environment of the near-field, the EBS, and the altered zone will affect any liquid water that may contact the WPs, the waste form, and any radionuclides released into the near-field and transported in the altered zone. The composition of the liquid phase will depend on the decay-heat-driven coupled thermal-hydrological-geomechanical-geochemical (T-H-M-C) processes experienced by packets of mobile fluid and by the rock along their respective flow paths which lie in the altered zone, which can extend more than hundreds of meters away from the repository. Flow processes, such as condensate refluxing and evaporation, can concentrate different dissolved components. Condensate may dissolve minerals from fracture walls as it drains down fractures and then precipitate those (or other) minerals as it evaporates. These changes may alter fracture apertures along various intervals, thereby altering the bulk permeability distribution. Solubility and dissolution of minerals depend on temperature changes, among other things. The geochemistry of water from surface infiltration contacting WPs will vary depending on whether it drains quickly down fractures or migrates slowly in the matrix, and on whether it was affected by refluxing or buoyant gas-phase convection. Chapters 3, 4, and 10 discusses these coupled processes.

Engineered Barrier System (EBS) performance: Radionuclide containment in (and eventual release from) the EBS is most notably affected by the distribution of temperature, relative humidity, liquid-phase saturation, and liquid-phase flux in the emplacement drifts and in the near-field rock. Sections 1.8.3 and 1.8.4 discuss the importance of T-H processes on (1) the near-field and EBS environments, (2) the integrity of WPs, which is a key factor in the containment of radionuclides in the EBS, (3) radionuclide release from WPs, (4) radionuclide transport in the EBS, and (5) eventual radionuclide release from the EBS.

Thermal management strategies: These strategies are implemented in the thermal design of the repository, including the overall areal mass loading of the repository and the details of how the decay-heat sources (i.e., the WPs) are distributed. The key decision in any strategy concerns whether to attempt to (1) minimize (to the extent possible) the thermal-hydrological effects of decay heat or (2) to use decay heat constructively to generate conditions that are more favorable for radionuclide containment in the EBS. Section 1.8.2 discusses these strategies.

The constructive use of decay heat: Section 1.8.2 describes the two fundamental approaches for the constructively heated (CH) repository strategy, which are:

Extended dryout (ED) approach: Use a high AML (>60 MTU/acre) to drive a large fraction of the initial pore water (in the rock) from the repository as a whole. The high areal power density associated with such an AML creates a thick superheated dryout zone (coalesced between emplacement drifts) and maintains above-boiling temperatures and low *RH* in the repository rock (and on WPs) for thousands of years.

Localized dryout (LD) approach: Maintain a temperature difference between the WP and the drift wall that is large enough to reduce *RH* on the WP. This is done with close axial WP

spacing (generating a high line-heat load) and/or the use of low-thermal-conductivity backfill in the drift. Wide drift spacings and low to intermediate AMLs (<50–60 MTU/acre) are used to (1) prevent the boiling zones from coalescing between drifts (and thereby limiting condensate buildup above the drifts) and (2) limit far-field temperature rise (as in the MH strategy). A hybrid LD–ED approach, which uses a high AML (>60 MTU/acre), close axial WP spacing, and wide drift spacing, would not limit temperature rise in the far field and condensate buildup above the boiling zone as with a lower AML; however, it is still possible to take advantage of both the drift-ΔRH effect and ΔRH_{rock}; moreover, highly concentrated line-heat loads and wide drift spacing will make it much more likely for condensate to drain through the rock pillar rather than into the emplacement drifts, unless permeability is reduced in the pillars due to coupled (geochemical/hydrothermal) processes.

Major thermal-hydrological flow regimes: These regimes are, in effect, the net outcome of intercoupled T-H and T-H-M-C processes (i.e., determined by the dominant processes). These regimes vary in time and space. The factors determining where and when a given regime dominates include (1) the distribution of natural system properties and conditions, (2) how the decay-heat sources (the WPs) are distributed, and (3) other engineering measures such as the use of backfill. Section 1.8.5 describes the major T-H regimes.

Thermal-hydrological testing: While this is not a T-H attribute, it is important to point out that the most effective means of determining the dominant T-H flow regimes and the importance of hydrogeological heterogeneity on T-H behavior is through sufficiently sized thermal testing conducted at the repository horizon for a sufficient duration. These tests are also needed to address key hypotheses about T-H behavior and coupled T-H-M-C processes. They are also needed to test coupled T-H-M-C process models and to provide sufficient confidence in the process models that are used to abstract the near-field and EBS subsystem performance models required by total systems performance assessment. Section 1.9 describes the thermal testing program, post-test analysis of past *in situ* tests, and pre-test analysis used to design and plan the ESF thermal tests.

The influence of repository design on thermal-hydrological behavior: The most significant design attribute is the WP layout (the axial spacing between WPs and the lateral spacing between drifts). How WPs are configured within the repository (e.g., in a square configuration as in the ACD rev 00 design versus a line-load configuration with tight axial WP spacing and wide drift spacing) plays a far greater role in determining whether near-field thermal-hydrological behavior is beneficial (versus deleterious) than the overall areal mass loading (AML) of the repository itself, and it may be more consequential than the variability and uncertainty in the natural system parameters. One of the primary objectives of Section 1.10 is to establish functional relationships (i.e., the parametric sensitivity) between repository system parameters and T-H behavior in the near field and EBS, and thereby help develop a quantitative framework upon which thermal management principles may be incorporated into the design of the repository system. These functional relationships are also needed to (1) provide guidance for T-H testing, (2) assist in the model abstraction process for total system performance assessment, and (3) provide a quantitative framework for comparing various alternatives that are being evaluated by the systems studies.

Thermal-hydrological flow processes and flow regimes in the SZ: Decay heat can also drive buoyant liquid-phase flow in the SZ that may be the dominant mechanism driving SZ flow and radionuclide transport for tens of thousands of years. Decay heat will also result in a significant rise in temperatures in the SZ that, together with the decay-heat-driven mixing of waters from different regions of the SZ, may result in significant alteration of the flow and transport properties in a large region (exceeding several repository areas) of the SZ. The effect of decay heat on T-H flow and radionuclide transport is discussed in Section 10.2 of Chapter 10.

1.1.2 Key Thermal-Hydrological Issues for Site Viability and Waste Isolation

Some of the most important issues that must be considered in evaluating the viability of the Yucca Mountain Site involve the dominant role that decay heat plays in determining the thermal-hydrological (T-H) conditions in and around the emplacement drifts and, in particular, on the WP itself. A key consideration for nuclear waste isolation is whether (or when and how) water contacts a WP, thereby affecting WP integrity and, if WPs are breached, waste form dissolution and release from the WPs. The manner in which decay heat influences the distribution of liquid saturation and liquid-phase flux within the drifts (also called the Engineered Barrier System or EBS) strongly affects radionuclide transport within the EBS and eventual radionuclide release from the EBS. The manner in which decay heat influences the distribution of liquid saturation and liquid-phase flux in the near field and altered zone affects radionuclide transport within those zones. Although not discussed in this chapter, the T-H effects of decay heat influence geomechanical and geochemical changes in the near field and altered zone (as a result of coupled T-H-M-C processes), which can also affect T-H flow and radionuclide transport within those zones. Coupled T-H-M-C effects will continue to influence radionuclide transport well after decay heat has stopped mobilizing gas-phase and liquid-phase flow in the UZ. These effects will be discussed in Chapters 3, 4, and 10.

A key attribute of the EBS, affecting its ability to contribute to waste isolation, is to cause an RH difference (ΔRH_{drift}) between the hotter (and drier) WP and cooler (and more humid) rock at the drift wall. The drift-ΔRH effect is quantified by the relationship $RH_{wp}/RH_{dw} = P_{sat}(T_{dw})/P_{sat}(T_{wp})$, which depends primarily on the temperature difference (ΔT_{drift}) between the WP and drift wall. Therefore, the heat transfer attributes of the EBS are key in determining the extent to which RH can be reduced on the WP. Of particular significance, is whether a low-Kth backfill is used to insulate the WP from the drift wall, which generates a much larger ΔT_{drift} than occurs when the drift remains open and thermal radiation is the primary mode of heat transfer between the WP and drift wall.

Water may contact a WP by either liquid-phase (advective or diffusive) flow or by condensation of water vapor that forms a liquid film on the WP. There are three ways by which this contact may arise:

Drift seepage: Advective liquid-phase flow of water that enters the drift (and flows through the backfill if present) as a result of ambient percolation or decay-heat-driven condensate flow. This can include episodic nonequilibrium fracture flow or a steady weep.

Wicking: Transport of moisture driven by matric potential gradients (i.e., capillary pressure gradients). This is primarily considered to be an advective liquid-phase transport process (called imbibition); however, binary gas-phase diffusion can also play a role. Because wicking can occur as two-phase flow, it does not necessarily require a continuous liquid phase.

Cold-trap effect: Axial vapor flow and condensation within the drift is driven by axial variations in T and P_v along the drift. Water vapor is transported (by gas-phase advection and diffusion) from areas of higher temperature and P_v to areas of lower temperature and P_v where it condenses, which causes RH to increase (even as high as 100%). Large condensation rates can arise in the cooler areas if the following three conditions are met: (1) high RH in the rock at the drift wall, (2) WP heat output varies substantially from WP to WP, and (3) WPs are thermally isolated from one another. It is important to note that this mechanism does not require water to enter the drift.

For all three of these effects, we find that the most important thermal-management design factor is the WP layout (e.g., WPs uniformly distributed in a square configuration versus in a line-load configuration with tight axial WP spacing and wide drift spacing) rather than the overall AML of the repository itself (e.g., high versus low AML).

Liquid-phase flux that may enter a drift is the result of ambient percolation flux and decay-heat-mobilized vapor and condensate flow. A key question is whether (or under what conditions) decay heat decreases or increases the magnitude (or probability) of liquid-phase flux entering a drift. Depending

on the AML, decay heat is capable of generating a zone of counter-current two-phase flow above the repository, which is sometimes called the refluxing zone or the heat-pipe zone [Nitao, 1988; Pruess et al., 1990; Buscheck and Nitao, 1994]; this zone is associated with liquid-phase fluxes that are much larger than ambient. If the AML is high enough, this zone can be displaced well above the repository horizon by the superheated (above-boiling-temperature) zone. If either the AML is not large enough or the ambient percolation flux is too large, it is possible for the heat-pipe zone to remain at the repository horizon. A heterogeneous permeability distribution can also cause the heat-pipe zone to remain at the repository horizon in regions where condensate flow is focused (Section 1.10.2.5). The fundamental relationship is between the local heat flux q_H and the heat flux that is required to vaporize the incoming local liquid-phase flux. In theoretical studies of the effect of decay heat on condensate flux [Nitao and Bradford, 1996], it was found that the tendency for either hot and dry conditions prevailing (rather than hot and wet conditions) depends on whether there is enough heat flux locally that is capable of evaporating the local liquid-phase flux. The local heat flux q_H (which, during the initial heat-up period is proportional to LML; thereafter it is proportional to AML) will prevail over the local liquid-phase flux q_{liq} if the following holds:

$$q_H > q_{liq}\rho_{liq}h_{fg} \quad , \tag{1}$$

where ρ_{liq} is the mass density of water and h_{fg} is the latent heat of vaporization. If there is too much liquid-phase flux, then there is insufficient heat flux to generate superheated conditions at the repository horizon.

A key question concerns whether heterogeneity in the natural system and/or engineered system parameters that govern the distribution of liquid-phase flux can focus enough liquid-phase flux (at least) locally to cause Eq. 1 not to hold true. In addition to affecting the distribution of liquid-phase flux, heterogeneity in the natural system and/or engineered system parameters can also cause the temperature and relative humidity *RH* on the respective WPs to vary substantially along the drift.

Natural System heterogeneity: Arises from variability in the following:

Percolation flux: This quantity, which is the liquid-phase flux in the host rock (the TSw2 unit), is the net result of infiltration and exfiltration and the ability of the PTn to divert the net infiltration flux which reaches the PTn unit. The temporal nature of percolation flux can range from episodic flow in fractures to steady-state flow in both the fractures and the matrix (see Sections 1.3 and 1.10.6). Imbibition in the PTn serves to dampen the influence of episodic infiltration events and thereby provide more time for exfiltration and lateral flow to influence the moisture balance in the PTn; all of which tend to reduce the percolation flux in the TSw2.

Ambient liquid saturation distribution: This quantity can be no less than what is caused by gravity-capillary-pressure equilibrium with the water table (Section 1.2.1). Liquid saturation increases with decreasing height above the water table (or perched water body). Liquid saturation also increases with percolation flux, particularly if that flux is steady (Section 1.10.6).

Distribution of fracture permeability and connectivity: This affects both small-scale and large-scale vapor and condensate flow. If fracture permeability is small enough (i.e., bulk permeability k_b < 1–10 millidarcy) and/or the distance between connected fractures is large enough, then advective dryout will be throttled. (Evidence to date is that throttling is not likely; both permeabilities are much higher and fracture spacing much smaller than required for throttling.) If k_b > 1–10 millidarcy and the distances between well connected fractures is small enough, then advective dryout will be unthrottled. If k_b > 1–10 darcy, then buoyant gas-phase convection significantly affects the magnitude and direction of vapor flux over the length scale for which fractures are ubiquitously connected (see Section 10.1.2.2). The connected length scale of fractures also affects the scale over which repository-scale condensation redistribution can occur. Zones of highly contrasting k_b can result in focused vapor and condensate flow in the near-field rock (Section 10.1.2.5). Note that observations of large k_b (> 1–10 darcy) being prevalent in the ESF imply that nonbuoyant or buoyant unthrottled advective

dryout will prevail and that throttled advective dryout will be limited to (at most) isolated regions of the host rock, if it occurs at all.

Distribution of matrix hydrological properties: This influences small-scale gas-phase and liquid-phase flow. Of particular importance is how the imbibition properties of the matrix influence the degree to which nonequilibrium liquid-phase fracture flow can occur (Section 1.3). The drying and rewetting characteristics of the matrix can influence the spatial extent of dryout (Section 10.1.3). The rewetting characteristics of the matrix also strongly influence gas-phase and liquid-phase rewetting of the dryout zone (Section 10.1.3).

Thermal conductivity K_{th} distribution in the rock: This is affected by both the K_{th} of the intact rock and the degree of fracturing.

Overburden thickness: This quantity, which is the distance between the repository and the ground surface, can vary significantly over the repository. Because this is the thickness of the "thermal blanket" that insulates the repository from the ground surface, it affects the time required to attain the peak rock temperature at the center of the repository. It also affects the vertical extent over which heat pipes may develop, with maximum vertical heat-pipe length increasing with overburden thickness. Peak temperatures at the edge of the repository are determined by the edge-cooling effect before the overburden thickness has any influence (Section 10.1.4 of Chapter 10).

Contribution of buoyant gas-phase convective vapor and heat flow: If k_b > 1–10 darcy, then buoyant gas-phase convection significantly affects the magnitude and direction of vapor flux over the length scale for which fractures are ubiquitously connected (see Section 10.1.2.2). If k_b > 40 darcy and fractures are ubiquitously connected over a length scale comparable to the width of the repository area (this is not likely to be the case), then buoyant gas-phase convection significantly affects heat flow and repository temperatures (Section 1.8.5).

Contribution of heat-pipe-driven convective vapor and heat flow: Depending on the ambient percolation flux and on whether heterogeneity in the k_b distribution and/or heating conditions result in zones of focused condensate flow, heat-pipes can result in a significant cooling effect and cause greater liquid saturation and liquid-phase flux in the vicinity of emplacement drifts (see Sections 1.10.5.1, 1.10.6, and 10.1.2.5). For ambient percolation fluxes greater than 1.0 mm/yr (certainly within the range of estimated flux), the tendency for heat pipes to cause cooler/wetter conditions near emplacement drifts increases with ambient percolation flux (Section 1.10.6).

Contribution of vapor-diffusion-driven vapor and heat flow: Depending on whether the binary diffusion of water and air is significantly enhanced (relative to "nominal" vapor diffusion), vapor diffusion can result in additional vaporization and vapor transport (relative to that driven by boiling alone) or cause significant vaporization and vapor transport after boiling has ceased (Section 10.1.3.2).

Engineered System heterogeneity: Arises from the following design aspects:

WP layout: This includes the axial spacing between WP centers and the lateral spacing between drift centers (Sections 1.10.5 and 1.10.6).

WP heat output: This can vary substantially among spent nuclear fuel (SNF) WPs; moreover, the Defense High-Level Waste (DHLW) WPs generate an insignificant amount of heat compared to even the coolest SNF WPs. For WPs that are thermally isolated from each other (as occurs in the ACD rev 00 design), the distribution of the respective WPs along the drift can make a large difference in determining their respective environments, including *T*, *RH*, liquid-phase saturation, and liquid-phase flux (Sections 1.10.5 and 1.10.6).

WP emissivity: This quantity determines the efficiency of thermal-radiative heat transfer from the WP to the drift wall and from WP to WP (Section 1.10.5.3).

Backfill thermal conductivity: This quantity determines the temperature difference ΔT_{drift} between the WP and the drift wall that can substantially reduce RH on the WP surface ΔRH_{drift} (relative to that in the adjacent near-field rock). The reduction in RH is most effective if the backfill does not wick moisture back to the WP (Section 1.10.5.5).

Backfill hydrological properties: These properties affect the degree to which wicking may transport moisture from the (cooler and more humid) near-field rock to the (hotter and less humid) WP surface. If wicking in the backfill is present, it can reduce ΔRH_{drift}. The k_b of the backfill will determine the degree to which buoyant gas-phase convection influences heat transfer between the WP and drift wall. Backfill hydrological properties also affect how effectively the drift seepage flux is able to drain out of the drift (Section 1.10.5.4).

Backfill configuration: The important items include: (1) the percentage of the drift that is backfilled (full versus partial backfill), (2) the configuration of the upper backfill surface (sloping versus horizontal), and (3) whether backfill is allowed to fill in between WPs. The temperature difference ΔT_{drift} between the WP and the drift wall depends on the percentage of the drift that is backfilled. This may also affect the degree to which buoyant gas-phase convection influences heat transfer between the WP and drift wall (Section 1.10.5.4).

Invert thermal conductivity: This quantity affects both the WP and drift wall temperatures. For cases with backfill, it, along with K_{th} in the backfill, determines the temperature difference ΔT_{drift} between the WP and the drift wall (Section 1.10.5.5).

Invert hydrological properties: These properties affect the degree to which wicking may be important. If wicking in the invert is important, it can moderately reduce ΔRH_{drift}. These properties also affect how effectively the drift seepage flux is able to drain out of the drift. Radionuclide transport will also be significantly affected, particularly as to whether transport is limited to liquid-phase diffusive transport (Section 1.10.5.4).

Proximity to the edge of the repository: The edge-rewetting/shedding effects tend to increase liquid-phase flux with proximity to the repository edge; the edge-cooling effect decreases the local heat flux that is available to vaporize the incoming liquid-phase flux with proximity to the edge. The edge-shedding effect can also increase the tendency for heat pipes to dissipate heat at the repository edge, thereby increasing the edge-cooling rate. Taken together, these effects increase the likelihood of greater-than-ambient liquid-phase fluxes reaching the repository horizon. (Section 1.10.6).

There are two fundamentally different ways that WPs can be arranged in the repository at Yucca Mountain. The first approach (called square spacing) attempts to uniformly distribute the WP decay heat over the repository area by placing the WPs with roughly the same axial and lateral spacing between WPs (as is done in the ACD rev 00 design). The second approach (called the line load) lineally concentrates the WP decay heat to the greatest possible extent by placing the WPs end-to-end along the emplacement drifts. For a given AML, this allows for the maximum possible spacing between drifts and requires the minimum possible total length of emplacement drift. The two primary 83.4-MTU/acre repository designs analyzed in Section 1.10 are:

ACD rev 00 design: This design utilizes a "square" geometry with the spacing between drift centerlines being roughly the same as the axial center-to-center spacing between SNF WPs. The ACD rev 00 has a lineal mass loading (LML) of 0.46 MTU/m and drift spacing = 22.5 m. Heating heterogeneity that arises from square WP spacing will add substantially to the effects of natural system heterogeneity on the spatial variability of T, RH, liquid-phase saturation, and liquid-phase flux along emplacement drifts.

Line-load design: This approach places WPs nearly end-to-end and the drifts are spaced far apart. An example of this approach assumes a 0.1-m gap between WPs, resulting in LML = 1.11 MTU/m and drift spacing = 53.8 m. In spite of the large differences in heat generation among the various WPs, the highly efficient thermal-radiative WP-to-WP heat transfer facilitated by the end-to-end WP spacing causes the line of WPs to function as though it were a uniform line-heat load.

Consequently, the line-load generates very uniform *T*, *RH*, liquid saturation, and liquid-phase flux along the drifts. Moreover, the high axial WP-to-WP heat conductance will homogenize some of the effects of natural system heterogeneity and edge-cooling/rewetting/shedding on conditions along the drift. In effect, the line of closely spaced WPs serves as a preferential heat-flow conduit that allows heat to be delivered to otherwise vulnerable areas of the drift.

Contents

1.1.3 Modeling and Analysis Methodologies

1.1.3.1 Modeling and Analysis Approach

The following steps articulate the methodology that is being used in the development, refinement, and validation of conceptual and numerical models used. The steps are not necessarily taken in order; the method is a process of iterative refinement as knowledge of the site-repository system increases. The method relies on a combination of mathematical models and laboratory and field data to develop conceptual models and parameter regimes and to test hypotheses.

1. Conceptual and Mathematical Model Development.

- Identify processes and interaction of processes that are important to thermal-hydrological (T-H) behavior in the near-field and altered zone.
- Develop a conceptual model of T-H behavior in the near-field and altered zone.
- Develop mathematical models of processes consistent with the conceptual model.
- Verify the mathematical models.

2. Process Analysis and Parameter-Sensitivity Studies.

- Develop an understanding of the important T-H processes and their intercoupling with geochemical and geomechanical processes through the use of detailed process models.
- Identify parameter regimes that govern T-H behavior for ambient and man-made conditions.
- Quantify the parameter sensitivity of T-H behavior to ambient and man-made conditions.
- Refine conceptual and mathematical models on the basis of results from detailed process models and parameter-sensitivity analyses.

3. Integration with Experiments.

- Conduct scoping calculations to help design laboratory- and field-scale experiments to quantify important parameters and properties.
- Refine conceptual and mathematical models on the basis of results from laboratory and field experiments.

4. Hypothesis Testing and Model Validation.

- Establish hypotheses critical to prediction of thermal-hydrological behavior.
- Establish hypotheses critical to EBS performance.
- Conduct scoping calculations to help design laboratory- and field-scale tests that critically test these hypotheses.
- Test hypotheses on the basis of testing, at the laboratory and field scale, and analysis, including bounding analysis.
- Validate conceptual and mathematical models on the basis of laboratory and field experiments and hypothesis testing.

5. Subsystem Performance Assessment.

- Determine the parameter sensitivity of EBS performance to natural and man-made processes.
- Develop simpler models (abstractions) for EBS and total systems performance assessment.

1.1.3.2 Mathematical Models

The behavior of thermal-hydrological processes, as described in Sections 1.7 and 1.8, is predicted with the use of mathematical models. These models are usually partial differential equations describing the balance of energy and the balance of mass of each important chemical species, which can include air and water. A species such as water can occur in both a gas and a liquid (or aqueous) phase. Mathematical models are usually defined at the macroscopic level: that is, they are derived from microscopic balance laws through volume-averaging [Bear and Bachmat, 1990] over a representative elementary volume (REV) of the porous medium. Predicted quantities are therefore averages over the REV, and any variations in these quantities are lost over distances less than the size of the REV.

The following assumptions are typical of macroscopic mathematical models for flow and transport in porous media:

- Darcy's law is assumed to hold for advective fluxes.
- Fick's law is assumed to hold for diffusive and dispersive fluxes.
- Either approximate local or partial thermodynamic equilibrium or assigned disequilibrium is assumed over the REV, or macroscopic kinetic rate laws can be used.

Whether or not a REV can be defined that is smaller than the system to be modeled is an open question, as is the question of whether the REV is the same for flow, transport, and heat transfer processes. Developments in the literature will be monitored, and mathematical models used will be tested against experiments as data become available to assess their adequacy for representing important processes and phenomena in fractured porous media. Three principal classes of mathematical treatments have been developed in the past:

1. Equivalent Continuum Model (ECM). This model assumes equality of the matric potentials of the fracture and matrix. Composite characteristic curves are used to define the unsaturated hydraulic conductivity and matric potential.

Advantages:

- Computationally simple because it uses a single continuum for both fractures and matrix.

Disadvantages:

- The assumption that the fracture and matrix are in equilibrium is adequate only if fracture fluxes are low enough [Nitao et al., 1993; Buscheck et al., 1991]. This assumption is adequate for modeling condensate drainage during the intermediate and late stages of repository-heat-driven moisture movement, but may be inadequate during early stages when high specific heat flux in the boiling region leads to high condensate drainage fluxes. This assumption is not adequate for modeling episodic infiltration events.
- Fractures are not treated as discrete features; rather, their effects are averaged over the whole spatial domain. In effect, fractures are treated as a porous medium.

2. Dual Permeability Model. This model treats the matrix and the fractures as two distinct porous continua with a transfer term to represent the flux between the two continua.

Advantages:

- Less computationally intensive than the discrete fracture-matrix model and although more computationally intensive than the ECM, is manageable in many cases.

- Can handle larger advective fluxes without producing conditions near 100% liquid-phase saturation in the matrix, because it does not assume capillary equilibrium between fracture and matrix.

Disadvantages:

- More computationally intensive than equivalent continuum method, so that for more complex analyses, it may be impractical.
- Typical fracture-matrix transfer terms cannot adequately treat fracture-matrix interaction, especially during early and intermediate stages of matrix imbibition.
- Fractures are not treated as discrete features; rather, their effects are averaged over the whole spatial domain. In effect, fractures are treated as a porous medium.

3. Discrete Fracture-Matrix Model (DFM). This model spatially discretizes the space occupied by the fractures and the matrix by finite element or finite difference elements. Because the location and morphology of individual fractures are not usually well known, their geometric characteristics are either (1) interpolated from field data, (2) randomly generated, or (3) represented using an idealized geometry.

Advantages:

- Actual fracture geometry is considered, including size of fractures and intersections.

Disadvantages:

- Highly computationally intensive.
- Available data may not justify the approach.

The selection of an approach must weigh the trade-off between computational complexity and physical accuracy. Factors that should be considered include (1) the magnitude of fracture fluxes, (2) the size of the domain being modeled, and (3) the scale over which results are desired. The discrete fracture approach is probably not practical for repository-scale and mountain-scale calculations, but it can be used to determine phenomenological parameters needed for the dual permeability approach. This approach can also be useful in interpreting the results of laboratory-scale experiments. Complementary use of these three approaches is probably the only effective way of incorporating some of the effects of nonequilibrium fracture-matrix behavior at any practical scale of analysis.

Mathematical models have the following limitations:

1. Because they are usually macroscopic (based on volume averaging), the effects of fine-scaled physical processes may be lost.
2. They have a somewhat limited ability to incorporate realistic spatial variability of input parameters as a result of geological heterogeneities.
3. They are subject to spatial uncertainty of input parameters as a result of limitations in geological data gathering.
4. All of the detailed physical and chemical processes cannot be implemented because of computational limitations.

An example of the first limitation is "dispersion of the liquid phase," a term used by Nitao and Buscheck [1991] in the context of the deviation in the movement of a liquid front relative to the mean position of the front as a result of viscous fingering and branching at fracture intersections as it percolates down a fracture network. Expressions for phase dispersion will involve deriving higher-order terms in macroscopically averaged models. The effect of the second and third limitations can be reduced by sensitivity analyses, stochastic realizations, and phenomenological models. To reduce the effect of the fourth limitation, conservative and judicious assumptions and simplifications must be used.

1.1.3.3 Numerical Models

The partial differential equations for the macroscopic balance of energy and mass are highly nonlinear for multiphase fluid flow with phase changes (i.e., evaporation and condensation). They must, therefore, be solved numerically. The codes V-TOUGH [Nitao, 1990] and NUFT [Nitao, 1994] have been used for this study. They both use the integrated finite-difference method. V-TOUGH considers only the transport of air, water, and energy; NUFT can also consider transport of other species, including radionuclides. NUFT also has mechanical dispersion of components; it has more physical and numerical options, is more flexible, is more computationally efficient, and is more user friendly. It can also handle additional fluid phases, such as a nonaqueous hydrocarbon phase. The following are the important output variables for the two codes:

V-TOUGH: Spatial and temporal distribution of gas- and liquid-phase pressure, gas- and liquid-phase saturation, air mass fraction in gas and liquid phases, water mass fraction in gas and liquid phases, and temperature.

NUFT: Same as V-TOUGH but, in addition, can solve for mass fraction of other components, including radionuclides.

Planned enhancements to NUFT include the following:

- Dual-permeability models.
- Higher-order models for dispersion and fracture-matrix interaction.
- Radioactive and chemical reactions.
- Geomechanical coupling with thermal-hydrological behavior.
- Extension of the current suite of numerical methods.

Software quality ssurance (SQA) will be carried out for V-TOUGH and NUFT according to the Individual Software Plan (ISP) developed for each code. The ISP will describe the configuration management and control of the codes, necessary documentation, walk-throughs, and benchmarking problems. Software verification will include the comparison of results of the codes with analytical solutions and with results of other selected numerical models. Because of uncertainties and heterogeneities, it is difficult to have enough information to explicitly validate a model based on a multiphase, nonisothermal porous media flow and transport code. Partial model validation will be performed using laboratory and field experiments by (1) determining whether calibration of the model is possible and (2) whether the conceptual model predicted by the model is consistent with observations.

V-TOUGH has been qualified for use in qualitiy affecting work. NUFT has been benchmarked against the V-TOUGH code for a wide range of problems related to decay-heat-altered nonisothermal flow and transport at Yucca Mountain; for all of the cases compared, NUFT and V-TOUGH predicted essentially identical results.

1.1.3.4 Model Geometries

The thermal-hydrological model calculations in Chapters 1 and 10 were conducted with five different types of models:

Drift-scale two-dimensional equivalent continuum model (ECM) model: This model represents (in very fine detail) two-dimensional T-H behavior in a plane transverse to the emplacement drifts (including the rock pillar separating the drifts), and one-dimensional mountain-scale T-H behavior that occurs from the water table to the ground surface; it does not represent three-dimensional mountain-scale T-H behavior. This model axially averages the heat output from a row of WPs with a decay-heat generation based on a mixture of 40% BWR WPs that contain 40 assemblies per WP and 60% PWR WPs that contain 21 assemblies per WP. Other mixtures of SNF WP types and SNF ages are also represented with this model. This model, which assumes a fixed-depth, constant-temperature water table. This model is used in Sections 1.10.2–1.10.7.

Drift-scale three-dimensional ECM model: This model represents detailed three-dimensional T-H behavior in and around the emplacement drifts (including the rock pillar separating the drifts) and one-dimensional mountain-scale T-H behavior that occurs from the water table to the ground surface; it does not represent three-dimensional mountain-scale T-H behavior. This model utilizes the equivalent continuum model (ECM) to represent fracture-matrix flow. This model represents six WPs, of which each has unique decay-heat characteristics. This model assumes a fixed-depth, constant-temperature water table. This model is used in Sections 1.10.5 and 1.10.6.

Mountain-scale ECM model: This model represents three-dimensional mountain-scale T-H behavior with an R–Z coordinate system and represents WP decay heat by uniformly distributing the heat over a disk-shaped area; this is sometimes called a smeared-heat-source model. This model utilizes ECM to represent fracture-matrix flow and represents T-H behavior from 1 km below the water table to the ground surface. The lower model boundary (1 km below the water table) has a fixed pressure and fixed temperature. This model is used in Section 1.10.6 and in Sections 10.1 and 10.2 of Chapter 10.

Hybrid drift-scale–mountain-scale ECM model: This model represents both the detailed three-dimensional drift-scale T-H behavior and three-dimensional mountain-scale T-H behavior from 1 km below the water table to the ground surface. This model is also used to check the appropriateness of the drift-scale model calculations in analyzing T-H behavior over the entire repository area. This model utilizes ECM to represent fracture-matrix flow. This model is used in Section 1.10.6.

Drift-scale two-dimensional discrete fracture-matrix (DFM) model: This model represents both (detailed) two-dimensional drift-scale T-H behavior and one-dimensional mountain-scale T-H behavior from the water table to the ground surface. This model utilizes the DFM that discretely models flow in the fractures and matrix block, and thereby accounts for nonequilibrium fracture-matrix interaction [Nitao and Buscheck, 1994]. This model axially averages the heat output from a row of WPs with a decay-heat generation based on a mixture of 40% BWR WPs that contain 40 assemblies per WP and 60% PWR WPs that contain 21 assemblies per WP. Other mixtures of SNF WP types and SNF ages are also represented with this model. This model assumes a fixed-depth, constant-temperature water table.This model is used to check the appropriateness of the drift-scale ECM model calculations in analyzing gas- and liquid-phase flow in the near field. This model is used in Section 1.10.7.

All of the models assume that the relative humidity *RH* of the atmosphere is fixed at a value that corresponds to being in vapor pressure equilibrium with the uppermost hydrostratigraphic (TCw) unit. This results in $RH \approx 99\%$ in the atmosphere, which precludes any diffusive loss of water vapor out of the top of the mountain.

1.1.3.5 Modeling Thermal-Radiative Heat Transfer in the Drifts

Thermal-radiative heat transfer is considered between all surfaces in the emplacement drift. For the two-dimensional drift-scale model all surfaces can emit heat to all other surfaces, while in the three-dimensional model the assumption is made that the primary direction of thermal-radiative heat transfer is from the WP surfaces to the drift wall and floor surface and axially from WP to WP. In the NUFT code, a thermal-radiative heat transfer coefficient must be specified for each pair of emitting surfaces. For most of the thermal radiation connections, the heat-transfer coefficient is based on the following derivation.

Consider the thermal radiative heat transfer between an area A_i on the WP surface and a portion of the drift wall with area A_j. (In our application, A_i is the surface of one of possibly many computational grid cells that represent the WP. Similarly, A_j is part of the surface of a cell at the drift wall.) Suppose that A_i is at temperature T_i and A_j is at temperature T_j. Because the drift enclosure is large compared to the size of the WP, thermal radiation from the WP can be considered to be a graybody inside of a large blackbody cavity. The thermal-radiative heat flux between A_i (the WP) and A_j (the drift wall or floor surface) is then given by

$$q_{ij} = \varepsilon\sigma A_i F_{ij}(T_i^4 - T_j^4) , \tag{2}$$

where ε is emissivity of surface A_i and σ is the Stephan-Boltzmann constant. The view factor (also called shape factor or form factor) is denoted by F_{ij} and is given by

$$F_{ij} = \frac{1}{A_i}\int_{A_i}\int_{A_j}\cos\phi_i\cos\phi_j\frac{dx_i\,dx_j}{\pi r_{ij}^2} , \tag{3}$$

This expression is found in most heat transfer texts [Holman, 1990]. The terms x_i and x_j are the integration variables over A_i and A_j, respectively. The terms ϕ_i and ϕ_j are the solid angles between the vector joining the two surfaces A_i and A_j and the normal vectors for these respective surfaces. The term r_{ij} is the distance between the two surfaces.

Note that Eq. (2) also applies to thermal radiation between to drift surfaces (such as between the drift wall and drift floor). If T is about the same for these two surfaces, or if the two surfaces are far apart, thermal radiation between these surfaces may be neglected. In the center-in-drift (CID) WP configuration, because the two sides of the drift are being equally heated, cross-drift thermal radiation will be negligible. In the off-center-in-drift (OCID) configuration, the asymmetrical heating of the drift surfaces will result in significant temperature differences from one side of the drift to the other. This situation is addressed with the detailed two-dimensional drift-scale model that includes thermal-radiative heat transfer connections between all surfaces in the drift. For the three-dimensional drift-scale model, the side-to-side symmetrical heating is assumed to preclude the need to include cross-drift thermal radiation.

If surfaces A_i and A_j are sufficiently small and/or the separation distance r_{ij} is sufficiently large, then the terms r_{ij}, ϕ_i and ϕ_j in Eq. (3) do not vary by much; therefore these terms may be replaced with constants and we have

$$F_{ij} \approx \frac{1}{A_i}\cos\phi_i\cos\phi_j\frac{A_iA_j}{\pi r_{ij}^2} , \tag{4}$$

where r_{ij}, ϕ_i and ϕ_j are evaluated at centroids of A_i and A_j. A way to determine whether the condition is satisfied is to compare r_{ij}, ϕ_i and ϕ_j at extremal points on the surfaces A_i and A_j with the centroid values.

When Eq. (4) does not hold, surface integration has to be performed analytically or numerically. In some cases it can be easily estimated. An example is given below for the thermal-radiative heat transfer between parallel disks.

To calculate the total thermal-radiative heat flux from a WP, the heat flux term q_{ij} is first summed over all A_j on the drift-wall surfaces that can be seen by surface A_i on the WP, and then summed over all A_i on the WP. Thus we have the total thermal-radiative heat flux equal to

$$q_{wp} = \sum_i \sum_j q_{ij} = \sum_i \sum_j \varepsilon \sigma A_i F_{ij} (T_i^4 - T_j^4), \quad (5)$$

Although emissivity of the rock can be 0.85 to 0.95, a value of 1.0 was assumed in all calculations. This assumption can be justified on the basis of the relationship [Holman, 1990] for thermal-radiative heat transfer q between two concentric cylindrical surfaces:

$$q = \frac{\sigma A_1 \left(T_1^4 - T_2^4\right)}{1/\varepsilon_1 + (A_1/A_2)(1/\varepsilon_2 - 1)}, \quad (6)$$

where A_1 and A_2 are the areas, T_1 and T_2 are the temperatures, ε_1 and ε_2 are the emissivities of the inner and outer cylindrical surfaces, and σ is the Stephan-Boltzmann constant. If the outer cylinder is much larger than the inner cylinder (A_1/A_2 approaches 0) or if ε_2 is close to 1, then Eq. (6) becomes:

$$q = \sigma A_1 \varepsilon_1 \left(T_1^4 - T_2^4\right), \quad (7)$$

which is readily applied to calculate the radiation heat transfer from a hot object to a large room. In effect, the hot object (or WP) functions as a nonblackbody (also called a graybody) with a given emissivity ε_1 and area A_1, while the surfaces of the room (or emplacement drift) function as though they were blackbodies.

One of cases for which Eq. (4) does not hold is for thermal-radiative heat transfer between the ends of WPs in the line-load design. The WP-to-WP thermal-radiative heat transfer for this situation can be represented by the relationship [Holman, 1990] for the net radiation heat exchange q_{net} between parallel disks:

$$q_{net} = \frac{\sigma A_1 \left(T_1^4 - T_2^4\right)}{(1-\varepsilon_1)/\varepsilon_1 A_1 + 1/A_1 F_{12} + (1-\varepsilon_2)/e_2 A_2}, \quad (8)$$

where A_1 and A_2 are the areas, T_1 and T_2 are the temperatures, ε_1 and ε_2 are the emissivities of the disks, F_{12} is the radiation shape factor between the disks, and σ is the Stephan-Boltzmann constant. The radiation shape factor F_{12} can be determined on the basis of the ratio d/x, where d is the diameter of the disks and x is the separation distance between the disks, and a graphical relationship given in Holman [1990]. For the 1.11-MTU/m line-load design, $d/x = 18$, which results in $F_{12} = 1$. For $\varepsilon_1 = \varepsilon_2 = 0.8$, $q_{net} = 0.667\sigma A_1$, while for $\varepsilon_1 = \varepsilon_2 = 0.3$, $q_{net} = 0.298\sigma A_1$; consequently, WP-to-WP thermal-radiative heat transfer is 2.24 times more efficient for the case with $\varepsilon = 0.8$ (than for the case with $\varepsilon = 0.3$).

1.1.3.6 Parameter Sensitivity and Process Analysis

The general methodology for this part of the study is to perform parameter-sensitivity analyses and to ascertain parameter regimes of characteristic behavior. The following analyses have been (and will continue to be) performed:

- Theoretical study of fracture-matrix interaction.
- Effect of nonequilibrium fracture flow arising from episodic infiltration events and condensate drainage.
- Effect of decay heat on moisture balance in the unsaturated zone (UZ).
- Nonisothermal processes involved in drift-scale and mountain-scale moisture movement.
- Effect of decay heat on buoyant gas-phase convection in the UZ and the implications of this convection for heat and moisture flow.
- Effect of decay heat on buoyant liquid-phase convection in the saturated zone (SZ) and the implications of this convection for heat and moisture flow.
- Sensitivity study of gas-phase and liquid-phase rewetting of the repository.
- Effect of natural system heterogeneity on condensate shedding and on the focusing of vapor and condensate flow.
- Effect of natural system heterogeneity on temperature T and RH in the repository.
- Effect of natural system heterogeneity on advective liquid-phase flow in the repository (i.e., seepage into emplacement drifts).
- Effect of thermal loading design (including WP layout) on T and RH in the EBS and on WPs.
- Effect of thermal loading design (including WP layout) on advective liquid-phase flow in the repository (i.e., seepage into emplacement drifts).
- Optimization of thermal loading design (including WP layout) to improve EBS performance and reduce uncertainty in the EBS environment.
- Determination (and ranking) of processes important to the release and transport of radionuclides from the EBS.
- Bounding analyses related to hypotheses critical to the prediction of thermal-hydrological (T-H) behavior (and EBS subsystem performance).
- Bounding analyses related to hypotheses critical to EBS performance.

The following analyses wil be performed in future studies:

- Effect of decay heat on the diffusive flux of water vapor at the ground surface.
- Interaction between T-H effects and surface infiltration.
- Sensitivity study of thermal-hydrological-geomechanical (T-H-M) coupling.
- Sensitivity study of thermal-hydrological-geochemical (T-H-C) coupling.
- Influence of T-H flow processes on the geochemistry of the water contacting the WP.
- Impact of repository depth on T-Hand T-H-M processes.
- Impact of drift ventilation on T-H and T-H-C processes.

Contents

1.2 Background and Available Data on Yucca Mountain

Yucca Mountain (YMP) consists of a series of variably fractured, nonwelded to densely welded tuff units with an eastward tilt of about 5 to 30° (Montazer and Wilson, 1984). The thickness of the unsaturated zone (UZ) varies from 500 to 750 m. The potential repository location is in Topopah Spring moderately to densely welded tuff (unit TSw2), which is about 350 m below the ground surface and 225 m above the water table (Klavetter and Peters, 1988). Montazer and Wilson (1984) report the absence of perennial streams at Yucca Mountain; therefore, recharge from rain and snow occurs episodically. Flint (1991) reports that mean annual precipitation at Yucca Mountain varies areally from 150 to 240 mm/yr (with an average of 170 mm/yr over the repository footprint).

1.2.1 Matrix and Fracture Saturation

One of the challenges in understanding the matrix and fracture saturation is that the interaction between moisture flowing through the fractures and matrix may not be in equilibrium. In this section we present the saturation data and an interpretation of those data, including calculations that are largely based on equilibrium conditions. A major conclusion from these analyses is that a noted discrepancy between calculated and observed saturation versus depth profiles may arise from ignoring the effects of transient behavior. This gives significant insight into the hydrologic system at Yucca Mountain.

The matrix properties of Yucca Mountain hydrostratigraphic units used in calculating saturation versus depth profiles in Rev. 0 of the NFER are summarized in Table 1.2.1-1 (Klavetter and Peters, 1988). The units generally fall into two categories: (1) welded tuffs of very low permeability and low porosity (TCw, TSw1, TSw2, and TSw3), and (2) nonwelded vitric tuffs of high permeability and high porosity (PTn and CHnv). The zeolitized nonwelded CHnz has low permeability and intermediate porosity, and the welded PPw has intermediate permeability and porosity. The matrix permeabilities of the nonwelded vitric tuffs are 4 to 5 orders of magnitude greater than those of the welded tuffs and the zeolitized nonwelded CHnz. Because of the very small matrix pore size of all of the units, water in the matrix pores should be held under high capillary suction potential, and if the system is in capillary equilibrium this should cause the zone of capillary rise to extend from the water table to the ground surface (Fig. 1-1) (see end of this section 1.2.1 for discussion of exceptions to capillary equilibrium conditions).

The solid curve in Figure 1.2.1-1 shows the calculated vertical saturation distribution (based on the capillary properties given in Table 1.2.1-1) from the water table (z = 568 m) to the ground surface (z = 0 m) for zero recharge flux, i.e., at gravity-capillary equilibrium. The calculated zone of capillary rise extends from the water table to the ground surface. The permeable nonwelded vitric PTn and CHnv units have a much lower saturation at a given moisture potential than the densely welded units. Given that, at gravity-capillary equilibrium, the potential is fixed by the distance above the water table, the saturation in these units is lower than the saturation in the neighboring welded units at essentially the same distance above the water table.

Presumably, fractures have a much lower saturation at a given potential than the adjacent matrix, and the fractures will be essentially drained of water at equilibrium, although there are few actual data on the capillary properties and relative permeability behavior of fractures. They will also have very low saturations, *at steady state*, with any value of steady flux well below the critical value for matrix-dominated flow (Nitao, 1991). This is the physical basis for the Equivalent Continuum Model (ECM), which forces local equilibrium between the fractures and the matrix. However, much work remains to be done to determine the limits of validity of the ECM. It is not clear that the UZ system at Yucca Mountain is even approximately described by the steady-state assumption, under either ambient or thermally perturbed conditions.

The intensity of precipitation, both during summer and winter, is highly variable spatially and temporally. Montazer and Wilson (1984) recognized the importance of episodic flow at Yucca Mountain. More by argument than by analysis, they estimated an average recharge flux (i.e., net infiltration) of 0.5 to 4.5 mm/yr. They also postulated the possibility of the temporary development of perched water within the nonwelded units, which then drains into fractures and flows directly to the water table. Moreover, they stated that most of the net infiltration is diverted eastward as lateral flow within and above the nonwelded PTn unit; the remainder is percolated vertically in the welded TCw unit, and is intercepted by structural features that transmit most of the infiltrated water to the water table.

Although precipitation is episodic, and one can thus expect episodic recharge, the saturation conditions in the rock tend to be dampened by rate-limited imbibition and matrix flow. Therefore, it was assured that estimates of long-term average flux can be made based on saturation conditions and the assumption of steady state. Core samples of the TSw2, TSw1, and TSw3 hydrostratigraphic units have an initial liquid saturation of 65 ± 19% [as reported in the *Yucca Mountain Project Reference Information Base* (*RIB*), DOE, 1990] and a porosity of 11% (Klavetter and Peters, 1988; Peters et al., 1984). With limited data, Montazer and Wilson (1984) attempted preliminary estimates of net infiltration within the major hydrostratigraphic units. They found the apparent net infiltration (or recharge flux) to vary with depth, including apparent positive fluxes (i.e., downward) in the nonwelded PTn and CHn and apparent negative fluxes (upward due to vapor flow) in the welded TSw. Gauthier (1990) attempted to fit more recent data using a one-dimensional steady-state ECM and assuming that the percolation flux is invariant with depth. Gauthier (1990) obtained the best overall fit of the saturation profile, using available matrix data, with a surface recharge rate of 0.01 mm/yr. Using a one-dimensional steady-state ECM, Buscheck and Nitao (1991a) determined that the observed range in saturation at the repository horizon is consistent with recharge flux ranging between –0.0005 and 0.05 mm/yr. (Fig. 1.2.1-1), and concluded that, given the uncertainty in matrix characteristic curves, the percolation flux at the repository horizon is effectively zero. The steady-state assumption is the crucial hypothesis to be tested. If it is not correct, the error in percolation flux could be very large.

In addition to the equilibrium case, Buscheck and Nitao (1991a) also calculated saturation profiles with the steady-state, equivalent continuum assumption, for recharge fluxes of 0.045 and 0.0132 mm/yr. As shown in Fig. 1.2.1-1, the resulting calculated saturation at the repository horizon is 85% and 95%, respectively. The capillary properties of the TSw2 and TSw3 cause their calculated steady-state saturation to be quite sensitive to the value of percolation flux. On the other hand, at low flux, saturation in the nonwelded vitric units is much less sensitive to variations in the steady-state recharge flux. Small changes in saturation in these units can accommodate large changes in flux unless the system is very near 100% saturation.

Saturation ranges obtained from the *RIB* are also shown on Fig. 1.2.1-1. While zero recharge flux results in a calculated saturation of about 10% for the PTn and CHnv, the *RIB* reports mean saturation values of 61% and 91%, respectively. Therefore, although a zero recharge flux is consistent with saturation data at the repository horizon, it is not consistent with the saturation data in the high-k_m vitric nonwelded PTn and CHnv. Some of this inconsistency may result from inadequate matrix-property data or a lack of correspondence between the matrix-property data and the saturation data (i.e., different physical samples may have been used for saturation measurements and capillary properties). However, this inconsistency is too great to be entirely attributed to such causes. Apparently, significant recharge fluxes (i.e., much greater than those shown in Fig. 1.2.1-1) are able to reach the high-k_m units without affecting the saturation of the neighboring low-k_m units. This strongly suggests that the system is not in equilibrium – that transient fracture flow occurs episodically through the TCw, TSw1, TSw2, and TSw3, for time periods too short to approach steady state (Buscheck and Nitao, 1991a; Buscheck et al., 1991a). Bomb-pulse ^{36}Cl measurements reported by Norris (1989) and saturation and water potential data reported by the DOE (1986) are also consistent with nonequilibrium fracture flow from the ground surface to considerable depths. Steady-state calculations, accordingly, are not believed to be adequate for modeling the effective percolation flux at the repository horizon.

The importance of fractures to the hydrology at Yucca Mountain cannot be overstated. They are responsible for the highly heterogeneous character of the hydraulic conductivity distribution. Depending on the hydrostratigraphic unit, the contrast between fracture and matrix permeability ranges from 1 to 7 orders of magnitude. Estimates of fracture density (based on core) range from 20 to 42 fractures/m^3 (Scott and Castellanos, 1984). Fracture mapping in the Exploratory Studies Facility (ESF) indicates that fractures occur with two dominant orientations, a NW striking nearly vertical set, and a sub-horizontal set with a north-easterly dip. Along the main drift, fracture density within the TSw2 is approximately 3-4 fractures/m and within the PTn and overlying units is <1 to 2 fractures/m (Barr, et al., 1996).

Montazer et al. (1985) measured bulk (air) permeability, k_b, in the TSw to a depth of 100 m, obtaining $7 \times 10^{-13} < k_b < 1 \times 10^{-11}$ m^2. For well J–13, Thordarson (1983) reported a bulk hydraulic conductivity of 1 m/day ($k_b = 1.7 \times 10^{-11}$ m^2). Using these estimates, Buscheck and Nitao (1991a, 1991b) calculated the hydraulic fracture aperture for the values of fracture spacing listed in Table 1.1.2-1, on the basis of the cubic law and the equivalent continuum model (ECM) definition of bulk permeability, $k_b = k_m(1 - \phi_f) + k_f\phi_f$, where k_m and k_f are the matrix and fracture permeability, and ϕ_f is the fracture porosity (the ECM calculation is accurate for calculating average bulk permeability to liquid for a completely saturated system or for the average bulk air permeability for a partially drained system, provided, in the latter case, that the fracture permeability is much greater than the matrix permeability). For this calculation, it was conservatively assumed that all fractures are vertical. At a spacing of 0.01 m between fractures (100 fractures/m), the available bulk permeability measurements indicate fracture apertures ranging from 43 to 127 μm. If we assume that the bulk permeability measurements made elsewhere represent the range within welded units exposed in the ESF, then, based on the ESF fracture density from main drift mapping (Barr, et al, 1996), an aperture range of 141 to 407 μm is indicated.

More recently, extensive testing of surface-based boreholes has been conducted by the U.S. Geological Survey (USGS) to determine air permeability in the UZ at Yucca Mountain. The best data released to date were for borehole SD-12 (LeCain and Walker, 1994). A new method of analysis for the pressure fall-off data was developed by Cox and Stellavato (1996), to take into account the effect of wellbore storage and skin in transient spherical flow. According to Cox and Stellavato, the data from 124 tests in the Tiva Canyon and Topopah Spring intervals in SD-12 were suitable for analysis, resulting in a range of permeability from 0.1×10^{-12} m^2 to 67×10^{-12} m^2, with an average of 7.4×10^{-12}. Most of the tests exhibited significant positive skin factors, indicating pervasive drilling damage to the fracture system, presumably caused by the invasion of drilling fines. The authors noted that the permeability of the most permeable zones may be seriously underestimated, since the pressure gauge resolution was only 10 Pa. Nevertheless, the dominance of fractures in determining the bulk permeability is clearly shown, since even the lowest value of k_b is about 5 orders of magnitude greater than the matrix permeability in the TCw and TSw.

Even in the non-welded Calico Hills, there is evidence of connected fractures, based on bulk permeability estimates, albeit in the saturated zone. Figure 1.2.1-2 shows the distribution of permeability values derived from laboratory measurements of core samples and from pump tests in the saturated zone, compiled by Loeven (1993). The curves were calculated from the log mean and log standard-deviation values given by Loeven. All three of the distributions are approximately log-normal, based on an examination of higher moments of log(k). The distribution of permeability values derived from pump tests is plotted in the rightmost curve of Fig. 1.2.1-2. From left to right, the σ values (standard deviation of the natural log of permeability) for these distribution functions are 2.763, 2.510, and 2.234, respectively. The pump tests clearly show much higher permeability values than the core measurements, and provide strong evidence of fracture flow within the Calico Hills where these tests were performed. All of the frequency plots span at least five orders of magnitude of permeability values, indicating that the system is strongly heterogeneous on both the laboratory scale and the scale of single borehole tests.

The existence of such a large range of permeability, particularly the contrast between fractures and matrix, imposes a corresponding range of time constants for transient behavior depending upon capillary characteristics and indicates that careful analysis is required to determine under what conditions and for what physical processes the use of steady-state and equivalent-contiuum assumptions is valid. It strongly

suggests that the discrepancy between calculated and observed saturation versus depth profiles may arise from ignoring the effects of transient behavior, rather than from variability in matrix properties measured in the laboratory.

Further evidence that the UZ fracture-matrix system is not at equilibrium is given by L. E. Flint (1996) and by Rousseau et al. (1996). Flint's data for mean porosity, volumetric water content, saturation, and water potential for all samples from the Paintbrush Group nonwelded rocks (PTn) and Topopah Spring tuff welded rocks (TSw) are summarized by Rousseau et al. in their Table 4.2.1-2 (1996). For uppermost lithostratigraphic units (Tpcpv2 and Tpcpv1) in the PTn, average water potential is given as -0.3 bars, based on a total of 20 measurements. For the lowest unit within the PTn (Tpbt2), the average water potential for 41 samples is also -0.3 bars. The remainder of the PTn averages -0.1 bars, based on 112 samples. Although the depth range is not given in Rousseau et al Table 4.2.1-2, typical distances of the PTn above the regional water table would correspond to equilibrium potentials of -55 to -60 bars at the top of the PTn and -50 to -55 bars at the base. At the repository horizon within the TSw (Tptpmn), 176 samples have an average water potential of -12.6 bars. At equilibrium, this interval would have a potential of about -35 bars. These data show that the system is substantially wetter, on the average, than would be the case if it were in capillary-gravitational equilibrium. They also suggest that comparisons of water potential versus depth may be more useful than saturation profiles. Finally, we note that all of these observations are not inconsistent with the concept of episodic fracture flow. In fact, the matrix suction potential is very small (compared to the capillary/gravity equilibrium) under ambient conditions.

Table 1.2.1-1. Matrix properties of Yucca Mountain tuff (Klavetter and Peters, 1988).

Unit[a]	Sample code	Porosity	Permeability (m^2)	S_r[b]	α[c] $10^{-2}m^{-1}$	β[c]
TCw	G4-1	0.08	9.7×10^{-19}	0.002	0.821	1.558
PTn	GU3-7	0.40	3.9×10^{-14}	0.100	1.500	6.872
TSw1	G4-6	0.11	1.9×10^{-18}	0.080	0.567	1.798
TSw2	G4-6	0.11	1.9×10^{-18}	0.080	0.567	1.798
TSw3	GU3-11	0.07	1.5×10^{-19}	0.080	0.441	2.058
CHnv	GU3-14	0.46	2.7×10^{-14}	0.041	1.60	3.872
CHnz	G4-11	0.28	2.0×10^{-18}	0.110	0.308	1.602
PPw	G4-18	0.24	4.5×10^{-16}	0.066	1.41	2.639

[a]Unit designations: TC, Tiva Canyon; PT, Paintbrush; TS, Topopah Spring; CH, Calico Hills; PP, Prow Pass; w, welded; n, nonwelded; v, vitric; z, zeolitized.
[b]S_r is the residual liquid saturation.
[c]α and β are the fitting parameters for the capillary pressure and relative permeability curves, respectively.

Table 1.2.1-2. Calculated fracture apertures based on reported bulk hydraulic conductivities (Montazer et al., 1985; Thordarson, 1983).

Assumed fracture spacing, B (m)	Fracture aperture, b (μm)
1.00	203 to 587
0.3	141 to 407
0.1	94 to 273
0.01	43 to 127

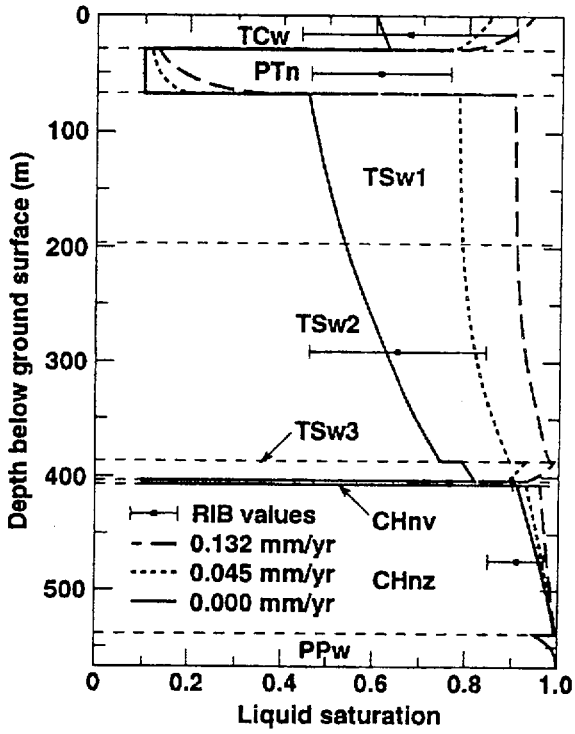

Figure 1.2.1-1. Liquid saturation profile obtained from several one-dimensional models of steady-state recharge flux versus saturation from the *Yucca Mountain Project Reference Information Base* (RIB) (DOE, 1990).

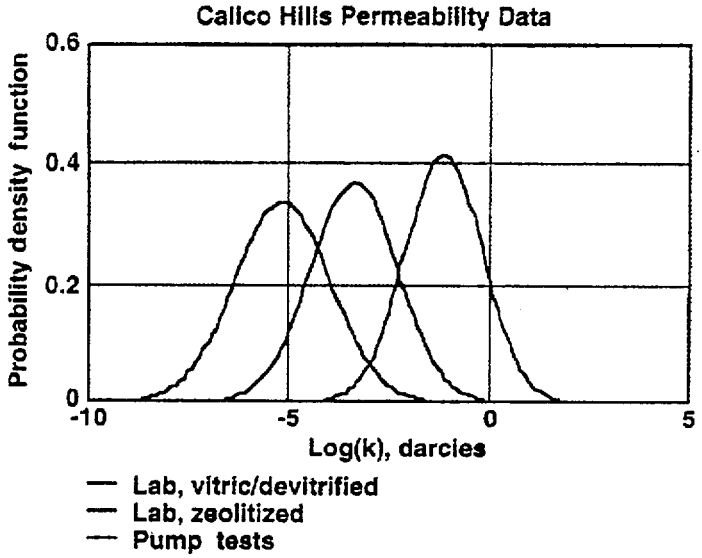

Figure 1.2.1-2. Summary of Calico Hills permeability data ("A Summary and Discussion of Hydrologic Data from the Calico Hills Nonwelded Hydrogeologic Unit at Yucca Mountain, Nevada," LA-12376-MS, Colleen Loeven).

1.2.2 Infiltration and Percolation

In Rev 0 of the PNFER, recharge flux was discussed without making a distinction between shallow infiltration and deeper percolation. Much evidence has accumulated that points to potentially significant differences between infiltration and percolation fluxes, and therefore, this Rev of the NFER will try to make a distinction between infiltration and potential repository horizon percolation fluxes.

1.2.2.1 Shallow Infiltration Flux Estimates. In spite of recent progress in characterizing the ambient state of Yucca Mountain, considerable uncertainty remains in the shallow infiltration rate, and consequently the percolation flux at the repository level. It has been commonly assumed (e.g., in the draft Environmental Impact Statement (EIS), the Site Characterization Plan (SCP), and various total system performance assessment calculations) that shallow infiltration at Yucca Mountain is very low, less than 1 mm/yr. However, the accumulation of evidence at and near Yucca Mountain, along with related studies in other arid regions, suggests that the shallow infiltration rate is likely to be higher than the upper limit proposed by Montazer and Wilson (1984). The assumed infiltration as well as the argument that water will be imbibed rapidly into the matrix because of the large suction potential are not supported by the observed transport of contaminants and bomb isotopes, which serves as a note of caution in applying infiltration and percolation estimates for the Yucca Mountain. However, since a significant but unknown amount of lateral diversion is believed to occur at the PTn, this does not *necessarily* mean that if the shallow infiltration is high that the percolation flux through the repository is also high (this will be discussed in 1.2.2.2).

Frequently, 0.1 mm/yr. has been used as the nominal value for calculating radionuclide release rates and transport through the vadose zone to the water table and thence to the accessible environment, although typically a range is used, covered by an assumed probability distribution, in Monte Carlo calculations for TSPA. A maximum value of 4.5 mm/yr. (probably taken from Montazer and Wilson) was used by J. H. Gauthier et al. (1992 IHLRWM Conference Proceedings, p. 892), for illustrating the "weeps" model for contact of waste packages by seepage into drifts. Some points to consider in attempting to understand infiltration are given below:

Bomb-pulse tritium peaks were reported at depths of 46-50 m in UE-25 UZ#4 and 34-36 m in UE-25 UZ#5, Pagany Wash, east flank of YM (In-Che Yang, 1992 IHLRWM Conference Proceedings, p. 734).

Chloride data in pore water contained in the alluvium underlying Frenchman Flat (Steve Conrad, 1993 IHLRWM Conference Proceedings, pp.132-134) can be interpreted as indicating either a relatively high infiltration flux or a very low flux. Conrad (1993) reports that the concentration of chloride ion in precipitation is $[Cl]_p = 0.8$ mg/L. If $[Cl]_s$ denotes the soil water chloride ion concentration, R is the recharge flux, and P = 120 mm/yr is the average precipitation, then, by a chloride mass balance,

$$R = \frac{[Cl]_p}{[Cl]_s} \cdot P, \quad \text{or } R = \frac{96}{[Cl]_s}$$

arbitrary point on the $[Cl]_S$ versus depth profile at about 30 m, with a chloride concentration of 2500 mg/L, giving R = O.0384, or about 0.032% of P. From a depth of 75 m all the way to the WT at 250 m, he reports $[Cl]_S$ to be essentially constant at 20 mg/L, giving R = 4.8 mm/yr., or about 4% of P.

This is essentially the same as the upper limit for YM given by Montazer and Wilson, (1984) although if the percentage of P is the same, YM would have R = 6 mm/yr., because it has higher average precipitation than Frenchman Flat.

A $^{36}Cl/^{35}Cl$ ratio over 750 chlorine units (1 CLU = 10^{-15}) was reported by Conrad (1993) at about 8 m depth in borehole ST-1 in Frenchman Flat, and other ratios from this borehole and borehole PW-1 at depths down to 35 m are 10% or more above the nominal (present-day) cosmogenic level of 500 CLU. Conrad did not even consider that these slightly elevated ^{36}Cl ratios might be a bomb-pulse signal,

advancing instead the single hypothesis that the cosmogenic ^{36}Cl production rate prior to 15,000 years b.p. was higher than the present rate because of geomagnetic field variations. A similar hypothesis is one of several alternatives offered by Fabryka-Martin et al. (1996) to explain slightly elevated ratios (500 to 1500 CLUs).

We note that Conrad's value of particle velocity would give a piston-like travel time of more than 500,000 years to reach the water table underneath Frenchman Flat. Even with an extremely heterogeneous travel time distribution and higher rates of ^{36}Cl production over the past 100,000 years, the ^{36}Cl ratio would have decayed substantially at 250 m, which is not supported by Conrad's data. Unfortunately, no tritium measurements were reported; this could have resolved the question of whether the elevated ^{36}Cl levels were from bomb tests or some other source.

Rainier Mesa (Russell, 1987) provides an interesting comparison with Yucca Mountain. The infiltration rate is about 5% to 10% of the average annual precipitation of 320 mm/yr. at Rainier Mesa, or 24 ± 8 mm/yr. The same percentage applied to Yucca Mountain's average annual precipitation of 170 mm/yr. would give an infiltration rate of 8.5 to 17 mm/yr., up to 34 *times* the often-quoted lower limit of 0.5 mm/yr. from Montazer and Wilson (1984), and 85 to 170 times the value of 0.1 mm/yr. commonly used in performance calculations. It is noteworthy that fracture flow is reported at Rainier Mesa, even though the surrounding matrix is not completely saturated.

Other arid regions also provide interesting observations that significant infiltration rates can occur even when evapotranspiration potential far exceeds the annual precipitation rate. In 1992, Jean-François Aranyossy and Cheikh Becaye Gaye (C. R. Acad. Sci. Paris, t 315, Série II, pp. 637-643) reported infiltration rates in north Senegal of 22 to 26 mm/yr. at precipitation rates of 338 and 325 mm/yr., respectively, based on analysis of bomb-pulse tritium peaks in highly permeable porous material. These precipitation levels are similar to those at Rainier Mesa, and infiltration is 6.5% to 8.0% of total annual precipitation, within the range of infiltration percentages for Rainier Mesa reported by the Lawrence Berkeley Laboratory Geologic Repository Project Group (Wang, et al., 1993) and by Russel et al. (1987).

A recent paper by Nativ and others (1994) documents relatively high infiltration rates and rapid solute transport from the surface to the water table, through fractured chalk in the Israeli Negev Desert. Precipitation averages about 200 mm/yr. The matrix permeability of the chalk is about 1 md (about 4 orders of magnitude higher than the TSw matrix), and it was believed that imbibition into the unsaturated matrix would restrict flow to the matrix. Infiltration rates were calculated from measurements in four boreholes of bomb-pulse tritium and of bromide originating from local industrial sources. Table 1.2.2-1 summarizes their results for R as a percentage of P. Fracture flow was clearly indicated by the rapid transport of industrial contaminants to the water table, the concentration of tritium in the saturated zone, and the seasonal fluctuation of groundwater levels in wells. Note that the percentage of precipitation entering the deep vadose zone as recharge is at least equal to, and perhaps higher than, the range quoted above for Rainier Mesa. Although the water table is much shallower in this part of the Negev than at Yucca Mountain, imbibition should be much more rapid, given the smaller fracture spacing and the higher matrix permeability.

The YM vadose zone contains about 10% water (by volume), and the repository is about 300 m below the surface. Water in storage above the repository is therefore on the order of 30 m^3 per m^2 of surface area. This represents 3,000, 30,000, or 300,000 years of infiltration at fluxes of 10, 1, or 0.1 mm/yr., respectively. Hence, depending upon whether the flux is near the low end or the high end of the range, the source of most of the water which could potentially contact a waste package during the first 10,000 years is the water that is already stored in the pores of the rock matrix and that could be mobilized by emplacement heat. However, this statement ignores the heterogeneous nature of fracture flow.

For comparison, note that the fractured granite in Sweden below the water table (which is near the surface) typically has only 0.1% water by volume in storage, and would therefore have only 0.3 m^3 of water per m^2 of area above a repository at the same depth as is proposed for YM. Neretnieks et al. (1987) have pointed out that the darcy flux in undisturbed Swedish bedrock is on the order of 0.1 mm/yr. (*in the saturated zone*). Hence, because the storage volume is so low, the average particle velocity must be higher

by a factor of about 100 than it would be at YM for the same flux. If the flux at YM is on the order of 10 mm/yr., then the particle velocity at YM is comparable to what it would be in Sweden in fractured granite, and more reliance on the Engineered Barrier System (as is envisioned in Sweden and many other countries) would be required.

Austin Long & Stuart W. Childs, (IHLRWM 93 Proceedings, pp. 112-121) constructed a detailed model of infiltration to study the probable impact of future climate changes using three types of surfaces: side slopes, shallow soil, and basin. The weighted site average is about 1 mm/yr. under current conditions, but individual years could have up to several mm/yr. The standard deviation about the average is about 0.5 mm/yr. Basin and shallow soil surfaces average 1.6 and 1.9 mm/yr, respectively, compared to about 0.6 mm/yr. for slope surfaces. For each surface type, regression of the annual infiltration against annual precipitation gave a straight line. The slopes and intercepts depended upon the type of surface. Regression of the whole site-weighted average net infiltration against annual precipitation also resulted in a straight line, with zero infiltration below a threshold value for precipitation of about 50 mm/yr. Similar regressions were performed for full glacial maximum conditions as well as other future climate scenarios. The site regression line under current conditions predicts an infiltration of only about 5 mm/yr. at an annual precipitation of 320 mm/yr., which is far below the estimated infiltration rate of 16 to 32 mm/yr. at Rainier Mesa. Even the full glacial maximum regression line predicts only about 15 mm/yr. of net infiltration at a precipitation rate of 320 mm/yr., just below the lower end of the range for Rainier Mesa. Accordingly, it seems that these model calculations may *underestimate* the infiltration rate at Yucca Mountain under current conditions, perhaps by a factor of 3 to 6. It would be very interesting to repeat Long and Childs (1993) model calculations for current conditions at Rainier Mesa, to determine whether it agrees more closely with the estimates cited above.

Karsten Pruess & Yvonne Tsang, (IHLRWM 93 Proceedings, pp. 568- ff.) studied heat-driven flow processes at YM, using the equivalent continuum approximation, for borehole emplacement. The r-z coordinate system used allowed a single central waste package to be modeled in detail, surrounded by a diffuse heat source with a density chosen to provide an initial thermal load of 57 kW/acre. At 0 infiltration with enhanced vapor diffusion, the natural gradient of 0.03°c/m drives about 0.04 mm/yr. of vapor flux, which is balanced by a downward liquid flux. They demonstrated that partial dry-out, extending approximately 30 to 100 m above and below the repository, persists for 10,000 yr. Capillary forces dominate gravity flow during this period, so that the net flux of water is toward rather than away from the repository. In the absence of localized, nonequilibrium fracture flow caused by heterogeneities, the resulting "capillary trap" would prevent aqueous transport of radionuclides away from the repository. It is a subject of active investigation whether or not the capillary trap actually works in a heterogeneous, pervasively fractured system. Pruess and Tsang (1993) also investigated the effects of surface infiltration fluxes of 1 and 10 mm/yr. starting 1000 yr. after emplacement. At 1 mm/yr., fracture flow to 10,000 yr. after emplacement (based on the ECM) persisted only to depths of 50 m, and the "capillary trap" condition persisted for the entire 10,000 yr. period. At 10 mm/yr., flow is toward the repository for 2,000 yr., but then changes to flow all the way to the water table at 3,000 yr. in central part of model and at 4,000 years for the central single waste package (WP).

During a February 1995 field trip to Apache Leap as part of the Evans Workshop on Fracture Flow and Transport, workshop participants were told by the Environmental Engineer for the Magma Copper Company that an average of about 2×10^6 gallons per year of water is pumped from the mine workings at depths of 4500 to 5000 feet below the surface. The mine is in carbonate rock overlain by the Apache Leap tuffs, similar to the Yucca Mountain Tuffs; much of the overlying rock is now unsaturated as a result of long-term pumping. The Magma representative mentioned that the pumping rate increases significantly (50% or more) in response to episodes of surface precipitation, with a time lag of 6 months to a year. This observation would not be accounted for by equivalent continuum models, which typically show "steady-state" behavior insensitive to temporal variations in surface influx below depths of a few tens of meters. These models filter out the higher frequency components of the "signal," leaving only the response to changes occurring over thousands of years. Although these observations are anecdotal, they should at least raise some suspicion that transient flow to depths of thousands of feet in fractured porous

rock is possible and must be accommodated in conceptual and mathematical models for the unsaturated zone (uz) at Yucca Mountain.

The most compelling data suggesting an infiltration rate much higher than 0.1 mm/yr. is summarized by Hudson and Flint (1996). This report documents the estimates of shallow infiltration based on periodic neutron logging of 69 boreholes with depths ranging from 6 m to 85 m between October 1984 and April 1995. The authors are careful to distinguish between shallow infiltration (water that percolates below all unconsolidated material at least 2 m into bedrock and thus escapes rapid evapotranspiration), and net infiltration, the flux deep in the unsaturated zone resulting from surface infiltrated water. How much of the shallow infiltration becomes net percolation through the repository block remains an open question that cannot be answered by continued surface-based borehole measurements alone.

The study area covered by the report comprises 230 km^2 surrounding Yucca Mountain. Over this area, the average estimated shallow infiltration flux is 11.6 mm/yr., for the time period observed. A map contained in the report indicates that the western 2/3 of the potential repository footprint (essentially the part west of the Ghost Dance fault) has an estimated 20 to 30 mm/yr. of average infiltration, while most of the remainder averages 10 to 20 mm/yr. A small part of the repository footprint, with deep alluvial fill, is shown with 0 mm/yr., as is Yucca Flat. The latter region of essentially 0 infiltration flux is consistent with Conrad's interpretation (1993) of data in Frenchman Flat. As a general observation, the authors note that locations with more than 2 m of alluvium over bedrock have no significant shallow infiltration, because water is retained in the zone of rapid evapotranspiration long enough for evaporation to occur before it reaches the bedrock.

There are many steps in developing the estimated infiltration flux map from borehole data, including a regression analysis on a number of variables. Nevertheless, the estimates are based on data as close as we have to direct observation on the movement of water in the shallow subsurface, and they indicate that the flux may be significantly higher than even the upper limit given by Montazer and Wilson (1984). The data also show that shallow infiltration is highly episodic, depending not only upon the intensity of a given storm but the time interval between storms. Work in progress by Hudson & Flint (1996)., using stochastic simulation to model infiltration over a typical 100-year interval, may reduce the estimates by adjusting for more typical weather fluctuations than were observed during the data-collection period, which contained 3 El Niño events, more than normally occur in an 8-year period. However, the averages over the potential repository footprint will probably still exceed 10 mm/yr.

We conclude that, since Revision 0 of the NFER was published, the uncertainty in shallow infiltration flux has been reduced, with a preponderance of evidence supporting on the order of 10 mm/yr. plus or minus about 5 mm/yr. as an average value under current climatic conditions.

1.2.2.2 Percolation Flux. The principal remaining uncertainty is: what happens to the infiltration flux after it passes through the first few meters of bedrock? Some fraction (some would claim nearly all) of it is expected to be diverted at the PTn, but unpublished results from several modeling groups indicate that the percentage that is diverted is not likely to exceed 60 or 70, even if the total flux at the top of this interval is much lower than 5 mm/yr. The percentage diverted laterally is expected to decrease as the flux at the top of the interval increases. Unfortunately, no direct measurements of percolation flux are available. Rev 0 of the PNFER discussed analyses by Buscheck and Nitao (1991a) in which they were able to calculate saturations using different fluxes and then match saturation data for TSw2 and TSw3, but were unable to match saturation of the PTn. The following is taken from the PNFER, with modifications to distinguish between percolation and infiltration.

> On the basis of the one-dimensional steady-state ECM, Buscheck and Nitao (1991a) found that the observed range in saturation at the repository horizon corresponds to a range in percolation flux of approximately 0.0005 to 0.05 mm/yr (Fig. 1.2.1). In light of the uncertainty inherent in the available matrix-property data, one-dimensional steady-state ECM-based percolation flux at the repository horizon is effectively zero.

Buscheck and Nitao (1991a) also obtained one-dimensional steady-state ECM-calculated saturation profiles for recharge fluxes of 0.045 and 0.0132 mm/yr, resulting in saturations at the repository horizon of 85% and 95%, respectively (Fig. 1.2.1). Because of the relatively small k_m of the TSw2 and TSw3, the saturation profile within those units is quite sensitive to variations in percolation flux. Because of its large k_m, the CHnv can sustain the steady-state flux at small saturations. The saturation profiles in the CHnz and PPw are less sensitive to variations in the steady-state percolation flux.

Saturation values obtained from the Reference Information Base (*RIB*) are also included in Fig. 1.2.1. While zero percolation flux results in a saturation of about 10% for the PTn and CHnv, the *RIB* reports mean saturation values of 61% and 91%, respectively. Therefore, although a zero percolation flux is consistent with saturation data at the repository horizon, it is not consistent with the saturation data in the high-k_m vitric nonwelded PTn and CHnv. Some of this inconsistency may result from inadequate matrix-property data or a lack of correspondence between the matrix-property data and the saturation data. However, this inconsistency is too great to be entirely attributed to such causes. Apparently, significant recharge fluxes (i.e., much greater than those shown in Fig. 1.2.1) are able to reach the high-k_m units without affecting the saturation of the neighboring low-k_m units. Nonequilibrium fracture flow through the TCw, TSw1, TSw2, and TSw3 is the most likely explanation for the inconsistency between the measured saturation data and the saturation profile predicted by the one-dimensional, steady-state ECM (Buscheck and Nitao, 1991a; Buscheck et al., 1991a).

The bottom line is that models relying on equilibrium conditions and uniform percolation fail to explain observations from YM. It appears that the percolation is an unknown, possibly small fraction of the infiltration (near zero in some conceptualizations) and is dominated by episodic fracture flow that is out of equilibrium with saturation conditions in the matrix (similar to the observations for the Apache Leap tuff).

Given this situation, we must then ask: what measurements can be made to more directly determine the percolation flux through the repository level or, essentially the equivalent, through the PTn? Direct measurement of flux into a drift is precluded unless the drift walls are protected from ventilation. Recent measurements of the increase in moisture content in ventilation air as it traverses the PTn indicate that the evaporation rate corresponds to a flux of more than 200 mm/yr., based on the surface area of the main ESF drift (Chesnut, Flint, and Wang, 1996). This exceeds the estimates of percolation flux and thus would indicate that water seeping into the drift at the rate of the percolation flux estimates for YM would all be removed by evaporation, so that observations of dryness (or even measurements of dripping if made) are potentially misleading. Although some of the water being removed by evaporation may result from evaporation from the muck as it travels on the conveyor belt, it is clear that even a steady flux of 10 mm/yr. through the drift walls would be hard to see in the face of this potential for evaporation. An additional complication is that the seepage flux is likely to be highly episodic, following a sufficiently intense surface precipitation event after a presently unknown lag time. It has been proposed to use Lexan panels to cover a section of the drifts in some protected area, such as the thermal test alcove or some other alcove, or to seal off an alcove to permit direct measurement of seepage if any should occur. Without some direct measurements, the percolation flux will continue to be a matter of conjecture.

Finally, the real issue is not the uncertainty about the percolation flux, but whether or not a repository can be designed for higher fluxes that provides a sufficient degree of confidence that it will perform adequately. This will have to be addressed in the next performance assessment (PA), although some insight can be gained from the hydrothermal modeling results given in subsequent sections in this report.

The one remaining issue that could potentially be addressed by additional surface-based borehole measurements is the lack of neutron logging data along the ridge of Yucca Mountain, where Hudson and Flint (1996) show the highest estimated shallow infiltration flux for the potential repository footprint. This would directly corroborate (or refute) the region of high shallow infiltration flux delineated by the

statistical analyses performed by Hudson and Flint. It would not provide data in time to affect the viability assessment, but could be very important in a License application, particularly if there is another El Niño.

Table 1.2.2-1. Estimated recharge rates as a percentage of annual precipitation (200 mm/yr.) for fractured chalk in the Negev Desert (Nativ et al., 1994).

Borehole	R Based on Tritium	R Based on Bromide
RH-2	20.5	25.0
RH-8	33.0	55.0
RH-10	13.0	15.0
RH-18	8.0	-

Contents

1.3 Episodic Non-equilibrium Fracture-Matrix Flow

The material contained in Rev 0 of the PNFER is still applicable, but for convenience of the reader is reproduced here with modification as appropriate to distinguish between infiltration and percolation, and to remove discussions of ground-water travel time and site suitability.

Because it cannot discriminate between more and less adverse flow conditions, the ECM cannot be used to improve the design and operation of the repository for the purpose of minimizing the interaction with the most adverse and problematic flow features at Yucca Mountain. Whether or not one chooses to assume capillary equilibrium between the fracture and matrix porosities has an absolutely profound impact on the conceptual framework for the unsaturated flow through Yucca Mountain. As will be shown, by arbitrarily assuming capillary equilibrium, the manner in which the system's hydrologic heterogeneities influence flow conditions is completely obscured. Regardless of how heterogeneous the system is, the ECM assumes that flow and transport behavior can be adequately represented by "bulk-averaged" flow behavior in porous media, as illustrated in Fig. 1.3-1a.

Other approximations besides the zeroth-order approximation (i.e., ECM) have been used to represent fracture-matrix interaction. The dual-porosity approach, effectively a first-order approximation, assumes that the mass transfer between the fracture and matrix block can be represented by a mass-transfer coefficient, implying quasi-steady-state flow from matrix block to fracture. The dual-porosity approach has been applied to model single-phase flow in fractured reservoirs (Barrenblatt et al., 1960; Warren and Root, 1963). Braester (1986) has applied dual-porosity models that treat relative-permeability effects arising from multiphase flow. The primary feature of the dual-porosity approximation is that the pressure field within a matrix block is represented by an averaged value. We have found that the diffusive nature of capillary imbibition is not readily treated by the first-order dual-porosity approach.

The second-order approximation (Buscheck and Nitao, 1988; Nitao and Buscheck, 1989; Nitao 1991) discretely accounts for the fracture and matrix porosities using the fracture-matrix model (FMM). Because of its discrete treatment, the model accounts for episodic nonequilibrium, nonsteady-state fracture-matrix behavior [Fig. 1.3-1]. On the basis of available fracture and matrix data for Yucca Mountain, Buscheck and Nitao (1991a) and Buscheck et al. (1991a) have shown that the ECM has an extremely limited domain of applicability. Moreover, the second-order FMM predicts flow behavior that is identical to that predicted by the ECM when the latter model is valid. Therefore, the FMM is the more comprehensive and appropriate modeling approach, and it is applicable to all situations for which the ECM is applicable.

Because the flow in fractures and matrix blocks is not in capillary equilibrium during episodic infiltration events, flow in the fractures may penetrate to considerable depths in Yucca Mountain. To resolve the apparent contradiction between the estimates of zero net percolation flux at the repository horizon (based on matching saturation data) and the estimates of infiltration flux as discussed in Section 1.2.2 , mechanisms are required to remove water from the vadose zone. These mechanisms may include vapor flow (Thorstenson et al., 1989) as well as vertical percolation to the water table and lateral liquid flow along high-matrix-permeability units such as the PTn and CHnv. As was discussed in section 1.2.2, it is judged that there is no more than 70% diversion of infiltration by the Ptn, which would leave 1-2 mm or more/yr net percolation flux below the PTn, Fracture flow that is not in capillary equilibrium with the matrix is the most likely mechanism for removing this water from the TSw2 and draining it to the water table. This is consistent with the ^{36}Cl data as discussed in Section 1.4.

1.3.1 Matrix-Dominated and Fracture-Dominated Flow Regimes

In theory, because of the very small matrix pore size, water in the matrix pores should be held under high suction (matric) potential under ambient saturation conditions. Because of the relatively low capillarity of all fractures except those with very small apertures, the fractures are drained of water under the ambient partially saturated conditions. When the flux into a fracture is sufficiently small, most of the water is imbibed by the matrix near the inlet before it moves a significant distance along the fracture (Nitao, 1991). The liquid front in the fracture lags behind the front in the matrix, and the speed of the wetting front is dominated by the matrix properties. This condition corresponds to matrix-dominated flow. The ECM is satisfactory for this case.

Fracture-dominated flow occurs at higher fluxes than those resulting from matrix-dominated flow. The liquid front in the fracture moves ahead of the front in the matrix, and matrix flow is primarily perpendicular to the fracture plane. Under these conditions, the speed of the front in the fracture is governed by the competition between gravity drainage in the fracture and capillary imbibition into the matrix. Nitao and Buscheck (1989) found that fracture-dominated flow can be classified into three physically interpretable, distinctive flow regions, corresponding to the relative extent to which matrix interaction retards the speed of the wetting front in the fracture, progressing from minimal retardation for flow period I, intermediate retardation for flow period II, and maximal retardation for flow period III (Fig. 1.3-2).

1.3.2 Implications of Flow Regimes on Engineered Barrier System/Near Field Performance

The extent to which the Yucca Mountain site contributes to the isolation of waste depends greatly on whether it can prevent liquid pulses from (1) reaching WPs, which would accelerate their failure, and (2) transporting radionuclides to the water table. Using a steady-state one-dimensional ECM, Buscheck and Nitao (1991a) and Buscheck et al. (1991a) found the repository horizon to be approaching 95% saturation for a recharge flux of 0.132 mm/yr. The capability of Yucca Mountain to prevent liquid pulses from reaching WPs and transporting radionuclides is critically dependent on the degree to which matrix imbibition retards the speed of the wetting front in the fracture. The impact of physical retardation on fracture flow is best understood by considering the two most extreme (i.e., asymptotic) examples of fracture-matrix interaction. The first example occurs when the matrix is impermeable, resulting in no interaction between the fracture and matrix (see "no fracture flow retardation" in Fig. 1.3-3). In this case, there is no transfer of liquid from the fracture to the matrix. Therefore, all of the water entering the top of the fracture remains in the fracture, resulting in the greatest possible movement of the liquid front in the fracture. Without fracture-matrix interaction, the matrix cannot retard the speed of the wetting front in the fracture. This case corresponds to flow period I in Figs. 1.3-2 and 1.3-3.

The second extreme example of fracture-dominated flow pertains to when the matrix permeability is extremely (effectively infinitely) large, resulting in infinite interaction between the fracture and the matrix (see "maximal fracture flow retardation" in Fig. 1.3-3). As soon as the flow in the fracture reaches a given level, imbibition into the matrix occurs so quickly that the entire matrix porosity lying between flowing fractures is saturated to 100%. In this extreme mode, matrix imbibition retards the speed of the wetting front in the fracture to the maximum possible extent. Under these conditions, for a wetting front driven by ponded conditions at the ground surface to reach the water table, Yucca Mountain would have to be entirely filled to 100% saturation. Incidentally, the ECM assumes that this extreme mode of fracture-matrix interaction is valid.

Fracture-dominated flow in Yucca Mountain lies between these two extremes. The extent to which the matrix imbibition retards the speed of the wetting front in the fracture always lies between the "no retardation" and "maximal retardation" examples. The three fracture-dominated

flow regimes identified by Nitao and Buscheck (1989) are not only identifiable spatially, but are also related to three corresponding flow periods.

During flow period I, flow in the matrix is not significant enough to affect flow in the fracture. Therefore, the speed of the liquid front is dominated by the driving forces in the fracture: fracture capillarity, the imposed boundary flux or pressure, and gravity. For ponded conditions at the inlet to vertical fractures, flow period I is dominated by gravity, and the liquid front moves linearly in time. During flow period II, the impact of matrix imbibition is fully developed, and the liquid front moves as $t^{1/2}$. During flow period III, the wetting zones from neighboring fractures have fully interfered, thereby reducing the effect of matrix imbibition. The movement of the front is again linear in time (but substantially reduced relative to flow period I) and is the same as that predicted by the ECM. For flow period III to occur in Yucca Mountain, the entire mountain must be approaching 100% saturation.

1.3.3 Summary of Fracture-Matrix Interaction at Yucca Mountain

With regard to the degree of fracture-matrix interaction, Buscheck and Nitao (1991a) and Buscheck et al. (1991b) found that the major hydrostratigraphic units fall in two relatively extreme categories: (1) high-matrix-permeability units, which give rise to a high level of fracture-matrix interaction and can thereby significantly retard fracture flow, and (2) very-low-matrix-permeability units, which give rise to much less fracture-matrix interaction and thereby have much less capacity to retard fracture flow. Accordingly, because of their very small matrix permeability, fracture-dominated flow will be greatest in the welded TCw, TSw1, TSw2, and TSw3 units, as well as in the zeolitized nonwelded CHnz unit (Fig. 1.3-4). The low permeability results in fracture-dominated flow period II for small- to medium-aperture fractures and fracture-dominated flow period I for large-aperture fractures. The large matrix permeability of the the vitric nonwelded PTn and CHnv tuffs results in either: (1) matrix-dominated flow for small- to medium-aperture fractures, (2) fracture-dominated flow period III for medium- to relatively-large-aperture fractures, or (3) fracture-dominated flow period II for very-large-aperture fractures. The estimates of Buscheck and Nitao (1991a) and Buscheck et al. (1991b) may change somewhat upon consideration of additional matrix imbibition data now becoming available. The fundamental distinction, however, between the effects of the low-matrix-permeability units (the welded units and CHnz) and the high-matrix-permeability vitric units (PTn and CHnv) on fracture flow still holds (Fig. 1.3-4).

Because fracture-dominated flow periods I and II result in the greatest amount of penetration of liquid flow along fractures, a hydrological performance assessment is very sensitive to the nature of vertically connected fracture networks in the low-matrix-permeability welded units. The high matrix-permeability of the vitric nonwelded tuffs may result in very substantial lateral matrix flow. The interaction of this lateral flow with vertically contiguous faults is a critical hydrological performance issue. Therefore, assessing the hydrological performance of the repository system needs to focus on whether (or how) fracture networks in the welded units facilitate fracture-dominated flow periods I and II and the interaction of lateral matrix flow within the vitric nonwelded units with vertically contiguous faults.

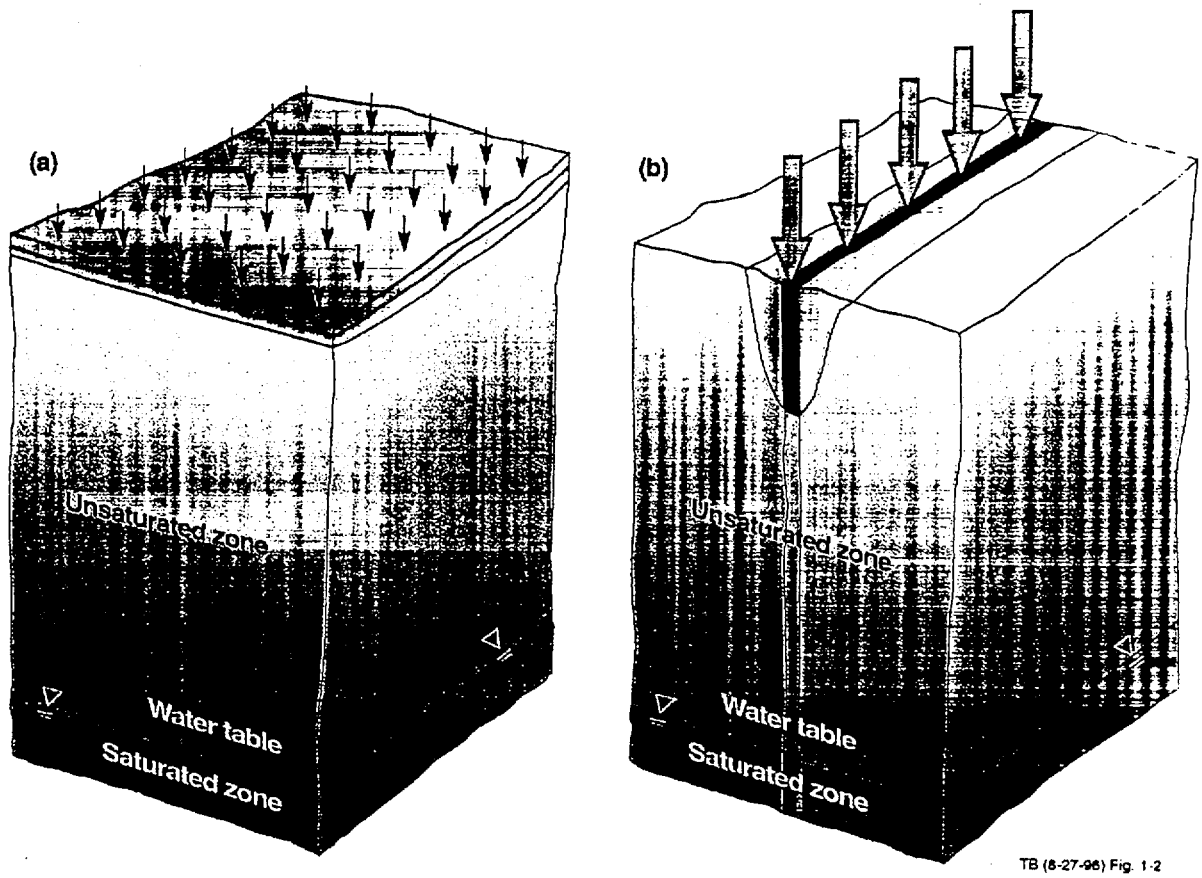

Figure 1.3-1. (a) The equivalent continuum model (ECM) assumes capillary equilibrium between fractures and matrix blocks, resulting in flow through a uniform porous medium. (b) An episodic infiltration event causes capillary disequilibrium between fractures and matrix blocks.

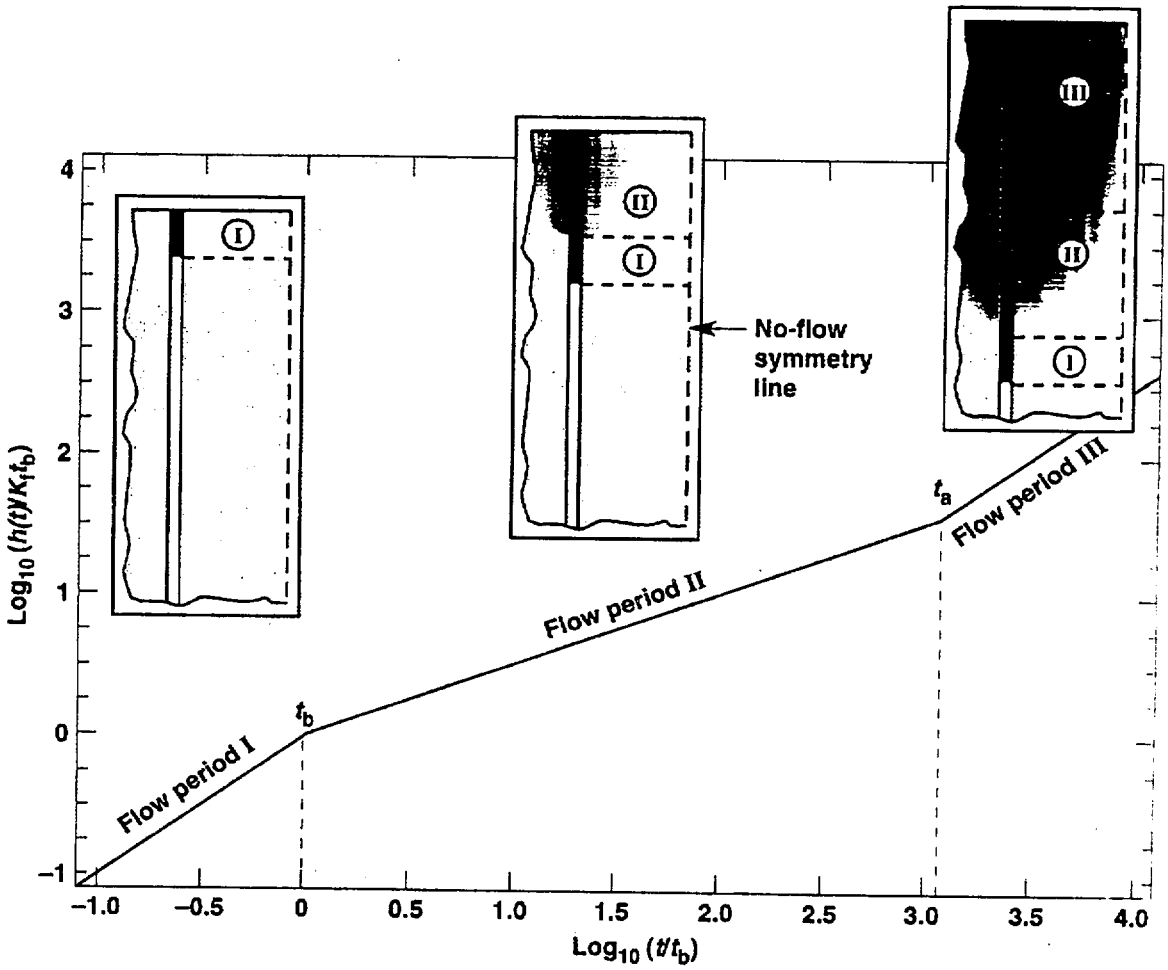

Figure 1.3-2. The three major flow periods of fracture-dominated flow. The asymptotic dimensionless fracture front penetration, $h(t)/K_f t_b$, is plotted against dimensionless time, t/t_b, where $h(t)$ is the fracture penetration, K_f is the saturated hydraulic conductivity of the fracture, t_a is the time it takes to fully saturate the matrix between neighboring fractures, and t_b is the time required for one fracture pore volume to be imbibed by the matrix. The relationship between flow periods and flow regions is depicted in the insets.

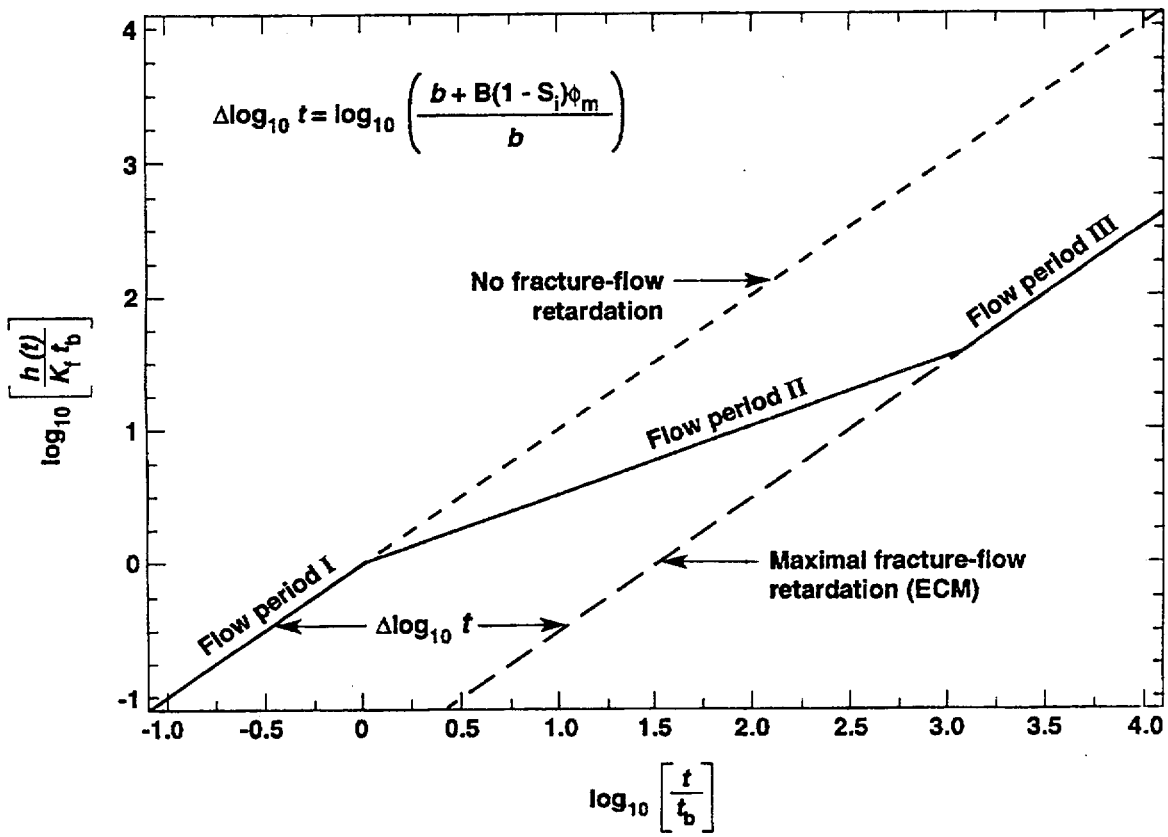

Figure 1.3-3. Fracture-flow retardation for the periods shown in Fig. 1.3-2. The extent of retardation ranges from none (flow period I) to maximal (flow period III), where b is the fracture aperture, B is the fracture spacing, S_i is the initial saturation of the matrix, and ϕ_m is the matrix porosity.

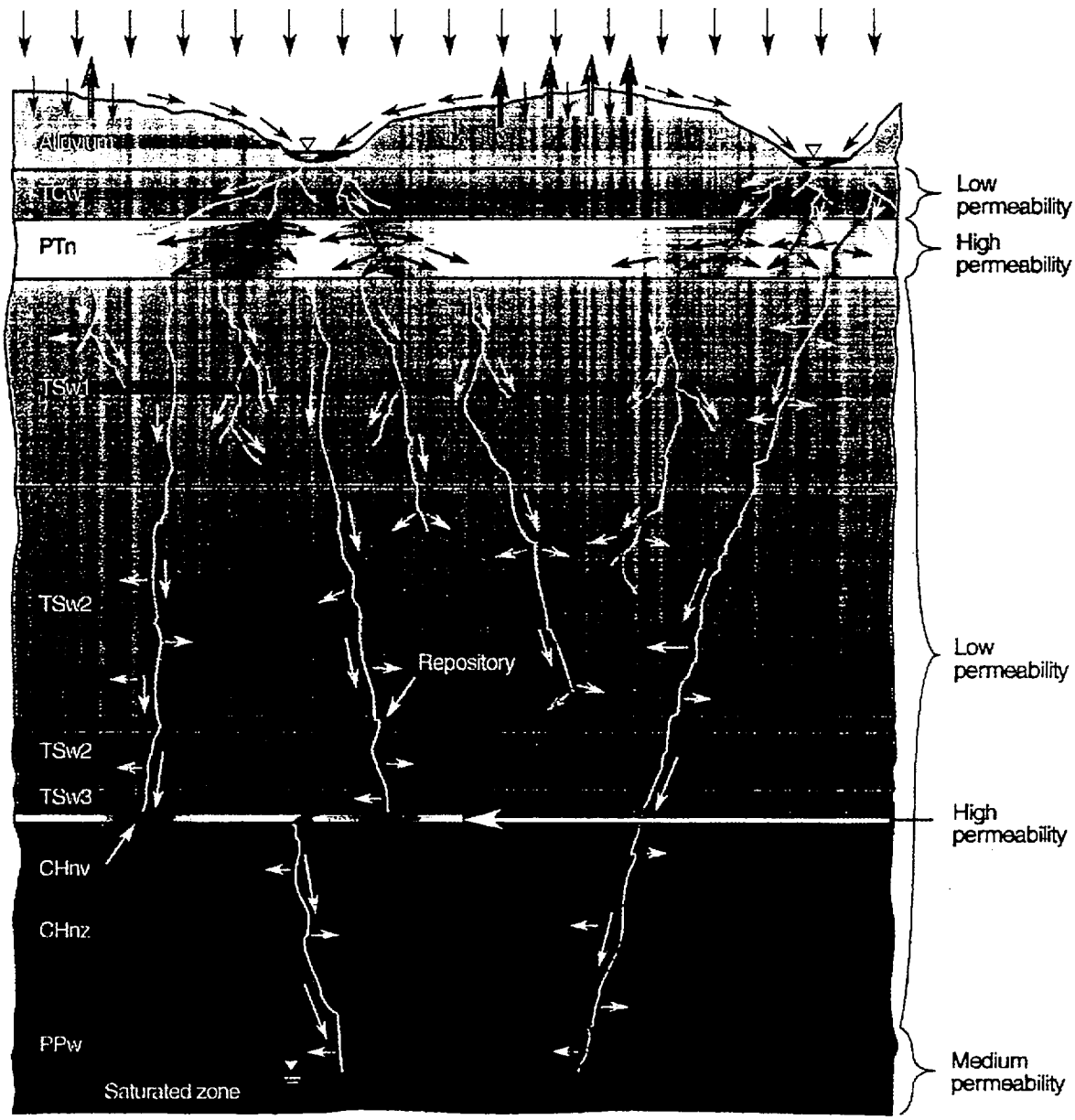

Figure 1.3-4. Episodic infiltration occurs as fracture-dominated flow in the low-matrix-permeability units and matrix-dominated flow in the high-matrix-permeability units.

Contents

1.4 Preferential Flow Pathways

Whether or not liquid water contacts a WP depends on two key factors: (1) whether the fractures intersecting the drifts are part of a fracture pathway that is hydraulically connected to an overlying source of water, and (2) the minimum effective hydraulic aperture of this pathway. If any pulse of fracture flow can reach the drift, it does so in a relatively short time (Nitao and Buscheck, 1989; Buscheck and Nitao, 1988, 1991a; Buscheck et al., 1991a, 1991b). The time it takes the liquid front to travel from the infiltration source to the WP could be from days to months. The hydrological performance analyses of these events must account for the transient, spatially heterogeneous behavior of nonequilibrium fracture network–matrix flow.

The measurement of radioisotope concentrations (^{14}C, ^{36}Cl, and ^{3}H) to indicate the flow paths and velocity of groundwater movement has been applied at Yucca Mountain and vicinity, as well as in other areas. All three of the isotopes listed were injected into the atmosphere by nuclear weapons tests, primarily in the 1950s and 1960s, producing "bomb-pulse" levels of these isotopes in infiltrating ground water. Both ^{14}C and ^{36}Cl are also produced naturally by cosmic-ray bombardment in the atmosphere. These cosmogenic isotopes then decay with half-lives of 5,730 yr. and 301,000 yr., respectively. The occurrence of levels of these isotopes in pore water above the cosmogenic background is direct evidence of a "fast path" from the surface to the point sampled: the residence time must be less than about 40 yrs. in order to obtain bomb-pulse levels at depth.

Liu et al. (1995) summarized data for ^{14}C and ^{36}Cl concentrations in core from surface-based boreholes drilled by the Yucca Mountain Project, and attempted to resolve the apparent lack of concordance between ^{14}C-based estimates of groundwater age and ^{36}Cl-based estimates, using modeling with the FEHMN code. They concluded that the elevated $^{36}Cl/^{35}Cl$ ratios observed in some borehole samples were inconsistent with matrix dominated flow, and were therefore sensitive indicators of fast paths along fractures. Till et al. attributed discrepancies between apparent ^{14}C and ^{36}Cl ages to mixing of water along different flow paths, and pointed out that the use of more than one isotope provides information that cannot be obtained from a single isotope.

More recently, Fabryka-Martin (1996) and others have reported results of a large number of ^{36}Cl measurements on samples from the Exploratory Studies Facility (ESF). The analysis of these results is still in progress at this writing, and will be reported in a Level 3 Milestone report at the end of FY96. Prior to the collection of these data, a ratio of $^{36}Cl/^{35}Cl$ greater than about 500×10^{-15} (500 CLUs) has been considered an indicator of possible bomb-pulse levels of this isotope, based upon data from alluvium below the depth of the bomb-pulse peak and other estimates. All but a few of the samples collected at 52 locations have ratios above 500 CLUs; most are between 500 and 1500. Evidence and calculations presented suggest that higher rates of ^{36}Cl production have occurred in the last few tens of thousands of years than the present rate of production. If this hypothesis is correct, then only ratios above 1500 can be considered unambiguous indicators of fast flow paths, and the data can be interpreted as showing that fast flow is confined to a few mappable features (i.e., faults). Clearly, the interpretation of these data is still a developing field and cannot be used without caution. However, such an interpretation does appear to offer the potential for characterizing heterogeneity of percolation flux over the temporal and spatial scales of interest for predicting the performance of a repository, and will be incorporated in the next revision of the NFER.

Contents

1.5 Spatial and Temporal Variability of Percolation Flux

A major problem in specifying the waste-package environment is determining the spatial distribution of flux entering the emplacement drifts and its variation over time, under both pre-emplacement and post-emplacement conditions, including the effects of radioactive decay heat. The post-emplacement evaluation of percolation flux is critical, because this flux controls the amount of water reaching the waste packages and other elements of the EBS. There are two challenging and important problems in the estimation of percolation flux.

The first problem is that flow is probably episodic, given episodic, highly transient surface infiltration boundary conditions. This was the focus of the Rev 0 discussion on the episodic nature of flow. The reader is referred to Section 1.5 of Rev 0 for a discussion of the effects of ponding and episodic flow. The impacts of episodic flow as discussed in Section of 1.5 of Rev 0 is modified and included below to reflect the changes in the emplacement configuration.

The second problem is to determine the spatial variability of flux arising from the natural heterogeneity of the hydrologic system, and the subsequent changes in hydrologic properties arising from time-dependent, hydrothermally driven geochemical processes. These changes are greatest in the altered zone, which is discussed in greater detail in Chapter 10 and Section 1.7.

The first problem (episodic flow) was considered in Rev 0, where it is noted that the high suction potential of the matrix (relative to the fractures) and gravity drainage of fractures results in the fractures being drained of water under conditions of low recharge flux. Similarly, the high suction potential of the matrix and open fractures results in the drifts being drained of water under low recharge flux, providing that rock is exposed and fractures remain open in the inverts of the drifts. This is the basis of one of the primary hydrological performance attributes of the WP emplacement: a capillary barrier exists between the WP and the drift walls, so no pore water should contact the WPs. As long as rock around the WP remains partially saturated and the capillary barrier is intact (i.e., there is no WP contact with drift walls or sloughing of rock into the drifts), there is no mechanism other than fracture flow and dripping into the drifts to allow water to contact the WPs. Therefore, on the basis that models of coupled fracture/matrix flow indicate that fracture flow is insignificant after removal of a ponded or constant-flux infiltration source (Buscheck and Nitao 1988 & 1991), the key considerations that determine whether water contacts the WP are: 1) the intensity and duration of the maximum possible infiltration episode (i.e., an event or a group of events that effectively act as a single event), and 2) the mobilization of water, currently residing in pores, resulting from evaporation by radioactive decay heat, allowing it to flow through fractures and drip into drifts. The conditions of mobilization and condensation are complex functions of time, emplacement loading, waste characteristics, etc. The potential for and impacts of mobilization and condensation are discussed in detail in Sections 1.7.2, 1.8, and 1.10. The potential for deep percolation of transient pulses of moisture under ambient conditions has also been considered by Wang et al. (1993). Their model for transient fracture flow is similar to the one given by Nitao et al. (1993), except that downward percolation in the Wang et al. model persists for a finite length of time after removal of the source.

The second major problem in determining the waste package environment is estimating the spatial distribution of flux entering the near-field environment and its variation over time, under both pre-emplacement and thermally perturbed conditions. The spatial flux distribution is further complicated by modifications in the hydrologic parameters resulting from coupled process driven by the elevation of temperatures in the unexcavated host rock. The greatest changes occur in the "altered zone," where water and elevated temperatures will be present over time frames sufficient to allow geochemical processes to modify the properties of the fractures and matrix. A detailed discussion of the altered zone and assessments of changes that might occur there is contained in Chapter 10 of this report.

1.5.1 Observations of Percolation Flux

The flux that passes through or enters the altered zone provides an upper "far-field" boundary condition for near-field hydrologic calculations. In fact, it may not be possible, given the complex transient flow coupling between the matrix and the fracture system and the extent of the thermally perturbed zone at Yucca Mountain, to define a boundary between the surface and the potential repository horizon at which a simple boundary condition can be specified. For this reason, modeling of the hydrologic conditions in the waste-package environment typically includes at least the entire unsaturated zone.

It is recognized that post-emplacement percolation conditions (the environment that is relevant to the NFE) will likely be modified from the pre-emplacement conditions (see Section 1.10 for a discussion). As discussed above, there are complex coupled processes that can change the spatial variability of flux with time. These processes are discussed in greater detail in Section 1.7 and Chapter 10. However, we must understand the features and processes that control the pre-emplacement percolation to determine how the coupling occurs and how this flux is modified by post-emplacement alteration. Thus, in this section, we consider only the variability of percolation flux under pre-emplacement conditions.

The most extensive direct measurements of seepage flux into underground openings were made by H. Abelin, L. Birgersson, J. Gidlund, and I. Neretnieks (1991) as part of the international Stripa Project conducted in an abandoned iron mine in Sweden. This experiment, in a deep saturated zone, affords the richest and most realistic set of data on the hydrologic behavior of a connected network of fractures, illustrating the extreme spatial variability of seepage rates arising from heterogeneity in fracture spacing, aperture, and connectivity. The crystalline rock at Stripa has very low matrix porosity (on the order of 0.1% or less) and permeability (on the order of 0.1 microdarcy), and therefore would not have a significant matrix contribution to flow. Hence, it is not a true analog for the fractured, partially saturated tuffs of Yucca Mountain, but it should provide a reasonable end-member, *viz.*, a system completely dominated by fracture flow, without the complications of relative permeability and capillary forces.

Figure 1.5.1-1 shows the spatial distribution of inflow rates measured at Stripa, which may be the only direct, long-term experimental measurement of the spatial variability of the flow of water crossing a plane parallel to the ground surface. The data (direct measurements of water inflow into 375 plastic rectangles covering two square meters each for about three years) show extreme heterogeneity, with 266 (70.9% of the total area) of the sheets averaging less than 0.1 mL/hr of total inflow, one sheet averaging 60 mL/hr, and an overall average (for the 109 sheets with flows greater than 0.1 mL/hr) of 6.75 mL/hr.

Similar data were obtained in a detailed survey (reported by Moreno, Neretnieks, and Gylling, 1993) of inflow into the SFR (final repository for radioactive operational waste) low- and intermediate-level nuclear waste repository constructed in granitic rock near Forsmark, Sweden. The total area of tunnels is much larger than was covered by the Stripa experiment, and the average flow rate was much higher. The latter observation may be related to the fact that the SFR repository is only about 80 m below the bottom of the Baltic Sea, under shallow water, and therefore has much lower effective stress than the rock at Stripa. Figure 1.5.1-2 shows the locations where inflow was observed in the SFR repository.

Both of these examples show that flow in fractures tends to be highly heterogeneous and channelized. Only a small fraction of observed fractures actually conducts water, and only a small fraction of the observable trace of a given fracture actually conducts water. Typical reported channel widths are less than 10 cm for flow in fractured crystalline rock at Stripa, SFR, and tunnels elsewhere in Sweden, according to Moreno, Neretnieks, and Gylling (1993).

Although both Stripa and SFR are below the water table in fractured crystalline rock, we might expect some similarity between these sites and Yucca Mountain in at least the general character of seepage. In particular, flow through fractures into these underground openings is highly variable from one location to another, and strongly localized, even under "steady" conditions. Also, the location of inflow channels or "weeps" at SFR changes over time intervals of a few weeks, calling into question the idea of temporally invariant inflow locations (D. A. Chesnut, personal communication with Svensk Kärnbränslehantering AB (SKB) the Swedish Nuclear Fuel and Waste Management Company staff

during a site visit as a member of the Äspö Hard Rock Laboratory Scientific Advisory Committee). The phenomenon of the location of seeps changing with time, as well as the observation that a small percentage of visible fractures is responsible for seepage, were also noted at the Spent-Fuel Test (SFT) that was performed at the Climax Stock in the northern portions of NTS (Wilder, 1987). At the SFT it was noted that seepage also was influenced by the emplacement of waste and activation of electrical heaters, which supports the concept that pre-emplacement percolation conditions will be modified.

1.5.2 Controlling Inflow in Openings below the Water Table and its Implications for Fracture Characteristics

The ability of flow in fracture networks to adjust to changes in fracture connectivity is also illustrated by experience of investigators in Finland with grouting to control water inflow into underground openings below the water table. Even after multiple stage grouting, typical seepage rates are reported to be reduced by only 75% of their values prior to grouting, according to presentations in March 1993 at the Äspö Hard Rock Laboratory Workshop on Design and Construction of Deep Repositories, Såstaholm Conference Center, Täby, Sweden (Chesnut and Wilder, 1993). The following excerpt from this source (1993) provides a more complete summary of the Finnish experience:

> "Reijo Riekkola, TVO, summarized Finnish experience with fractured rock in several contexts. They classify fracture zones according to two sources of problems:
>
> 1. Transmissivity (water inflow), and
> 2. Rock engineering (stability of openings).
>
> In general, water inflow problems do not involve the same sets of fractures as those important for rock engineering.... In addition to the [Finnish] VLJ [Repository] project, [other] field experiences were reviewed for construction of the Helsinki sewer system, the Pasilo District heating tunnel, the Helsinki Metro, and a sea sewer in connection with an underground sewage treatment plant for Helsinki...
>
> Conclusions based on these experiences include:
>
> - Grouting may not permanently reduce water inflow to tunnels;
> - Better investigation methods are needed to obtain a more realistic description of zones to be grouted;
> - The amount of grout needed may be seriously overestimated or seriously underestimated, depending upon local conditions;
> - The floor of tunnels and other openings is the most difficult area to seal effectively;
> - Sealing by grouting is usually *very* expensive.
>
> During the discussion following the Finnish presentation, Gunnar Gustafsson mentioned that if the transmissivity of a fracture zone is only about ten times the transmissivity of the average rock, then the total inflow will be about the same after grouting as before. When the fracture zone has much higher transmissivity, then the inflow can be reduced by grouting."

Although this experience does not translate directly into an understanding of drift-scale seepage under unsaturated conditions, it does indicate that the overall connectivity of fracture networks may be the most important feature to understand. It also suggests that attempting to predict, or describe quantitatively, the aggregate hydrologic behavior of a fracture network from detailed investigations of individual fractures may not prove to be a productive approach. Some simple conceptual models that appear promising for Yucca Mountain are described in the next section.

1.5.3 Conceptual Models

The need to account for the possible occurrence of fracture flow at Yucca Mountain has received increased attention by Project scientists since about 1991. Earlier repository performance calculations were based conceptually on the "equivalent continuum model" (ECM) for fractured rock, which uses a weighted average of Yucca Mountain matrix and fracture properties in order to simplify the flow equations. The approximation is valid for some applications, but can lead to serious error in others, because fracture flow can occur in the ECM only if the system is nearly saturated with water. The validity of the approximation (under essentially isothermal conditions) depends upon the relative time constants for capillary imbibition into the matrix and gravity drainage through the fractures. Because fracture flow is the likely mode of water entry into a drift that could lead to water contact with waste packages (and ultimately with waste), it is very important to model it correctly for determining waste-package failure rates and in calculating radionuclide transport in the near field and altered zone.

1.5.3.1 The Weeps Model. The "weeps model" (Gauthier, et al., 1992) was used to estimate the repository performance consequences of fracture flow at Yucca Mountain in TSPA93. Each weep is assumed to have the same flow rate, and the total number of weeps within the repository footprint is adjusted to accommodate the total infiltration through the repository area. For the example given by Gauthier, et al. (1992), if the infiltration flux is 4.5 mm/yr. and the footprint area is 5.61×10^6 m^2, the total infiltration rate through the repository block would be 2.52×10^4 m^3/yr. Assuming that each weep flows for one month each year at an annual rate of 23.1 m^3/yr. (saturated gravity flow in a hypothetical fracture with an aperture of 100 μm), 13,100 weeps would be required to accommodate the average annual infiltration.

Weeps were assumed to be randomly distributed over the repository footprint area, and the distribution was assumed to be temporally invariant. By assigning a "contact area" to each waste container, the probability of contact was calculated. For 35,000 canisters, in the SCP borehole emplacement conceptual design, and 13,100 weeps, an average of 82 containers would be contacted by water, with a standard deviation of 9. (One should note that the current conceptual design envisions drift emplacement instead of the borehole emplacement configuration considered at the time of the Gauthier et al. study.) Note the following observations from the study by Gauthier et al.:

- Decreasing the assumed fracture aperture increases the number of weeps and, consequently, the probability of contacting a container with water: at 12 μm, the number of weeps would increase to 6,000,000, and *all containers* would be contacted by water.
- Conversely, increasing the aperture decreases the number of weeps: at 910 μm, the number of weeps would decrease to 160, and only *one* container would be contacted by water, on the average.

These two limiting cases have very different consequences for radionuclide release. If there are many weeps, there is no flow focusing, the entire radionuclide inventory after waste-package failure would eventually be contacted by water, and would dissolve, given sufficient time. If there are only a few weeps, then the ultimate total radionuclide release is limited to the number of containers contacted multiplied by the inventory per container. Careful examination of the cases considered by Gauthier et al. (1992) shows that, for the long-lived radionuclides, the total release rate for the entire repository is always equal to the average flux times the contact area per container times the waste solubility per m^3 of water, up until the time it takes for all the waste to be dissolved from the number of containers contacted. At that point the release rate drops to zero: nothing else ever leaves the repository.

Thus, the weeps model may not be conservative, in that it could seriously underestimate the fraction of the total radionuclide inventory that is eventually contacted by water. In part, this potential lack of conservatism arises from the assumption that all weeps flow at the same rate, and in part it arises from the assumption of temporal invariance in the spatial location of the weeps. In the next section, we present a somewhat more complicated, but still simple, model with a conceptual distribution of weep rates based on the observations at Stripa.

1.5.3.2 The Log-Normal Model

1.5.3.2.1 Origins. The Stripa data suggest the following conceptual model for the spatial distribution of flow in fractured rock:

1. A fraction ξ (equal to 0.709 for Stripa) of the total inflow area has zero flow
2. A fraction $1-\xi$ (equal to 0.291 for Stripa) of the total inflow area has a continuous distribution of flow, with an unknown distribution function.

The form of this distribution function was suggested by the work of Chesnut, Cox, and Lasaki (1979) on the performance of waterflooding heterogeneous petroleum reservoirs. Waterflooding is the process of injecting water into a petroleum reservoir through some wells while continuing to produce fluids from the remaining wells. It has been in commercial use for many decades and is therefore a rich source of data for the effects of heterogeneity on relatively large-scale (≈ 500 m) fluid flow and transport phenomena.

Two distinct normalized breakthrough curves can be defined:

1. The total fluid (oil + water) production rate divided by the water injection rate, $(q_o + q_w)/i_w$, plotted versus time
2. The total water production rate divided by the water injection rate, q_w/i_w, also plotted versus time.

Chesnut, Cox, and Lasaki (1979) showed that waterflood breakthrough curves in heterogeneous porous media can be represented accurately by log-normal probability integrals. The derivation assumes that a heterogeneous medium can be approximated as a "layer cake" of independent infinitesimal layers connecting the injection and producing wells. These layers are assumed to have a log-normal permeability distribution, with log-standard-deviation σ, and the injected water is allocated among the layers in proportion to their respective permeability-thickness products. According to the resulting equations, plots of the normalized production rates on a cumulative normal probability scale versus the logarithm of time result in two parallel straight lines, with slopes proportional to σ.

1.5.3.2.2 Log-Normality of Stripa Inflow Data. Chesnut found (1992) that the Stripa data fit a log-normal distribution, provided that only the sheets with measurable flow were included in the analysis. Table 1.5.3-1 shows the histogram data from Neretnieks et al. (1987) for only those sheets that had measurable flow rates. The sum of the geometric means of the histogram upper and lower limits, weighted by the number of sheets in the corresponding flow rate interval, is 651.0 mL/hr, compared with the reported total flow rate of 647.7 mL/hr; indicating that a reasonably accurate statistical analysis can be performed from the histogram. The remaining columns in Table 1.5.3-1 are used in calculating the log mean and log standard deviation (base e); the resulting value of σ is 1.583.

Based on the success of the log-normal distribution in fitting waterflood breakthrough time data, it was natural to attempt to fit the Stripa data for non-zero inflows to the same distribution. Figure 1.5.3-1 is a plot, using log-normal axes, of the cumulative distribution of the inflow data from Stripa. A straight line on this plot indicates that the underlying distribution of the data is approximately log-normal, and the slope is proportional to the natural log standard deviation, σ, of the inflow rate. The value of σ from the slope of the least-squares straight line shown on the plot is 1.596, in good agreement with the log-standard deviation (1.583) calculated in Table 1.5.3-1.

Hence, at least for fractured, non-porous rock, a reasonable model for the spatial distribution of groundwater flux is given by the following equations:

$$P(u_w = 0) = \xi$$

$$P(0 < u_w \le x) = (1-\xi)\cdot\Phi\left\{\frac{\ln(x/\bar{u}_w)+\sigma^2/2}{\sigma}\right\} \qquad (1)$$

where $\bar{u}_w = \frac{i_w}{1-x}$ is the average flux for the fraction $1-x$ of an arbitrary surface over which the measured flow is nonzero.

In this equation, i_W is the nominal average flux over the entire surface. The parameters ξ, σ, and π_w have to be estimated or determined experimentally for each specific site. The parameter σ is a quantitative measure of heterogeneity: as it tends to zero, the spatial distribution of flux becomes completely uniform, with each area receiving the same seepage rate. Conversely, as σ increases, the range from lowest to highest observed flux increases, i.e., the spatial distribution becomes highly variable from place to place.

Similar measurements in other mines or underground openings would be very useful for determining whether log-normality is commonly observed and would also provide a range of values for specific geologic settings. It is perhaps noteworthy to mention that the heterogeneity parameter, σ, for Stripa (a saturated fractured granite) is about twice as large as typical values for successful waterfloods in which fractures generally do not play a dominant role. However, it is about the same as a value for partially saturated soil calculated from a typical coefficient of variation for the hydraulic conductivity of unsaturated soil given by Harr (1987).

Stripa data show that the *spatial* distribution of flux within a fractured *non-porous* medium (granite) may well be log-normal under "steady" flow conditions. Several questions must be raised:

1. If we could measure tracer breakthrough at Stripa on the same scale as the water inflow measurements (*i.e.*, from the ground surface to the mine), would it show a log-normal travel time distribution? In other words, does the distribution of flux have the same heterogeneity as the distribution of travel time?
2. How does the spatial distribution vary over time in response to changes in surface infiltration?
3. In a partially saturated fractured porous medium, is the distribution approximately log-normal if it is log-normal under fully saturated conditions? If so, how do the parameters (log mean and log standard deviation) of the log-normal distribution change with average saturation?

These questions cannot be answered completely with currently available information. They will be considered further in a later section, along with recommended modeling that could help provide some of the answers. In the next section, we assume that the log-normal distribution adequately describes seepage into emplacement drifts, and compare the results of this assumption to the weeps model.

1.5.4 Comparison of Log-Normal Seepage Distribution to the Weeps Model

Relatively small water fluxes become very important if the compliance time horizon is extended beyond 10,000 years. One approach to evaluate the importance of flux is to assume that the flux occurs uniformly over the entire repository area. The area of a multi-assembly cask, being considered for YM, projected onto a horizontal plane is about 8.5 m^2, and each cask would contain on the order of 8 to 8.5 MTU, so there is about 1 m^2 of horizontal waste-package area per MTU. A percolation flux of 1 mm/yr. is 1L/m^2/yr. If each metric ton of waste were contacted by the average percolation flux times its projected area, we would have about 1 L/water/yr. contacting each metric ton of waste. No matter what rate of solution of waste is used, it is clear that the time required to dissolve a waste form is directly proportional to the amount of water contacting waste per year. The total radionuclide release is then proportional to the number of waste packages contacted by water. However, as was just discussed, the flux not uniformly distributed over the repository area, and a more realistic method of estimating the impact of flux on waste dissolution is needed.

The Stripa flux distribution can be used directly to consider the contact of water with waste packages. Because the scale of measured areas in the Stripa study is different than the area of the multi-assembly container considered for Yucca Mountain, the analysis done first for a hypothetical waste package with a size equal to the scale of measurement at Stripa. If we were contemplating constructing a repository with the Stripa distribution of flow containing waste packages with a horizontally projected area of 2 m^2, then this experiment would be a direct measure of the distribution of the flow rate of water contacting containers: almost 71% of the containers would be "dry," and only 29% would be "wet," at any given

time. If the inflow locations did not change over time, then only 29% of the containers would *ever* get wet. As noted previously, the temporal invariance of discrete seepage locations is not supported by the SFR observations.

Figure 1.5.4-1 shows the observed and calculated numbers (forced to be integers) of hypothetical "waste packages" that would be contacted by water under conditions observed at Stripa. The inflow distribution is highly heterogeneous, with a natural log standard deviation, σ, equal to 1.58. The 7 wettest "waste packages" receive almost 45% of the total flow. It is interesting to note that the average flux over the total drift area at Stripa, including "dry" regions, is only a little more than 7.5 mm/yr., which is less than the percolation flux at Rainier Mesa, and less than the estimated surface infiltration rates in some areas of Yucca Mountain. However, it is almost double the approximately 4.5 mm/yr. value commonly used for an upper limit at Yucca Mountain and many times larger that the lower values used in some Total System Performance Assessment (TSPA) calculations.

Similar calculations were performed for Yucca Mountain to assess the plausibility of the "weeps" model. Current conceptual designs envision drift emplacement of 8489 large casks with a projected area of about 8.5 m^2 each. The repository area depends upon the thermal loading strategy finally adopted, but for these calculations we assume the SCP loading of 57 kW/acre, corresponding to a repository footprint of 4.63×10^6 m^2. This is equivalent to 544,500 "waste-package-sized" areas of 8.5 m^2 each; only 1.6% of these actually contain a package. If we assume the same distribution of inflow as for Stripa, then 70% of the packages are "dry," and only 2547 could be contacted by some water. For direct comparison with the "weeps" model summarized above, we assume an average flux of 4.5 mm/yr., as was used in the "weeps" analyses. There is some indication that σ at Yucca Mountain may be larger than σ for Stripa; however, the Stripa value (1.58) was used in these calculations.

Figure 1.5.4-2 shows that a log-normal distribution results in a large fraction of waste packages receiving much less water than the average flux multiplied by the projected area of a waste package. However, there are still hundreds of packages that would be contacted by the average or greater flux. Increasing the heterogeneity (larger σ) reduces the number receiving as much or more flux than the average, but the numbers remain much greater than the number of wetted packages (82±9) in the "weeps" calculation. Hence, the weeps model may not give a conservative limit to the number of waste packages contacted by a significant amount of water, and may therefore underestimate the amount of waste that eventually dissolves.

Note from Fig. 1.5.4-2 that more than 600 "waste packages" would be contacted by more than 100 L of water per year. Because each waste package contains on the order of 10 MTU of waste, the contact flow rate for these wet packages is on the order of 10 L/yr./MTU. Even if the dissolution rate is limited by the solubility of uranium oxide, a waste form could be dissolved in less than 40,000 yrs. by flow rates of this magnitude.

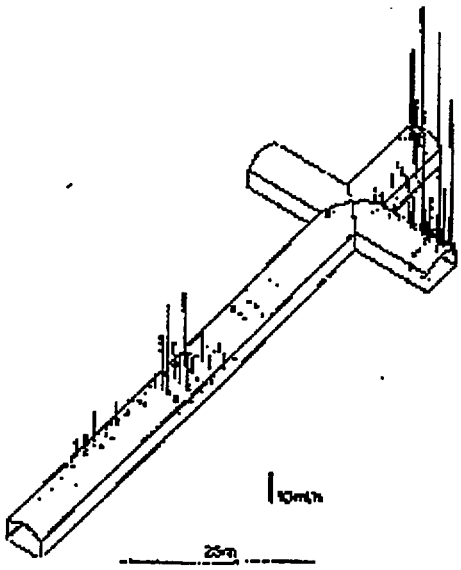

Figure 1.5.1-1. Spatial distribution of seepage flux measured at Stripa (after Neretnieks, Abelin, and Birgersson, 1987). Bars are proportional to the three-year average hourly flow rates into 375 2-sq-m areas isolated from each other by plastic sheets. Only 109 of the areas had measured rates greater than the lower detection limit of 0.1 mL/hr.

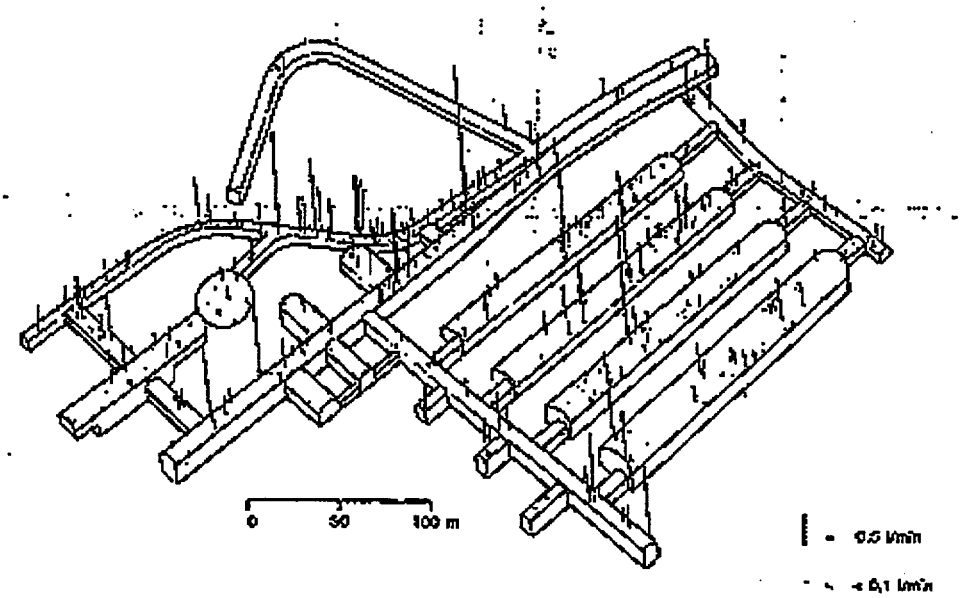

Figure 1.5.1-2. Distribution of inflow into the SFR low-level waste repository (after Moreno, Neretnieks, and Gylling, 1993). The length of the bars is proportional to the flow rate in liters per minute.

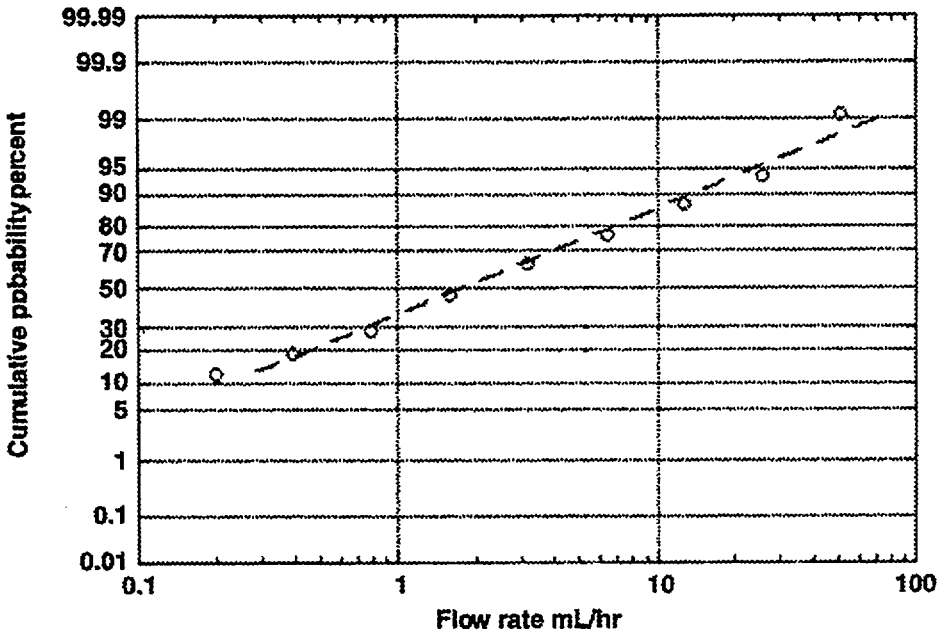

Figure 1.5.3-1. Distribution of inflow rates per 2 m^2 for Stripa. Circles represent measured data, plotted at the upper limit of each flow rate range; the dashed line is a least-squares fit to a log-normal distribution. Rectangles with no reported flow were not included in the cumulative probability.

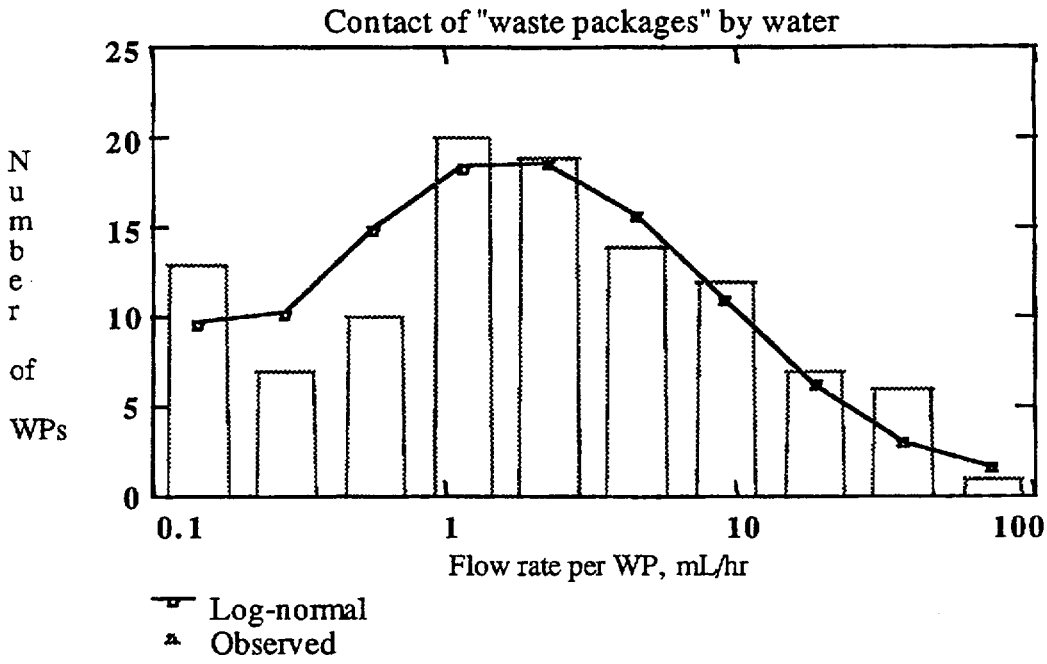

Figure 1.5.4-1. Histogram for contact of hypothetical waste packages for Stripa conditions. Bars are actual observations; points are from a discrete log-normal approximation with mean 5.94 mL/hr and natural log standard deviation (σ) 1.58.

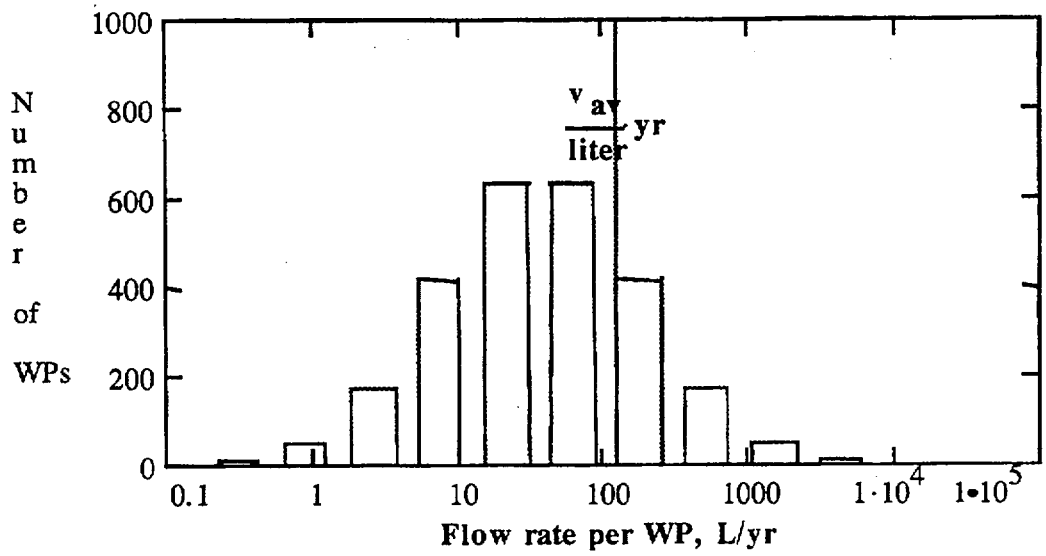

Figure 1.5.4-2. Histogram for number of MPC-sized waste packages that would be contacted by water, assuming the same heterogeneity and fraction "dry" that was observed at Stripa. Infiltration of 4.5 mm/yr. was assumed for comparison with the "weeps" model.

Table 1.5.3-1. Analysis of Stripa inflow data. Only sheets with measurable inflow (more than 0.1 mL/hr) are included in the analysis.

Lower Limit	Upper Limit	Mean Ln (MLn)	N	N*MLn	N*(MLn)^2	(LL*UL)^.5 (Lbar)	N*(Lbar)
0.10	0.20	-1.9560	13	-25.4281	49.7378	0.14	1.84
0.20	0.40	-1.2629	7	-8.8401	11.1638	0.28	1.98
0.40	0.80	-0.5697	10	-5.6972	3.2458	0.57	5.66
0.80	1.60	0.1234	20	2.4686	0.3047	1.13	22.63
1.60	3.20	0.8166	19	15.5150	12.6692	2.26	42.99
3.20	6.40	1.5097	14	21.1361	31.9097	4.53	63.36
6.40	12.80	2.2029	12	26.4345	58.2317	9.05	108.61
12.80	25.60	2.8960	7	20.2721	58.7085	18.10	126.71
25.60	51.20	3.5892	6	21.5350	77.2927	36.20	217.22
60.00	60.00	4.0943	1	4.0943	16.7637	60.00	60.00
		Sums	109	71.4903	320.0275		651.00
			Means	0.6559	2.9360		5.97
				σ	1.5830		
				vbar	6.7450		

Contents

1.6 (REV 0) Diffusion-Controlled Radionuclide Release

Diffusion-controlled releases are discussed in Section 1.8 of this report and therefore the section numbering has changed.

1.6 (REV 1) Impact of Repository Construction/Operational Activities

The material in this section is essentially the same as in section 1.7 of Rev 0 of the PNFER, modified to reflect drift rather than borehole emplacement.

The preceding sections primarily discussed how the physical attributes of the hydrological system in Yucca Mountain affect the near-field environment (NFE) without addressing the effects of construction activities. The construction of the access and emplacement drifts alter the ambient near-field (NF) hydrological environment in several ways. First, excavation activities enhance both the density and aperture of the fracture system for at least two room-diameters surrounding the openings. Second, the introduction of mining and drilling fluids may increase the matrix saturation surrounding the openings. Third, mine ventilation dries the matrix around the drifts for some undetermined distance from the rock surface.

The impact of drilling fluids on the ambient saturation conditions during the Prototype Engineered Barrier System Field Test (PEBSFT) in G-Tunnel was addressed by Buscheck and Nitao (1988). Buscheck and Nitao (1991a) conducted a study on nonequilibrium fracture-matrix flow that is driven by ponded conditions at the repository horizon. This work was motivated by performance assessment calculations for the "human-intrusion drilling scenario." In this scenario, once an exploratory drilling operation has penetrated an emplacement drift, circulation of drilling fluid would be lost, thereby introducing enough fluid to maintain a ponded condition for a limited time. Repository mining and drilling operations may result in ponded conditions lasting for a period of days to weeks. Because of the small matrix permeability of TSw2, ponded conditions lasting for this period will result in only centimeters of lateral imbibition flow from the fracture into the matrix. Depending on the spacing between fracture networks that are hydraulically connected to the mining/drilling fluid source, several centimeters of wetting front penetration into the matrix may or may not be significant relative to the bulk saturation of the system.

To quantify the impact of the introduced drilling fluids, we define the effective fracture spacing, B_{eff}, to be the spacing between fractures hydraulically connected to ponded conditions arising from a mining/drilling operation. S_e, which was defined in Eq. (2), is the bulk dimensionless saturation averaged over the interval B_{eff}. Therefore, $\overline{S}_e$ is the fraction of the initially unsaturated porosity (bulk-averaged over B_{eff}) that has been wetted because of imbibition from the fracture into the matrix. The $\overline{S}_e$ resulting from this mining/drilling operation is given by

$$\overline{S}_e = \frac{d_{imb}}{B_{eff}}, \qquad (2)$$

where d_{imb} is the penetration of the imbibition front into the matrix. Buscheck and Nitao (1988) conducted calculations that can be used to estimate the impact of drilling fluids on the saturation distribution at the repository horizon. It is reasonable to assume that drilling might result in ponded conditions persisting for two days at the top of any given fracture intersected by the borehole. For a two-day-ponded infiltration event, Buscheck and Nitao (1988) found that matrix imbibition resulted in d_{imb} = 0.02 m. Assuming b_{eff} = 1 m and d_{imb} = 0.02 m results in $\overline{S}_e$ = 0.02. Therefore, about 2% of the initially unsaturated porosity along the fractures (that are hydraulically connected with the source of mining/drilling water) has been saturated by the mining/drilling operation.

For welded tuff—either Grouse Canyon, in which the (PEBSFT) was conducted, or TSw2—Buscheck and Nitao (1988) found that it took about a year for the saturation distribution in the wetting zone along

the fractures to nearly equilibrate to background saturation. By that time, the saturations over the interval B_{eff} have become nearly uniform as given by

$$S_{pert} = S_i + \bar{S}_e(1 - S_i), \quad (3)$$

where S_{pert} is the "perturbed" saturation and S_i is the initial (or ambient) saturation. For the above example, if $S_i = 0.65$, then $S_{pert} = 0.657$, which is very close to ambient. If the fracture networks at the repository horizon have limited connected path lengths, then the imbibition of mining/drilling fluid will be confined accordingly.

The experience of Ramirez et al. (1991) indicates that drilling fluids had a negligible impact on the ambient saturation conditions in the vicinity of the G-Tunnel heater. In their neutron probe surveys taken prior to heating, they could not detect variations in the saturation distribution that could be attributed to the water used to drill the heater and instrumentation boreholes. Moreover, although boiling generated a large volume of vapor and condensate, the neutron probe surveys taken during and after heating did not indicate significant buildup of matrix saturation along fractures caused by the imbibition of condensate. The densely welded tuff of Grouse Canyon, like TSw2, has a very small matrix permeability, which minimizes the effect of matrix imbibition. Perhaps the effective fracture spacing, B_{eff}, of fractures conducting condensate away from the condensation zone is relatively large, further tending to make $\bar{S}_e$ small.

On the basis of the above discussion, the most significant impact of the human-intrusion drilling scenario appears to be in the direct introduction of fluids in the drifts, which could cause temporary ponding within the drifts that could pick up radionuclides if any containers were already breached. However, the imbibition and fracture drainage would not support ponding in the drifts for long periods of time required to cause failures of the containers (it is possible that long-term impacts on RH could occur if there were significant volumes of fluids introduced to the extent that the packages cooled considerably, but again this is probably a temporary condition). If radionuclides did get dissolved in the drilling fluids, they would not likely be recirculated in the drill fluids because circulation would be lost in the drifts, but the ponding in the drift could possibly cause migration below the repository by driving fracture flow. Again, this fracture flow could only be sustained as long as there was ponding of the fluids in the drift. Of secondary significance the scenario's effect on increasing the matrix saturation of the NF, thereby enhancing diffusion-controlled radionuclide release modes.

The effects of mine ventilation depend on the mine ventilation rates and the duration of ventilation (i.e., time to backfilling and closing the emplacement drifts). Recent work by Chesnut, Flint, and Wang (1996) estimated water removal by the ventilation system within the ESF drift, and found that this could be significant (see Section 1.2.2.2). If the ESF ventilation is typical of the emplacement drift ventilation, then significant dryout can occur as result of ventilation. Furthermore, if ventilation is continued after emplacement, the combination of ventilation and thermal loading could cause significant volumes of water to be removed from the rock surrounding the emplacement drifts. Finally, the movement of water toward the drift by capillarity, followed by evaporation near the drift wall, could deposit significant amounts of dissolved solids in the rock immediately surrounding the drifts.

References

Abelin, H., Birgersson, L., and Neretnieks, I., (1987), "Some Recent Observations of Channeling in Fractured Rocks — Its Potential Impact on Radionuclide Migration," *Proceedings, DOE/AECL Conference*, September 15–17, San Francisco, CA, pp. 387–410.

Abelin, H., L. Birgersson, J. Gidlund, and I. Neretnieks, "A Large-Scale Flow and Tracer Experiment in Granite, 1. Experimental Design and Flow Distribution," *Water Resources Research* 27, 3107–3117 (1991).

Buscheck, T. A., and J. J. Nitao, *Nonequilibrium Fracture-Matrix Flow During Episodic Infiltration Events in Yucca Mountain*, Lawrence Livermore National Laboratory, Livermore, CA, UCRL-ID-108311 (1991).

Chesnut, D. A., Alan L. Flint, , and Joseph S. Y. Wang, *Coordinated Exploratory Studies Facility (ESF) Construction-Phase Testing and Monitoring Program*, Scientific Programs Operations, Management and Operating Contractor Milestone Report M4-TR31K5M, May 28, 1996.

Chesnut, D. A., D. O. COX, and G. L. ASAKI, "A Practical Method for Waterflood Performance Prediction and Evaluation," *Proceedings, Pan American Congress of Petroleum Engineering*, Mexico City, March 19–23 (1979).

Chesnut, Dwayne A., "Characterizing the Altered Zone at Yucca Mountain: The Beginning of a Testing Strategy," *Proceedings, Third International High-Level Radioactive Waste Management Conference;* American Nuclear Society, Inc.: Las Vegas, NV, pp. 1026–1039 (1992).

Chesnut, Dwayne A., and Dale G. Wilder, Foreign Trip Report: Äspö Hard Rock Laboratory Workshop on Design and Construction of Deep Repositories, Såstaholm Conference Center, Täby, Sweden, March 30–April 1, 1993 (Submitted to Lawrence Livermore National Laboratory, May 7, 1993).

Cox, Dave O., and Nick Stellavato, "Analysis of Air Permeability Tests at Yucca Mountain, Nevada," *Proceedings, ??? Annual International High-Level Radioactive Waste Management Conference, Las Vegas, Nevada.* April 29–May 3, 1996.

Fabryka-Martin, J. T., P. R. Dixon, S. Levy, B. Liu, H. J. Turin, and A. V. Wolfsberg, *Summary Report of Chlorine-36 Studies: Systematic Sampling for Chlorine-36 in the Exploratory Studies Facility*. Level 4 Milestone Report 3783AD, Los Alamos National Laboratory, March 29, 1996.

Flint, Lorraine E., *Matrix Properties of Hydrogeologic Units at Yucca Mountain, Nevada*, U.S. Geological Survey, Water Resources Investigations Report 96-xx (in review, 7/22/96).

Gauthier, John H., Michael L. Wilson, and Franz C. Lauffer, "Estimating the Consequences of Significant Fracture Flow at Yucca Mountain," *Proceedings, Third International High-Level Radioactive Waste Management Conference*, American Nuclear Society, Inc.: Las Vegas, NV, pp. 891–898 (1992).

Harr, M. E., *Reliability-Based Design in Civil Engineering*, McGraw-Hill Book Company (1987).

Hudson, David B., and Alan L. Flint, *Estimation of Shallow Infiltration and Presence of Potential Fast Pathways for Shallow Infiltration in the Yucca Mountain Area, Nevada.* U.S. Geological Survey, Water Resources Investigations Report xx-xxx, 1996 (in press).

LeCain, G. D., and J. N. Walker, "Results of Air Permeability Testing in a Vertical Borehole at Yucca Mountain, Nevada," *Radioactive Waste Management*, pp. 2782–2788, 1994.

Liu, Beiling, June Fabryka-Martin, Andy Wolfsberg, Bruce Robinson, and Pankaj Sharma, "Significance of Apparent Discrepancies in Water Ages Derived from Atmospheric Radionuclides at Yucca Mountain, Nevada," *Water Resources at Risk,* American Institute of Hydrology Conference, Denver, Colorado, May 14–18, 1995.

Loeven, Colleen, *A Summary and Discussion of Hydrologic Data from the Calico Hills Nonwelded Hydrogeologic Unit at Yucca Mountain, Nevada*, Report LA-12376-MS, Los Alamos National Laboratory 1993.

Moreno Luis, Ivars Neretnieks, and Björn Gylling, "Modeling of Fluid and Solute Transport in Fractured Rock," *Proceedings, Fourth International High-Level Radioactive Waste Management Conference*, American Nuclear Society, Inc.: Las Vegas, NV, pp. 1128–1133 (1993).

Nativ, Ronit, Eilon Adar, Ofer Dahan, and Mebus Geyh, "Water recharge and solute transport through the vadose zone of fractured chalk under desert conditions," *Water Resources Research* 31, No. 2, pp. 253-261, (Feb. 1995).

Rousseau, Joseph P., Edward M. Kwicklis, and Daniel C. Gillies, editors: *Hydrogeology of the Unsaturated Zone, North Ramp Area of the Exploratory Studies Facility, Yucca Mountain, Nevada*, U.S. Geological Survey, Water Resources Investigations Report 96-xx (in review, 8/96).

Russel, C.E., J.W. Hess, and S.W. Tyler, *Hydrolgeologic Investigation of Flow in Fractured Tuffs, Rainier Mesa, Nevada Test Site,* Flow and Transport through Unsaturated Fractured Rock, D. D. Evans and T. J. Nicholson (editors), Geophysical Monograph #42, AGU, Washington, DC, 1987.

Wang, J. S. Y., N. G. W. Cook, H. A. Wollenberg, C. L. Carnahan, I. Javandel, and C.F. Tsang, "Geohydrologic Data and Models of Rainier Mesa and Their Implications to Yucca Mountain," *Proceedings, Fourth Annual International High-Level Radioactive Waste Management Conference*, Las Vegas, NV, April 26–30, 1993.

Wilder, D. G., *Influence of Stress-Induced Deformations on Observed Water Flow in Fractures at the Climax Granitic Stock*, Rock Mechanics: Proceedings of 28th U.S. Symposium, Tucson, AZ; Edited by I.W. Farmer, J.J.K. Daemen, C.S. Desai, C.E. Glass and S.P. Neuman; A.A. Balkema, Rotterdam, 1987.

Contents

1.7 Thermal-Hydrological Processes

This section describes, at a detailed level, the thermal-hydrological (T-H) processes that affect the environment of the Engineered Barrier System (EBS), including backfill, waste package (WP), man-made materials, and waste form. Functionally, near-field processes are those EBS-affecting processes that are the result of, or are affected by, the EBS itself (including radioactive decay heat from the WPs), and processes that must be understood to predict EBS performance. The spatial extent of near-field processes depends on individual processes and on the EBS design (particularly the thermal design). The interaction and intercoupling of thermal-hydrological processes with geochemistry and geomechanics also must be assessed.

Sections 1.7 and 1.8 complement each other. Section 1.7 describes the primary coupled T-H processes (and coupled T-H-M-C processes) at a detailed phenomenological level, while Section 1.8 describes the T-H behavior , which is the net result of those T-H processes, in the context of the following:

EBS performance: Radionuclide containment in (and eventual release from) the EBS is most notably affected by the distribution of temperature, relative humidity, liquid-phase saturation, and liquid-phase flux in the emplacement drifts and in the near-field rock.

Thermal management strategies: These strategies are implemented in the thermal design of the repository, including the overall areal mass loading of the repository and the details of how the decay-heat sources (i.e., the WPs) are distributed. The key decision in any strategy concerns whether to attempt to (1) minimize (to the extent possible) the thermal-hydrological effects of decay heat or (2) to use decay heat constructively to generate conditions that are more favorable for radionuclide containment in the EBS.

Major thermal-hydrological flow regimes: These regimes are, in effect, the net outcome of intercoupled T-H and T-H-M-C processes (i.e., determined by the dominant processes). These regimes vary in time and space. The factors determining where and when a given regime dominates include (1) the distribution of natural system properties and conditions, (2) how the decay-heat sources (the WPs) are distributed, other engineering measures such as the use of backfill.

We begin this section by listing the fundamental T-H-M-C processes in Section 1.7.1. Section 1.7.2 is a detailed discussion of the primary coupled T-H processes. Sections 1.7.3 and 1.7.4 briefly describe intercoupling between T-H processes and geochemical and geomechanical processes.

1.7.1 Fundamental Thermal-Hydrological-Geomechanical-Geochemical Processes

Thermal-hydrology comprises processes that result from coupling basic thermal and hydrological processes. Thermal processes include the generation and transport of thermal energy. Hydrological processes involve the generation and transport of water in both the liquid and vapor state. The generation and transport of dissolved chemical species (including radionuclides) result from thermal, hydrological, and geochemical processes that may be coupled and thus may influence one another.

The following are sources, basic mechanisms, and conditions affecting the thermal energy balance at Yucca Mountain and the potential repository. Investigations are being conducted to determine the extent to which they are operative at Yucca Mountain; the results to date will be discussed in this section (and following sections, including Sections 10.1 and 10.2 of Chapter 10). The sources, mechanisms, and conditions are as follows:

- Generation of thermal energy by radioactive decay of nuclear waste.
- Generation of thermal energy by geothermal sources below Yucca Mountain, as evidenced by the geothermal gradient.
- Net energy flux at the ground surface from solar radiation and from eddy diffusion of latent heat from evaporation and latent heat of condensation of water vapor.

- Incoming thermal energy that is advected by infiltrating water and the lateral flow of water that enters the system.
- Outgoing thermal energy that is advected by the lateral flow of water that leaves the system.

The following are the basic mechanisms that may be involved in the transport of thermal energy at Yucca Mountain and the potential repository. These will be investigated further to determine the extent to which they are operative at Yucca Mountain:

- Thermal conduction in the bulk rock matrix.
- Liquid-phase advection, including transport of latent heat of water vapor.
- Gas-phase advection.
- Species diffusion in the liquid and gas phases.
- Thermal radiation, conduction, and convection from the WP to the drift walls.
- Storage of thermal energy in the rock matrix by heat capacity.
- Change in thermal energy from condensation of water vapor and evaporation of liquid water (called latent heat effects).

The following are basic hydrological processes involved in the movement of water at Yucca Mountain and the potential repository:

- Liquid-phase advection of liquid water driven by liquid-phase pressure gradients.
- Liquid-phase advection of liquid water driven by matric potential gradients.
- Liquid-phase advection of liquid water driven by gravitational and buoyancy forces.
- Gas-phase advection of water vapor driven by gas-phase pressure gradients.
- Gas-phase advection of water vapor driven by gravitational and buoyancy forces.
- Gas-phase diffusion of water vapor, possibly including enhanced diffusion [Philip and De Vries, 1957].
- Evaporation and condensation of water.
- Partitioning of water between liquid and gaseous phases.
- Vapor-pressure-lowering phenomena [Edlefsen and Anderson, 1943; Nitao and Bear, 1994].
- Changes in permeability and porosity as a result of dissolution and precipitation of minerals.

The following are chemical and hydrological transport related processes at Yucca Mountain and the potential repository:

- Liquid-phase advection.
- Gas-phase advection (for gaseous species).
- Liquid-phase diffusion.
- Gas-phase diffusion.
- Adsorption on solids.
- Colloidal suspension.
- Dissolution and precipitation reactions.
- Chemical reactions, mineral alteration, and dehydration reactions.
- Radioactive decay.

The following are some potential geomechanical processes related to thermal-hydrology at Yucca Mountain and the potential repository:

- Change in fracture permeability as a result of thermal stresses.

- Fracturing of the rock matrix as a result of increased pore pressure during boiling of water in the matrix blocks.
- Microfracturing of rock matrix as a result of increased stresses.
- Increased fracture propagation as a result of the presence of liquid water or steam or increased mechanical stresses.
- Change in geomechanical properties of the fracture as a result of mineral dissolution and precipitation or dehydration.
- Change in porosity and geomechanical properties as a result of temperature and saturation changes.
- Change in porosity and geomechanical properties of the matrix as a result of mineral dissolution and precipitation.

The following are the primary conditions that could bear on WP failure in the potential repository:

- Thermodynamic conditions in the EBS and at the WP surface, including gas-phase pressure P_g, relative humidity RH, and temperature T.
- Liquid-phase flux distribution in the EBS and at the WP surface.
- Gas-phase flux distribution in the EBS and at the WP surface.

The following are related to the source-term release from breached WPs at the potential repository:

- Amount of water flowing around the waste-form.
- Thermodynamic properties of the water contacting the waste-form, including its chemistry and temperature.
- Diffusion of radionuclides from the waste form, through the EBS material, to the near-field rock.
- Advection of radionuclides from the waste form, through the EBS materials, to the near-field rock.

1.7.2 Fracture-Matrix Vapor Transport and Condensate Flow

Gas-phase advective transport of water vapor is driven by (1) gas pressure gradients caused by barometric pumping and generation of water vapor by radioactive decay heat, (2) thermal expansion of the gas phase driven by radioactive decay heat, and (3) density gradients caused by the geothermal gradient, seasonal temperature differences, and temperature gradients created by radioactive decay heat. Gas-phase transport over extended distances will occur primarily by advection in fractures when bulk advective velocities are high. At low velocities, advective gas-phase transport will occur in both matrix and fractures. Diffusion of water vapor into the matrix will retard the overall movement of water vapor for the low-velocity case, where gas-phase transport is not dominated by fracture flow.

Diffusive transport of water vapor is treated by Fick's Law, i.e., the flux is proportional to the local mass fraction gradient of water vapor in the gas phase. If local thermodynamic equilibrium prevails, the mass fraction of water in the gas depends on temperature, total gas pressure, and liquid-phase saturation. Gradients in any of these quantities can lead to diffusion of water vapor. For example, all other factors being equal, vapor diffusion will occur from regions of higher to regions of lower temperatures because water vapor mass fraction in the gas phase increases with temperature. Gas-phase diffusion can occur in both the fracture and matrix. Diffusion in the matrix can be affected by the amount of water in the matrix because a higher liquid saturation will reduce the gas-filled pore space and increase the tortuosity to the gas phase. Diffusion of water vapor can be "enhanced" under a temperature gradient [Philip and De Vries, 1957] relative to the diffusion of a noncondensable gas.

An important feature of the unsaturated zone at Yucca Mountain is its high fracture density. Moreover, the Topopah Spring tuff, which occurs at the potential repository depth, is one of the most densely fractured hydrostratigraphic units. This is significant because, without fractures, the rock throughout most of the unsaturated zone (including the repository horizon) would be extremely impermeable. In general, decay heat moves moisture by (1) vaporization, (2) driving water vapor from high to low gas-phase pressure, (3) condensation, and (4) gravity- or capillary-driven flow of condensate. Without fractures, the rock would be too impermeable to allow significant vaporization and advective movement of water vapor. The flow of condensate would also be very slow. A system of connected fractures facilitates significant repository-heat-driven fluid flow as well as natural infiltration. Enhanced gas-phase diffusion may significantly contribute to water vapor transport in unfractured (relatively impermeable) rock.

Model calculations have indicated that the general thermal-hydrological behavior of the repository can be divided into three sequential periods: drying, quasi-steady, and rewetting [Buscheck and Nitao, 1993a, 1993b]. The concept of these three periods is applicable over dynamically changing *spatial* regimes. Therefore, at a given time, certain locations in a repository (such as the edge of the repository) may already be in the rewetting regime while other locations (such as the center of the repository) may remain in the drying regime.

During the initial *drying period,* the rate of evaporation is greater than the rate of condensation. (Note that the duration of these sequential periods, including the initial drying period, depend on the location in the repository.) Depending on the thermal loading of the repository and the repository location (e.g., the center of the repository), the drying period can last from tens of years to up to about two thousand years and can extend several to hundreds of meters vertically [Buscheck and Nitao, 1993a, 1993b]. The important thermal-loading parameters include:

- Areal Mass Loading (AML, expressed in metric tons of uranium per acre, MTU/acre).
- Age of spent nuclear fuel.
- Depth of the repository below the ground surface.

During the drying period, the cumulative volume of water removed from the WP zone increases monotonically. As the repository heating rate decreases and the volume of the boiling region increases, conditions stabilize to a quasi-steady state in which the rate of evaporation is equal, or nearly equal, to the rate of condensation. Temperature, liquid saturation, and relative humidity *RH* in the repository change very little during this period. Depending on the AML and SNF age, this *quasi-steady period* may last up to several thousand years, and the drying/rewetting front may be located well away from the repository. As the repository heating rate further decreases, the *rewetting period* begins as temperature, degree of liquid saturation, and *RH* begin to slowly return to ambient values. During the rewetting period, the net volume of water removed from the WP zone decreases monotonically.

During all three periods, heat is transferred between the WP and the drift walls by a combination of thermal radiation, conduction, and convection. Thermal radiation will play a major role in an open drift, whereas conduction is likely to dominate heat transfer in a backfilled drift. Buoyant gas-phase convective heat transfer may be significant in an open drift or if k_b of the backfill is high enough. The relative contribution of these heat transport processes will be analyzed by drift-scale model calculations. The rise in temperature may change the chemical, mechanical, and thermal-hydrological properties of the backfill material.

Under sufficiently high thermal loading conditions (i.e., high enough global AML or high enough local AML), the heat of decay will raise temperatures in the surrounding rock mass to the boiling point of water within the matrix. The terms "boiling zone," "boiling point," and the like are used in this discussion, regardless of whether the water actually boils, in the sense of forming bubbles within the liquid phase, or merely evaporates rapidly enough that the partial pressure of water P_v within the matrix is equal to the local saturated vapor pressure of water P_{sat} at the local temperature. The term "above-boiling" is used to refer to superheated conditions.

Boiling will occur near the fracture surfaces first and proceed into the matrix (see Fig. 1.8.1.2 in Section 1.8.1). The increase in gas pressures in the matrix caused by the generation of steam leads to an advective gas-phase flux that transports steam from within the matrix blocks to the nearest fracture. The increasing gas pressure in the matrix increases the boiling point of the water, so that temperatures in the boiling zone can be above the ambient boiling point, with some water remaining in the pores in the interior of the matrix blocks. Some diffusion of water vapor also drives steam from the matrix to the fractures, but the diffusive flux of water vapor is not significant except for very low matrix permeabilities, in which case advective velocities are low. The progress of the boiling front is relatively slow and is expected to be on the order of a few centimeters per year except during the first few hundred years, during which it could move at decimeters per year to as much as a few meters per year immediately after emplacement.

Once the steam reaches a fracture, it is transported by advection and diffusion. Advective fluxes are driven by gas-pressure and gas-density gradients (buoyancy). If the bulk permeability k_b of the rock mass is high enough, gas pressures in the fracture cannot build up much in the boiling region; under these conditions, density gradients dominate the advective gas-phase flux at the repository, and convection cells may develop. The size of these cells depends on the scale of connectedness of the fracture network. These cells can carry steam from the boiling zone both below and above the repository to a condensation region above the upper boiling zone.

If k_b is not high enough for buoyant gas-phase convection to dominate vapor transport, then the advective gas-phase flux is dominated by the boiling-driven gas-phase pressure gradients, which drive steam from the boiling zone away from the repository, where it condenses. If k_b is low enough, dryout due to boiling may be substantially suppressed (i.e., throttled). This throttling can arise in two ways. Throttling can arise because the gas-phase conductivity in the fractures is low enough to restrict fracture flow and cause a buildup in gas-phase pressure that results in an increase in the saturation temperature T_{sat} (i.e., the boiling point) in the fractures themselves. Throttling that results from restricted fracture flow has been modeled with equivalent continuum models [Buscheck and Nitao, 1993a; Buscheck and Nitao, 1993b], and with discrete fracture-matrix models [Buscheck and Nitao, 1991], and has also been analyzed with an analytical model [Manteufel and Powell, 1994]. Throttling can also result from restricted matrix-to-fracture flow that causes a gas-phase pressure buildup within matrix blocks. Thus, throttling may be more pronounced in sparsely fractured regions (with large matrix blocks) and may be less pronounced in intensely fractured regions (with small matrix blocks). Throttling that occurs because of restricted matrix-to-fracture vapor flow has been modeled with discrete fracture-matrix models [Buscheck and Nitao, 1991]. The discrete fracture-matrix model used by Nitao and Buscheck [1995] can also be extended to address throttling caused by restricted fracture flow and by restricted matrix-to-fracture flow. Where gas-phase advection is throttled, dryout may still be substantial if binary gas-phase diffusion is very enhanced. As boiling continues, water vapor displaces air away from the WPs and may replace it completely for sufficiently high AMLs. Knowing whether (or for how long) air is displaced from the repository is important in assessing the effect of oxidative corrosion on WP integrity.

As liquid water forms in the condensate zone, it will condense within the matrix pores or within the fractures. The potential effects of condensation within the matrix pores are unknown at present, and will be examined by a limited amount of detailed, small-scale modeling. If water condenses within the fractures, it will imbibe into the matrix or flow downward by gravity in a process sometimes called "condensate shedding." The theory of fracture-matrix interaction [Nitao and Buscheck, 1991; Nitao et al., 1993] indicates that if the rate of boiling, and hence the rate of condensate generation, is high enough, then condensate flow is fracture-dominated, and downward flow by gravity can be very fast as long as there is a sufficiently connected fracture network, even if the matrix is not completely saturated. A portion of the condensate drainage above the repository can return directly to WPs, where it reboils if the WP is hot enough. Some of the remaining condensate may drain through the pillars between the emplacement drifts, or through the drifts between the WPs, and leave the vicinity of the repository, resulting in a net removal of water from the near-field environment. Some of this condensate may also drain onto cooler WPs that are not hot enough to reboil this water. The cyclic boiling and condensation

of water can set up what has been called a gravity-driven heat pipe. Pruess and others [1984, 1990] were the first to model the heat-pipe effect in the context of thermal-hydrological behavior at Yucca Mountain. Their calculations pertained to a capillary-driven heat pipe. The effect of a gravity-driven heat pipe has been demonstrated in repository- and sub-repository-scale model calculations [Buscheck and Nitao, 1993a; Buscheck and Nitao, 1993b]. Under most conditions, the heat-pipe mechanism is more efficient than thermal conduction in transporting heat away from the repository.

Initially, the boiling fronts propagate radially away from each of the emplacement drifts. Before these cylindrical boiling zones coalesce, the rate of boiling can be fairly high. Condensate shedding through the repository horizon is most likely to occur during this period. As these zones coalesce, eventually forming a continuous surface or sets of continuous surfaces, and as the coalesced boiling zone propagates farther away from the repository horizon, the specific heat flux (the heat flux per unit area of the boiling front, in W/m^2) at the boiling front decreases. The specific boiling flux (the mass flux of generated steam per unit area of the boiling front, in kg s^{-1} m^{-2}) may become so low that the resulting low condensate flux can be fully imbibed by the matrix until the matrix saturates, at which stage fracture flow occurs. Under these conditions, the continual, long-term refluxing of condensate above the upper boiling region occurs under capillary equilibrium between the fractures and matrix and is, therefore, adequately described by the equivalent continuum approach discussed in Sec. 1.1.3.2 [Buscheck and Nitao, 1993b]. Some condensate may be lost along the sides of the upper boiling region at the outer edges of the repository, or at the edges of repository panels, if there is sufficient fracture connectivity. Natural infiltration fluxes can add to the condensate flux and must be included in "performance analyses" (analyses related to the EBS and to UZ transport).

Vaporization of water can occur even under sub-boiling conditions, because the higher temperatures around the WPs and the surrounding rock increase the mass fraction of water vapor in the gas phase. This higher water vapor concentration in the gas phase can advect and diffuse away from the repository horizon. Advective gaseous transport of water vapor for sub-boiling repositories is dominated by density gradients, because there is little increase in pressure due to vaporization of water. Depending on k_b, density-driven advection can move at least as much water from below to above the repository as the advection driven by an above-boiling repository [Buscheck and Nitao, 1994a].

As mentioned above, buoyant gas-phase convection cells can form at different scales depending on whether k_b at a given scale is large enough. Thus, it is possible to form convection cells at drift, repository, and mountain scales. The location and extent of the cells are controlled by heterogeneities in the natural system. High-k_b rubbelized zones and faults are key candidates for mountain-scale convection cells. These cells may lead to condensate refluxing because of the large vapor flux, and they may dominate the thermal-hydrology, leading to less predictable conditions at the repository.

Repository heat can also induce the formation of convection cells in the saturated zone (SZ), even for a sub-boiling repository [Buscheck and Nitao, 1993b]. These cells may dominate the potential to transport radionuclides in the SZ for tens of thousands of years; they may also significantly affect the heat transfer characteristics of the SZ, which, in turn, can influence heat flow in the UZ and EBS.

Regardless of the AML, repository-heat-driven temperature gradients are expected to extend all the way to the ground surface, resulting in a gradient in water vapor mass fraction from the repository all the way to the ground surface. Water vapor will therefore diffuse to the ground surface, where it is transferred to the atmosphere by eddy diffusion, whose rate depends on temperature, *RH*, and wind velocity. These conditions can fluctuate diurnally and seasonally. Precipitation and plant transpiration processes may also play a strong role. Ground surface conditions can have a noticeable effect on the overall moisture balance and on local conditions in the EBS. Conversely, repository heat can dominate the moisture transport and liquid saturation conditions at the ground surface.

During the rewetting period, the mechanisms for restoring the liquid-phase saturation and *RH* conditions in the repository to ambient (humid) conditions are matric-potential forces and the binary gas-phase diffusion of air and water vapor. The rate of rewetting has important implications for the EBS environment during this period. Rewetting by matric forces may be retarded by fractures or rubbelized zones and by low-permeability regions. Changes in fracture properties, such as filling of

apertures by precipitates formed during refluxing, may also retard rewetting. Although temperature decrease in the interior of the repository is largely governed by one-dimensional (vertical) heat flow, heat flow becomes increasingly two-dimensional as the repository edge is approached, thereby increasing the cooling rate [Buscheck and Nitao, 1994b]. This edge-cooling effect reduces both the magnitude and duration of the temperature buildup responsible for driving moisture away from the repository. Rewetting the interior of the repository to ambient conditions is also largely a one-dimensional process, but again the process becomes increasingly two-dimensional as the edge is approached. Edge-cooling/rewetting effects decrease the time required to restore the repository edge to ambient conditions.

1.7.3 Coupling with Geochemical Phenomena

The geochemical environment of the near-field and the EBS will affect any liquid water that may contact the WPs, the waste-form, and any radionuclides released into the near-field. The composition of the liquid phase will depend on the isothermal and nonisothermal flow processes and reaction history experienced by packets of mobile fluid along their respective flow paths. Intermediate flow processes, such as condensate refluxing and evaporation, can concentrate different dissolved components. Condensate may dissolve minerals from fracture walls as it drains down fractures and then precipitate those (or other) minerals as it evaporates. These changes may significantly increase or decrease fracture apertures along various intervals, thereby altering the bulk permeability distribution. Solubility and dissolution of minerals depend on temperature changes, among other things. The geochemistry of water from surface infiltration contacting WPs will vary depending on whether it drains quickly down fractures or migrates slowly in the matrix, and on whether it was affected by refluxing or buoyant gas-phase convection. It may also depend on the pathways followed by the water and on the temperature gradient along those pathways.

Changes in *RH*, saturation, and temperature can change hydrological properties, such as fracture and matrix permeability, through precipitation, dissolution, or mineral alteration. Adsorptive properties of various units may be affected by temperature, saturation, and compositional changes.

Changes in temperature and the mixing of groundwater (driven by repository-heat-driven, buoyant, liquid-phase convection) could alter hydrological and adsorptive properties in the saturated zone and could thereby affect radionuclide transport in the SZ [Buscheck and Nitao, 1993b].

1.7.4 Coupling with Geomechanical Phenomena

Changes in geomechanical stresses imposed by thermal-hydrological effects could affect hydrological properties. For example, as a result of thermal stresses, fractures may close and open or undergo shear displacement, which would change their permeability. Microfracturing could occur as the result of pressure buildup driven either by boiling of matrix water or by thermally induced stresses. Mineral alteration or dehydration arising from changes in temperature and/or the flow of liquid water or steam could weaken the rock, thereby facilitating fracture propagation. Swelling of clay minerals could change the strength of the matrix and could contribute to the overall perturbation of the mechanical stress field. The potential for subcritical crack growth depends on the liquid-phase saturation.

Contents

1.8. Understanding and Managing the Thermal-Hydrological Effects of Decay Heat

1.8.1 The Importance of Decay Heat on Moisture Movement and the Moisture Balance at Yucca Mountain

To safely and permanently store nuclear waste, the potential repository system must limit gas- or liquid-phase transport of radionuclides to the accessible environment. In the failure scenario of greatest concern, liquid water would contact a waste package (WP), accelerate its failure rate, and eventually transport radionuclides to the water table. The degradational mechanisms of greatest concern for WP integrity, such as stress and pitting corrosion or microbial attack, require the presence of liquid water. The rates for many of these degradational mechanisms are increased under warm, humid conditions. For a repository located in the unsaturated zone, the primary concern is whether liquid water may contact the WP. This contact can arise from two effects. First, mobile liquid water, particularly water flowing in fractures, may contact the WP. Second, if *RH* is high enough, a liquid film can exist on the surface of the WP even if mobile liquid water is absent.

Fluid flow in the UZ at Yucca Mountain involves liquid- and gas-phase flow through the fractures and through the rock matrix. Under ambient conditions, the gas phase contains about 98.5% air and 1.5% water vapor. An important feature of the unsaturated zone at Yucca Mountain is its high fracture density. Moreover, the Topopah Spring tuff (TSW2), which occurs at the potential repository depth, is one of the most densely fractured hydrostratigraphic units. This is significant because, without fractures, the rock throughout most of the unsaturated zone (including the repository horizon) would be extremely impermeable. In general, repository heat moves moisture by (1) vaporization, (2) driving water vapor from high to low gas-phase pressure, (3) condensation, and (4) gravity- or capillary-driven flow of condensate. Without fractures, the rock would be too impermeable to allow significant vaporization and movement of water vapor. The flow of condensate would also be very slow. A system of connected fractures facilitates significant decay-heat-driven fluid flow as well as natural infiltration. Enhanced gas-phase diffusion of water vapor may significantly contribute to vaporization in unfractured (relatively impermeable) rock.

Modeling and analytical studies of high-level radioactive waste isolation have demonstrated the potential importance of nonequilibrium flow processes between the fractures and the matrix [Buscheck et al., 1991; Nitao et al., 1993]. Except for regions with a perched water table or during transient recharge episodes, capillary forces cause most fractures to be drained of liquid water. Matrix permeability is extremely low, so matrix flow is of less concern than fracture flow for water contact by advective liquid flow and for radionuclide transport. This water may arise from three origins:

1. Natural infiltration of rainfall and snowmelt.
2. Condensate generated under *boiling conditions*.
3. Condensate generated under *sub-boiling conditions*.

The first source arises from the ambient system; the second and third are generated by radioactive decay heat, primarily from SNF. Decay-heat-driven, buoyant vapor flow, occurring either on a sub-repository scale or on a mountain scale (Figs. 1.8.1.1a and b), may play an important role in generating the second and third sources of liquid water. Decay-heat-driven binary diffusion of water vapor and air (called vapor diffusion) may also play important roles in condensate generation [Buscheck and Nitao, 1994a]. A heterogeneous distribution of bulk permeability k_b can influence vapor and condensate flow under both boiling and sub-boiling conditions. Of particular concern are k_b distributions that

promote the focusing of condensate flow, which could cause water to drip onto WPs [Fig. 1.8.1.1c] even if average behavior would indicate otherwise [Buscheck and Nitao, 1994a].

Decay heat also drives buoyant, liquid-phase convection in the saturated zone (Fig. 1.8.1.1b). Analyses of this type of flow indicate that it is likely to be the dominant means of driving radionuclide transport in the saturated zone for tens of thousands of years [Buscheck and Nitao, 1993b; Buscheck and Nitao, 1994a]. A k_b distribution that facilitates deep convective mixing of radionuclides in the saturated zone would be more likely to meet a dose-based standard than a stagnant water table.

Table 1.8.1.1 summarizes the time and length scales involved in how repository heat influences the three major sources of fracture flow. Mountain-scale effects depend on the overall heating conditions for the entire repository. Several studies [Buscheck and Nitao, 1992; Buscheck and Nitao, 1993b; Buscheck and Nitao, 1994a] have shown that the most useful macroscopic thermal loading parameter quantifying the time-integrated heat content of the waste in the repository is the Areal Mass Loading [(AML), expressed in metric tons of uranium per acre, MTU/acre]. Mountain-scale effects depend primarily on the AML of the entire repository, and they are insensitive to the details of WP emplacement, such as WP size and spacing, and spent nuclear fuel (SNF) age. These effects also depend on the distribution of thermal and hydrological properties throughout the unsaturated zone.

Sub-repository-scale (also called drift-scale) effects depend on the local heating conditions around WPs. Important factors include (1) the number of spent nuclear fuel assemblies per WP, (2) the axial spacing between WPs, (3) the lateral spacing between emplacement drifts, and (4) SNF age. In general, the number of fuel assemblies per WP is directly related to the WP size. Large WPs, containing a large number of assemblies generally have a higher thermal output. Younger fuel has a higher thermal output than older fuel for some period of time. The Local Areal Mass Loading (LAML) depends on the WP size and spacing. For a given LAML, drift-scale effects are very different, depending on whether widely spaced, large WPs or tightly spaced, small WPs are used. These effects also depend on the near-field distribution of thermal and hydrological properties within a few tens of meters of the WPs.

Figure 1.8.1.2 show the effect of decay heat on the flow of water vapor and condensate in the vicinity of an emplacement drift. Heat flow away from the WPs occurs as heat conduction, the convection of latent and sensible heat, and thermal radiation. Because of the large bulk permeability of fracture networks, gas-phase pressures in the fractures remain very close to atmospheric, even during boiling. Consequently, as temperatures reach the nominal boiling point (≈96°C), boiling first occurs along fractures (Fig. 1.8.1.2) and proceeds into the matrix blocks. Accordingly, dry-out due to boiling is more suppressed in sparsely fractured regions (with large matrix blocks) and less suppressed in intensely fractured regions (with small matrix blocks). As boiling continues, water vapor displaces air away from the WPs and may replace it completely for sufficiently high AMLs. The question of whether (or how long) air is displaced from the repository is important in assessing the impact of oxidation corrosion on WP integrity.

Most of the water vapor reaching the fracture network is eventually driven away from the emplacement drift by higher gas-phase pressures in the boiling zone to where cooler temperatures cause it to condense along fracture walls (Fig. 1.8.1.2). Buoyant, gas-phase convection can cause more of the vapor flow to be driven upward to where it condenses above the dry-out zone. In general, regardless of where the condensate is generated, there are three things that can happen to it:

(1) It can drain away from the boiling zone.

(2) It can drain back toward the boiling zone.

(3) It can be imbibed by the matrix.

Because the small matrix permeability limits the rate at which the matrix can imbibe the condensate by capillary suction, it can drain for considerable distances down fractures before being completely imbibed. Below the boiling zone, condensate drainage is away from the boiling zone (Fig. 1.8.1.2), enhancing the dry-out rate. Above the boiling zone, condensate tends to drain back toward the boiling zone, where it reboils, thereby retarding the net rate of dry-out.

The return flow of condensate back toward the heat source causes refluxing, which is the counter-current flow of water vapor and condensate. It is important to note that refluxing does not require boiling conditions [Buscheck and Nitao, 1994a]. Heat-driven, buoyant gas-phase flow can drive refluxing under sub-boiling conditions. Under boiling conditions, refluxing results in a heat transfer mechanism (driven by the convection of latent heat) called the heat-pipe effect. Given adequately high mass flux rates of water vapor and condensate, heat pipes are capable of sustaining a given heat flux with a much flatter temperature gradient than is associated with heat conduction. Consequently, heat pipes are manifested by a flat temperature profile, with temperatures close to the nominal boiling point. Pruess and others [1984, 1990] were the first to model the heat-pipe effect in the context of thermal-hydrological performance at Yucca Mountain. Depending on the AML, these effects can occur at the sub-repository scale or on a mountain scale (Table 1.8.1.1).

Figure 1.8.1.3 shows the various decay-heat-driven processes and ambient site conditions that may significantly affect the moisture balance in the UZ. The moisture balance in the UZ (and, in particular, in the region above the repository) may play a very important role in the performance of the EBS, the natural barriers, and the total system. In general, decay heat will result in regions of dryout and condensate buildup in the UZ. Modeling studies [Buscheck and Nitao, 1993a; Buscheck and Nitao, 1993b; Buscheck and Nitao, 1994a; Buscheck et al., 1994] have indicated that decay-heat-driven changes in the saturation distribution can persist for more than 100,000 yr, even for low AMLs that never drive temperatures close to the boiling point. These effects, along with temperature changes, can alter the hydrological, geochemical, and geomechanical properties that influence fluid flow and radionuclide transport. Decay heat might drive enough water vapor out of the top of the mountain to significantly reduce the UZ moisture content for tens of thousands of years. Conversely, mountain-scale, buoyant gas-phase convection might drive enough water vapor up from the SZ (into the UZ) to *increase* the UZ moisture content for tens of thousands of years [Buscheck and Nitao, 1994a; Buscheck et al., 1994].

The important site-scale features that may signicantly affect decay-heat-driven, mountain-scale, thermal-hydrological flow include:

Paintbrush vitic nonwelded tuff(PTn): This unit (colloquially called the "tin roof") probably plays a dominant role in (1) the attenuation (in space and time) of episodic nonequilibruim fracture flow and (2) the reduction of net infiltration to the repository. Because it has a much lower k_b than the densely welded tuff units that lie above it (the TCw unit) and below it (the TSw1 unit), the PTn significantly influences mountain-scale gas-phase flow both under ambient and decay-heat-disturbed conditions. Analyses of mountain-scale buoyant gas-phase convection [Buscheck and Nitao, 1994a; see also Chapter 10.0 of this report] indicate that it will probably significantly limit (or cap) the upper spatial extent of large-scale gas-phase convection cells in the UZ. This could significantly affect the magnitude of moisture redistribution in the UZ by this mechanism.

Basal vitrophyre of the Topopah Spring tuff (TSw3): This unit (sometimes colloquially called the "tin basement") appears to be associated with regions of perched water, which may be the result of restricted fracture flow arising from clay fillings. If fracture permeabilty (andk_b) is signicantly reduced in the TSw3, this would have a significant effect on condensate drainage and on mountain-scale buoyant gas-phase convection. A reduced k_b could significantly limit the lower spatial extent of large-scale gas-phase convection cells in the UZ. This could significantly affect the magnitude of moisture redistribution in the UZ by this mechanism.

Calico Hills nonwelded tuff (CHn): Both the zeolitic (CHnz) and vitric (CHnv) portions of this unit probably have a significantly lower k_b than the overlying TSw sequence. If k_b is not reduced in the TSw3, k_b in the CHnv and CHnz is probably small enough to significantly limit the lower spatial extent of large-scale gas-phase convection cells in the UZ. This could significantly affect the magnitude of moisture redistribution in the UZ by this mechanism.

1.8.2 Thermal Loading Strategies

Geological nuclear waste isolation at Yucca Mountain is affected by three key considerations: (1) ambient conditions at the proposed repository horizon are very humid (relative humidity $RH \approx 98$–99%) and are therefore very corrosive for most candidate WP materials; (2) ambient fracture flow is highly variable in time and space; and (3) radioactive decay heat significantly affects fluid flow for any practical AML. Two thermal loading strategies have been proposed to manage the thermal-hydrological (T-H) effects of decay heat:

Minimally heated (MH) repository: Select an AML and a thermal load distribution that limit (1) heat-driven vapor and condensate flow and (2) far-field temperature rise. The MH strategy relies on performance attributes other than decay heat (such as high-performance WP materials and capillary/diffusion barriers in the engineered and natural systems) to counter the effects of high *RH* and fast fracture flow.

Constructively heated (CH) repository: Select an AML and a thermal load distribution that use decay heat constructively—that is to substantially reduce *RH* and fracture flow near WPs. The CH strategy relies on demonstrating that heat, vapor, and liquid flow (including heterogeneous fracture flow) near WPs are dominated by heat conduction (and possibly vapor diffusion) and are therefore very predictable.

Various modeling studies [Buscheck and Nitao, 1994a; Buscheck and Nitao, 1994b; Buscheck et al., 1995] have identified two fundamental CH approaches:

Extended dryout (ED) approach: Use a high AML (>60 MTU/acre) to drive a large fraction of the initial pore water (in the rock) from the repository as a whole. The high areal power density associated with such an AML creates a thick superheated dryout zone (coalesced between emplacement drifts) and maintains above-boiling temperatures and low *RH* in the repository rock (and on WPs) for thousands of years.

Localized dryout (LD) approach: Maintain a temperature difference between the WP and the drift wall that is large enough to reduce *RH* on the WP. This is done with close axial WP spacing (generating a high line-heat load) and/or the use of low-thermal-conductivity backfill in the drift. Wide drift spacings and low to intermediate AMLs (<50–60 MTU/acre) are used to (1) prevent the boiling zones from coalescing between drifts (and thereby limiting condensate buildup above the drifts) and (2) limit far-field temperature rise (as in the MH strategy).

There are two major thermal-hydrological (T-H) issues for the ED (high-AML) approach. The first issue must be addressed for all AMLs; the second is unique to the ED approach. These two major T-H issues are as follows:

Coupled T-H-M-C effects: Thermal-hydrological-mechanical-chemical effects in the near and far field must be addressed regardless of AML; however, their impact on waste isolation may depend on AML. The effects of particular concern are (a) alteration of the vitric nonwelded Paintbrush tuff (PTn) unit, which may reduce its ability to attenuate (in time and space) net infiltration to the repository and (b) alteration of the basal vitrophyre (TSw3) unit, which may influence whether water perches in (or immediately above) that unit and may reduce the mechanical stability of the drifts in the repository.

Condensate buildup above the boiling zone: This effect may result from condensate and infiltration flux that is held up by the thick (coalesced) superheated zone created by a high-AML repository.

These two issues will affect the containment, mobilization, and migration of radionuclides.

The LD approach (like the MH strategy) tends to limit far-field T-H-M-C effects and allows condensate to drain through the repository; neither of these results is as readily achieved with the ED approach. The LD approach can be implemented by a wide range of thermal design options [Buscheck et al., 1995], ranging from those that never cause above-boiling rock temperatures to those in which the boiling zones coalesce between the drifts (as in the ED approach).

1.8.3 Importance of Thermal-Hydrology on Radionuclide Containment in Waste Packages

A major concern for radionuclide containment is how water contacts a WP, thereby affecting its integrity and (if containment is breached) affecting radionuclide dissolution and eventual transport to the water table. The degradational mechanisms of greatest concern for WP integrity, such as stress and pitting corrosion or microbial attack, require the presence of liquid water. The rates for many of these mechanisms increase, in general, with temperature and relative humidity.

The two primary modes of water contact on the WP are (1) advective liquid-phase flow and (2) condensation of water vapor that forms a liquid film on the WP. The critical factor for the second mode is the relative humidity *RH* on the WP. Relative humidity is given by

$$RH = P_v/P_{sat}(T), \tag{1}$$

where P_v is the local vapor pressure and P_{sat} is the local saturated vapor pressure. If 100% of the gas phase is water vapor, as is the case for boiling conditions, then $P_v = P_g$, where P_g is the total gas-phase pressure. For example, if $P_v = P_g = 1$ atm and $T = T_{wp} = 225°C$, then (from steam tables) $P_{sat} = 25.48$ atm and $RH_{wp} = 3.9\%$. The assumption that $P_v = 1$ atm is reasonable if there is enough fracture connectivity and conductivity so that bulk permeability $k_b > 1$ millidarcy. If there were no fractures in the repository rock, then we would have $k_b << 1$ millidarcy, and P_v would be much higher than 1 atm; this would increase *RH* by a corresponding factor. An important question, resolvable with *in situ* thermal tests [Buscheck and Nitao, 1995], is whether fracture conductivity and connectivity are sufficient to prevent substantial pressurization of the gas phase near WPs.

1.8.3.1 Relative Humidity Reduction Mechanisms

Regardless of whether mobile liquid water is present, ambient *RH* at the repository horizon is humid (~98–99%). If the ambient *RH* could be reduced enough, WP corrosion rates would be minimal [Stahl et al., 1994]. Moreover, even for breached WPs, waste-form dissolution (and radionuclide release) would be minimal if no mobile liquid water were present. There are two ways to reduce *RH* on the WP:

1. Drive a large fraction of the ambient pore water (in the rock) away from the drifts. (This reduces *RH* in the rock; *RH* on the WP is generally no greater than *RH* in the rock.) This is most readily accomplished using the ED approach.

2. Maintain a large temperature difference between the (hotter) WP and the (cooler) drift wall. (This makes *RH* on the WP lower than *RH* in the rock at the drift wall.) This can be accomplished in either the ED or LD approaches.

The primary means of driving pore water from the vicinity of WPs are ventilation and decay-heat-driven drying. To reduce *RH* to 70%, the liquid saturation S_L (the fraction of the pore space filled with liquid water) must be reduced to less than 20% (based on measurements made on TSw2). An AML that does not drive repository temperatures well above the boiling point will reduce average *RH* conditions in the rock only slightly. Refer to Section 1.10.3 (Table 1.10.3.1) for an example of the relationship between AML and *RH* reduction resulting from rock dryout (ΔRH_{rock}).

Even if repository heat does not substantially reduce average *RH* conditions in the repository rock, it is still possible to substantially reduce *RH* on the WP itself for a considerable time. A reduction in *RH* between the drift wall and the WP arises from the temperature difference ΔT_{drift} between these locations. This effect (the "drift-ΔRH effect") occurs in addition to any *RH* reduction resulting from rock dryout (ΔRH_{rock}). Assuming uniformP_v in the drift, the *RH* on the WP, RH_{wp}, is given by

$$RH_{wp} = RH_{dw} \quad P_{sat}(T_{dw}) / P_{sat}(T_{wp}) \ , \tag{2}$$

where RH_{dw} is RH in the rock at the drift wall, T_{dw} and T_{wp} are the drift wall and WP temperatures. For example, if T_{dw} = 80°C, T_{wp} = 100°C, and RH_{dw} = 98.4% (ambient RH), then we have RH_{wp} = 46%. Figure 1.8.3.1.1 illustrates the drift-ΔRH effect. Refer to Section 1.10.5.2 (Fig. 1.10.5.2.1) for an example of how ΔT_{drift} and RH reduction between the drift wall and WP (ΔRH_{drift}) are related.

A persistent ΔT_{drift} arises because the rows of WPs act like line-heat loads that impose a temperature increase on top of the temperature rise ΔT_{rock} in the repository rock; ΔT_{rock} depends primarily on AML and the thermal conductivity K_{th} of the mountain [Buscheck and Nitao, 1993b; Buscheck and Nitao, 1994a; Buscheck and Nitao, 1994b]. Because ΔT_{drift} depends only on lineal mass loading (LML, expressed in MTU/m of drift) and the thermal properties of the drift, ΔT_{drift} is increased by high LML and/or the use of low-K_{th} granular backfill in the drift [Buscheck and Nitao, 1995]. This can be accomplished in either the LD or ED approaches. Thermal-hydrological model calculations show that with suitable backfill, ΔT_{drift} can keep RH on the WP below 70% for 10,000 yr, even for AMLs that result in negligible rock dryout [Buscheck et al., 1995]. Proving that heat flow in the backfill is dominated by conduction establishes that ΔT_{drift} is very predictable. Note that Eq. (2) is applicable when P_v on the WP is in equilibrium with P_v in the rock at the drift wall. Nonuniform (or episodic) rewetting of the drift by heterogeneous (particularly nonequilibrium) fracture flow may locally (or temporarily) cause RH to be higher than predicted by Eq. 2.

During the repository heatup period, the rock surrounding the drift will become desaturated if k_b and the local AML are high enough, resulting in a reduced RH in the rock (and on the WP itself). This reduction in RH will persist at least as long as rock temperatures remain high, and it may persist long after the WP temperature has dropped below the boiling point. The reduction in RH will decrease both the likelihood and magnitude of WP corrosion, and the reduction in liquid-phase saturation will decrease the rate of liquid-phase diffusion of radionuclides in the backfill and host rock. For high AMLs, this desirable scenario may last for tens of thousands of years. For low to intermediate AMLs, the duration of the reduced-RH period (resulting from rock dryout) may be substantially less, at least for average RH conditions in the repository rock.

Higher AMLs will increase the volume of rock in which S_L and RH are reduced. Because the boiling front is driven farther from the emplacement drifts, the probability that refluxing condensate will reach the drifts will be reduced. Because of the larger volume that must be rewetted, rewetting the repository to ambient (humid) conditions will take longer for a high-AML repository than for a low-AML repository. A large enough increase in the duration of reduced-RH conditions reduce the temperatures associated with a given value of RH because the repository rock cools down faster than it rewets. Consequently, once humid RH conditions are eventually restored, WP temperatures will have decreased considerably, which is more favorable for reducing WP corrosion rates. Ideally, WPs would remain relatively dry until they are relatively cool.

Besides RH and T, the potential for advective liquid-phase flow reaching the WP is of concern. An important issue for WP integrity involves the scenario of liquid water reaching and evaporating on a WP, thereby leaving an evaporative buildup of salt on the WP surface. The condensation of an aqueous surface film on the WP will depend on RH and on the quantity and composition of any hygroscopic salts on the WP surface. The critical relative humidity RH_{crit} for significant atmospheric corrosion is extremely sensitive to this effect [Jones, 1992]. Keeping liquid-phase flux away from the WP surface would prevent salts from precipitating on the WP and would thereby help keep RH_{crit} very high. On the basis of the corrosion data reported by Jones (1992), the absence of salts on the WP could result in RH_{crit} > 90% and thereby greatly extend WP lifetimes and the period of radionuclide containment. The use of a suitable backfill might significantly reduce the likelihood that evaporating water would leave salts on the WP surface.

Microbially induced corrosion is also of concern and is strongly dependent on temperature and *RH*. High temperature and low *RH* are generally detrimental to microbial growth, whereas intermediate temperatures and high *RH* may favor microbial growth.

Condensate flow, whether driven by heat from an above-boiling or a sub-boiling repository, is one source of advective liquid-phase flow that may reach a WP. On average, the matrix will imbibe condensate fluxes until it becomes saturated. However, heterogeneities in the natural system can cause variations about the average flow field that could focus condensate onto WPs. Counteracting this variability in return condensate flux is the heat flux from the WPs, which will continue to boil condensate. In some cases, a higher AML may result in higher condensate fluxes and more variability, but the correspondingly higher heat flux will mitigate the problem of focused condensate drainage [Buscheck and Nitao, 1993a; Nitao et al., 1995]. The system is nonlinear, so it is difficult to determine optimum thermal loading without (1) extensive sensitivity analyses of alternative thermal designs, (2) experimental information obtained from *in situ* thermal tests, and (3) better information and understanding concerning how repository heat affects the overall UZ moisture balance (see Fig. 1.8.1.2).

1.8.4 Importance of Thermal-Hydrology for Radionuclide Release and Transport

Release of aqueous radionuclides to the natural environment would require that the WP was breached and that there was enough liquid water to dissolve radionuclides and transport them by advection or diffusion from the waste form to the surrounding rock. Both waste-form dissolution and advective radionuclide transport are minimized if no mobile liquid water is present. Diffusive radionuclide transport in the EBS is minimized if the liquid-phase saturation is low enough, particularly if a granular backfill and/or invert is used and if *RH* in the drift remains low. The likelihood of this scenario depends strongly on T-H processes. The chemistry and temperature, and the advective velocity of the aqueous phase, will all affect waste-form degradation and radionuclide dissolution. Possible sources of advective liquid-phase flow are episodic surface infiltration and condensate drainage.

If the flux of water leaving the EBS (and carrying dissolved radionuclides) is high enough, some of the water will flow down fractures, where it will eventually be imbibed into the matrix or continue to the water table. Radionuclides imbibed in the matrix will be immobilized until the next pulse of fracture flow, whereupon some of the radionuclides will diffuse into the incoming stream if it is at a lower concentration. The remaining radionuclides will continue to imbibe and diffuse deeper into the matrix block. The likelihood of this advective transport scenario may be significantly reduced with the use of a suitable backfill or invert. The spatial and temporal extent of decay-heat-driven rock dryout will also play a very important role in the dynamics of fracture-matrix liquid-phase flow interaction and, consequently, in aqueous transport of radionuclides in the engineered and natural barrier systems. Because decay-heat-driven T-H processes can dominate advective gas movement, they will also have a strong effect on the release and transport of gaseous radionuclides.

1.8.5 Major Thermal-Hydrological Flow Regimes

Perhaps the single most important purpose of the ESF thermal tests is to determine the major decay-heat-driven thermal-hydrological (T-H) flow regime(s) that will govern the magnitude and direction of vapor flow (and the resulting condensate flow) in the UZ at Yucca Mountain. We list below the three major T-H flow regimes with respect to advective rock dryout. Note that the numbered points (describing various attributes of the regimes) are listed in parallel: the first point addresses the dominant mode of heat flow, the second point addresses *RH* reduction, points 3 and 4 address the relative contribution of vapor diffusion to rock dryout, and point 5 addresses the predominant direction

of vapor flow. Points 6 through 8 pertain only to the unthrottled buoyant regime. The following discussion is summarized in Table 1.8.5.1.

Throttled, nonbuoyant, advective rock dryout: the regime in which k_b is low enough ($k_b < 1$ millidarcy) to significantly throttle the rate of boiling-driven advective rock dryout. The threshold k_b below which rock dryout is throttled decreases with increasing AML.

1. Heat flow is conduction-dominated, resulting in a vertically symmetrical temperature profile.
2. Because P_g could rise substantially above 1 atm, *RH* reduction may be substantially less than would be the case under unthrottled conditions.
3. For high AMLs, vapor diffusion (if significantly enhanced) may significantly contribute to rock dryout and vapor transport.
4. For low AMLs, vapor diffusion (if significantly enhanced) is the major contributor to rock dryout and vapor transport.
5. Vapor transport and the development of the dryout zone are dominated by temperature gradients, and are therefore generally vertically symmetrical about the heated horizon.

Unthrottled, nonbuoyant, advective rock dryout: the regime in which k_b is high enough ($k_b > 1$ millidarcy) not to significantly throttle the rate of boiling-driven advective rock dryout, but not high enough ($k_b < 5$ darcy) to allow buoyant gas-phase convection to dominate the direction of vapor flow.

1. Heat flow is conduction-dominated, resulting in a vertically symmetrical temperature profile, unless focused liquid flow depresses the upper boiling front.
2. Because P_g does not rise significantly above 1 atm (particularly for $k_b > 10$ millidarcy), *RH* reduction can be large.
3. For high AMLs, the relative contribution of vapor diffusion (even if enhanced) to rock dryout and vapor transport is small.
4. For low AMLs, the relative contribution of enhanced vapor diffusion to rock dryout and vapor transport can be large.
5. Vapor transport and the development of the dryout zone are dominated by temperature gradients and are therefore generally vertically symmetrical about the heated horizon unless focused liquid flow strongly depresses the upper boiling front.

Unthrottled, buoyant, advective rock dryout: the regime in which k_b is high enough not to throttle the rate of boiling-driven advective rock dryout and is also high enough ($k_b > 5$ darcy) to allow buoyant gas-phase convection to dominate the direction of vapor flow.

1. Heat flow is primarily conduction-dominated (although the temperature profile is vertically asymmetrical) unless focused liquid flow depresses the upper boiling front. For $k_b > 40$ darcy, buoyant gas-phase convection dominates heat flow, significantly reducing the duration of boiling conditions at the repository horizon.
2. Because P_g does not rise significantly above 1 atm, *RH* reduction can be large.
3. For high AMLs, the relative contribution of vapor diffusion (even if enhanced) to rock dryout and vapor transport is small.
4. For low AMLs, the relative contribution of enhanced vapor diffusion to rock dryout and vapor transport can be large.
5. Vapor transport and the development of the dryout zone are dominated by gas-phase density gradients that drive much of the vapor flow above the repository horizon, resulting in vertically asymmetrical temperature and S_L profiles.

6. For high AMLs, buoyant gas-phase convection does not contribute significantly to rock dryout unless $k_b > 40$ darcy.
7. For low AMLs, buoyant gas-phase convection may be the major contributor to rock dryout (even contributing to *RH* reduction).
8. For all AMLs, enhanced vapor diffusion can significantly *reduce* the magnitude of buoyant gas-phase convection.

Natural infiltration	Buoyant, gas-phase convection and condensate drainage *		Boiling and condensate drainage	
	Sub-repository scale	Mountain scale	Sub-repository scale	Mountain scale
Affected by repository-heat-driven changes to the • moisture distribution • intrinsic hydrological, geochemical, and geomechanical properties	Local heating conditions Local Areal Mass Loading Waste package size Waste package spacing	Global heating conditions Areal Mass Loading Repository size Repository location	Local heating conditions Local Areal Mass Loading Waste package size Waste package spacing	Global heating conditions Areal Mass Loading Repository size Repository location
	Near-field thermo-hydrological properties	Unsaturated zone-scale thermo-hydrological properties	Near-field thermo-hydrological properties	Unsaturated zone-scale thermo-hydrological properties
	$t < 1000$ yr ** $t < 2000$ yr ***	$1000 < t < 100{,}000$ yr	$t < 50$ yr ** $t < 400$ yr *** for 27 MTU/acre $t < 1000$ yr ** for 49 MTU/acre $t < 50$ yr for 155 MTU/acre	$t < 1000$ yr $t < 100{,}000$ yr for residual effects

* Can occur under both sub-boiling and boiling conditions

** Assuming small waste packages

*** Assuming large waste packages

Table 1.8.1.1. The various time and length scales involved in how decay heat influences the three major sources of vapor and condensate flow.

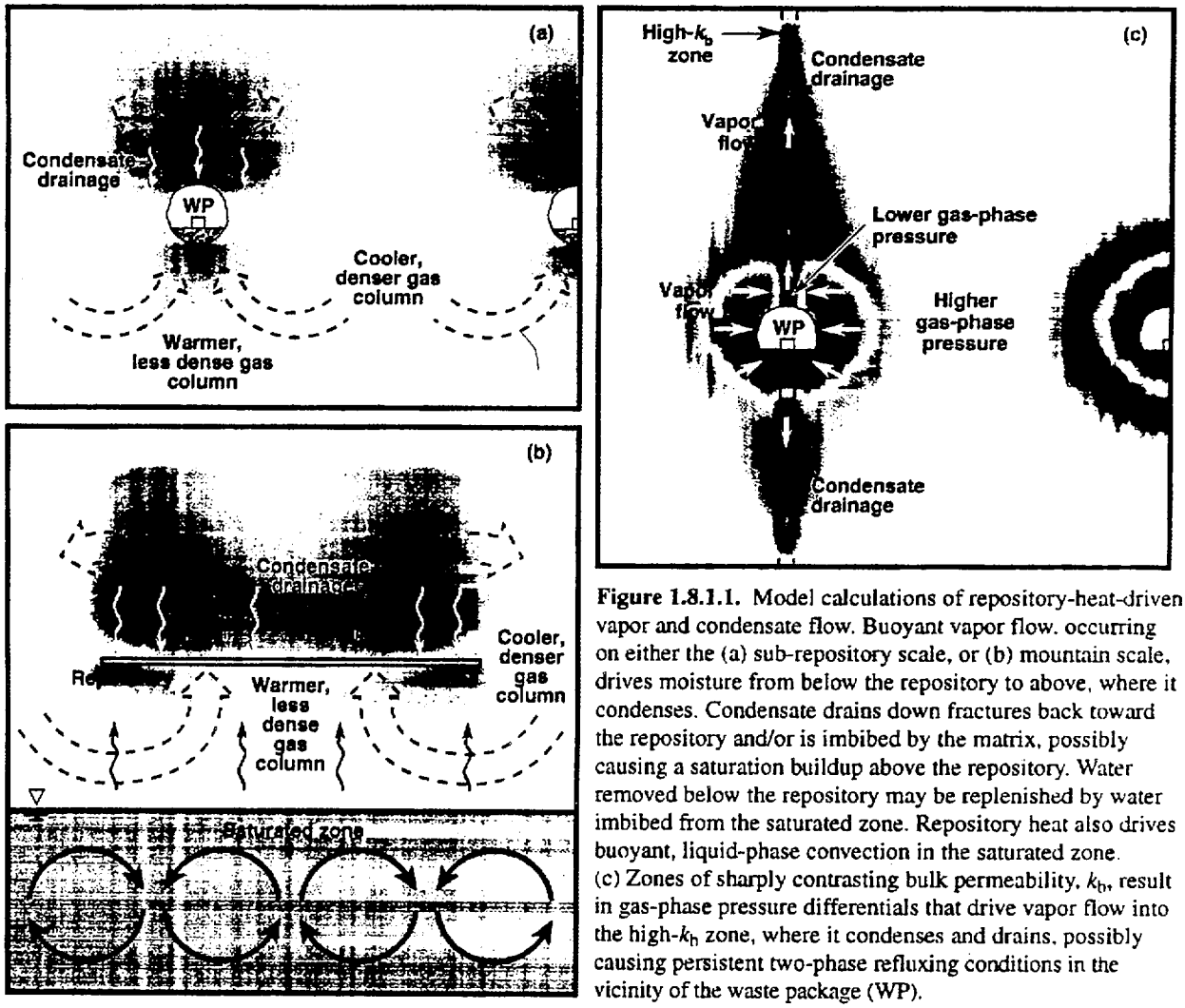

Figure 1.8.1.1. Model calculations of repository-heat-driven vapor and condensate flow. Buoyant vapor flow, occurring on either the (a) sub-repository scale, or (b) mountain scale, drives moisture from below the repository to above, where it condenses. Condensate drains down fractures back toward the repository and/or is imbibed by the matrix, possibly causing a saturation buildup above the repository. Water removed below the repository may be replenished by water imbibed from the saturated zone. Repository heat also drives buoyant, liquid-phase convection in the saturated zone. (c) Zones of sharply contrasting bulk permeability, k_b, result in gas-phase pressure differentials that drive vapor flow into the high-k_b zone, where it condenses and drains, possibly causing persistent two-phase refluxing conditions in the vicinity of the waste package (WP).

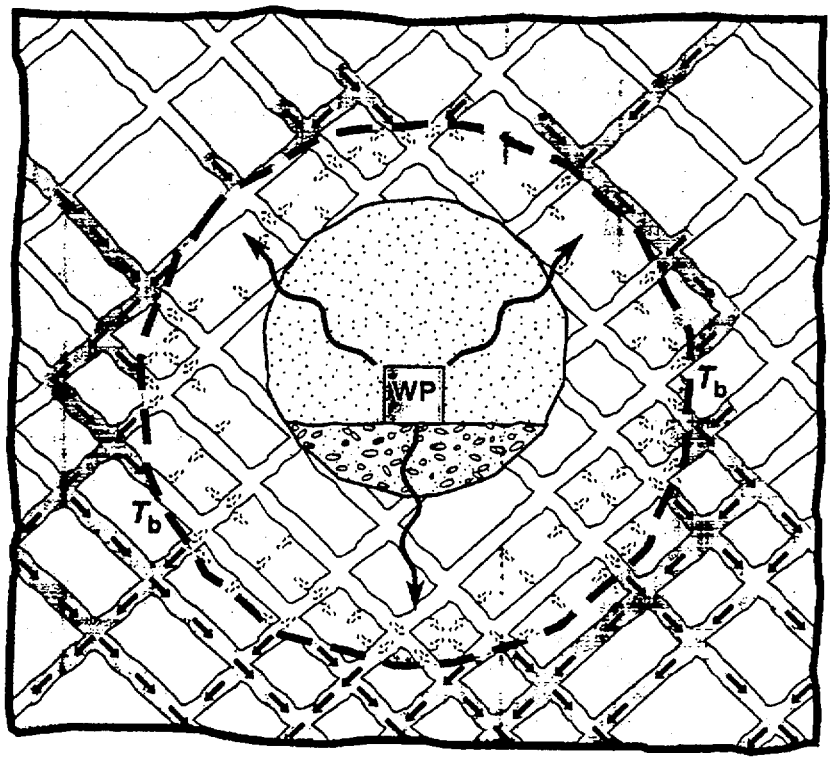

Figure 1.8.1.2. Schematic of hydrothermal flow near the emplacement drift. Rock dry-out occurs as boiling drives water vapor out of the rock matrix. Upon reaching the fracture network, vapor is driven away from the boiling zone to where cooler temperatures cause it to condense along fracture walls. Because the small matrix permeability limits the rate of matrix imbibition, condensate drainage persists for considerable distances down fractures.

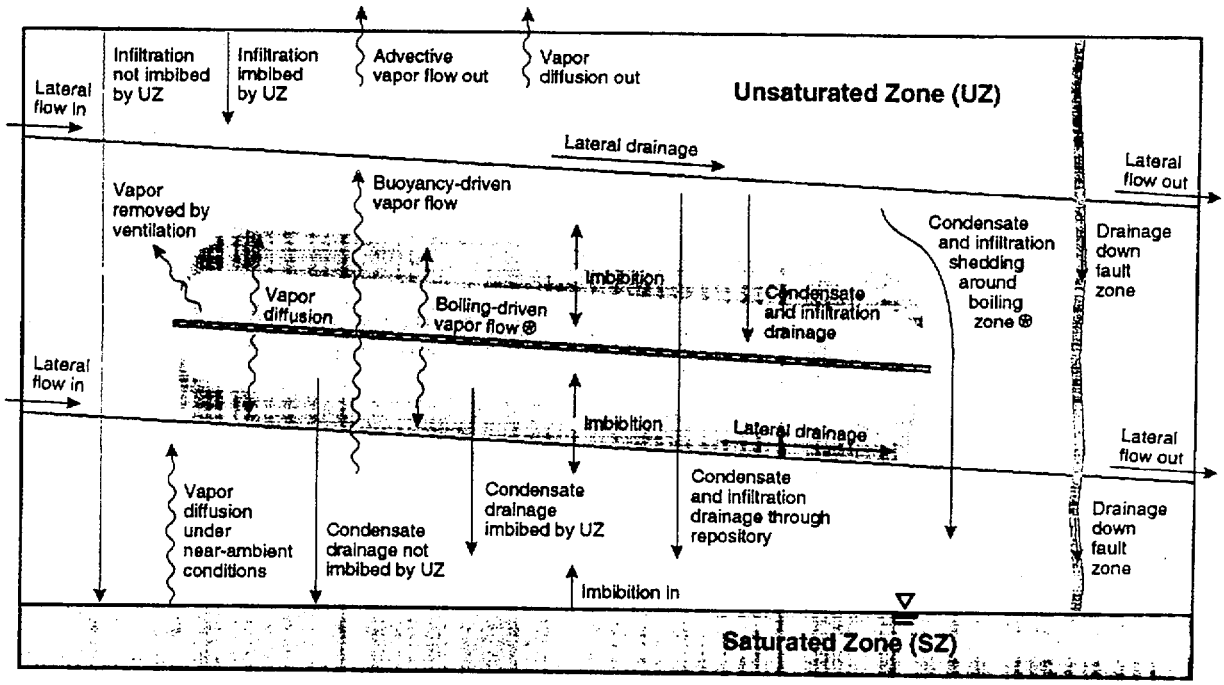

Figure 1.8.1.3. Moisture balance in the unsaturated zone (and above the repository itself) is affected by both ambient and decay-heat-driven processes. The two processes labeled with an asterisk (*) are applicable only to above-boiling conditions; all other processes shown can occur under both sub-boiling and above-boiling conditions.

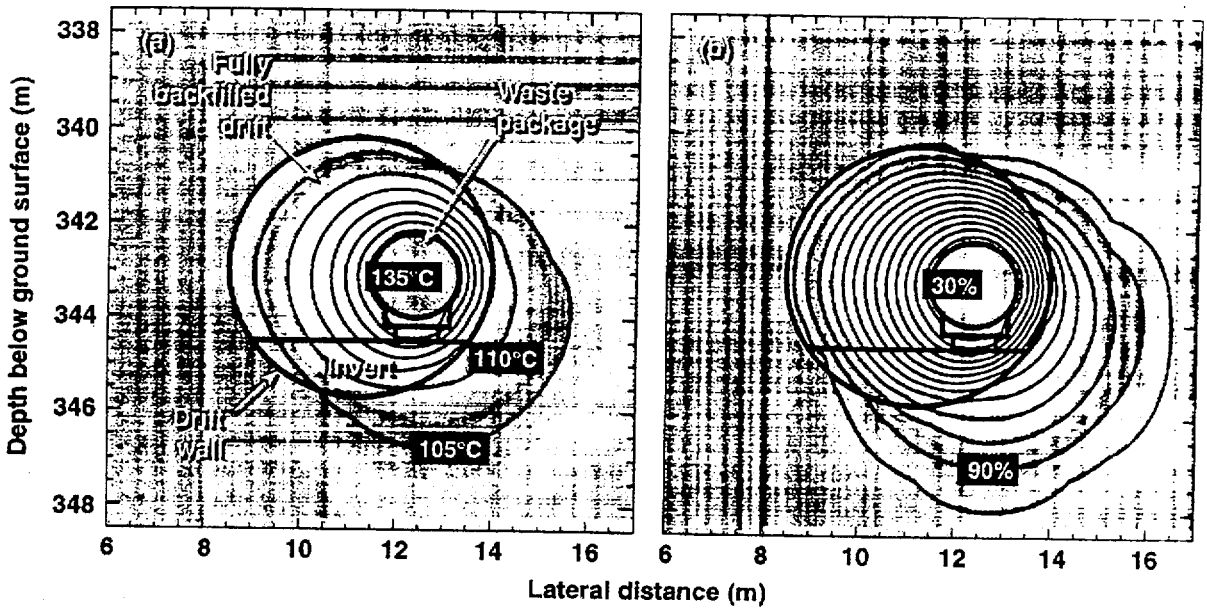

Figure 1.8.3.1.1. Near-field temperature (a) and relative humidity (b) distribution at t = 120 yr for the ACD rev 00 design, AML = 83.4 MTU/acre, LML = 0.46 MTU/m, 40-darcy TSw2 tuff gravel invert, 10-darcy full sand overfill at 100 yr with K_{th} = 0.6 W/m°C, off-center in-drift (OCID) emplacement, drift diameter = 5.5 m, WP emissivity = 0.3, and ambient percolation flux = 0.3 mm/yr. Calculation was done with a two-dimensional model that averages the heat output from a mixture of 26-yr-old BWR WPs and 26-yr-old PWR WPs into a uniform line-heat load. Color contours (a) correspond to temperature distribution, with blue corresponding to lower temperatures and yellow corresponding to higher temperatures. Color contours (b) correspond to relative humidity distribution, with blue corresponding to more humid conditions and yellow corresponding to drier conditions. Temperature contour interval (a) is 5°C. Relative humidity contour interval (b) is 5%.

Table 1.8.5.1. Summary of major decay-heat-driven thermal-hydrological flow regimes.

Thermal Processes	Throttled nonbuoyant regime	Unthrottled nonbuoyant regime	Unthrottled buoyant regime
Boiling-driven rock dryout	• For high AMLs, is a major contributor to rock dryout • For low AMLs, is only locally significant*	• For high AMLs, is the major contributor to rock dryout • For low AMLs, is only locally significant*	• For high AMLs, is the major contributor to rock dryout • For low AMLs, is only locally significant*
Buoyant gas-phase convection-driven rock dryout	• Insignificant contribution to rock dryout	• Insignificant contribution to rock dryout	• For high AMLs(k_b >40 darcy), contributes to rock dryout • For low AMLs, is a major contributor to rock dryout • Enhanced vapor diffusion can significantly reduce buoyant gas-phase convection
Vapor diffusion-driven rock dryout	• For high AMLs, may be a significant contributor to rock dryout (if enhanced) • For low AMLs, is the major contributor to rock dryout (if enhanced)	• For high AMLs, is a minor contributor to rock dryout • For low AMLs, is a major contributor to rock dryout (if enhanced)	• For high AMLs, is a minor contributor to rock dryout • For low AMLs, is a major contributor to rock dryout (if enhanced)
Total rock dryout	• Dominated by heat conduction	• Dominated by heat conduction, unless focused liquid flow strongly depresses the upper boiling front	• For high AMLs, is dominated by heat conduction, unless focused liquid flow strongly depresses the upper boiling front
Heat flow	• Conduction-dominated • Enhanced vapor diffusion can increase the repository cooling rate	• Conduction-dominated, unless focused liquid flow strongly depresses the upper boiling front • Enhanced vapor diffusion can increase the repository cooling rate	• Conduction-dominated, unless k_b >40 darcy and/or focused liquid flow strongly depresses the upper boiling front • For k_b >40 darcy, buoyant gas-phase convection becomes dominant, particularly at the edge of the repository
Heat-pipe zones	• Will be limited	• May be significant, particularly where focused liquid flow occurs	• May be significant, particularly where focused liquid flow occurs
***RH* reduction**	• May be small, because P_g rise is large	• May be large, because P_g rise is small	• May be large, because P_g rise is small

*In the vicinity of the emplacement drifts.

Contents

1.9 Thermal-Hydrological Testing

1.9.1 Overview

This section describes the modeling and scoping analysis that will be used to help design and plan the large-scale *in situ* heater tests to be conducted in the exploratory studies facility (ESF), which will be located in the unsaturated zone (UZ) at Yucca Mountain. This section primarily addresses the first ESF thermal test, which will be installed and conducted as soon as tunnel access to the repository host rock (TSw2) is available; however, Section 1.9.7 discusses the post-test analysis of the G-Tunnel Single-Element Heater Test. The current planning for this test calls for a drift-scale test that represents the emplacement of large waste packages (WPs), containing either 21 PWR spent nuclear fuel (SNF) assemblies or 40 BWR SNF assemblies in an emplacement drift. The heater drift will contain a row of large-WP-sized heaters, and will be flanked, on either side, by arrays of borehole-emplaced "wing" heaters, placed close enough together to create a planar heat source on either side of the heater drift. Section 1.9.8.3 explains why the single-drift, winged thermal test is the recommended configuration for the first ESF thermal test.

The first ESF thermal test will be followed by a longer-duration, larger-scale, multiple-drift ESF thermal test. In preparation for the year-2001 license application (LA) for the repository construction authorization, we must establish sufficient confidence in our ability to predict long-term thermal-hydrological (T-H) behavior in the engineered barrier system (EBS) and natural barriers. It is therefore anticipated that the first ESF thermal test will need to be conducted under an accelerated heating and cooldown schedule. The multiple-drift ESF thermal test will be conducted under a less-accelerated heating and cooldown schedule that will provide data for the year-2008 LA update (LU) for emplacement of waste in 2010.

A major objective of this study is to model and analyze a range of heater test sizes, heating rates, and heating durations for a range of plausible hydrological conditions to help optimize an *in situ* thermal test design that provides sufficient information to determine the following:

1. The dominant mode(s) of heat flow.

2. The major T-H regime(s) and thermal-hydrological-geomechanical-geochemical (T-H-M-C) processes that govern the magnitude and direction of vapor and condensate flow.

3. The major T-H regime(s), coupled T-H-M-C processes, and site conditions (such as ambient liquid flux) that govern dryout and rewetting of the dryout zone.

4. The influence of heterogeneous properties and conditions on the flow of heat, vapor, and condensate, with particular emphasis on rock dryout and rewetting.

Historically, heater tests in the ESF have been considered primarily to pertain to T-H-M-C behavior in the near-field (or WP) environment. The Site Characterization Plan (SCP) [DOE, 1988] refers to the ESF thermal tests as the Engineered Barrier System Field Test (EBSFT), indicating what was then regarded as the focus of those tests on providing information relevant to EBS and WP performance. With respect to WP performance, a primary goal of the ESF heater tests is understanding water contact modes (on WPs), including liquid-phase flow and condensation of water vapor, and the related temperature and chemistry. Another important goal is understanding how coupled T-H-M-C processes influence radionuclide mobilization (from the waste form), release (from the WP), and transport (in the EBS and near field). The influence of introduced (man-made) materials, such as backfill, on coupled T-H-M-C processes is an important consideration. Since the SCP was written, numerous studies [Buscheck and Nitao, 1992; Buscheck and Nitao, 1993a; Buscheck and Nitao, 1993b] have shown that significant decay-heat-driven T-H effects (and possibly, significant T-H-M-C effects) extend upwards all the way to the ground surface and downwards to deep into the saturated zone (SZ) below the water table. The ESF heater tests must therefore provide critically important

information about decay-heat-driven T-H behavior and related coupled T-H-M-C processes that occur in a zone (called the altered zone) that is likely to extend vertically through much of the UZ and into the SZ. Another important goal for the ESF thermal tests is to help understand how coupled T-H-M-C processes influence radionuclide transport in the altered zone.

For the analysis of the first ESF drift-scale thermal test described in this section, we apply the hydrological and thermal properties and hydrostratigraphy used in previous modeling studies of decay-heat-driven thermal-hydrological flow [Buscheck et al., 1993a; Buscheck et al., 1993b]. We examine the trade-offs between (1) meeting the 2001 LA schedule, (2) perturbing thermal-hydrological conditions in a large enough volume of rock relative to the spatial variability of fracture and matrix properties, and (3) generating conditions that are applicable to repository performance during the entire thermal loading cycle, including heatup and cooldown.

1.9.2 Use of Hypothesis Testing

The subject of hydrological model validation has generated considerable debate. Konikow and Bredehoeft [1992] believe that the terms *model validation* and *verification* are misleading and that their use in groundwater science should be abandoned in favor of more meaningful model-assessment descriptors. This view echoes that of Popper [1959], who states: "We cannot validate, we can only invalidate." Konikow and Bredehoeft believe that this "obligates us as scientists to perform a critical set of experiments in an attempt to test, or invalidate, our model (or hypothesis)." For many published "model validation" studies, the modelers history-matched their models, and in the process, used their models to estimate parameter distributions, stresses on the system, and boundary and initial conditions. The modelers imply that the resulting good fit constitutes model validation.

Konikow and Bredehoeft [1992] ask, rhetorically, "If the models cannot be validated, why are they useful?" They answer their question by stating: "Models provide a tool for critical analysis. They are a means to organize our thinking, test ideas for their reasonableness, and indicate which are the sensitive parameters. They point the way for further investigation. They help formulate critical experiments with which to test hypotheses." In our modeling studies of decay-heat-driven T-H flow, we have utilized idealizations of (1) the repository thermal load, (2) the distribution of hydrological and thermal properties, and (3) boundary and initial conditions. No individual model of the repository-UZ-SZ system is itself a "valid" representation; however, the combined use of our suites of model calculations provides a means to identify critical dependences, evaluate worst-case scenarios, and develop fundamental hypotheses, which can be addressed by subsequent analysis and testing.

A primary motivation for the minimally heated (MH) repository strategy is to avoid or limit the significance of heat-mobilized fluid flow in the UZ. The underlying assumption is that by eliminating or limiting the spatial and temporal extent of boiling, one minimizes the major significant mechanism for mobilizing heat-driven fluid flow. However, there are mechanisms that occur under sub-boiling conditions that must be addressed in order to justify this assumption.

Testing the following hypotheses will determine whether a low-AML repository system based on the MH strategy avoids (or limits) significant heat-mobilized fluid flow near WPs:

MH-1: Mountain- and drift-scale buoyant gas-phase convection does not significantly mobilize moisture in the UZ.

MH-2: Vapor diffusion does not significantly mobilize moisture in the UZ.

MH-3: Heterogeneity in the heat load distribution and/or in gas- and liquid-phase pathways does not focus enough condensate drainage to drip onto WPs or to significantly increase liquid-phase flow in the UZ.

For repository systems with thermal loads that significantly mobilize fluid flow, as is certainly the case with a high-AML repository, these same hypotheses address how that mobilization occurs.

Field tests, including the Large-Block Test (LBT), to be performed at Fran Ridge [Lin et al., 1994], and *in situ* thermal tests in the ESF will provide the most conclusive means of evaluating issues associated with thermal loading, including resolution of the major hypotheses. Portions of these tests should be conducted under sub-boiling conditions to support the resolution of hypotheses MH-1, MH-2, and MH-3. Portions of the tests will be conducted under above-boiling conditions to address the effect of boiling for either a low- or high-AML repository system, and to provide information critical to establishing the maximum design thermal load of the repository.

Hypothesis testing can also help determine the extent to which a low- or high-AML repository system based on the CH strategy can generate conditions that enhance WP integrity and that reduce the potential for radionuclide dissolution and transport. The primary CH hypotheses are as follows:

CH-1: Heat, vapor, and liquid flow (including heterogeneous fracture flow) near WPs are dominated by heat conduction (and possibly vapor diffusion) and are therefore predictable.

CH-2: WP temperatures above the boiling point, and/or a ΔT between the WP and drift wall, result in a significant reduction in *RH* and the absence of mobile liquid water on WPs.

CH-3: Ambient (humid) WP conditions are restored after WP temperatures have substantially cooled (i.e., well after the end of the boiling period).

The above-boiling heating stages of the LBT and of ESF thermal tests are needed to support the resolution of hypotheses CH-1, CH-2, and CH-3 and to further support the resolution of hypotheses MH-1, MH-2, and MH-3. It is easier to evaluate the significance of buoyant gas-phase convection when thermal testing is conducted under above-boiling conditions [Buscheck et al., 1993b]. As discussed in Sec. 1.9.8.4.1, the cooldown rewetting stage of an above-boiling thermal test can provide significant diagnostic information about the degree of vapor diffusion enhancement.

Resolution of hypothesis CH-1 would be facilitated by testing the following subsidiary hypotheses:

CH-1a: Mountain-scale, buoyant gas-phase convection does not dominate heat flow in the UZ.

CH-1b: The net infiltration flux above the repository (and below the PTn unit) is not high enough to substantially decrease the vertical thickness of the superheated zone (the zone of above-boiling temperatures) above the repository.

CH-1c: The integrity of the superheated zone is not substantially compromised by variability in the heat load distribution (including edge-cooling effects) or by heterogeneity in the distribution of infiltration flux and condensate drainage. In other words, focused advective liquid-phase flow does not overwhelm the decay-heat-driven heat flux enough to permanently collapse (down to WP locations) local regions of the superheated zone.

If it is substantially enhanced, vapor diffusion increases the heat loss from the repository (and from WPs) in a predictable manner (which is very similar to that resulting from heat conduction). The net infiltration flux (in particular, that below the PTn unit) may be reduced if the decay-heat-steepened, near-ground-surface temperature gradient increases the evapo-transpirative loss of moisture to the atmosphere.

Resolution of hypothesis CH-2 would be facilitated by testing the following subsidiary hypotheses:

CH-2a: Variability in the heat load distribution and/or heterogeneity in gas- and liquid-phase (fracture) pathways does not focus enough infiltration flux and condensate drainage to drip onto WPs.

CH-2b: Vaporization and vapor flow are not throttled by low k_b to cause a large enough increase in P_g that suppresses *RH* reduction.

In addition to heterogeneity, subsidiary hypothesis CH-2a also depends on whether the net infiltration flux is high enough (at least locally) to collapse regions of the superheated zone. If it is substantially enhanced, vapor diffusion tends to mitigate the effects of nonequilibrium liquid-phase fracture flow and thereby helps to maintain drier WP conditions.

Resolution of hypothesis CH-3 would be facilitated by testing the following subsidiary hypothesis:

CH-3a: The net infiltration flux above the repository (and below the PTn unit) is not high enough to allow the rewetting front in the rock matrix to closely follow the retreat of the nominal boiling front.

A highly spatially heterogeneous and episodic distribution of infiltration flux could focus liquid-phase flux onto no more than a few WPs, while reducing the overall rate of rewetting of the dryout zone. The latter effect would occur if episodic nonequilibrium liquid-phase fracture flow drained quickly through the dryout zone before being completely imbibed by the rock matrix. Whether the liquid-phase flux reaching WPs occurs primarily as episodic pulses or as steady "seeps and weeps" will significantly affect waste-form degradation and radionuclide dissolution and release from WPs. If it is substantially enhanced, vapor diffusion tends to suppress fast liquid-phase rewetting of the rock matrix and nonequilibrium liquid-phase fracture flow.

1.9.3 Purpose of Thermal-Hydrological Testing

In situ thermal tests (also called heater tests) have been included in the SCP [DOE, 1988] in response to regulatory requirements for site characterization and to test the coupled thermal-hydrological-geomechanical-geochemical (T-H-M-C) process models required to assess the total system performance at the site. *In situ* heater tests conducted under thermal loading conditions that are reasonably representative of repository conditions are required to provide an understanding of coupled processes, including the following:

1. T-H behavior, with emphasis on identifying the dominant mode(s) of heat flow and the dominant T-H regime(s) (Sec. 1.8.5); the degree of vapor diffusion enhancement; modes of water contact on WPs; and heat-driven alteration of flow and transport properties in the engineered and natural barriers.

2. Geochemical behavior, with emphasis on coupling with T-H behavior; alteration of flow and transport properties; and the resulting chemistry of water that returns to the EBS (possibly including backfill) and WP locations.

3. Geomechanical behavior, with emphasis on heat-driven opening and closing of fractures and the initiation of new fractures and on the influence of those effects on flow and transport properties, on T-H behavior, and on the geomechanical stability of the emplacement drifts.

4. The influence of introduced (man-made) materials, such as backfill, on coupled T-H-M-C processes, with emphasis on water contact modes and the related chemistry.

Several tests, whose objective is to understand these processes, are described in the SCP [DOE, 1988]. To understand the many coupled processes that are likely to occur in the host rock, and to adequately sample the variety of rock types required for repository performance assessment, more than one type and location of test are likely to be required. The sufficiency of any test (with respect to scope, size, and duration) for making findings on the compliance of the site with the performance objectives will depend on adequate representation of the heterogeneity of the rock being tested and on the waste isolation strategy that is adopted by the Civilian Radioactive Waste Management System (CRWMS). A waste isolation strategy is currently being developed by CRWMS, but has not yet been formally adopted. A waste isolation strategy that is based on taking advantage of waste emplacement in the UZ and on the constructive use of decay heat could include the following five elements:

- Favorable environment for WPs provided by (a) the unsaturated host rock, (b) the low liquid-phase flux near WPs, and (c) an extended period of low relative humidity *RH* on WPs (low *RH* until WPs are relatively cool).

- Long-term radionuclide containment provided by robust WPs in conjunction with a favorable WP environment.

- Limited mobilization of radionuclides within the WPs provided by minimal moisture contact by liquid-phase flux and condensation of water vapor.
- Slow release and transport of radionuclides through the engineered barrier system (EBS) provided by limited liquid-phase flux and low moisture content in the EBS.
- Slow migration and significant dilution of radionuclides in the geosphere.

Slow rewetting of the dryout zone (addressed by hypothesis CH-3) may be a major factor contributing to slow radionuclide migration in the UZ. Decay-heat-driven, buoyant liquid-phase convection in the SZ may be the major mechanism driving radionuclide dilution in the geosphere for tens of thousands of years [Buscheck and Nitao, 1993b; Buscheck and Nitao, 1994a]. Heater testing in the ESF and the LBT [Lin et al., 1994] and related analyses will provide key essential technical input for virtually all of the waste isolation elements.

1.9.4 Factors Affecting Thermal Test Size and Duration

The required size and duration of *in situ* thermal tests are influenced by regulatory requirements, model testing needs, and the need for scientific credibility. The requirements of the Nuclear Regulatory Commission (NRC) relevant to *in situ* testing are found in 10 CFR 60 [NRC, 1990]. Site characterization must include *in situ* exploration and testing at the depths at which WPs would be emplaced unless the Commission determines that this is not necessary for a specific site [NRC, 1990]. The results of *in situ* testing will be used to develop the information contained in the safety analysis report (SAR) that will be part of the license application (LA). The SAR must include a description of the hydrological, geochemical, and geomechanical properties and conditions of the site and the anticipated response of these systems to the maximum design thermal load of the repository [NRC, 1990].

The assessment of the site presented in the SAR must include an evaluation of repository performance and a description of the measures used to test the adequacy of the process models that provide the basis for performance assessment. The analyses must be supported by an appropriate combination of *in situ* tests, laboratory tests representative of field conditions, monitoring data, and natural analog studies [NRC, 1990]. The NRC issued its "Generic Technical Position on *In situ* Testing During Site Characterization for High-Level Nuclear Waste Repositories" (GTP) to provide guidance to the DOE on *in situ* testing [NRC, 1985] The introductory sections of the GTP state that *in situ* tests should represent a realistic repository environment as closely as possible. However, it was recognized that the time available for these tests is far shorter than the period of post-closure performance. The NRC staff [NRC, 1985] specifically noted that there is a "deficient understanding of the effects of heat on rock and mineral behavior as well as the induced hydrological and geochemical changes." The results of *in situ* tests can be used to test the process models and to reduce the uncertainties in the prediction process.

1.9.5 Physical Criteria Affecting Thermal Test Size and Duration

Because of limited time before the license application (LA) in 2001, some of the *in situ* ESF thermal tests will have to be accelerated relative to actual thermal loading conditions. A major objective of *in situ* thermal test analysis [Buscheck et al., 1993a; Buscheck et al., 1993b] is to examine the trade-offs between test duration (and heating rate) and the generation of T-H conditions applicable to repository performance during the entire thermal loading cycle, including heatup and cooldown. During both heatup and cooldown, the thermal test will accelerate changes in time and space, including the following:

1. The transition from sub-boiling to boiling conditions.
2. The transition from boiling to above-boiling conditions.
3. The transition from above-boiling to sub-boiling conditions.

It is important that the accelerated thermal cycle not preclude the occurrence of coupled T-H-M-C phenomena that may be important to boiling, dryout, and rewetting under actual repository conditions. It is equally important that the accelerated thermal cycle not introduce complex phenomena that are not relevant to actual repository conditions.

An important part of this study is to conduct T-H scoping calculations of the ESF thermal tests in order to design tests that provide useful and timely information needed for resolution of the major hypotheses and to observe potentially critical intercoupling between thermal-hydrological processes and geomechanical and geochemical processes. The heat load must be applied to the rock during the tests in a way that is relevant to repository conditions, and the experimental design must allow substantial resolution of the major MH and CH hypotheses described in Sec. 1.9.2.

A primary concern is that the area of heated rock be large enough to accomplish the following:

- Incorporate a network of fractures that is sufficiently connected to allow examination of important decay-heat-driven processes such as boiling, vapor diffusion, buoyant gas-phase convection, and nonequilibrium, liquid-phase fracture flow.
- Permit the possible development of condensate perching above the boiling zone.
- Examine whether heterogeneity in the gas- and liquid-phase pathways focuses enough condensate drainage to cause water to drip onto WPs.
- Prevent edge-cooling effects from dominating T-H behavior.
- Diagnose the significance of buoyant gas-phase convection on moisture movement and heat flow.

Model calculations have already been conducted [Buscheck et al., 1993a; Buscheck et al., 1993b] that address the question of *in situ* thermal test size. Those calculations show that a heated area of 1475 m^2 would be adequate to prevent edge-cooling effects from dominating T-H behavior at the center of the test. Section 1.9.8.2.1 addresses the question of thermal test size.

To determine the size and duration of the *in situ* thermal tests, the following criteria should also be considered:

1. Volume of the dryout zone.
2. Rate of change of temperature.
3. Maximum rock temperatures.
4. Spatial temperature gradients.
5. Extent and duration of condensate perching.
6. Velocity of the dryout front.

The first criterion relates to the scale of the dryout zone relative to the scale of the heterogeneity of the fracture properties, particularly fracture spacing and connectivity. Because boiling-driven dryout and buoyant gas-phase convection are very dependent on the fracture system, it is necessary to dry out a sufficient volume of rock to include an interconnected fracture system. Past estimates of this volume were based on the assumption of at least one fracture per foot horizontally and many fewer fractures per foot vertically. We estimated that a rock mass of about 20 m diameter would be large enough to have interconnected fracture clusters [Buscheck et al., 1993b]. If the dryout zone is small relative to the scale of heterogeneity or connectivity, it may be that boiling-driven dryout, buoyant gas-phase convection, and condensate drainage are completely dominated by the local heterogeneity. Moreover, models that incorporate bulk averages of matrix and fracture properties require tests in which bulk averages are statistically meaningful.

The second, third, and fourth criteria relate to the potential for geomechanical and geochemical effects to significantly alter the T-H properties in a way that is not representative of repository thermal loading conditions. The fifth and sixth criteria relate primarily to thermal-hydrological-geochemical coupling at the refluxing front, which may result in geochemical alteration of fracture and matrix properties. If the dryout front is driven too quickly, there will be inadequate time for geochemical effects to occur. Note that an increase in boiling (and dryout rate) will be accompanied by

an increased condensate flux in the refluxing zone. One might therefore expect that the increased condensate flux would compensate for the reduced overall time during which a given region of fractured rock is exposed to refluxing conditions. If condensate sheds off the sides of the boiling zone, there will be a net loss of fluid from the refluxing system, increasing the overall rate of dryout. If condensate shedding is particularly effective, substantial overdriving of the dryout rate (relative to applicable repository conditions) will have the effect of reducing the potential for reflux-driven redistribution of minerals in fractures.

1.9.6 Numerical Models and Assumptions

1.9.6.1 V-TOUGH and NUFT Thermal-Hydrological Flow Codes

All thermal-hydrological calculations were carried out using the V-TOUGH (Vectorized Transport of Unsaturated Groundwater and Heat) code [Nitao, 1989] and NUFT (Nonisothermal Unsaturated-Saturated Flow and Transport) code [Nitao, 1993]. V-TOUGH is Lawrence Livermore National Laboratory's enhanced version of the TOUGH code, which is a member of the Mulkom family of multiphase, multicomponent codes developed at Lawrence Berkeley Laboratory [Pruess, 1987]. Both V-TOUGH and NUFT are multidimensional numerical simulators capable of modeling the coupled transport of water, vapor, air, and heat in fractured porous media. In addition to coupled multiphase heat and fluid flow, NUFT can handle multicomponent aqueous- and nonaqueous-phase species transport. NUFT is a highly efficient and robust integrated finite difference code that describes the flow of multiple phases and transport of multiple components in porous media under isothermal or nonisothermal conditions [Nitao, 1993]. NUFT solves the (nonlinear) partial differential equations for the balance of component mass and energy. NUFT has an extensive suite of linear equation solvers that allows efficient solution of practical three-dimensional problems that have tens of thousands of elements, great contrasts in element size, and sharp nonlinearities in the governing equations. For this work NUFT was configured to solve the flow and transport of air, water, and energy.

For both V-TOUGH and NUFT, the flow of fluid phases is governed by the multiphase version of Darcy's law, the diffusion of air and water vapor by Fick's law, and thermal conduction by Fourier's law. Air, water vapor, and heat are transported by fluid advection in two phases, aqueous and gaseous. Local thermodynamic equilibrium is assumed between solid and fluid phases. Water property values are calculated from steam tables. The code calculates the vaporization and condensation of water, and the resulting absorption or release of latent heat, based on local thermodynamic equilibrium.

1.9.6.2 Equivalent Continuum Model

Because of the impracticality of discretely accounting for all of the fractures at Yucca Mountain, it is often found to be necessary to account for fractures using the equivalent continuum model (ECM). The assumption of capillary-pressure and thermal equilibrium between fractures and matrix allows the fracture and matrix properties to be pore-volume-averaged into an equivalent medium. The bulk porosity ϕ_b, bulk saturation S_b, and bulk hydraulic conductivity K_b of the equivalent medium are given by the relations

$$\phi_b = \phi_f + (1 - \phi_f)\phi_m , \tag{1}$$

$$S_b = \frac{S_f\phi_f + S_m(1 - \phi_f)\phi_m}{\phi_f + (1 - \phi_f)\phi_m} , \tag{2}$$

$$K_b = K_m(1 - \phi_f) + K_f\phi_f \quad (3)$$

where the subscripts m and f refer to the matrix and fractures, respectively. Because of the low K_m in the UZ, the value of K_b is almost completely determined by K_f and ϕ_f for most fracture spacings and permeabilities.

1.9.6.3 Thermal-Hydrological Properties

All major hydrostratigraphic units in the UZ at Yucca Mountain are included in the models [Klavetter and Peters, 1986; Peters et al., 1984]. This hydrostratigraphic profile has been used in previous modeling studies of nonequilibrium liquid-phase fracture flow [Buscheck et al., 1991], studies of T-H behavior at the drift and repository scale [Buscheck and Nitao, 1992; Buscheck and Nitao, 1993a; Buscheck and Nitao, 1993b; Buscheck et al., 1994; Buscheck and Nitao, 1994a; and Buscheck and Nitao, 1994b], and scoping studies of large-scale *in situ* thermal tests [Buscheck et al., 1993a; and Buscheck et al., 1993b]. The data for wet and dry thermal conductivity K_{th} were obtained from the Reference Information Base (RIB) [DOE, 1990]. We applied the RIB version 3 K_{th} values, as we did in previous T-H calculations [Buscheck and Nitao, 1992; Buscheck et al., 1993a; and Buscheck et al., 1993b]. As in those previous studies, we assumed initial saturation conditions corresponding to the steady-state saturation profile obtained by Buscheck et al. [1991] for a net infiltration flux of 0 mm/yr, yielding a saturation of 68% at the thermal test horizon.

The reference-k_b case assumed k_b = 280 millidarcy (equivalent to three 100-μm fractures per meter). To investigate the sensitivity of T-H behavior to k_b, we considered k_b = 1, 10, and 280 millidarcy, and 84 darcy. Most of the calculations assumed "nominal" vapor diffusion (vapor diffusion tortuosity factor τ_{eff} = 0.2). For k_b = 280 millidarcy, we also considered the case of "enhanced" vapor diffusion (τ_{eff} = 20) in which the rate of vapor diffusion is 100 times greater than in the nominal case.

1.9.6.4 Initial and Boundary Conditions

We assume the same initial vertical distribution of temperature T, liquid-phase saturation S_L, and gas-phase pressure P_g as in previous calculations for a zero net infiltration flux [Buscheck et al., 1991; Buscheck and Nitao, 1992; Buscheck and Nitao, 1993a; Buscheck and Nitao, 1993b; Buscheck et al., 1993a; Buscheck et al., 1993b; Buscheck et al., 1994; Buscheck and Nitao, 1994a; Buscheck and Nitao, 1994b]. We assume that the *in situ* thermal tests are to be conducted at the repository horizon, which is assumed to be 343.1 m below the ground surface [Buscheck et al., 1993a; and Buscheck et al., 1993b]. Because of the relatively short duration of the *in situ* thermal tests, there is not sufficient time for the heaters to interfere with the model boundaries. Therefore, the results of this study are insensitive to whether we treat the water table as a fixed-depth, constant-temperature boundary or explicitly represent T-H flow in the SZ. The results are also insensitive to the depth at which the ESF thermal test is conducted, as long as it is conducted primarily in the TSw2 unit (the repository host rock). Differences in T, S_L, and P_g within the TSw1-TSw2 depth interval are negligible with respect to depth.

1.9.6.5 Thermal Test Configuration

This section describes the analysis of three basic types of *in situ* thermal test design:

a. Plate thermal test: A uniformly heated disk-shaped area is approximated with the use of horizontal-borehole-emplaced heaters in closely spaced, parallel, small-diameter boreholes. The

model used to analyze this test configuration assumes a uniform, planar, disk-shaped heat source with a vertical thickness of 1.5 m.

b. **Single-drift thermal test:** This consists of a row of large-WP-sized heaters located on the center of the floor of a drift having dimensions similar to those of an actual WP emplacement drift. The model assumes that the heaters can be approximated by an infinitely long, line-heat load.

c. **Single-drift, winged thermal test:** This has the same geometry as the single-drift thermal test with the addition of two arrays of "wing" heaters, which are emplaced in closely spaced, small-diameter horizontal boreholes that effectively create a uniform planar heat load on either side of the heater drift. This heating configuration can effectively simulate accelerated coalescence of the boiling zones between neighboring WP emplacement drifts without resorting to excessively high temperatures near the heater drift.

The *in situ* heater tests are represented with two kinds of models [Buscheck et al., 1993a; and Buscheck et al., 1993b]: (1) a two-dimensional, X-Z, vertical-cross-sectional model that assumes that the heated footprint of the test is infinitely long in the third dimension, and (2) a "quasi-three-dimensional" R-Z model that assumes axisymmetry about the vertical axis through the center of the heater array. The R-Z model is used to represent thermal test configuration a.

For thermal test configurations b and c, the X-Z model explicitly represents the details of the drift heaters, heater drifts, and wing heater arrays in the vertical plane transverse to the drift axis. The cross-sectional dimension of the heater is 1.5 × 1.5 m. The cross-sectional dimension of the heater drift is 4.4 × 4.4 m. For the *reference* single-drift, winged thermal test configuration, the wing heater array is assumed to generate a planar heat load over the interval $4 < |x| < 14$ m from the drift centerline (on either side of the heater drift). For the reference heating-rate case, the lineal heat load generated by the drift heaters is 0.8 kW/m along the drift axis, corresponding to an areal power density (APD) of 100 W/m^2 averaged over the interval ($-4 < x < 4$ m) separating the two wing heater arrays. The inner half of the wing heater arrays ($4 < |x| < 9$ m) generates an APD of 105 W/m^2, while the outer half generates an APD of 157.5 W/m^2. The entire heater array (drift heaters plus wing heaters) generates an APD of 122 W/m^2 averaged over the 28-m-wide heated area. Because it is two-dimensional, this model assumes that the heater drifts are infinitely long, effectively neglecting heat loss due to heat flow parallel to the drift axes. Two accelerated single-drift, winged thermal tests were also analyzed with APDs of 177 and 236 W/m^2 averaged over the 28-m-wide heated area.

The R-Z model represents a disk-shaped uniform heat source with a given radius and a vertical thickness of 1.5 m. The R-Z model can be also used to approximate the effects of a finite-length, single-drift, winged thermal test heating a square region covering the same area as the disk. Because the single-drift, winged heater test is designed to create a coalesced dryout region at very early time, it can be approximated by a smeared-heat-source model. The R-Z model has the advantage of accurately accounting for the overall heat flow (including the heat flow in the axial direction of the single-drift, winged heater tests). In an earlier study of multi-drift heater tests [Buscheck et al., 1993a; and Buscheck et al., 1993b], comparisons between the two-dimensional X-Z model and the R-Z model showed outstanding agreement in rock temperature at the center of the heater array for the first 4 yr of full-power heating. The dryout behavior predicted by the respective models also agreed reasonably well for $t > 2$ yr. For the current study, we used the R-Z model to analyze heated areas of 50, 270, 490, 1475, and 5077 m^2.

For the reference heating-rate case (APD = 122 W/m^2), we considered three heating durations: 1-, 2-, and 4-yr full-power heating periods. The heater power is linearly ramped to zero in one year following the end of the full-power heating period. For the accelerated-rate cases (APD = 177 and 236 W/m^2), we considered 1- and 2-yr full-power heating periods.

1.9.7 Post-Test Analysis of G-Tunnel Single-Element Heater Test

Decay-heat-driven moisture movement in the unsaturated zone at Yucca Mountain has been modeled in the past using either equivalent-continuum (ECM) or (less commonly) discrete-fracture (DFM) models. The ECM assumes local thermodynamic equilibrium between the fractures and matrix within a composite representative elementary volume (for a description of an implementation of the ECM see Nitao [1988]). Effectively, the ECM is a single-continuum model with composite characteristic curves given as functions of bulk-averaged saturation. The DFM, on the other hand, separates the fractures and matrix into distinct spatially discretized domains, which, therefore, can represent disequilibrium between matrix and fractures. Because of this feature, the DFM is well suited to investigating the dynamics of decay-heat-generated condensate, on how much water imbibes into the matrix by matric suction or drains down fractures. However, the ECM is much more computationally efficient than the DFM, so that it is important to understand conditions under which use of the ECM is appropriate. Section 1.1.3.2 summarizes the advantages and disadvantages of the ECM and DCM.

Comparisons of thermal-hydrological behavior between the ECM and the DFM by Pruess et al. [1990] assumed axisymmetry with no gravity, and there was, therefore, very little difference between the results obtained by the two approaches. Our work shows that the influence of gravity can lead, in some cases, to significant differences. Forsythe [1990] has performed one of the few thermal-hydrological calculations with discrete fracture and matrix elements including the effect of gravity. However, our experience and theoretical work suggests that Forsythe's matrix grid resolution was not fine enough to accurately calculate the fracture-to-matrix imbibition term, which strongly affects whether condensate drains.

About 6 to 9% of the volume of the matrix rock at the repository horizon is occupied by liquid water. Decay heat can vaporize significant amounts of this pore water under both sub-boiling and boiling conditions. Which mechanisms dominate transport of the resulting vapor depends on the overall connectedness and fluid conductivity of the fracture system, as characterized by the large-scale bulk permeability k_b [Buscheck and Nitao, 1994a]. There are three regimes with respect to advective gas transport, which are characterized by k_b ranges: (1) low-k_b range (k_b < 1–10 millidarcy), (2) intermediate-k_b range (1–10 millidarcy < k_b < 1–10 darcy), and (3) high-k_b range ($k_b \geq$ 1–10 darcy). In the intermediate- and high-k_b ranges, advective gas transport is not throttled by k_b and can therefore dominate moisture movement at the drift and repository scales. Gas-phase pressure gradients generated by the evolving water vapor drive gas (air and water vapor) away from the dehydrating (boiling) region; this advection is the primary mode of vapor transport for the intermediate-k_b range, while it is one of the two primary modes for the high-k_b range. In the high-k_b range, the other primary mode of vapor transport is decay-heat-driven buoyant gas-phase convection. For the low-k_b range, because advective vapor transport is throttled by k_b, vapor diffusion is the primary mode of vapor transport; vaporization creates a region of increased vapor pressure (centered at WPs), which causes an outward diffusive vapor flux.

As water vapor in fractures is driven away from the repository, it reaches regions in which the temperature is below the local boiling point of water, where it condenses. Some of the condensate will be imbibed into the matrix by suction potentials. The remaining condensate will drain downwards in fractures by gravity, imbibing into the matrix as it travels, until either (1) it returns to the dehydrating region, where it is revaporized, (2) all of the water in the fracture is eventually imbibed into the matrix, (3) the fracture dead-ends, or (4) the water table or perched water body is reached. Water in (1) may recondense again above the dehydrating zone, where it can repeat the process, creating a refluxing system [Nitao, 1988] called a gravity-driven heat pipe.

A field test [Ramirez et al., 1991] (Prototype Engineered Barrier Test) was performed in 1988-1989 by Lawrence Livermore National Laboratory for the Yucca Mountain Project in the G-tunnel Complex at the Nevada Nuclear Test Site. The test took place within the Grouse Canyon member of the formation, a fractured welded tuff similar to that at the potential Yucca Mountain repository horizon. A 3-kW, 3-m-long heater assembly was emplaced into a horizontal borehole 30 cm in diameter and was energized for approximately 130 days followed by a 65 day linear rampdown period. Thermocouples, neutron

probes, and psychrometers monitored the thermal and moisture response. Packed air-injection tests were performed before and after heating, indicating bulk permeabilities mostly within the 1-100 darcy range. Some important observations were the following: (1) temperatures generally followed a thermal conduction profile, except in a region to the side of the heater where, for a time, temperatures stayed at the boiling point; (2) the drying volume was accurately predicted by the ECM; (3) local drying in the matrix occurred mostly adjacent to fractures; (4) gas phase pressures in the matrix were higher than in fractures; (5) slightly more drying was observed below the heater than above; (6) temperature profiles at some points were slightly higher above the heater than at corresponding distances below; (7) there was very little imbibition of condensate; and (8) some drainage into the borehole from fractures occurred early in the test.

The test was simulated using NUFT to construct a three-dimensional hybrid DFM/ECM model. A single discrete fracture is represented by a two-dimensional plane of elements that traverses the heater at its midplane. The matrix on both sides of the fracture is 0.15 m thick and is modeled by a three-dimensional slab of elements. The rest of the model consists of a three-dimensional system of ECM elements. In this way we can model a finite heat source without the infinite-source assumption, which would have overpredicted temperatures and rock dryout. Because of the approximate symmetry plane at the fracture midplane, we modeled the half-domain lying on one side of the fracture. Heat transfer across the air gap from the heater to the borehole wall is modeled using the ΔT^4 radiation law. Grid resolution in the fracture plane was on the order of 0.1 m within the zone of interest in the vicinity of the heater. Grid sizes in the matrix next to the fracture were on the order of hundreds of micrometers. The resulting model has approximately 19,000 elements and takes around 10-20 hours to run on the IBM RISC 6000/550. A pure-ECM model was also run for comparison.

Cases were run for fracture apertures of 100, 524, and 1048 μm, corresponding to k_b = 0.280, 40, and 320 darcies, respectively, consistent with the range of gas permeability measurements at G-tunnel and Yucca Mountain. Fracture characteristic curves were those for a sandy material. Matrix porosity (20%), intrinsic matrix permeability (1.9 microdarcies), and initial liquid saturation (60%) were based on laboratory measurements. The capillary parameter α in the van Genuchten matric potential correlation was calibrated using an imbibition test [Buscheck and Nitao, 1988]; the value of the m parameter was taken from Peters et al. [1984]. The calibrated α parameter effectively reduces the matric suction by a factor of 40 with respect to the value in Peters et al. [1984].

Temperature histories at the lower borehole wall and at points 0.55 m below and 2.4 m above the heater axis showed good agreement (Fig. 1.9-1). The 1048-μm case shows a higher-than-measured temperature above the heater, possibly because buoyant gas-phase convection is being overpredicted. The 100- and 524-μm cases appear to give the best fit. The three cases give a good idea of the sensitivity of temperature on aperture, which in the field is highly spatially variable. The good agreement of temperature at the borehole was somewhat surprising, considering that there was a 30-40°C difference between the top and bottom of the heater container surface, a difference that was also observed in a laboratory benchtop experiment. Previous calculations using a linear heat transfer model across the air gap gave slightly higher temperatures [Buscheck and Nitao, 1991] than measured. Rock matrix dryout volume, as measured by the neutron probes, was predicted reasonably well by both DFM and ECM (Fig. 1.9-2). The narrower dryout predicted by the DFM is caused by calculated flow resistance to vapor as it escapes from the matrix into the fractures; the ECM approach, because of its equilibrium assumption, has no matrix-to-fracture resistance. However, closer agreement by the ECM indicates that boiling is not being "throttled" by the matrix, perhaps because of microfractures not considered in our model or because the effective fracture spacing in the field was smaller. In the 524- and 1048-μm cases, the ECM predicts much more buildup of condensate in the matrix, whereas the DFM predicts much less because of higher condensate drainage fluxes and upward vapor dispersal by buoyant convection. Some condensate buildup is predicted by both approaches in the 100-μm case. Note that the diameter of the averaging kernel "seen" by the neutron probe was approximately 30 cm [Buscheck and Nitao, 1988]. Consistent with field measurements, the 1048-μm DFM predicts slightly more drying below and slightly less drying above the heater.

The 100-μm DFM predicts very little nonequilibrium condensate drainage in the fracture plane, as indicated by the liquid saturation in the fracture plane, while there is significant condensate drainage in the 1048-μm case (Fig 1.9-3). At early times fracture flow in the 1048-μm case is dominated by gravity (Fig. 1.9-3c); at the end of the full-power heating period (Fig. 1.9-3d), buoyant gas-phase convection begins to play an important role by moving vapor from below to above the heater, where it condenses. Figures 1.9-4a,c show the dimensionless saturation in the matrix, averaged in the direction transverse to the fracture plane. The shapes of the contours reflect the shape of condensate in the fracture. (The dimensionless saturation is the normalized amount of dryout compared to initial saturation. It equals one at full saturation and minus one at complete dryout.) The medium-to-dark shading around the heater is the region of relative dryout, with dark shading indicating strong dryout. The narrow white shading around this region is no net change in saturation separating the regions of dryout and increased relative saturation. Dark shading in the latter region indicates large increases in saturation, while light shading indicates small increases. Figures 1.9-4b,d show the dimensionless matrix saturation in the vertical plane in the heater centerline perpendicular to the fracture plane. The vertically symmetric profile in the 100-μm case indicates that the effect of gravity in the fracture is negligible, while in the 1048-μm case, the matrix below the heater is drier while that above is wetter (as observed in the field test), because of buoyant gas-phase convection. Our model results indicate that buoyant gas-phase convection probably played a role in vapor movement. In both cases drying occurs preferentially next to the borehole and fractures, which was also observed in the test.

Calculations of the G-tunnel heater test show that gravity drainage and buoyant gas-phase convection are likely reasons why condensate buildup in the matrix was not observed in the *in situ* heater test. Preferential drying below and wetting above the heater lend some support for the possibility that buoyant convection in the fractures is a factor driving moisture movement. Temperature predictions by all models were good, reflecting the fact that heat transfer in the rock was primarily by thermal conduction. Because of the short duration and small spatial scale of the test, the local condensate drainage flux during the G-tunnel test was probably much higher than that to be expected for a repository beyond the first few hundred years.

1.9.8 Pre-Test Analysis of ESF Thermal Tests

1.9.8.1 Overview

When this modeling study began, five major thermal test configurations were under consideration:

1. Single-element thermal test.
2. Plate thermal test.
3. Single-drift thermal test.
4. Single-drift, winged thermal test.
5. Multi-drift thermal test.

Because of their respective merits, early planning contemplated the concurrent running of at least three of these configurations during the first set of ESF thermal tests. More recently, planning for the first set of ESF thermal tests has focused on configurations 1 and 4. Configuration 5 (multi-drift thermal test) will be used in the second set of ESF thermal tests, which will heat a larger area and will have longer heatup and cooldown periods. In the following sections, we analyze configurations 2, 3, and 4. Analyses of configuration 5 have also been conducted [Buscheck et al., 1993a; Buscheck et al., 1993b]. Calculations of small-area plate thermal tests (e.g., the 50-m^2 test described in Sec. 1.9.8.2) can be applied to analyzing configuration 1, whereas calculations of large-area plate thermal tests (e.g., the 5077-m^2 test described in Sec 1.9.8.2) can be applied to analyzing configuration 5.

In Sec. 1.9.8.2 we use the *R*-Z model to evaluate plate thermal test size and duration. The *R*-Z model, which is effectively a smeared-heat-source model, is directly applicable to the plate thermal test; however, it can also be used to approximate the heating from a square heater array having the same heated area as the disk-shaped heater array. This approximation yields a reasonably accurate representation of the temperature distribution for the multi-drift thermal test configuration [Buscheck et al., 1993a; Buscheck et al., 1993b]. After the dryout zones coalesce ($t \geq 2$ yr), the *R*-Z model yields a good representation of dryout behavior in the multi-drift test. Because the single-drift, winged heater test is designed to create a coalesced dryout region at very early time, it can be accurately approximated with the smeared-heat-source *R*-Z model. Therefore, the evaluation of plate thermal test size and duration in Sec. 1.9.8.2 is also applicable to the single-drift, winged heater test.

In Secs. 1.9.8.3 and 1.9.8.4 we use the *X*-Z vertical-cross-sectional model, which explicitly represents the details of the drift heaters, heater drifts, and wing heater arrays in the vertical plane transverse to the drift axes. In Sec. 1.9.8.3 we analyze the single-drift heater test and compare it with the reference single-drift, winged heater test. In Secs. 1.9.8.4.1, 1.9.8.4.2, and 1.9.8.4.3 we analyze the single-drift, winged heater test, and we discuss how the thermal tests can be used to differentiate between the three major T-H regimes and to determine the degree to which vapor diffusion is enhanced. In Sec. 1.9.8.4.1 we evaluate heater test size and duration and the representativeness of T-H behavior in the single-drift, winged heater test as compared to the expected drift-scale T-H behavior in the actual repository. In Sec. 1.9.8.4.2 we evaluate the effect of a heterogeneous distribution of bulk permeability k_b on dryout and rewetting behavior and on the temperature distribution, and we consider the implications these effects may have on a recommended thermal test duration. Finally, in Sec. 1.9.8.4.3 we evaluate accelerated heating schedules.

1.9.8.2 Plate Thermal Test

In the plate thermal test, a disk-shaped area is uniformly heated. The plate heating configuration could be achieved with horizontal-borehole-emplaced heaters in closely spaced, parallel, small-diameter boreholes. This heating geometry was considered because it offers the advantage of being accurately represented by an *R*-Z axisymmetric model. The *R*-Z model is computationally much more economical than a corresponding three-dimensional model, and that economy makes it amenable to parameter sensitivity analyses. The *R*-Z model also has the advantage (over two-dimensional vertical-cross-sectional models) of being able to represent three-dimensional heat flow, so it is better able to represent the heat balance during the thermal test (particularly at late time). The finite areal extent of the heater array can be explicitly accounted for with this model. The *R*-Z model assumes a uniform planar disk-shaped "smeared" heat source with a vertical thickness of 1.5 m. The *R*-Z model is also useful in analyzing the single-drift, winged thermal test.

1.9.8.2.1 Evaluating Thermal Test Size and Duration

With the *R*-Z model, we analyzed heater array areas of 50, 270, 490, 1475, and 5077 m^2, which (more than adequately) span the range of insufficiently sized to sufficiently sized thermal tests. In this section, we focus on the ability of the thermal tests to differentiate between two of the three major thermal-hydrological (T-H) regimes described in Sec. 1.9.8.2, namely unthrottled, nonbuoyant advective rock dryout and unthrottled, buoyant advective rock dryout. We therefore considered two values of bulk permeability, with k_b = 280 millidarcy resulting in T-H behavior that is characteristic of the unthrottled nonbuoyant regime and k_b = 84 darcy resulting in T-H behavior that is characteristic of the unthrottled buoyant regime. Our goal is to identify the thermal test size and duration that are sufficient to facilitate the determination of the dominant T-H regime(s) in a timely fashion. We assumed the value of $\tau_{eff} = 0.2$ for the vapor diffusion tortuosity factor, which corresponds to the case in which vapor diffusion is not enhanced.

The ability to distinguish between the buoyant and the nonbuoyant unthrottled regimes has been covered in previous studies [Buscheck et al., 1993a; Buscheck et al., 1993b]. Figure 1.9-5 shows the

dimensionless liquid saturation distributions for a plate thermal test with a radius of 21.7 m and areal power density APD = 78 W/m^2 averaged over the 1475-m^2 heated area. As in past studies [Buscheck et al., 1993b], when analyzing dryout and re-wetting behavior we use the dimensionless liquid saturation $\bar{S}_L$ given by

$$\bar{S}_L = \frac{S_L - S_{L,init}}{S_{L,init}}, \qquad \text{if } S_L < S_{L,init}, \tag{4}$$

$$\bar{S}_L = \frac{S_L - S_{L,init}}{S_{L,max} - S_{L,init}}, \qquad \text{if } S_L > S_{L,init}, \tag{5}$$

where S_L is the current liquid saturation, $S_{L,init}$ is the initial (or ambient) liquid saturation, and $S_{L,max}$ is the maximum liquid saturation (usually taken to be unity). For the 280-millidarcy case (Fig. 1.9-5a,b), buoyant gas-phase convection does not significantly affect the direction of vapor flow, so vapor flow is vertically symmetrical about the heater horizon. The effect of the symmetrical vapor flow is partially offset by condensate shedding, which results in a greater condensate volume below the heater horizon (Fig. 1.9-6f). The equivalent continuum model (ECM) probably underrepresents how nonequilibrium fracture flow may result in significant condensate shedding during the thermal tests.

For the 84-darcy case (Fig. 1.9-5c,d), buoyant gas-phase convection dominates the direction of vapor flow, so that all of the vapor flow is driven upward to where it condenses above the dryout zone. The effect of the vertically asymmetrical vapor flow on the condensate distribution can also be seen in Fig. 1.9-6d–f. Condensate shedding resulting from nonequilibrium fracture flow may substantially offset (i.e., mask) the effects of buoyant gas-phase convection on the condensate distribution. Consequently, *in situ* measurements of changes in the liquid saturation distribution may be an inadequate indicator of the significance of gas-phase buoyancy. It is therefore desirable to have some other means of diagnosing the significance of gas-phase buoyancy. If the heated area is large enough (as is the case for 1475 m^2), the temperature distribution is highly diagnostic of the importance of gas-phase buoyancy and is insensitive to whether substantial condensate shedding occurs.

The influence of vapor and condensate flow on the temperature profile is very apparent in the 280-millidarcy and 84-darcy cases (Fig. 1.9-6a–c). The temperature profile is flattened at the nominal boiling point ($T_b \approx 96$°C). Vapor is driven (by higher P_v in the boiling zone) away from the heater horizon to where lower temperatures cause it to condense. Above the heater horizon, much of this condensate returns to the boiling zone, driven by three mechanisms: (1) capillary imbibition in the matrix, (2) capillary imbibition in small-aperture fractures, and (3) gravity drainage in fractures. Gravity drainage in the matrix is not significant in comparison with matrix imbibition, which is driven by very strong capillary pressure gradients that arise from liquid saturation gradients at the dryout front. Below the heater horizon, only the first two mechanisms, capillary imbibition in the matrix and fractures, contribute to condensate flow back toward the boiling zone; the third mechanism, gravity drainage in fractures, tends to drain condensate away from the boiling zone.

Above the heater horizon, the return flow of condensate toward the boiling zone establishes a heat transfer mechanism (driven by the convection of latent heat) called the gravity-driven heat-pipe effect [Nitao, 1988]. If this heat transfer mechanism occurs below the heater horizon, it is driven by the capillary-driven heat-pipe effect. Pruess et al. [1984] were the first to model the capillary-driven heat-pipe effect in conjunction with T-H behavior at Yucca Mountain. Given adequately high mass flux rates of the countercurrent flow of vapor and condensate, heat pipes can sustain a given heat flux with a much shallower temperature gradient than is associated with conduction. Consequently, heat pipes are associated with a flat temperature profile, with temperatures close to 96°C, if k_b is large enough not to cause P_v to rise substantially above 1 atm. Mass fluxes associated with gravity-driven fracture flow are generally greater than those associated with capillary-driven flow in either the matrix or fractures. Above the heater horizon, condensate drainage in fractures is generally the dominant source of liquid

flow back to the boiling zone. While the flattening of the temperature profile above the heater horizon results primarily from gravity-driven refluxing (the heat-pipe effect), the flattening of the temperature profile below the heater horizon in the 280-millidarcy case results from capillary-driven heat-pipe effect. Because all of the vapor flow is upward in the 84-darcy case, there is no heat-pipe zone below the heater horizon.

The vertical temperature profiles (Fig. 1.9-6a–c) are clearly diagnostic of buoyant versus nonbuoyant behavior. For the 280-millidarcy case, the vertical temperature profile is vertically symmetrical about the heater horizon. The flattening of the temperature profile at 96°C occurs both above and below the heater horizon in the 280-millidarcy case, while for the 84-darcy it occurs only above the heater horizon. The vertical extent of the upper flattened-temperature zone (i.e., the heat-pipe zone) in the buoyant (84-darcy) case is more than three times that in the nonbuoyant (280-millidarcy) case. The upper boiling front is also higher in the buoyant than in the nonbuoyant case. This difference in front heights amounts to 3 m at t = 1 yr, 6 m at t = 2 yr, and 9 m at t = 4 yr (Fig. 1.9-6a–c). For the 84-darcy case, the vertical asymmetry is quite evident at t = 2 yr; the upper boiling front is 12 m above the heater horizon, while the lower boiling front is only 3 m below the heater horizon. Therefore, within the first 2 yr of full-power heating, the 1475-m^2 test can clearly discriminate between the buoyant and nonbuoyant unthrottled regimes.

Figures 1.9-7 and 1.9-8 provide virtually the same picture as those in Figs. 1.9-5 and 1.9-6, but for a plate thermal test with a radius of 40.2 m and APD = 78 W/m^2 averaged over the 5077-m^2 heated area. Figures 1.9-8a–c indicate that the difference in the upper boiling front heights is virtually the same as that in the 1475-m^2 case. Therefore, with respect to the ability of these respective thermal tests to discriminate between the buoyant and nonbuoyant unthrottled regimes, there is no apparent advantage to going to a larger test size than the 1475-m^2 case.

To investigate the minimum thermal test size that could be used to diagnose the significance of gas-phase buoyancy, we analyzed a plate thermal test with a radius of 4.0 m and APD = 247 W/m^2 averaged over the 50-m^2 heated area (Figs. 1.9-9 and 1.9-10). As in the 1475-m^2 and 5077-m^2 tests, the 280-millidarcy case results in vertically symmetrical vapor flow (Fig. 1.9-9), while the 84-darcy case results in vertically asymmetrical vapor flow (Fig. 1.9-9). Unlike the larger tests, the 50-m^2 test creates very little condensate buildup above the dryout zone for the 280-millidarcy case (Fig. 1.9-10e–f).

The 1475-m^2 and 5077-m^2 tests (Figs. 1.9-5a,b and 1.9-7a,b) result in very broad, tabular dryout zones and well-developed, tabular zones of condensate buildup, whereas the 50-m^2 test results in a spherical dryout zone, surrounded by a very diffuse, weakly-developed zone of condensate buildup (Fig. 1.9-9a,b). Because of their size, the 1475-m^2 and 5077-m^2 tests have a broad region in which heat flow is effectively linear (upwards and downwards), while heat flow in the 50-m^2 test is essentially spherical. In the 1475-m^2 and 5077-m^2 tests, the temperature at the center of the heater array increases almost linearly with time (Fig. 1.9-11a). Accordingly, the vertical thickness of the dryout zone also grows linearly with time (Fig. 1.9-11b). Because of the spherical heat flow in the 50-m^2 test, the maximum temperature is nearly attained within the first year (Fig. 1.9-10a–c and 1.9-11a). Accordingly, the maximum spatial extent of dryout zone in the 50-m^2 test is effectively attained within the first year (Fig. 1.9-11b). Because the boiling front is not expanding after the first year, a diminishing mass flux of water vapor is being generated. Condensate buildup is consequently minimal because condensate can shed off the sides of the boiling zone and/or be imbibed by the surrounding rock matrix about as fast as it is generated. This behavior is consistent with observations made during the G-Tunnel single-element heater test [Ramirez et al., 1991], in which there was virtually no indication of any increase in liquid saturation in the condensation zone (or anywhere outside the dryout zone). It is important to note that any single-element heater test (regardless of its heated length) would result in minimal condensate buildup (and minimal refluxing) above the boiling zone. The absence of any refluxing zone would seriously degrade the ability of a thermal test to provide for observations of potentially important intercoupling between T-H and geochemical processes, particularly how it may influence fracture-matrix flow behavior.

For the 84-darcy case, the 50-m^2 thermal test does result in a narrow zone of condensate buildup above the boiling zone (Fig. 1.9-10d–f). However, the effect of buoyant convection-dominated vapor flow is not apparent in the vertical temperature profile (Fig. 1.9-10a–c). The corresponding vertical temperature profiles for the 280-millidarcy and 84-darcy cases are virtually indistinguishable from each other. A 50-m^2 thermal test is therefore not large enough to diagnose the significance of gas-phase buoyancy. It is important to note that any single-element heater test (regardless of its heated length) is unlikely to provide any useful information about the significance of gas-phase buoyancy.

To continue the determination of the minimum thermal test size that could be used to diagnose the significance of gas-phase buoyancy, we analyzed a plate thermal test with a radius of 9.3 m and APD = 117 W/m^2 averaged over the 271-m^2 heated area. As in the three test sizes already analyzed, the 280-millidarcy case results in vertically symmetrical vapor flow (Fig. 1.9-12), while the 84-darcy case results in strong vertical asymmetry. Unlike the 50-m^2 test, the 271-m^2 test does result in a narrow zone of condensate buildup for the 280-millidarcy case (Fig. 1.9-13d–f), which effectively reaches its maximum extent within the first year. Because of its small size, the 271-m^2 test effectively results in spherical heat flow. The effect of gas-phase buoyant convection-dominated vapor flow can be seen in the vertical temperature profile (Fig. 1.9-13a–c); however, the resulting upward shift in the upper boiling front is only 2 m at t = 2 yr (as against 6 m in the 1475-m^2 test) and does not continue to grow as in the 1475-m^2 and 5077-m^2 tests (Figs. 1.9-6a–c and 1.9-8a–c). The 271-m^2 thermal test is therefore only marginally useful in diagnosing the significance of gas-phase buoyancy.

To better determine the minimum thermal test size that could be used to diagnose the significance of gas-phase buoyancy, we analyzed a plate thermal test with a radius of 12.5 m and APD = 105 W/m^2 averaged over the 490-m^2 heated area. As in the four test sizes already described, the 280-millidarcy case results in vertically symmetrical vapor flow (Fig. 1.9-14), while the 84-darcy case results in strong vertical asymmetry (Fig. 1.9-14). The difference in upper boiling front heights (in the buoyant versus nonbuoyant case) amounts to 3 m at t = 1 yr, 4 m at t = 2 yr, and 6 m at t = 4 yr (Fig. 1.9-15a–c). For the 84-darcy case, the vertical asymmetry is already evident at t = 1 yr; the upper boiling front is 6.4 m above the heater horizon, while the lower boiling front is only 2 m below the heater horizon. At t = 2 yr, the upper boiling front is 10.4 m above the heater horizon, while the lower boiling front is only 3.7 m below the heater horizon. Within the first 2 yr of full-power heating, the 490-m^2 heater test can therefore clearly discriminate between the buoyant and the nonbuoyant unthrottled regimes.

It is important to consider the relation between dryout zone thickness and temperature (Fig. 1.9-11c) in optimizing a thermal test design. Ideally, an adequately thick dryout zone could be created without resorting to temperatures that were too high to be representative of actual repository conditions. For a relatively short-duration, accelerated-rate thermal test, it is desirable to create an adequately thick dryout zone in about 1.5 to 4 yr. As is discussed in Sec. 1.9.8.4.3, achieving a given dryout zone thickness sooner (as is accomplished with an accelerated heating rate) will come at the price of higher temperatures. One can limit the temperature required to achieve a given dryout zone thickness within a given time if the heated area is large enough. The APDs of the five cases considered in this section (Fig. 1.9-11) were chosen so that the temperature T_c at the center of the heater array fell in the range $215 < T_c < 230$°C at t = 4 yr. Because the influence of the edge-cooling effect on T_c increases with decreasing test size, the smaller tests require a higher APD to achieve a given T_c at a given time. Figure 1.9-11c clearly shows that the T_c associated with a given dryout zone thickness increases with decreasing thermal test size. Because the edge-cooling effect is greater for a smaller test size, it is necessary to drive T_c higher to compensate for the greater lateral heat loss and still dry out a given thickness within a given time. Note that the 1475- and 5077-m^2 tests have virtually the same relationship between dryout zone thickness and temperature. Apparently, for (at least) the first five years, the temperature behavior at the center of the 1475- and 5077-m^2 tests is essentially that of an infinitely large heated area. The nearly linear temperature rise (Fig. 1.9-11a) and linear increase in dryout zone thickness (Fig. 1.9-11b) are also indicative of this fact.

A close inspection of the 490-, 1475-, and 5077-m^2 tests (Fig. 1.9-11c) indicates that the minimum test area that limits the temperature rise associated with a given dryout zone thickness falls in the range 1000 to 1500 m^2. (These areas correspond to disk radii of 17.8 and 21.8 m, respectively.) This

minimum area is applicable to a test having up to a 5-yr full-power heating period. The minimum test size would be larger for a longer-term thermal test.

1.9.8.3 Single-Drift Thermal Test

In this section we continue to address the ability of thermal tests to differentiate between two of the three major T-H regimes described in Sec. 1.9.8.2, namely unthrottled, nonbuoyant advective rock dryout and unthrottled, buoyant advective rock dryout. For the single-drift test, we considered k_b = 280 millidarcy, which results in T-H behavior that is characteristic of the unthrottled nonbuoyant regime, and k_b = 84 darcy, which results in T-H behavior that is characteristic of the unthrottled buoyant regime. Our goal is to identify the thermal test size and duration that are sufficient to facilitate the determination of the dominant T-H regime(s) in a timely fashion.

The single-drift thermal test is analyzed using the *X-Z* model, which explicitly represents the details of the drift heaters and heater drifts in the vertical plane transverse to the drift axes (Fig. 1.9-16). The *X-Z* model assumes an infinitely long row of drift heaters. If the heated length is long enough, this assumption can be reasonable. In an earlier study of multi-drift heater tests [Buscheck et al., 1993a; and Buscheck et al., 1993b], comparisons between the *X-Z* and *R-Z* models showed outstanding agreement in rock temperature at the center of the three-drift, 1475-m^2 thermal test for the first 4 yr of full-power heating. The dryout behaviors at the center of the test predicted by the two models also agreed reasonably well after the dryout zones coalesced (t > 2 yr). The heated length of the three-drift test was 38.4 m. It is therefore reasonable to assume that if the single-drift thermal test has a heated length of about 40 m, then T-H behavior at the center of the test should be that of an infinitely long heater test.

We analyzed a range of lineal heat loads and found that a lineal heat load of at least 2.1 kW/m was needed to create a vertical dryout zone thickness of 20 m within 4 yr (Figs. 1.9-17f and 1.9-18b). The substantial lateral heat loss in a single-drift test necessitates a very high centerline temperature T_c to achieve a significant vertical dryout zone thickness. As in the plate heater test, the 280-millidarcy case results in vertically symmetrical vapor flow, while the 84-darcy case results in strong vertical asymmetry (Fig. 1.9-16). The difference in upper boiling front heights (in the buoyant versus nonbuoyant case) amounts to 2 m at t = 1 yr, 4 m at t = 2 yr, and 8 m at t = 4 yr (Fig. 1.9-17a–c). For the 84-darcy case, the vertical asymmetry is already evident at t = 2 yr; the leading edge of the upper boiling zone is 15 m above the heater horizon, while the leading edge of the lower boiling zone is only 5.5 m below the heater horizon. Within the first 2 yr of full-power heating, the 2.1-kW/m, single-drift thermal test can therefore clearly discriminate between the buoyant and nonbuoyant unthrottled regimes.

For the 280-millidarcy case, the zone of condensate buildup is relatively narrow (Fig. 14.9-17d–f). The line-head load geometry results in radial heat flow and a cylindrical dryout zone that is surrounded by a well-developed zone of condensate buildup (Fig. 1.9-16a–b). Because the ECM does not account for nonequilibrium fracture flow, it probably underrepresents condensate shedding around the dryout zone and overrepresents condensate buildup. Therefore, the single-drift thermal test may not be able to create a significant refluxing zone above the heaters. The absence of any refluxing zone would seriously degrade the ability of a thermal test to provide for observations of potentially critical intercoupling between T-H and geochemical processes.

1.9.8.3.1 Minimizing the Effect of Lateral Heat Loss

Because of the strong lateral heat loss associated with the single-drift heater test, achieving a given dryout zone thickness comes at the price of high temperatures (Fig. 1.9-18c). To achieve a dryout zone thickness of 20 m, it is necessary to drive T_c to 315°C. One can limit the temperature required to achieve a given dryout zone thickness within a given time if the heated area is large enough.

To minimize the temperature rise associated with a given dryout zone thickness, we considered the single-drift, winged heater configuration. In this configuration, the heater drift is flanked by two horizontal-borehole-emplaced arrays of closely spaced wing heaters. Because of the close heater spacing, the wing heater array is assumed to generate a planar heat load. We considered several wing heater configurations:

1. Wing heater arrays generating an APD of 105 W/m^2 averaged over the interval $4 < |x| < 9$ m from the drift centerline.

2. Wing heater arrays generating an APD of 105 W/m^2 averaged over the interval $4 < |x| < 14$ m.

3. Wing heater arrays generating an APD of 105 W/m^2 averaged over the interval $4 < |x| < 9$ m and 157.5 W/m^2 over the interval $9 < |x| < 14$ m. (This is the reference single-drift, winged thermal test case.)

For all three cases, the lineal heat load generated by the drift heaters is 0.8 kW/m along the drift axis, corresponding to an areal power density (APD) of 100 W/m^2 averaged over the interval ($-4 < x < 4$ m) separating the two wing heater arrays.

The second configuration did a better job of minimizing the centerline temperature T_c associated with a given dryout zone thickness than the first configuration. The third configuration did a still better job, and it also achieved a given dryout zone thickness sooner than the other configurations. Increasing the APD by 50% for the outer half of the wing heater array substantially reduces lateral heat loss. This configuration functions like a test with a wider wing-heater span. For the reference wing-heater case, a dryout zone thickness of 20 m is achieved (Fig. 1.9-18c) with $T_c = 239°C$, whereas $T_c = 315°C$ is required when no wing heaters are used.

1.9.8.4 Single-Drift, Winged Thermal Test

In this section, we analyze the reference single-drift, winged heater test configuration, which was established on the basis of the analysis described in Sec. 1.9.8.3.1. The reference case has an APD of 122 W/m^2 averaged over the heated area. In this section, we address the ability of the thermal tests to differentiate between the three major thermal-hydrological (T-H) regimes described in Sec. 1.9.8.2. To address all three regimes, we considered k_b = 1, 10, and 280 millidarcy, and 84 darcy. For most of the calculations we assumed the value $\tau_{eff} = 0.2$ for tortuosity factor, which corresponds to the case of nominal vapor diffusion (in which vapor diffusion is not enhanced). For k_b = 280 millidarcy, we also considered the case of "enhanced" vapor diffusion ($\tau_{eff} = 20$) in which the rate of vapor diffusion is 100 times greater than in the nominal case.

Figure 1.9-19 shows the dimensionless liquid saturation distributions for the 280-millidarcy case during a 4-yr full-power heating period. The dryout zones created by the drift heaters and wing heater arrays are just beginning to coalesce at $t = 0.5$ yr; at $t = 1$ yr, coalescence is fairly complete; and at $t = 2$ yr, a well-defined tabular dryout zone, surrounded by a tabular zone of condensate buildup, has developed. Because the 280-millidarcy case pertains to the unthrottled nonbuoyant regime, vapor flow is vertically symmetrical about the heater horizon. The effect of the symmetrical vapor flow is partially offset by condensate shedding, which results in a larger condensate volume below the heater horizon (Fig. 1.9-19c,d). The ECM probably underrepresents how nonequilibrium fracture flow may result in significant condensate shedding during the thermal tests.

Figure 1.9-20 shows the vertical temperature profile along the centerline of the single-drift, winged thermal test at $t = 2$ yr. The vertical temperature profile is vertically symmetrical except inside the heater drift. This asymmetry results from the vertically asymmetrical heating geometry inside the drift: the heater sits directly on the floor of the drift, and the upper wall of the drift is 2.9 m above the top of the drift heaters. The temperature gradient above the heater arises from thermal radiation from the drift heaters to the drift wall surfaces, whereas the temperature gradient below the heater arises from heat conduction in the rock.

All of the calculations in this report were conducted with the RIB version 3 data for thermal conductivity K_{th} [DOE, 1990]. Most of the recent calculations [Buscheck and Nitao, 1994a; Buscheck and Nitao, 1994b] of decay-heat-driven T-H behavior at Yucca Mountain use the RIB version 4 K_{th} data. We repeated the calculation of the single-drift, winged heater test with RIB version 4 K_{th} data and found very small differences in T-H behavior between these two cases. Because the dry value for K_{th} for the TSw2 is somewhat lower in RIB version 3 (1.88 W/m°C) than in RIB version 4 (2.1 W/m°C), temperatures on the drift heater and upper drift wall are about 10°C higher in the RIB version 3 case. Therefore, had we conducted the calculations in this report with the more recent RIB version 4 K_{th}, it would have made little difference, except that slightly lower maximum temperatures (near the heaters) would have been predicted.

Figure 1.9-21 shows the horizontal temperature and liquid saturation profiles at the elevation of the upper drift wall (2.9 m above the top of the drift heaters) during a 4-yr full-power heating period. At t = 1 yr, the temperature along most of heated horizon is at the nominal boiling point (96°C); temperatures are above boiling only in the immediate vicinity of the heater drift. The near-boiling temperatures and liquid saturation buildup (Fig. 1.9-21b) at t = 1 yr are indicative of refluxing conditions. Notice the two regions of pronounced condensate buildup (the outer edge of the heater drift and the outer edge of the wing heater array), which are indicative of regions of significant condensate flow. At t = 2 yr, the existence of a coalesced tabular dryout zone is evidenced by the above-boiling temperatures and the large reduction liquid saturation profile along the entire heated horizon. The region of nearly saturated conditions at the outer edge of the wing heater array indicates a zone of substantial condensate shedding. A close inspection of the corresponding temperatures confirms this observation. During a 4-yr full-power heating period, the outer condensate shedding zone is gradually displaced laterally away from the heaters as it grows in width; the width of the shedding zone is about 4 m at t = 2 yr, and it grows to about 10 m at t = 4 yr. This gradual movement of the condensate shedding zone results in regions of rock being exposed to condensate shedding for considerable periods (2 to 3 yr) during the 4-yr full-power heating period. For a 2-yr full-power heating period, regions of rock would be exposed to condensate shedding for up to 1 yr. Prolonged periods of condensate shedding in fractures will provide an outstanding opportunity to observe potentially important intercoupling between T-H and geochemical processes.

To address the ability of the single-drift, winged heater test to discriminate between the throttled and unthrottled nonbuoyant T-H regimes, we considered k_b = 1, 10, and 280 millidarcy. Figure 1.9-22 shows the vertical profiles of temperature T, liquid saturation S_L, and gas-phase pressure P_g along the centerline of the reference single-drift, winged heater test at t = 2 yr for these cases. The 280-millidarcy case (Fig. 1.9-22a) is associated with a distinct flattening of the temperature profile at 96°C, both above and below the heater horizon. The flattened temperature zones correspond to the refluxing (i.e., heat pipe) zones. Such zones do not develop in the 1-millidarcy case; instead, temperatures increase sharply with decreasing distance to the heater horizon. In the 10-millidarcy case, the flattened temperature zones develop in a modified fashion, with temperatures increasing modestly with decreasing distance to the heater horizon. On the basis of this analysis, it appears that the single-drift, winged thermal test will allow observations that will help determine the significance of heat-pipes within the first 1 to 2 yr of full-power heating (item 1 in Table 1.9-1).

The differences in temperature profiles among these three cases are related to their different gas-pressure profiles (Fig. 1.9-22c); for the 280-millidarcy case, P_g rises only 0.05 atm above ambient, whereas P_g rises 3.5 atm above ambient in the 1-millidarcy case. The much higher P_g substantially increases the saturation temperature T_{sat} (i.e., the actual boiling temperature). This increase in T_{sat} throttles the rate of rock dryout in the 1-millidarcy case, thereby decreasing the spatial extent of the dryout zone (Fig. 1.9-22b). Because the rates of vaporization and return condensate flow are substantially reduced, the large increase in P_g also shuts down (or at least reduces) the heat-pipe effect. In the 10-millidarcy case, P_g rises 0.8 atm above ambient, resulting in a modest increase in T_{sat}. Rock dryout in this case is therefore only slightly throttled, so that its liquid saturation profile differs only slightly from that of the 280-millidarcy case. Therefore, for k_b = 10 millidarcy, T-H behavior during the thermal test is characteristic of the unthrottled nonbuoyant regime. In analyses of repository conditions [Buscheck and Nitao, 1993a; Buscheck and Nitao, 1993b], k_b = 10 millidarcy results in T-H

behavior that falls in the unthrottled nonbuoyant regime for high AMLs, while for low AMLs, T-H behavior is marginally throttled.

On the basis of this analysis, it appears that the single-drift, winged thermal test can clearly discriminate between the throttled and unthrottled nonbuoyant T-H regimes within the first 1 to 2 yr of full-power heating (item 2 in Table 1.9-1). However, one must note the importance of isolating the heater drift from direct pneumatic interference with the rest of the tunnel system in the ESF. If the heater drift were not sufficiently isolated from the tunnel system, the buildup in gas-phase pressure in the heater drift (and the resultant throttled dryout behavior) might be compromised. It is therefore important that measures be taken to pneumatically isolate the heater drift from the rest of the ESF tunnel system. Because of safety concerns, it may not be possible to allow P_g to build up in the heater drift more than a few tenths of an atmosphere. It may therefore be necessary to bleed-off some of the P_g buildup and monitor the flux of water vapor leaving the heater drift through such a pressure relief system. The vapor flux through this system would be indicative of the degree of throttling of advective dryout that would have occurred had the P_g buildup not been limited by bleeding off the excess steam.

To address the ability of the single-drift, winged heater test to discriminate between the buoyant and nonbuoyant unthrottled T-H regimes, we considered k_b = 280 millidarcy and 84 darcy. Figure 1.9-23 gives the vertical profiles of temperature T, liquid saturation S_L, and gas-phase pressure P_g along the centerline of the reference single-drift, winged heater test at t = 2 yr for these cases. The 280-millidarcy case results in vertically symmetrical vapor flow, while the 84-darcy case results in strong vertical asymmetry (Fig. 1.9-23b). At t = 2 yr, the upper boiling front in the buoyant case is 7 m higher than in the nonbuoyant case (Fig. 1.9-23a). The vertical asymmetry is quite evident in the 84-darcy case; the upper boiling front is 17 m above the heater horizon, whereas the lower boiling front is only 5.5 m below the heater horizon. Within the first 1 to 2 yr of full-power heating (items 3 and 4 in Table 1.9-1), the single-drift, winged thermal test can therefore clearly discriminate between the buoyant and nonbuoyant unthrottled regimes.

The degree of vertical asymmetry in the temperature profile will be a strong indication as to whether buoyant gas-phase convection dominates overall heat flow in the test region. Because the degree of vertical asymmetry will be evident within the first 1 to 2 yr, the single-drift, winged thermal test will be indicative of the relative importance of buoyant gas-phase heat convection (item 5 in Table 1.9-1). As is discussed in Sec. 1.9.8.4.1, the temperature history in the heater drift (Fig. 1.9-24), particularly during the cooldown period, will also be diagnostic of whether buoyant gas-phase convection dominates overall heat flow in the test region.

The cause of the nonbuoyant versus buoyant vapor flow is clearly evident in the P_g profiles (Fig. 1.9-23c). For the 280-millidarcy case, the P_g gradients are driven by boiling conditions. In the superheated zone straddling the heater horizon, there is virtually no more water to be vaporized and advected away; so there is a minimal P_g gradient in this zone. The boiling zones are evidenced by the relatively steep portions of the P_g profile. The P_g gradients are steepest in the boiling zones, because that is where virtually all of the vaporization and vapor advection take place. Note that vapor diffusion also contributes to vapor transport, but it is not generally significant unless advective dryout is throttled. In the 84-darcy case, the P_g gradients are dominated by the gas-phase density distribution and are virtually unaffected by the existence of boiling conditions; consequently, there is no buildup in P_g near the heater horizon (Fig. 1.9-23c).

1.9.8.4.1 Evaluating Thermal Test Duration

The objective of this section is to determine the minimum thermal test duration that facilitates sufficient determination of the dominant T-H regime(s) and that does not preclude the occurrence of potentially critical intercoupling between T-H processes and geomechanical and geochemical processes. For the reference single-drift, winged thermal test (APD = 122 W/m^2), full-power heating periods of 1, 2, and 4 yr were considered. The full-power heating period is followed by a 1-yr linear-rampdown to zero power. To address all three major T-H regimes, we considered k_b = 1, 10, and 280 millidarcy, and 84 darcy. For most of the cases we assumed that vapor diffusion is not enhanced (τ_{eff} = 0.2). For k_b = 280 millidarcy, we also considered the case of enhanced vapor diffusion (τ_{eff} = 20).

Figure 1.9-24 shows the temperature on the drift heater and the upper drift wall for all of the cases considered in this section. With the exception of the 84-darcy case, the drift heater temperatures are virtually the same for all of these cases. For the 84-darcy case, buoyant gas-phase convection increases the overall heat loss from the test region, which reduces both the peak temperature and the duration of the boiling period. For all but the 84-darcy case, heat flow is dominated by heat conduction. Even when enhanced by two orders of magnitude, the potential effect of vapor diffusion on increasing overall heat loss from the repository is not apparent in any of these tests. Slightly higher peak temperatures occur on the upper drift wall for the 1- and 10-millidarcy cases during the 1- and 2-yr full-power heating periods; however, the duration of the boiling period is virtually the same for all but the 84-darcy case. In general, the temperature history at a particular location is far less diagnostic than the vertical temperature profile in determining the major T-H regime(s).

While the temperature history in the heater drift is of marginal use, the gas-phase pressure P_g and relative humidity *RH* in the drift during heatup and cooldown (Fig. 1.9-25) can provide information that is very diagnostic of the dominant T-H regime(s). If the heater drift can be adequately isolated from the rest of the ESF tunnel system, a 1-yr full-power heating period is long enough for P_g in the drift to be clearly indicative of whether the throttled nonbuoyant regime dominates T-H behavior. The situation improves for the 2- and 4-yr full-power heating periods. For a heterogeneous k_b distribution, a longer test will provide more information about k_b at a larger spatial scale.

If full-power heating lasts for at least 2 yr, *RH* in the drift (Fig. 1.9-25c,e) is also extremely diagnostic of the major T-H regimes and is also extremely diagnostic of whether vapor diffusion is substantially enhanced. Although Fig. 1.9-25 plots *RH* on the drift heater, any *RH* measurement in the drift can serve the same general purpose. Three factors can govern the shape of the *RH* curves:

1. The spatial extent of rock dryout.
2. Throttled vapor advection causing a substantial increase in P_v that suppresses *RH* reduction.
3. How fast the rock surrounding the drift is rewetted to ambient *RH* conditions.

Three processes cause rock dryout: (i) boiling, (ii) buoyant gas-phase convection, and (iii) vapor diffusion. The second and third processes do not require above-boiling conditions. During heatup it takes about 6 months for the rock to reach boiling conditions, so the 1-yr full-power test spends much of its heatup time below the boiling point. Therefore, dryout processes that do not require boiling conditions will play a larger role in determining the spatial extent of rock dryout during this test than during the 2- and 4-yr full-power tests. Differences in the *RH* behavior in the drift for the 1-yr full-power test are more substantially influenced by the spatial extent of dryout than by how fast the rock around the drift rewets to ambient conditions. The 2- and 4-yr full-power tests spend much more of their heatup periods above the boiling point; consequently, boiling conditions dominate the spatial extent of rock dryout. For the 2- and 4-yr full-power tests, differences in *RH* behavior in the drift reflect differences in how fast the rock rewets to humid conditions (rather than how much rock dryout occurred).

Four major processes govern how fast the dryout zone rewets to ambient (humid) conditions: (i) net infiltration of meteoric water, (ii) capillary-imbibition-driven rewetting of the rock matrix, (iii) vapor diffusion of humid air into the dryout zone, and (iv) buoyant gas-phase convection-driven advection of humid air into the dryout zone. Figures 1.9-25b,c clearly show how the second, third, and fourth rewetting processes influence *RH* behavior in the drift. For the 1-millidarcy case, the large increase in vapor pressure P_v throttles advective rock dryout and suppresses *RH* reduction in the drift during heatup, particularly for the 1- and 2-yr full-power tests. Moreover, throttled advective rock dryout results in a smaller dryout volume that takes less time to rewet to ambient (humid) conditions than in the unthrottled nonbuoyant cases with nominal vapor diffusion. Even though P_g rises noticeably in the 10-millidarcy case, it is not enough to throttle advective rock dryout and to suppress *RH* reduction; consequently, the 10- and 280-millidarcy cases with nominal vapor diffusion have nearly identical *RH* behavior.

The effect of substantial buoyant gas-phase convection on advecting humid air into the dryout zone becomes evident by $t = 6$ yr for the 4-yr full-power test (Fig. 1.9-25e); however, for the 2-yr full-power

test, this effect does not become evident until after 10 yr (Fig. 1.9-25c). The effect of (enhanced) vapor diffusion of humid air into the dryout zone (for $\tau_{eff} = 20$) becomes quite evident at about $t = 4$ yr for the 4-yr full-power test, whereas it requires 6 yr to become evident in the 2-yr full-power test. The degree of vapor diffusion enhancement can be determined within 4 yr for the 4-yr full-power test, whereas it takes about 6 yr for the 2-yr full-power test (item 6 in Table 1.9-1).

In the 1-yr full-power test, differences in the *RH* history in the drift (Fig. 1.9-25a) are either too minor or too ambiguous to permit any determination about the major T-H regimes or about the degree of vapor diffusion enhancement. Contrary to the relation between rewetting mechanisms and *RH* behavior seen for the 2- and 4-yr full-power tests (Fig. 1.9-25c,e), the 84-darcy and enhanced-vapor-diffusion cases appear to rewet more slowly than the other cases. This arises because the sub-boiling rock dryout mechanisms create a larger dryout zone than in the cases where boiling is the primary cause of rock dryout.

In general, a 1-yr full-power test provides inconclusive and/or misleading information about the dominant T-H regime(s) and the relative contributions of the major rewetting mechanisms addressed in this study. Both the 2-yr and 4-yr full-power tests provide clear and unambiguous information about all three major T-H regimes and all of the rewetting mechanisms addressed in this study; however, the 4-yr full-power test allows for an earlier determination about the degree of vapor diffusion enhancement.

Figures 1.9-26 and 1.9-27 compare temperature, *RH*, and rock dryout behavior for the 1-, 2-, and 4-yr full-power heating tests with drift-scale behavior calculated for an 80-MTU/acre repository with two combinations of drift and WP spacing. Temperature rises during the first 2 yr of the 2- and 4-yr full-power tests are only slightly more accelerated than repository behavior (Fig. 1.9-26a,c). At $t = 4$ yr, the upper drift wall temperature is 252°C in the thermal test, while it is 157°C in the 80-MTU/acre repository with a lineal mass loading LML of 1.25 MTU/m. Moreover, *RH* behavior on the WP in both of the 80-MTU/acre cases is quite similar to that of the 4-yr full-power test. An earlier comparison between thermal test and repository T-H behaviors [Buscheck and Nitao, 1993a; Buscheck and Nitao, 1993b] inappropriately used average repository T-H behavior calculated with a mountain-scale model. This comparison should have been done with a drift-scale model of repository T-H behavior. The use of a mountain-scale model gave rise to the appearance of a larger disparity between the thermal test and repository T-H behaviors than would have been seen had a drift-scale model of the repository been used.

Figure 1.9-27 shows that the dryout and boiling zones during the 4-yr full-power test grow about twice as fast as in the 80-MTU/acre case with LML = 1.25 MTU/m. At $t = 4$ yr, the vertical dryout zone thickness is 21.6 m in the thermal test (Fig. 1.9-27a), whereas it is 12.3 m in the 80-MTU/acre repository. It takes 14 yr for the 80-MTU/acre repository to dry out 22 m vertically. At $t = 4$ yr, the boiling zone has a vertical thickness of 30 m, whereas for the 80-MTU/acre repository it is 15.7 m. In general, the reference single-drift, winged thermal test does not appear to be overly accelerated relative to repository conditions.

In optimizing a thermal test design, it is important to consider the duration of refluxing conditions (Fig. 1.9-28) created by the thermal test. Ideally, refluxing conditions during the test would last long enough for any potentially important intercoupling between T-H behavior and geochemical processes to take place. In Fig. 1.9-28, we assume that refluxing occurs if the temperature is between 95°C and 97°C. If vapor pressure lowering is particularly pronounced, refluxing may occur over a wider temperature range than that. Nonetheless, Fig. 1.9-28 provides a useful means of comparing the ability of the 1-, 2-, and 4-yr full-power tests to provide T-H conditions that may lead to significant coupled T-H-C coupled effects. The 1-yr full-power test (Fig. 1.9-28a) provides a rather limited opportunity (at best) to observe the potential for reflux-driven coupled T-H-C effects. The 2-yr full-power test appears to be a significant improvement over the 1-yr full-power test in this regard, while the 4-yr test provides a fairly extensive zone over which coupled T-H-C effects may develop. The 4-yr full-power test appears to allow determination of the relative importance of reflux-driven geochemical alteration of flow and transport properties within the first 4 yr of the test (item 7 in Table 1.9-1). Note that a heterogeneous k_b distribution may focus these effects into certain regions of the test, so that finding (and sampling)

such locations may pose a significant challenge. Increasing the volume of rock within which coupled T-H-C effects may develop should certainly increase the chances of encountering such areas.

1.9.8.4.2 Evaluating the Effects of Heterogeneity

So far we have analyzed thermal test cases in which the hydrological and thermal property distributions were assumed to be homogeneous and isotropic. We now consider two cases in which the k_b distribution is highly heterogeneous (Fig. 1.9-29). In both cases, the high-k_b zones are assumed to have k_b = 84 darcy. Adjacent to the high-k_b zones are "nominal"-k_b zones in which k_b = 1 millidarcy. Both cases result in similar behavior in the heater drift. Zones of sharply contrasting k_b can dominate condensate drainage during a thermal test (or in the repository). Because the k_b contrast between neighboring zones is large, the P_g differential drives water vapor into the high-k_b zone, where it condenses and drains, causing persistent refluxing and condensate drainage into heater drift at t = 2 yr (Fig. 1.9-29a,b). The resulting heat-pipe effect enables the temperature at the top of the drift to remain at the boiling point (Fig. 1.9-29c,d), causing a depression in the dryout zone (Fig. 1.9-29a,b), Whether rock heterogeneity will dominate vapor and condensate flow will be very evident within the first 1 to 2 yr of the single-drift, winged thermal test (item 8 in Table 1.9-1).

The amount of vapor flow focusing into the high-k_b zone and the resulting duration of refluxing at the heater test horizon depend on three factors. First, k_b in the nominal-k_b zone must be high enough not to significantly throttle the rate of vapor generation due to boiling (or due to evaporation, under sub-boiling conditions). Second, a large contrast in k_b between the high- and nominal-k_b zones results in a difference in gas-phase pressure P_g between these zones that drives vapor flow into the high-k_b zone (Fig. 1.9-29a,b). If enough vapor enters and condenses in the high-k_b zone, the return condensate flux will be large enough to maintain refluxing at the heater test horizon, possibly resulting in water draining into the heater drift. Third, there must be sufficient spacing between the high-k_b zones to drive enough water vapor into these zones to result in the local condensate drainage flux being substantially greater than the mean condensate flux.

The heat-pipe zone "attracts" heat (mainly by conduction) from the neighboring, nominal-k_b rock. In effect, the heat-pipe zone functions as a "cooling fin" that is manifested by an elongated region of liquid saturation buildup (Fig. 1.9-29a,b). The process of gas-phase focusing into the heat-pipe zone develops more quickly than the process of attracting heat (by heat conduction) from the neighboring rock. Focused condensate drainage causes a sharp depression in the temperature field (Fig. 1.9-29c,d) at t = 2 yr. In the case with multiple high-k_b zones (Fig. 1.9-30a), this sharp depression results in near-boiling temperatures (96°C) at the elevation of the upper drift wall at t = 2 yr, while just a few meters away at this horizon temperatures are well above boiling. Within 4 yr (Fig. 1.9-30b), enough heat is being conducted into the central high-k_b zone to overwhelm its heat pipe, causing the top of the heater drift to begin to dry out and drift temperatures to climb well above 96°C. The heat pipe in the high-k_b zone located roughly midspan along the wing heater array has also been overwhelmed by heat conduction, causing the temperature to exceed 150°C. Because of the edge-cooling effect, there is not enough heat conducted into the high-k_b zone at the edge of the heated area to overwhelm its heat pipe; consequently, the temperature continues to be 96°C at the outer edge of the wing heater array (Fig. 1.9-30b).

At t = 6 yr, focused vapor and condensate flow continues to cause refluxing in the high-k_b zones at elevations above the heater horizon. Preferential heat conduction into the high-k_b zone continues to dry it out, and the influence of focused vapor and condensate flow on temperatures (Fig. 1.9-30c) at (or above) the heater horizon is no longer evident, except that the heat-pipe zones at the outer edge of the wing heater array continue to result in near-boiling temperatures at the margins of the heated area. At late time, the primary effect of the heat pipes above the main heater area is to increase the overall heat loss from the thermal test region, which results in lower temperatures than in the homogeneous-k_b cases above the dryout zone; however, the temperature distribution in the vicinity of the heater drift (and for most of the heater horizon) is as it would be if heat conduction dominated heat flow. It is interesting to note that although the k_b (averaged over the heater array) for the highly

heterogeneous-k_b case is only 17 darcy, the convective cooling effect is greater than it is for the 84-darcy case (Fig. 1.9-30c).

The effect of heat being conducted toward the high-k_b zone (from neighboring regions of the superheated rock) and thereby overwhelming the heat pipe in the high-k_b zone was seen in drift-scale and mountain-scale T-H calculations [Buscheck and Nitao, 1993a; Buscheck and Nitao, 1994a]. In a similar calculation for a 155-MTU/acre repository, heat conducted from neighboring regions overwhelmed the heat pipe in the high-k_b zone and began drying out the top of the emplacement drift 8 yr after emplacement of the WPs. In that calculation, the high-k_b zones were spaced every 38.4 m, which is comparable to the scale of the reference single-drift, winged thermal test. The analysis in this section indicates that confirmation of major hypothesis MH-3 (Sec. 1.9.2) and whether heat conduction will eventually overwhelm the effects of heterogeneity-dominated vapor and condensate flow (item 9 in Table 1.9-1) may require a thermal test with a full-power period of 6 yr or more. Short-duration tests may leave the misleading impression that focused liquid flow could persistently overwhelm the heat conduction flow field and thereby result in liquid water persistently draining into emplacement drifts.

1.9.8.4.3 Evaluating Accelerated Heating Rates

To evaluate the feasibility of accelerating the heating schedule of the single-drift, winged thermal test, we considered tests in which the overall APDs (177 and 236 W/m^2) were roughly 50% and 100% greater than in the reference case (APD = 122 W/m^2). We assumed k_b = 280 millidarcy and τ_{eff} = 0.2 (nominal vapor diffusion) for these three APDs and 1- and 2-yr full-power heating periods (Figs. 1.9-31 and 1.9-32). The full-power period is followed by a 1-yr linear-rampdown to zero power.

Figure 1.9-31 shows that the temperature increase in the drift is proportional to APD. The 177-W/m^2 case with a 2-yr full-power heating period causes *RH* behavior in the drift (Fig. 1.9-31d) to be very similar to that of the reference case (APD = 122 W/m^2) with a 4-yr full-power heating period (Fig. 1.9-25e). Temperature behaviors for the reference case (Fig. 1.9-24e,f) and the 177-W/m^2 case (Fig. 1.9-31f) are also quite similar. Moreover, the 177-W/m^2 case dries out nearly as much rock (Fig. 1.9-32c) as the reference case (Fig. 1.9-27a); in both cases, the vertical thickness of the dryout zone exceeds 20 m. In general, the 177-W/m^2 case with a 2-yr full-power heating period appears to have all of the advantageous characteristics of the reference case with a 4-yr full-power heating period, while not requiring greater peak temperatures. The rate of temperature rise will, of course, be greater for the accelerated test. Additional calculations are underway to extend the analysis of the 177-W/m^2 case to include evaluation of enhanced vapor diffusion and rock heterogeneity.

1.9.8.5 Summary of Pre-Test Analysis of ESF Thermal Tests

In situ thermal tests, which are to be conducted in the Exploratory Studies Facility (ESF) at Yucca Mountain, will provide a major portion of the experimental basis supporting the testing of coupled T-H-M-C process models required to assess the total system performance. The ESF thermal tests must provide an understanding of coupled T-H-M-C processes that are relevant to expected repository conditions. Current ESF thermal test planning has identified two tests: (1) the first ESF (drift-scale) thermal test, which will be conducted under an accelerated heatup and cooldown schedule, and (2) a second ESF (multi-drift) thermal test, which will be a larger-scale, longer-duration test, conducted under a less accelerated heatup and cooldown schedule.

With the V-TOUGH code, we modeled and evaluated a range of heater test sizes, heating rates, and heating durations under a range of plausible hydrological conditions to help optimize an *in situ* thermal test design that provides sufficient (and timely) information to determine the following:

1. The dominant mode(s) of heat flow.

2. The major thermal-hydrological (T-H) regime(s) and the thermal-hydrological-geomechanical-geochemical (T-H-M-C) processes that determine the magnitude and direction of vapor and condensate flow.

3. The influence of heterogeneous properties and conditions on the flow of heat, vapor, and condensate.

Perhaps the single most important purpose of the ESF thermal tests is to determine which major decay-heat-driven T-H flow regime(s) will govern the magnitude and direction of vapor flow (and the resulting condensate flow) in the UZ at Yucca Mountain. With respect to advective rock dryout, the three major T-H flow regimes are as follows:

Throttled, nonbuoyant, advective rock dryout: the regime in which k_b is low enough ($k_b < 1$ millidarcy) to significantly throttle the rate of boiling-driven rock dryout. The threshold k_b at which rock dryout is throttled decreases with increasing AML.

Unthrottled, nonbuoyant, advective rock dryout: the regime in which k_b is high enough ($k_b > 1$ millidarcy) not to significantly throttle the rate of boiling-driven rock dryout, but not large enough ($k_b < 5$ darcy) to allow buoyant gas-phase convection to dominate the direction of vapor flow.

Unthrottled, buoyant, advective rock dryout: the regime in which k_b is high enough not to throttle the rate of boiling-driven rock dryout and is also large enough ($k_b > 5$ darcy) to allow buoyant gas-phase convection to dominate the direction of vapor flow.

How these major T-H regimes influence the flow of heat, vapor, and condensate depends in part on whether vapor diffusion is substantially enhanced. Therefore, another major purpose of the thermal tests is to determine the degree of vapor diffusion enhancement.

We evaluated (1) thermal test sizes of 50, 270, 490, 1475, and 5077 m^2; (2) three heating schedules, including 1-, 2-, and 4-yr full-power heating periods; and (3) three heating rates (122, 177, and 236 W/m^2). We then determined a minimum thermal test size, minimum heating duration, and a preferred heating rate based the following criteria: (1) the ability of the test to discriminate between the major T-H regimes, (2) the rock dryout volume, (3) peak rock temperatures, (4) duration of refluxing conditions, (5) ability to observe the influence of heterogeneity, and (6) ability to observe whether heat conduction is able to overwhelm the effects of heterogeneity.

We started with an evaluation of the plate thermal test, which was the basis for recommending a minimum heated area of 1000 to 1500 m^2. This heated area is needed to diagnose whether buoyant or nonbuoyant behavior predominates and to minimize the peak temperatures associated with a given dryout zone thickness.

We then evaluated the single-drift thermal test (without wing heaters) and found that the substantial lateral heat flow from this test necessitated very high peak temperatures in order to create a thick enough dryout zone; moreover, we found that this test does not promote enough condensate perching to generate significant refluxing conditions. We then evaluated a number of single-drift, winged thermal tests and determined that an optimal configuration consists of the following: a row of drift heaters that generates 0.8 W/m along the drift access, flanked by wing heater arrays generating an APD of 105 W/m^2 averaged over the interval $4 < |x| < 9$ m and 157.5 W/m^2 over the interval $9 < |x| < 14$ m. This configuration (called the reference case) generates an APD of 122 W/m^2 averaged over the heated area.

We then evaluated the reference single-drift, winged thermal test and found that a 2-yr full-power heating period is required to provide clear and unambiguous information about all three major T-H regimes and about whether vapor diffusion is substantially enhanced. We also found that a 4-yr full-power test provides an earlier determination than the 2-yr full-power test of the degree of vapor diffusion enhancement and of whether buoyant gas-phase convection of humid air significantly increases the rate at which the dryout zone rewets to humid conditions.

For determining the dominant T-H regime(s) and dominant heat flow mode(s), we found that the most diagnostic measurements are the following:

1. Vertical temperature distributions.

2. Vertical gas-phase pressure distributions.

3. Gas-phase pressure history in the drift during heatup.

4. *RH* history in the drift during heatup.

For determining the degree of vapor diffusion enhancement, we found that the most diagnostic measurements is

1. *RH* history in the drift during cooldown.

We then evaluated the ability of the tests to allow observations about the influence of heterogeneity on the flow of heat, vapor, and condensate. We found that the influence of heterogeneity will be observable within the first 1 to 2 yr of the test (after a sufficiently large boiling zone has developed). The effects of heterogeneity are quite apparent in the temperature distribution. We found that a full-power heating period of at least 6 yr might be required to determine whether heat conduction is able to overwhelm the effects of heterogeneity on the temperature and liquid saturation distributions near the heater horizon.

For determining the influence of heterogeneity on the flow of heat, vapor, and condensate, we found the most diagnostic measurements are the following:

1. Horizontal temperature distributions.

2. Horizontal liquid saturation (or *RH*) distributions.

3. *RH* history in the drift during heatup.

We also evaluated whether the tests provide for refluxing conditions of sufficient duration and over a large enough volume to allow for observations of potentially important coupled T-H-C processes. We found that the 4-yr full-power test was far more likely to promote conditions necessary to make these observations than the 1- or 2-yr full-power tests.

We then evaluated heating rate and made a preliminary determination that the 177-m^2 2-yr full-power test has virtually all of the advantages of the 122-m^2 4-yr full-power test. We plan to conduct additional analyses of the 177-m^2 2-yr full-power test to determine whether we can recommend it for the first ESF thermal test.

Table 1.9-1. Time requirements for diagnosing various T-H-M-C effects.

T-H regimes and processes, T-H-C processes, and the influence of rock heterogeneity	Minimum required full-power heating period	Time at which diagnosis is possible	Supporting figure numbers
1. Significant heat-pipe zones develop	1–2 yr	1–2 yr	Figs. 3, 4, 12, 14, 17, 19, 20, 27
2. Throttled advective rock dryout	1–2 yr	1–2 yr	Figs. 19, 22
3. Unthrottled nonbuoyant rock dryout	1–2 yr	1–2 yr	Figs. 3, 4, 12, 19, 20, 22
4. Buoyant gas-phase convection dominates vapor flow	1–2 yr	1–2 yr	Figs. 3, 4, 12, 20, 22
5. Buoyant gas-phase convection dominates heat flow	1–2 yr	1–2 yr	Figs. 3, 4, 12, 20, 21
6. Degree of vapor diffusion enhancement	2–4 yr	4–6 yr	Fig. 22
7. Reflux-driven geochemical alteration of flow and transport properties	4 yr	4 yr	Fig. 25
8. Rock heterogeneity dominates vapor and condensate flow	1–2 yr	1–2 yr	Fig. 26
9. Heat conduction overwhelms effects of heterogeneity-dominated vapor and condensate flow*	6+ yr	6+ yr	Fig. 27

*Is only applicable if item 8 was found to be important.

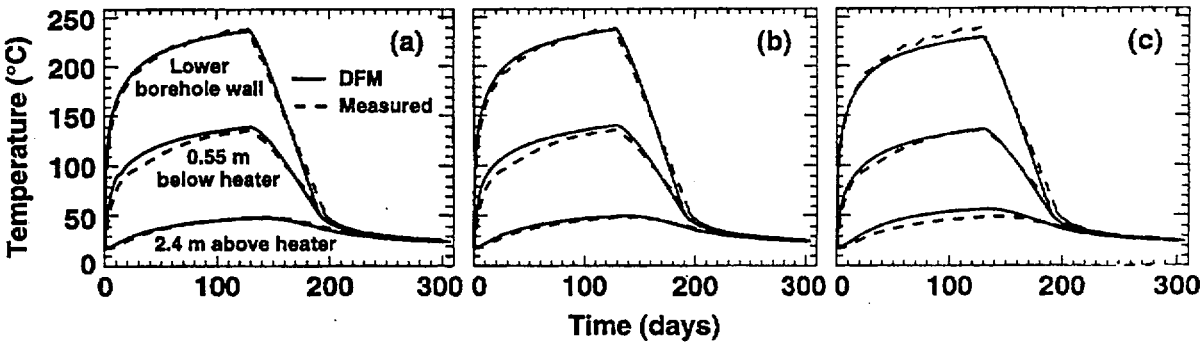

Figure 1.9-1. Temperature histories at three points on the heater midplane for fracture apertures of (a) 100 μm, (b) 524 μm, and (c) 1048 μm.

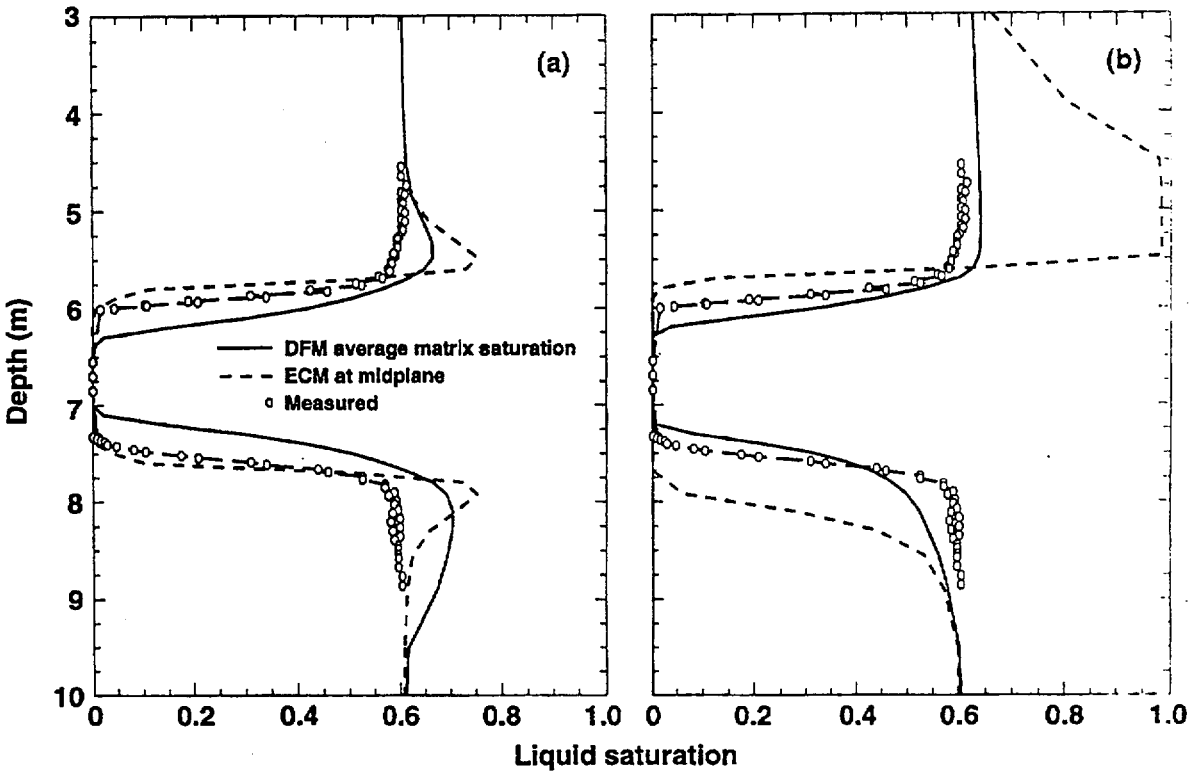

Figure 1.9-2. Vertical profile of ECM bulk liquid saturation and DFM matrix-averaged liquid saturation in heater midplane at 130 days for fracture apertures of (a) 100 μm and (b) 1048 μm.

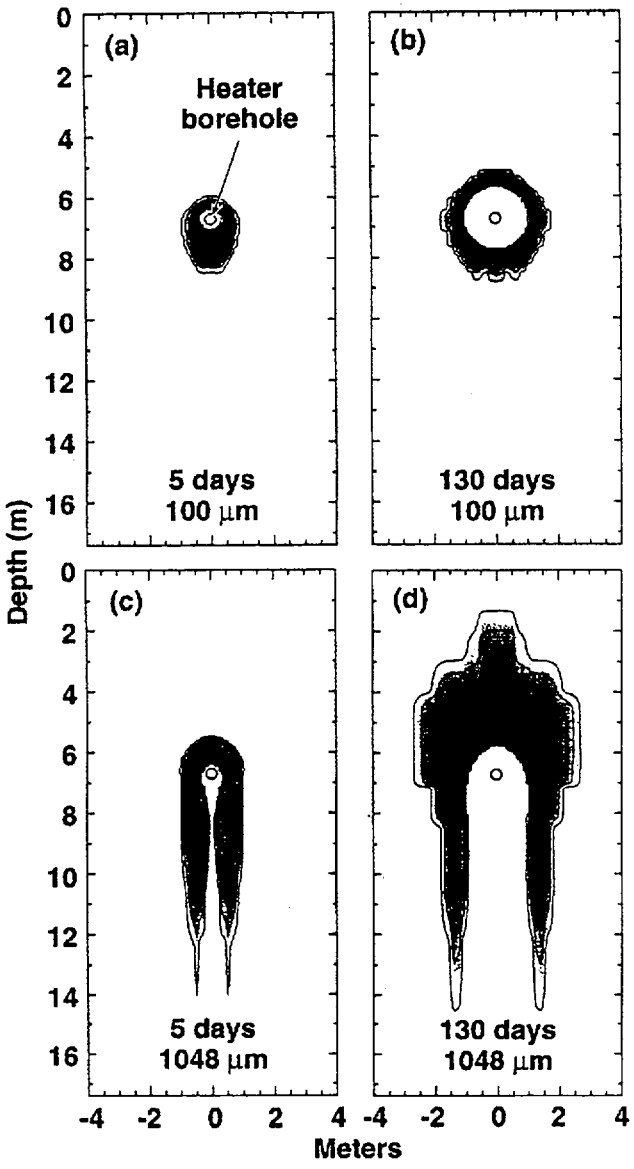

Figure 1.9-3. DFM calculated liquid saturation in fracture at (a) 5 days and (b) 130 days for 100 μm fracture aperture, and (c) 5 days and (d) 130 days for 1048 μm fracture aperture.

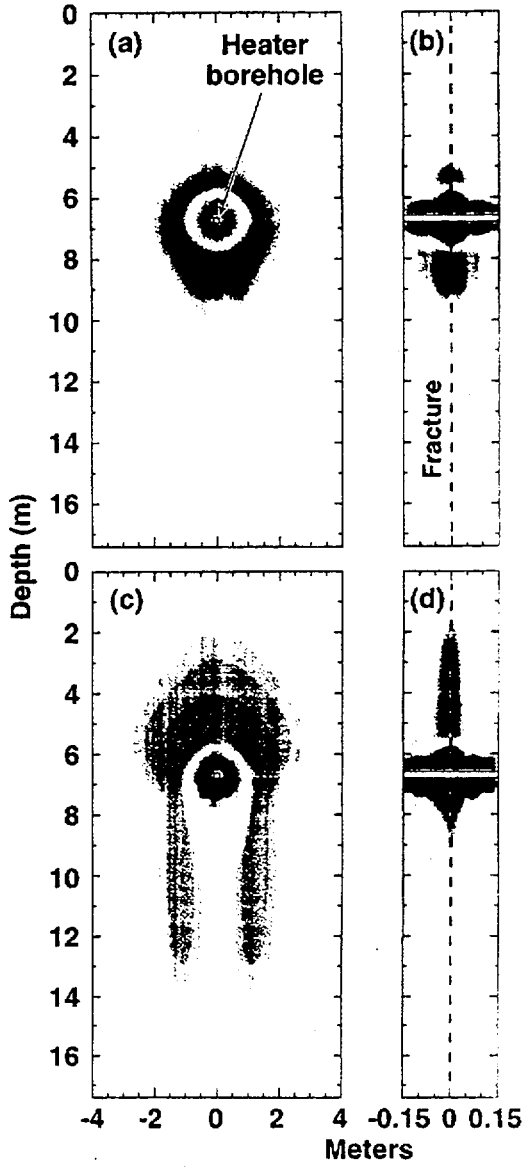

Figure 1.9-4. At 130 days the 100-μm DFM (a) matrix-averaged dimensionless liquid saturation in the heater midplane, and (b) matrix dimensionless saturation in the vertical plane of the heater, and (c) and (d) is for the 1048-μm DFM. See text for explanation of shading.

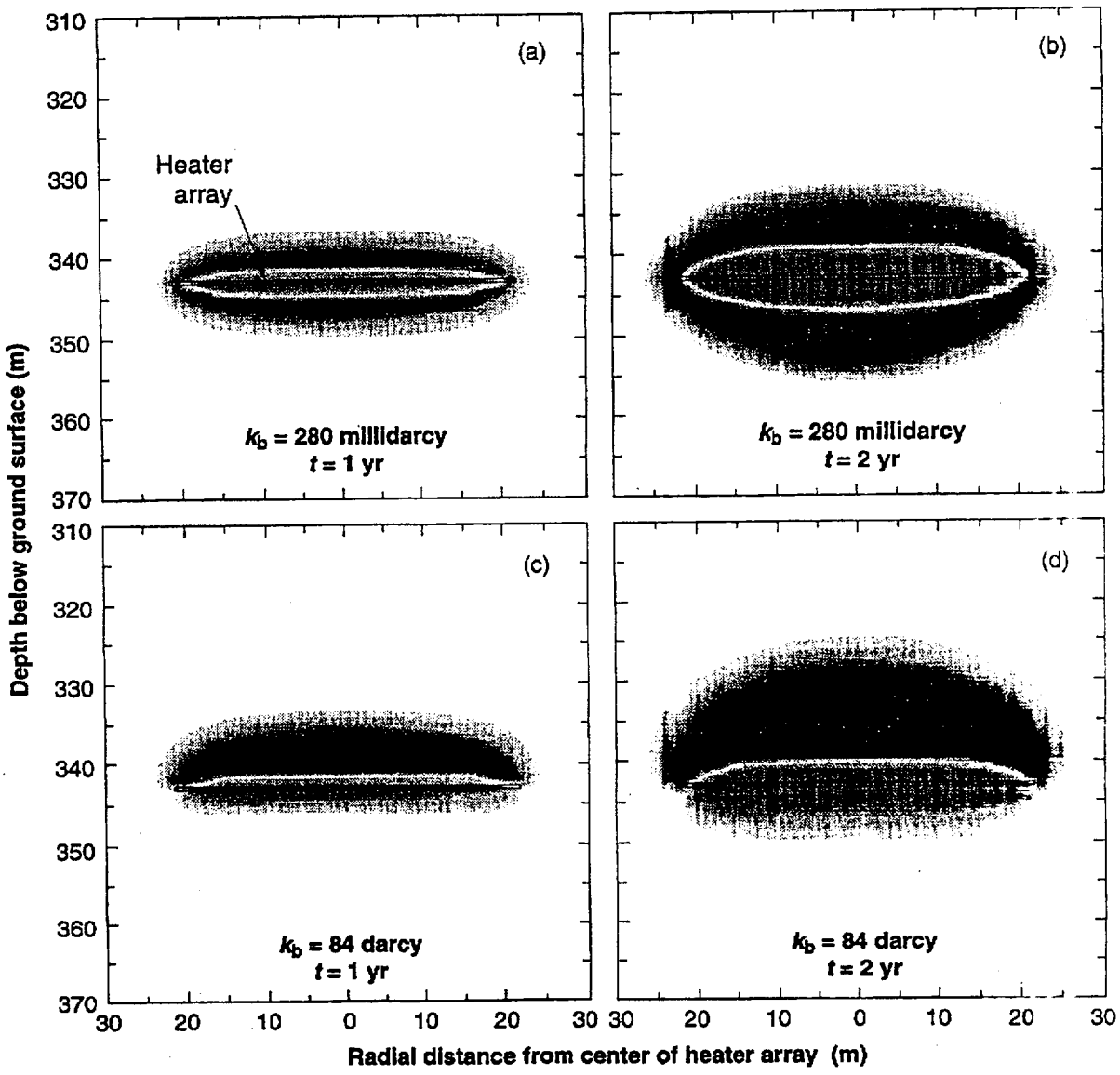

Figure 1.9-5. Dimensionless liquid saturation distribution for an array of horizontal-borehole-emplaced heaters heating a disk-shaped area with a radius of 21.7 m and APD = 78 W/m^2 averaged over the 1475-m^2 heated area. Vapor diffusion tortuosity factor τ_{eff} = 0.2. The medium-shaded area surrounding the heater array corresponds to regions that are drier than ambient liquid saturation (dryout zone). The dark-shaded areas correspond to regions that are wetter than ambient liquid saturation (condensation zone). The light shading surrounding the dark-shaded area corresponds to a small rise in liquid saturation (outer edges of the condensation zone). No shading indicates no change in liquid saturation.

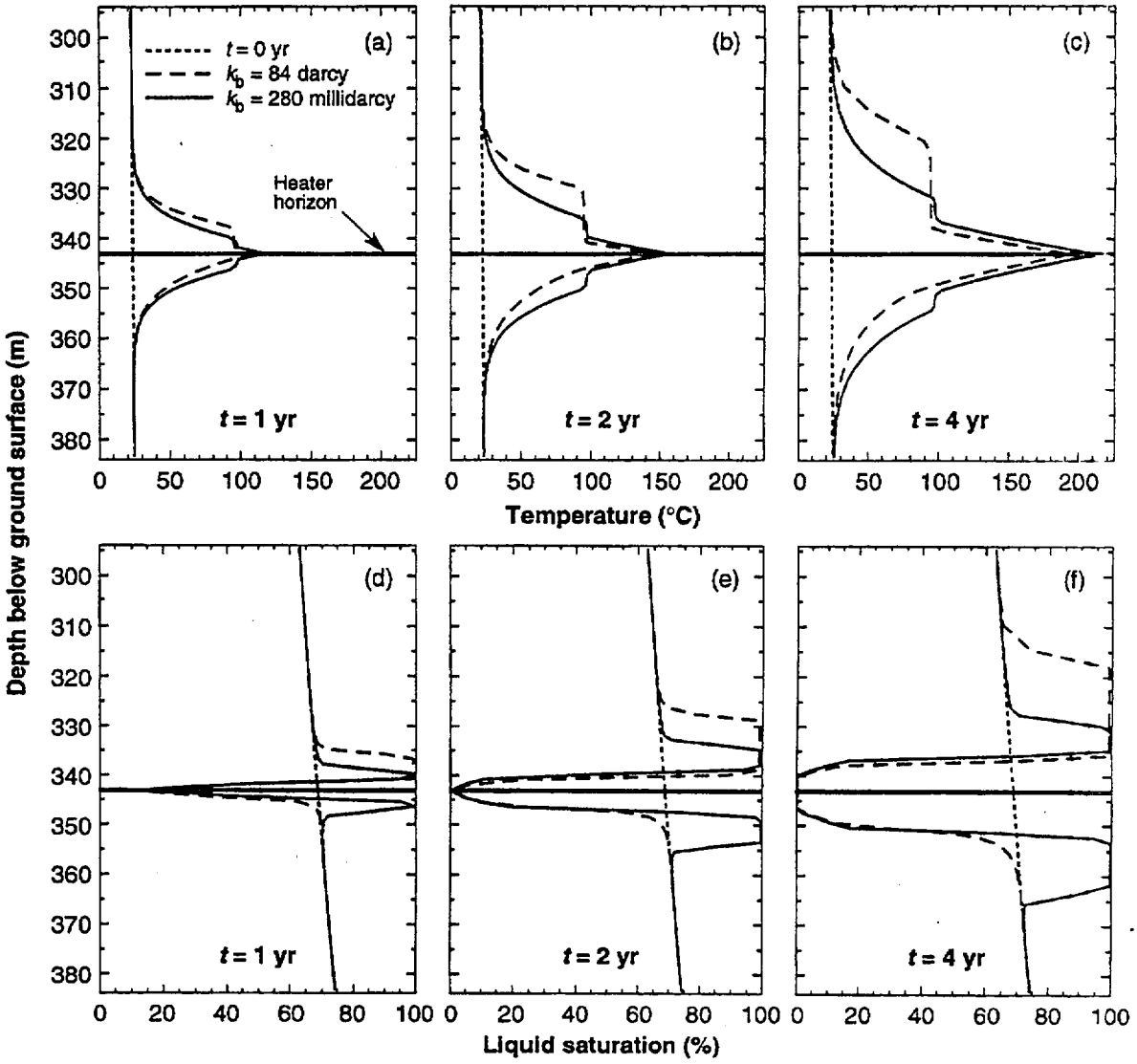

Figure 1.9-6. (a, b, c) Vertical temperature profile and (d, e, f) liquid saturation profile along the centerline of an array of horizontal-borehole-emplaced heaters heating a disk-shaped area with a radius of 21.7 m and APD = 78 W/m^2 averaged over the 1475-m^2 heated area. Vapor diffusion tortuosity factor τ_{eff} = 0.2.

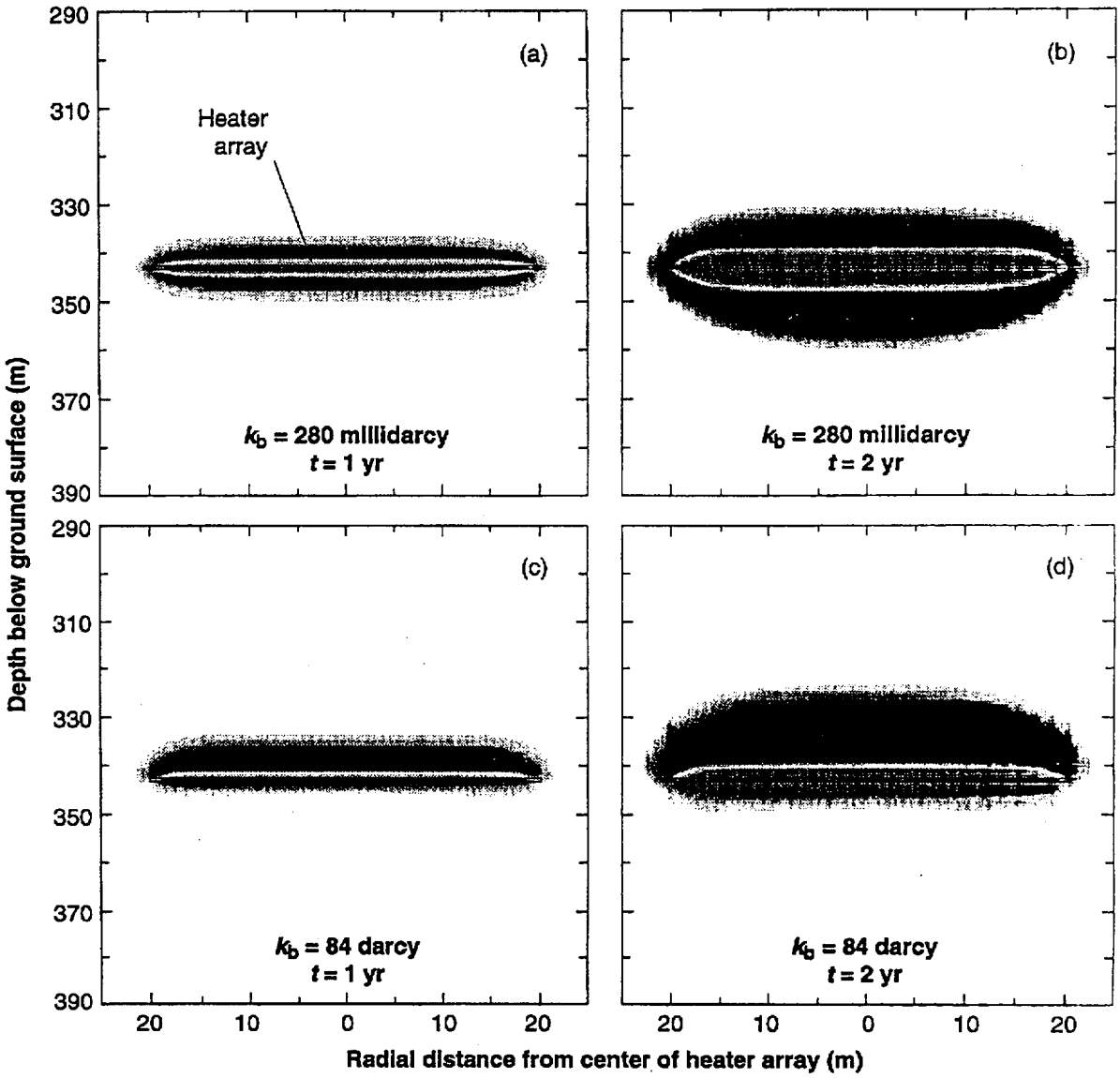

Figure 1.9-7. Dimensionless liquid saturation distribution for an array of horizontal-borehole-emplaced heaters heating a disk-shaped area with a radius of 40.2 m and APD = 78 W/m^2 averaged over the 5077-m^2 heated area. Vapor diffusion tortuosity factor τ_{eff} = 0.2. The medium-shaded area surrounding the heater array corresponds to regions that are drier than ambient liquid saturation (dryout zone). The dark-shaded areas correspond to regions that are wetter than ambient liquid saturation (condensation zone). The light shading surrounding the dark-shaded area corresponds to a small rise in liquid saturation (outer edges of the condensation zone). No shading indicates no change in liquid saturation.

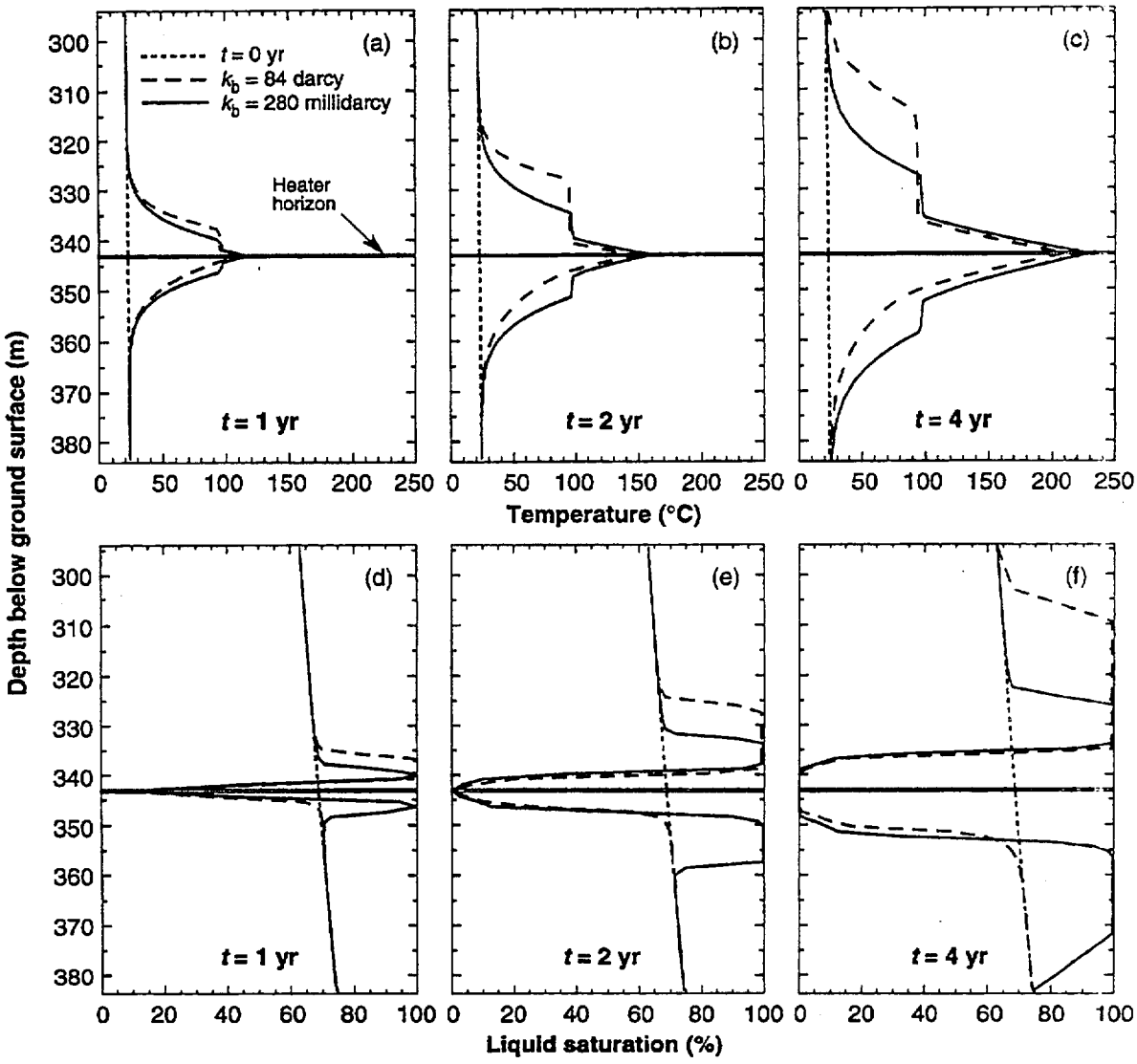

Figure 1.9-8. (a, b, c) Vertical temperature profile and (d, e, f) liquid saturation profile along the centerline of an array of horizontal-borehole-emplaced heaters heating a disk-shaped area with a radius of 40.2 m and APD = 78 W/m^2 averaged over the 5077-m^2 heated area. Vapor diffusion tortuosity factor $\tau_{eff} = 0.2$.

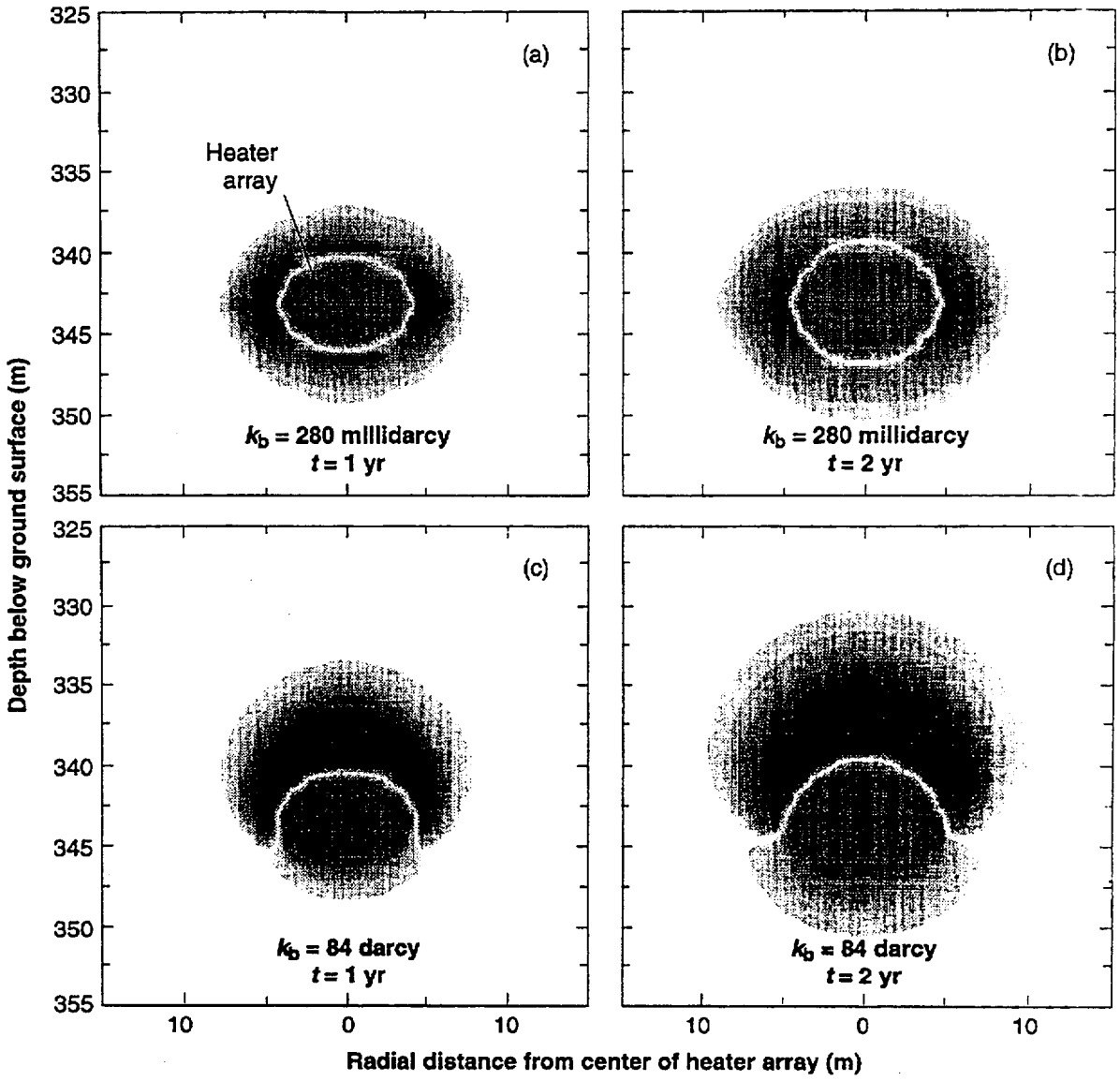

Figure 1.9-9. Dimensionless liquid saturation distribution for an array of horizontal-borehole-emplaced heaters heating a disk-shaped area with a radius of 4.0 m and APD = 247 W/m^2 averaged over the 50-m^2 heated area. Vapor diffusion tortuosity factor τ_{eff} = 0.2. The medium-shaded area surrounding the heater array corresponds to regions that are drier than ambient liquid saturation (dryout zone). The dark-shaded areas correspond to regions that are wetter than ambient liquid saturation (condensation zone). The light shading surrounding the dark-shaded area corresponds to a small rise in liquid saturation (outer edges of the condensation zone). No shading indicates no change in liquid saturation.

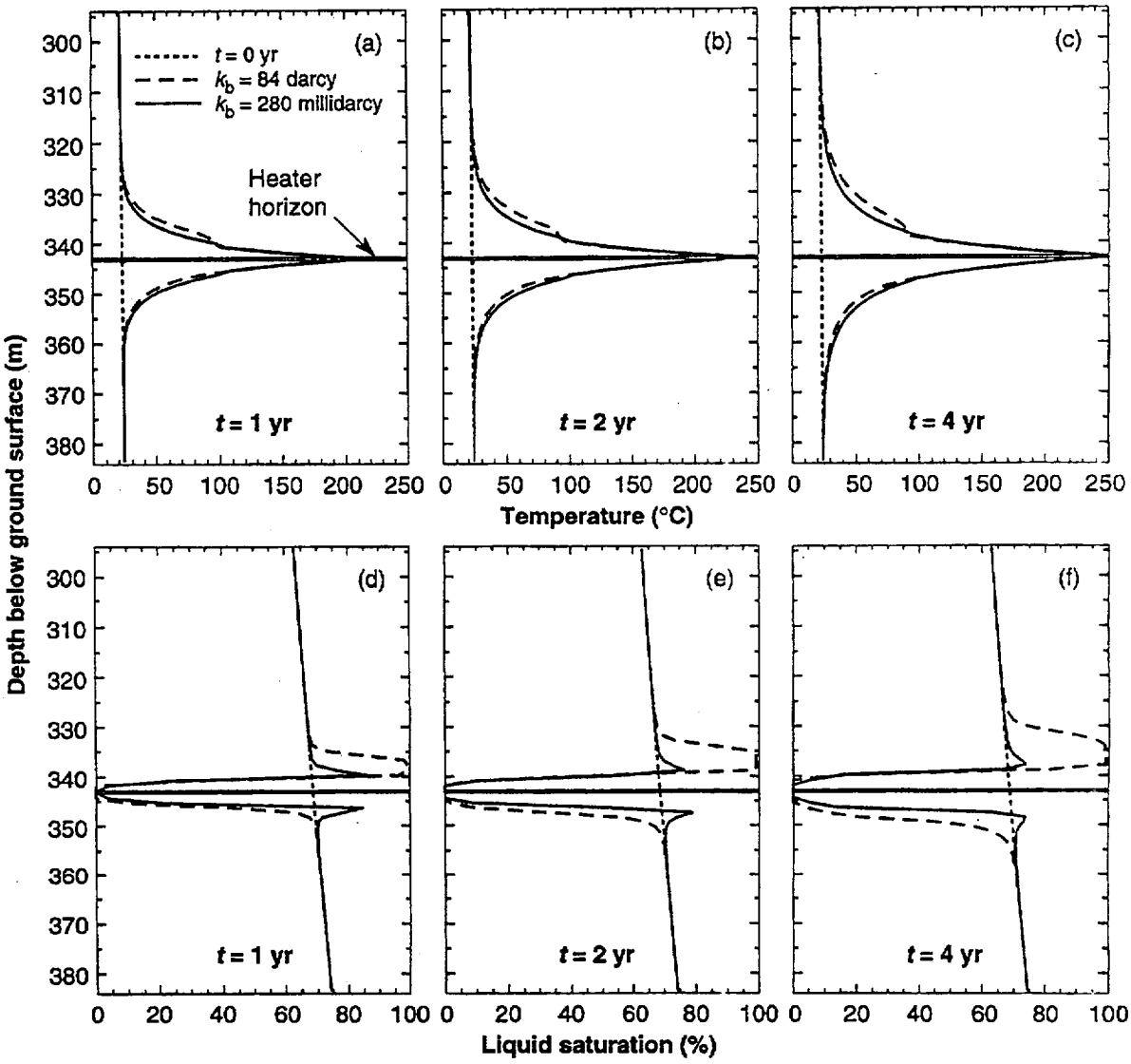

Figure 1.9-10. (a, b, c) Vertical temperature profile and (d, e, f) liquid saturation profile along the centerline of an array of horizontal-borehole-emplaced heaters heating a disk-shaped area with a radius of 4.0 m and APD = 247 W/m^2 averaged over the 50-m^2 heated area. Vapor diffusion tortuosity factor $\tau_{eff} = 0.2$.

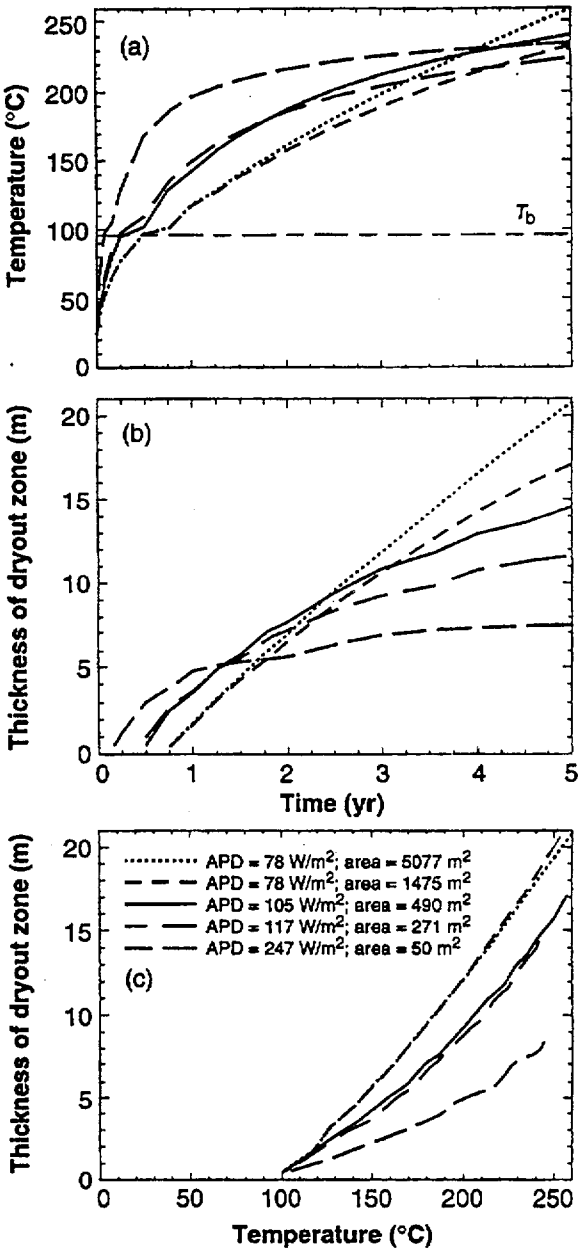

Figure 1.9-11. Results of heating at full power for 5 yr. (a) Temperature and (b) vertical dryout zone thickness at the center of an array of horizontal-borehole-emplaced heaters heating a disk-shaped area for various combinations of APD and heated area. The APD is averaged over the listed areas. (c) Vertical dryout zone thickness vs temperature at the center of the heater array. Bulk permeability k_b = 280 millidarcy and vapor diffusion tortuosity factor τ_{eff} = 0.2.

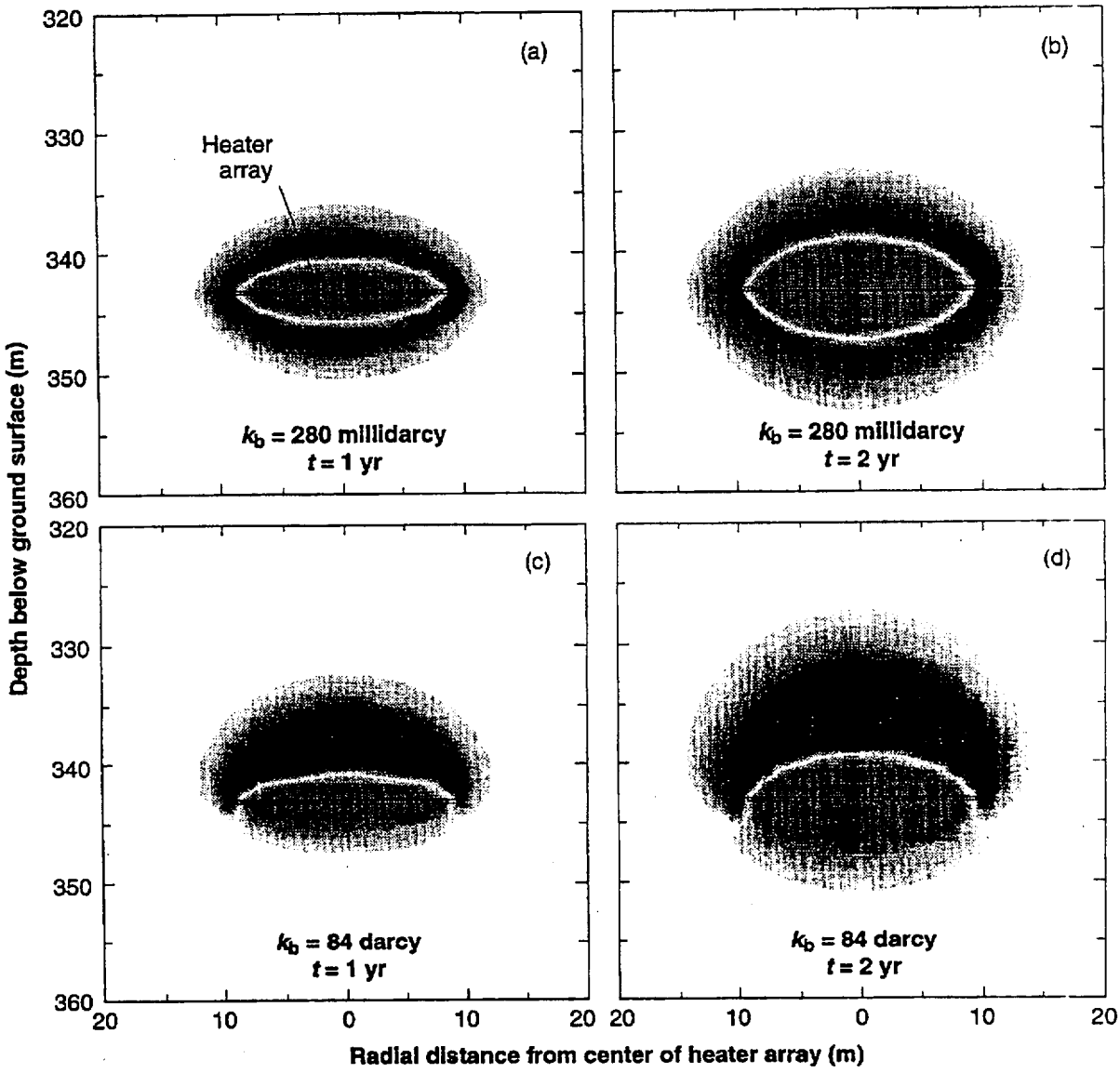

Figure 1.9-12. Dimensionless liquid saturation distribution for an array of horizontal-borehole-emplaced heaters heating a disk-shaped area with a radius of 9.3 m and APD = 117 W/m^2 averaged over the 271-m^2 area. Vapor diffusion tortuosity factor τ_{eff} = 0.2. The medium-shaded area surrounding the heater array corresponds to regions that are drier than ambient liquid saturation (dryout zone). The dark-shaded areas correspond to regions that are wetter than ambient liquid saturation (condensation zone). The light shading surrounding the dark-shaded area corresponds to a small rise in liquid saturation (outer edges of the condensation zone). No shading indicates no change in liquid saturation.

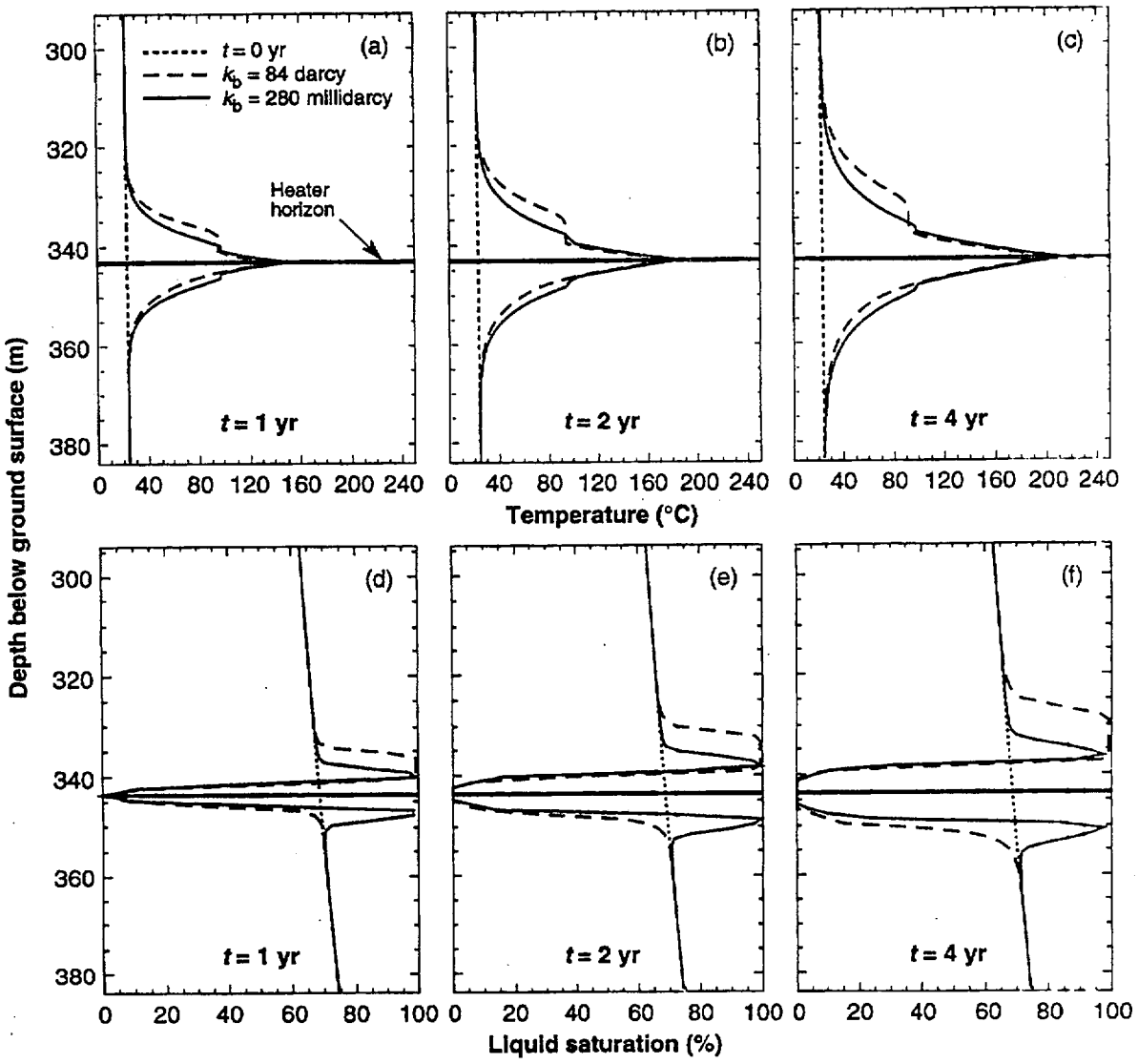

Figure 1.9-13. (a, b, c) Vertical temperature profile and (d, e, f) liquid saturation profile along the centerline of an array of horizontal-borehole-emplaced heaters heating a disk-shaped area with a radius of 9.3 m and APD = 247 W/m^2 averaged over the 271-m^2 heated area. Vapor diffusion tortuosity factor τ_{eff} = 0.2.

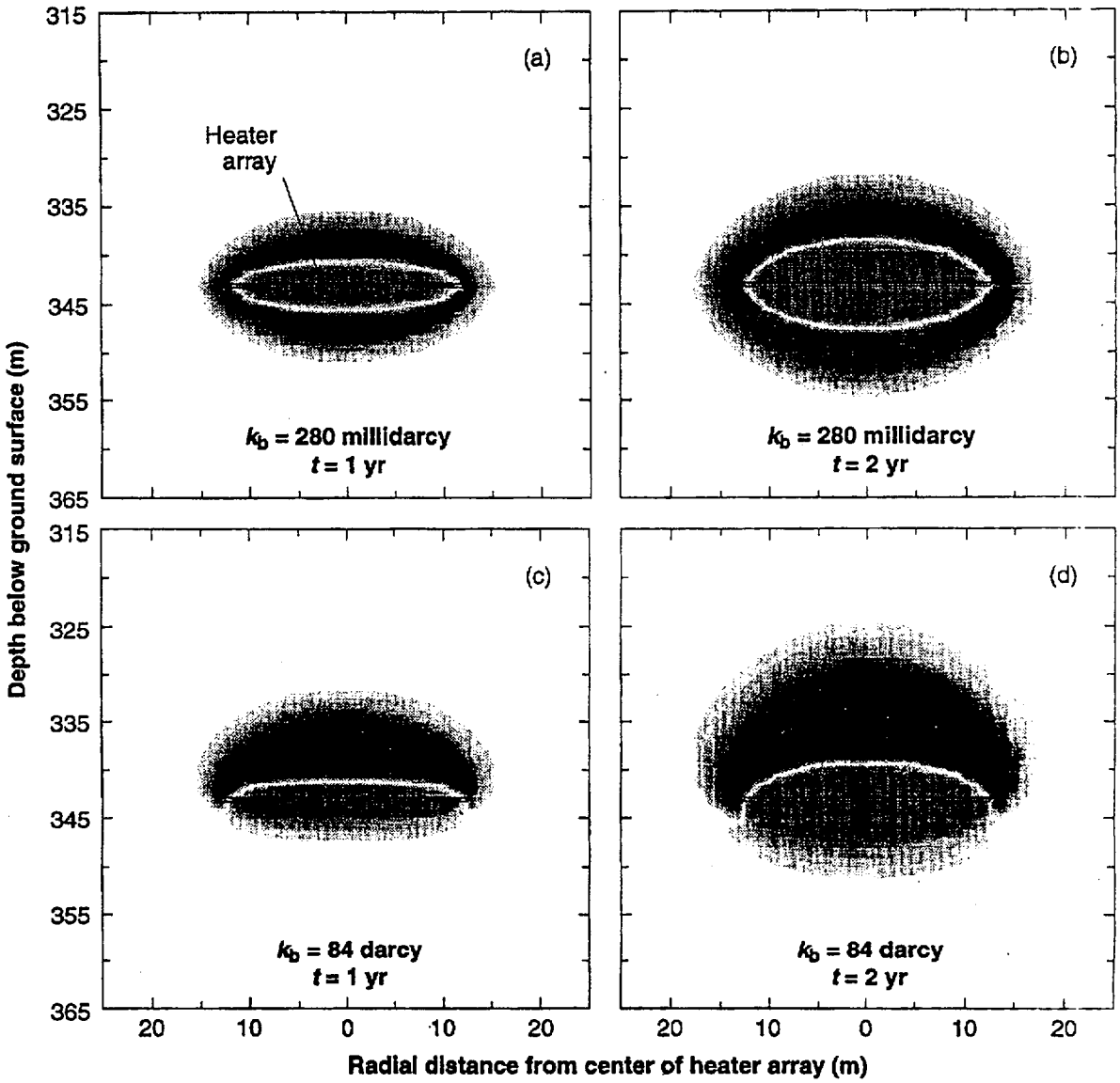

Figure 1.9-14. Dimensionless liquid saturation distribution for an array of horizontal-borehole-emplaced heaters heating a disk-shaped area with a radius of 12.5 m and APD = 105 W/m^2 averaged over the 490-m^2 heated area. Vapor diffusion tortuosity factor τ_{eff} = 0.2. The medium-shaded area surrounding the heater array corresponds to regions that are drier than ambient liquid saturation (dryout zone). The dark-shaded areas correspond to regions that are wetter than ambient liquid saturation (condensation zone). The light shading surrounding the dark-shaded area corresponds to a small rise in liquid saturation (outer edges of the condensation zone). No shading indicates no change in liquid saturation.

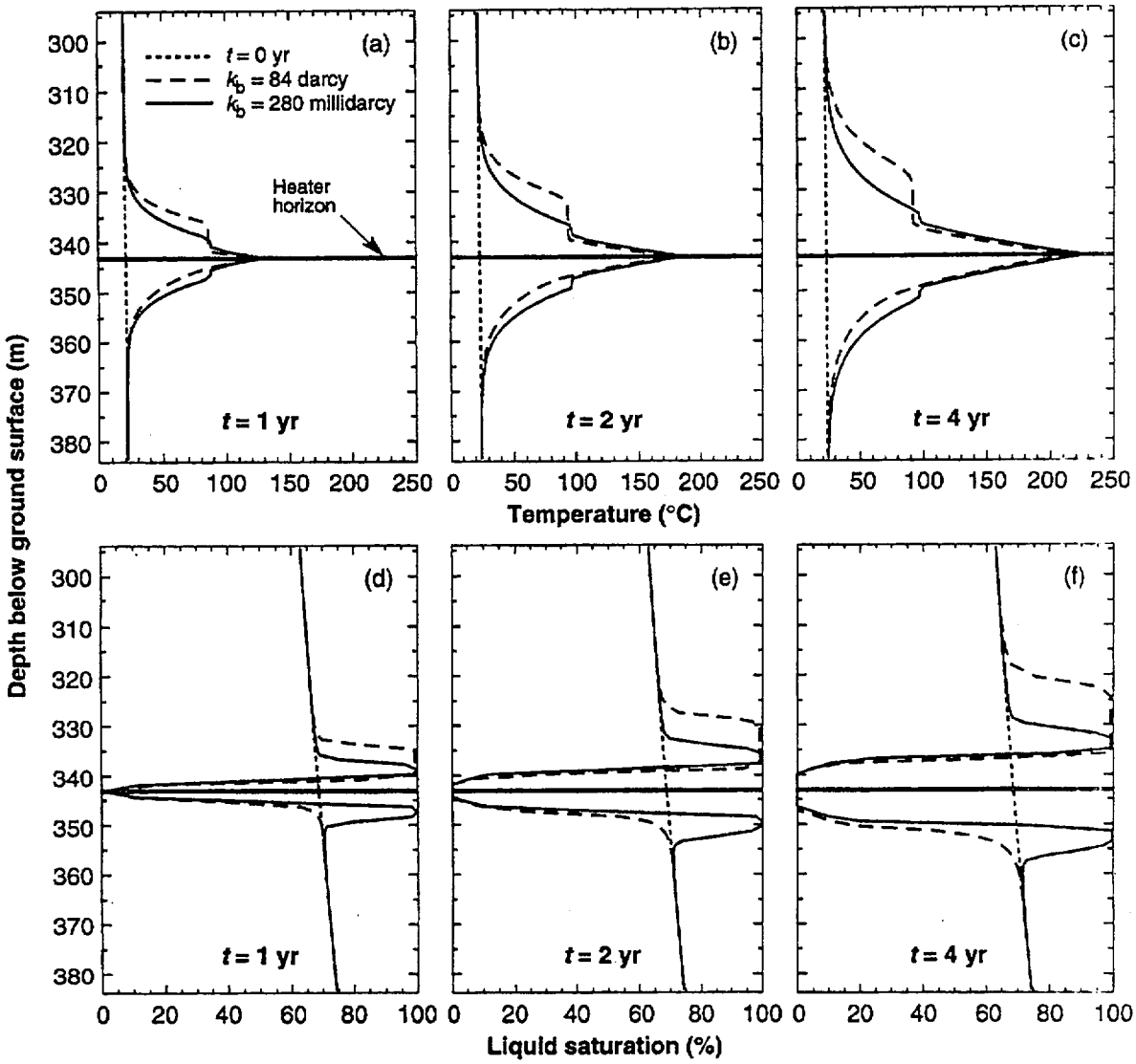

Figure 1.9-15. (a, b, c) Vertical temperature profile and (d, e, f) liquid saturation profile along the centerline of an array of horizontal-borehole-emplaced heaters heating a disk-shaped area with a radius of 12.5 m and APD = 105 W/m^2 averaged over the 490-m^2 heated area. Vapor diffusion tortuosity factor $\tau_{eff} = 0.2$.

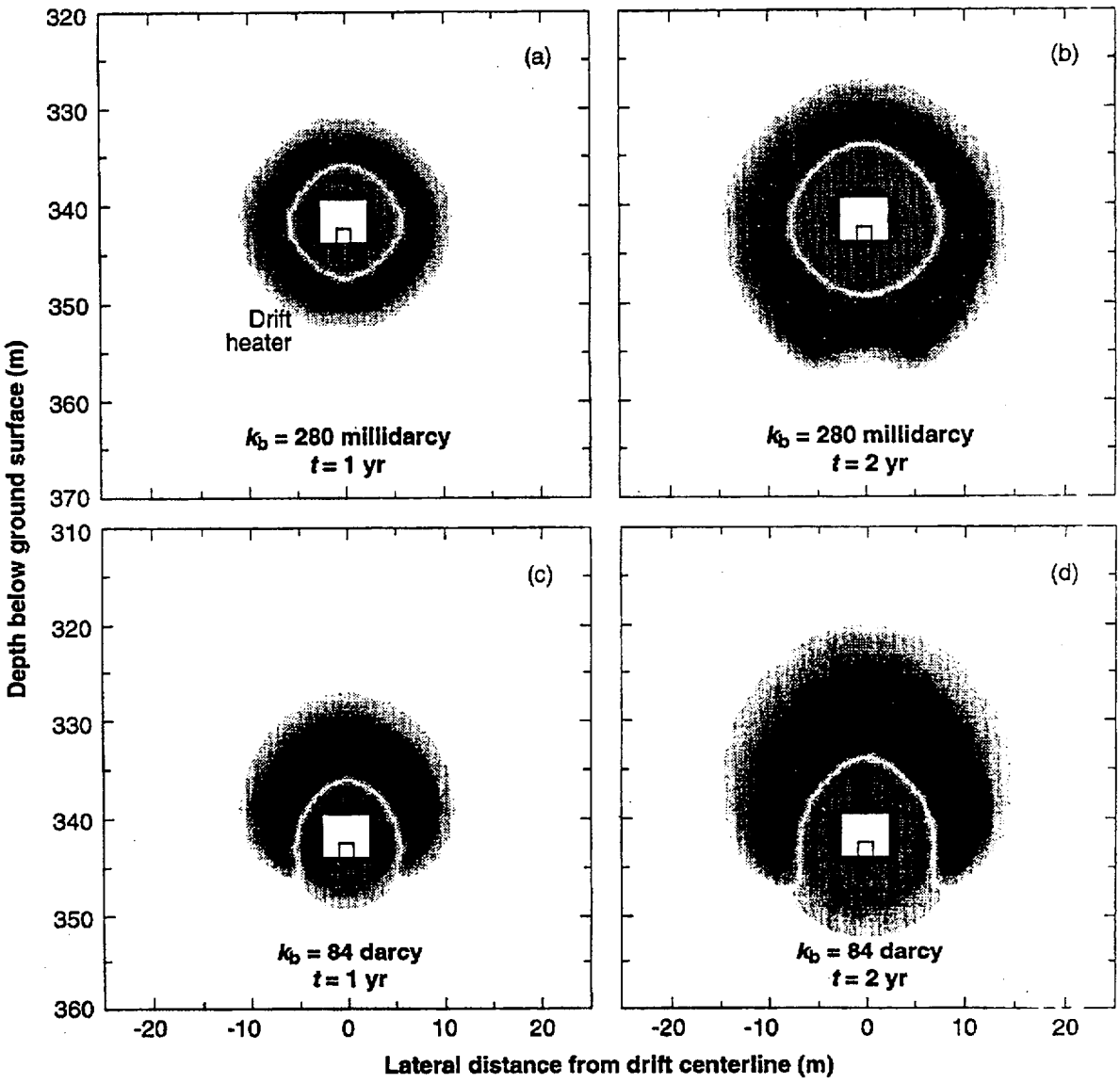

Figure 1.9-16. Dimensionless liquid saturation distribution orthogonal to a row of drift-emplaced, large-WP-sized heaters generating a lineal heat load of 2.1 kW/m. Vapor diffusion tortuosity factor $\tau_{eff} = 0.2$. The medium-shaded area surrounding the heater array corresponds to regions that are drier than ambient liquid saturation (dry-out zone). The dark-shaded areas correspond to regions that are wetter than ambient liquid saturation (condensation zone). The light shading surrounding the dark-shaded area corresponds to a small rise in liquid saturation (outer edges of the condensation zone). No shading indicates no change in liquid saturation.

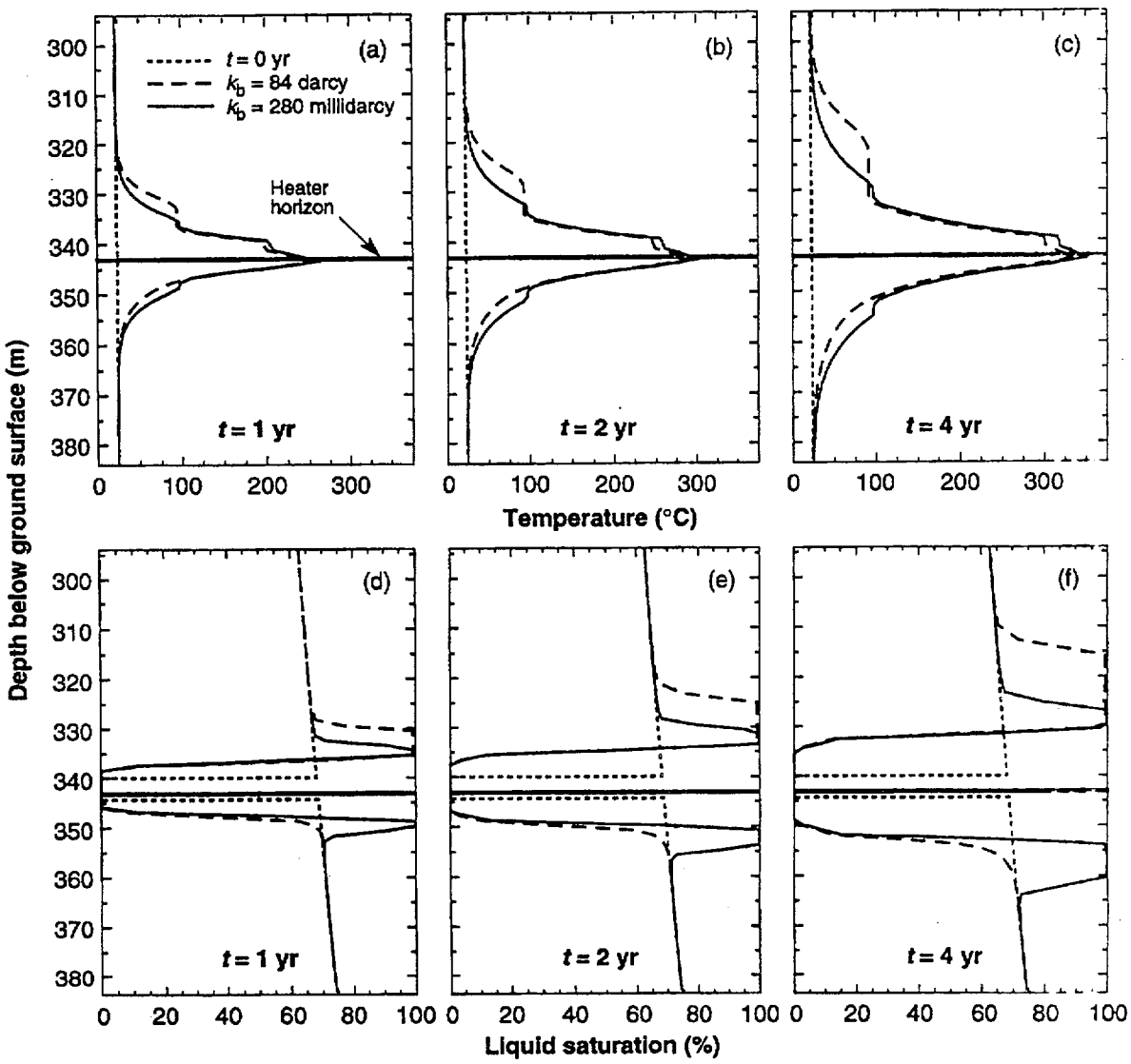

Figure 1.9-17. (a, b, c) Vertical temperature profile and (d, e, f) liquid saturation profile along the centerline of a row of drift-emplaced, large-WP-sized heaters generating a lineal head load of 2.1 kW/m. Vapor diffusion tortuosity factor $\tau_{eff} = 0.2$.

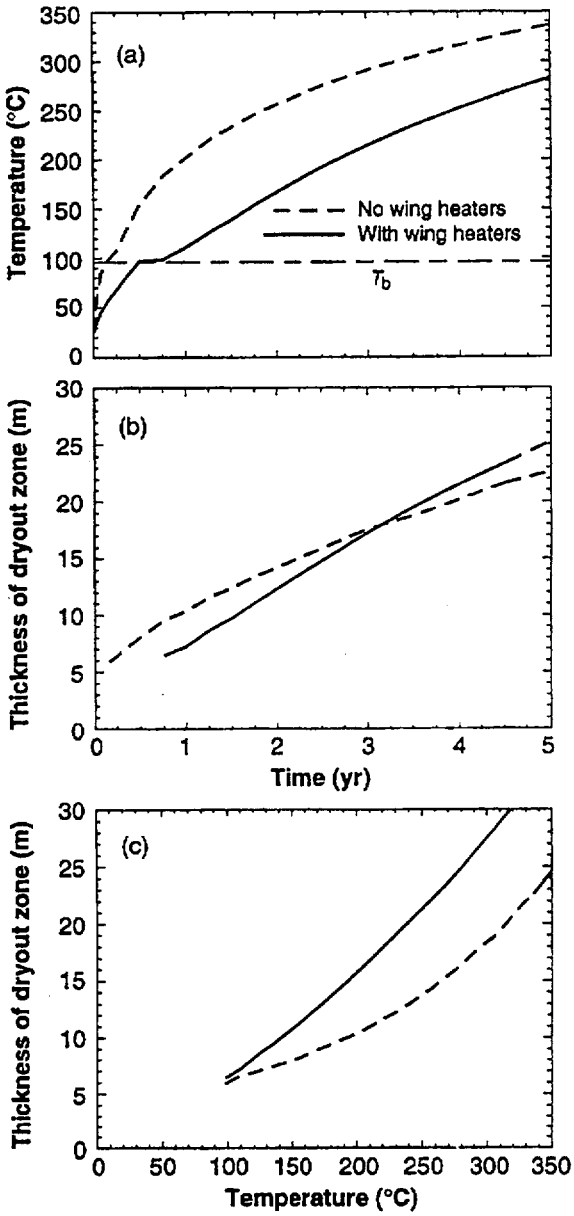

Figure 1.9-18. (a) Temperature at the upper drift wall and (b) vertical dryout zone thickness along the centerline of a row of drift-emplaced, large-WP-sized heaters generating a lineal heat load of 0.8 kW/m (for the wing heater case) and flanked by two horizontal-borehole-emplaced wing heater arrays. The heater arrays are generating an APD of 105 W/m^2 over the interval $4 < |x| < 9$ m and 157.5 W/m^2 over the interval $9 < |x| < 14$ m from the drift centerline. For the case with no wing heaters, the lineal heat load is 2.1 kW/m. (c) The vertical dryout zone thickness plotted as a function of temperature at the upper drift wall. Bulk permeability $k_b = 280$ millidarcy, and vapor diffusion tortuosity factor $\tau_{eff} = 0.2$.

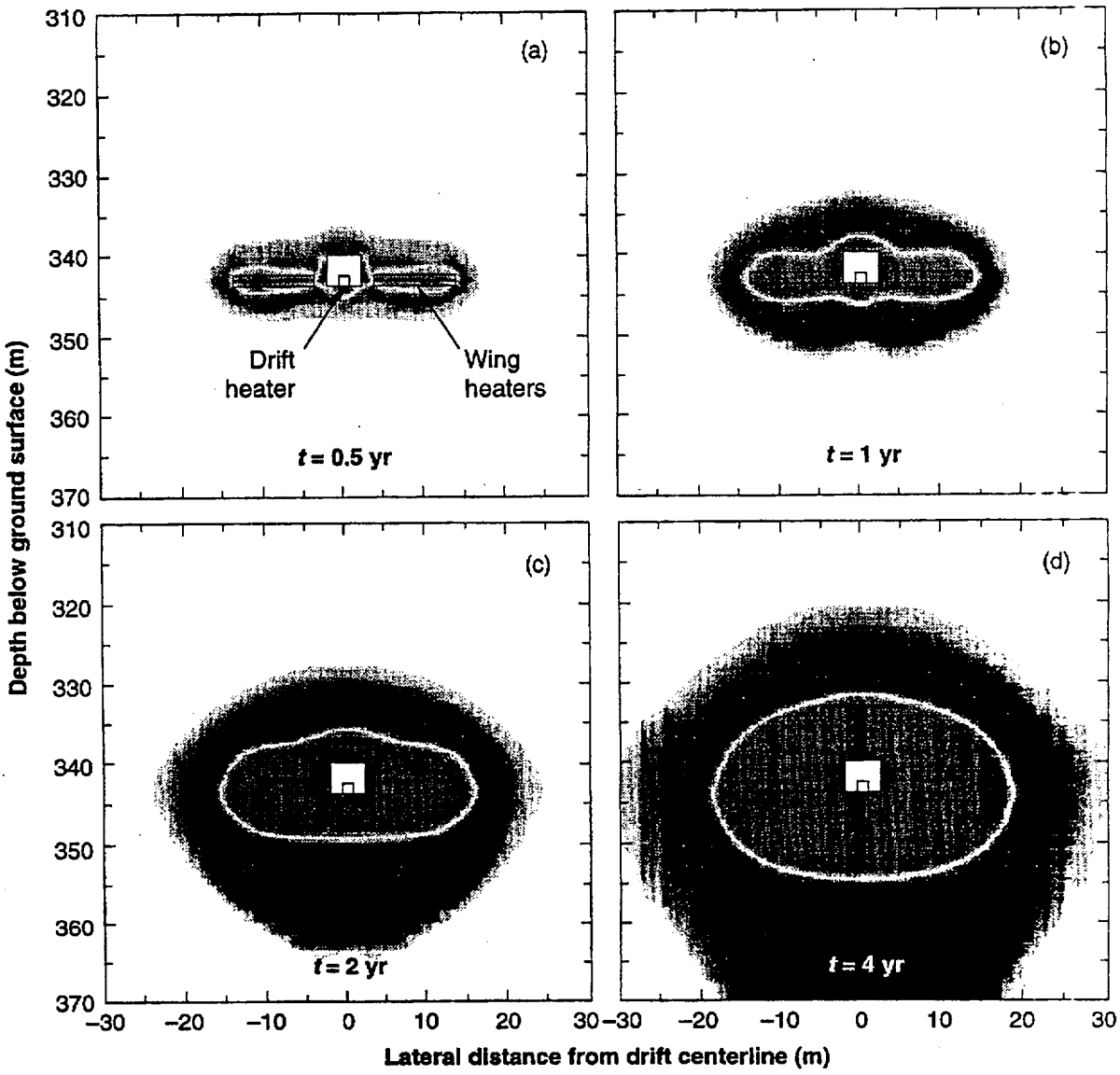

Figure 1.9-19. Dimensionless liquid saturation distribution orthogonal to a row of drift-emplaced, large-WP-sized heaters generating a lineal heat load of 0.8 kW/m and flanked by two horizontal-borehole-emplaced wing heater arrays. The heater arrays are generating an APD of 105 W/m^2 over the interval $4 < |x| < 9$ m and 157.5 W/m^2 over the interval $9 < |x| < 14$ m from the drift centerline. Bulk permeability k_b = 280 millidarcy, and vapor diffusion tortuosity factor τ_{eff} = 0.2. The medium-shaded area surrounding the heater array corresponds to regions that are drier than ambient liquid saturation (dryout zone). The dark-shaded areas correspond to regions that are wetter than ambient liquid saturation (condensation zone). The light shading surrounding the dark-shaded area corresponds to a small rise in liquid saturation (outer edges of the condensation zone). No shading indicates no change in liquid saturation.

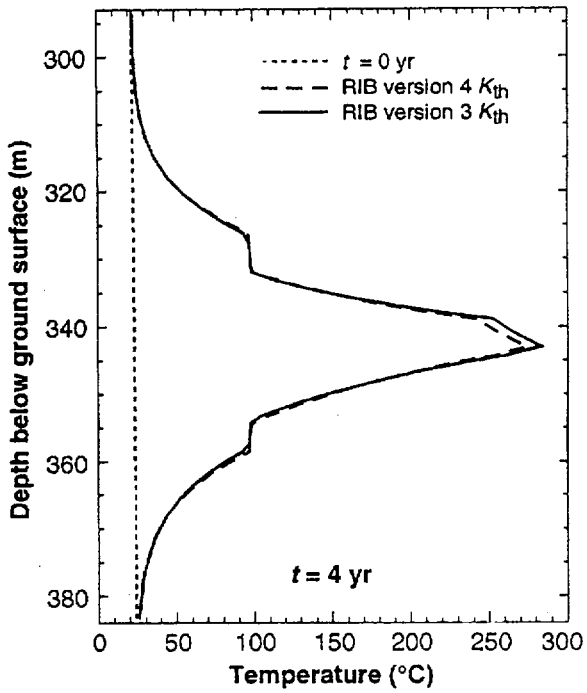

Figure 1.9-20. Vertical temperature profile along the centerline of a row of drift-emplaced, large-WP-sized heaters generating a lineal heat load of 0.8 kW/m and flanked by two horizontal-borehole-emplaced wing heater arrays. The heater arrays are generating an APD of 105 W/m^2 over the interval $4 < |x| < 9$ m and 157.5 W/m^2 over the interval $9 < |x| < 14$ m from the drift centerline at $t = 4$ yr. Bulk permeability $k_b = 280$ millidarcy, and vapor diffusion tortuosity factor $\tau_{eff} = 0.2$. Curves are shown for two different thermal conductivity K_{th} sets, including the RIB version 3 K_{th} values (reference case) and the RIB version 4 K_{th} values.

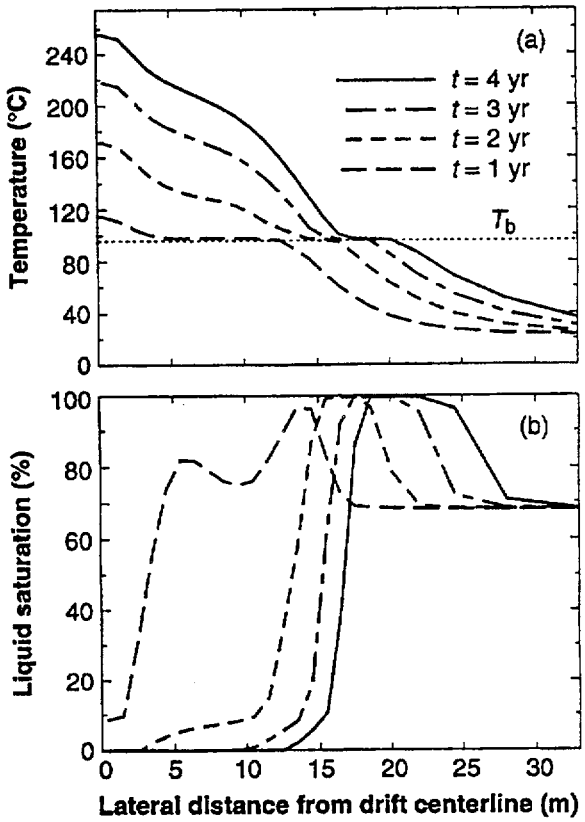

Figure 1.9-21. (a) Horizontal temperature profile and (b) liquid saturation profile at the elevation of the upper drift wall (2.9 m above the top of the drift heaters) for a row of drift-emplaced, large-WP-sized heaters generating a lineal heat load of 0.8 kW/m and flanked by two horizontal-borehole-emplaced wing heater arrays. The heater arrays are generating an APD of 105 W/m^2 over the interval $4 < |x| < 9$ m and 157.5 W/m^2 over the interval $9 < |x| < 14$ m from the drift centerline. Bulk permeability $k_b = 280$ millidarcy, and vapor diffusion tortuosity factor $\tau_{eff} = 0.2$.

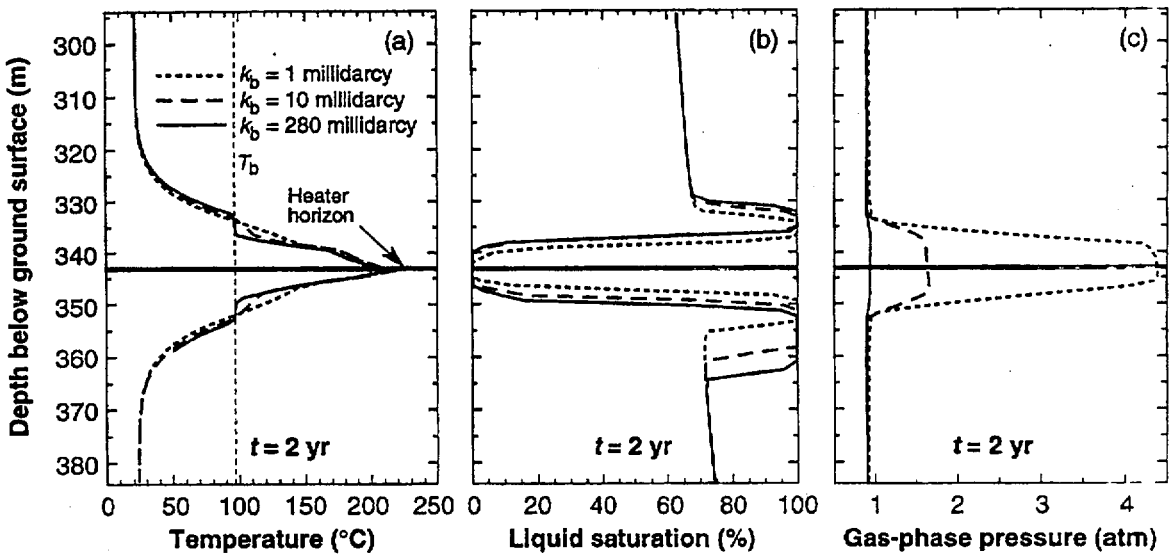

Figure 1.9-22. (a) Vertical temperature profile, (b) liquid saturation profile, and (c) gas-phase pressure profile along the centerline of a row of drift-emplaced, large-WP-sized heaters generating a lineal heat load of 0.8 kW/m and flanked by two horizontal-borehole-emplaced wing heater arrays. The heater arrays are generating an APD of 105 W/m^2 over the interval $4 < |x| < 9$ m and 157.5 W/m^2 over the interval $9 < |x| < 14$ m from the drift centerline at $t = 2$ yr. Vapor diffusion tortuosity factor $\tau_{eff} = 0.2$.

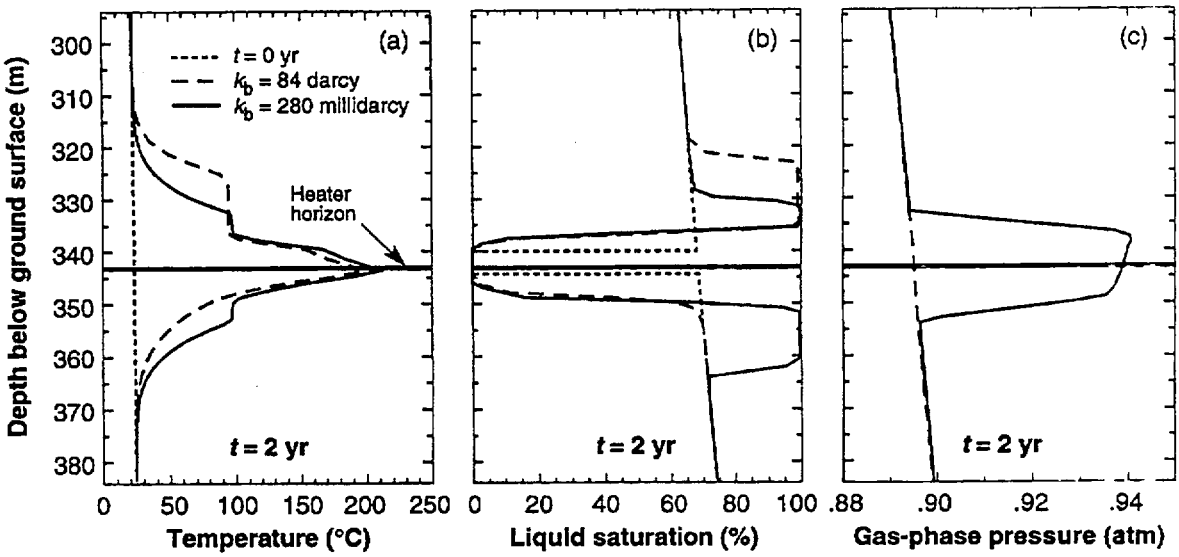

Figure 1.9-23. (a) Vertical temperature profile, (b) liquid saturation profile, and (c) gas-phase pressure profile along the centerline of a row of drift-emplaced, large-WP-sized heaters generating a lineal heat load of 0.8 kW/m and flanked by two horizontal-borehole-emplaced wing heater arrays. The heater arrays are generating an APD of 105 W/m^2 over the interval $4 < |x| < 9$ m and 157.5 W/m^2 over the interval $9 < |x| < 14$ m from the drift centerline at $t = 2$ yr. Vapor diffusion tortuosity factor $\tau_{eff} = 0.2$.

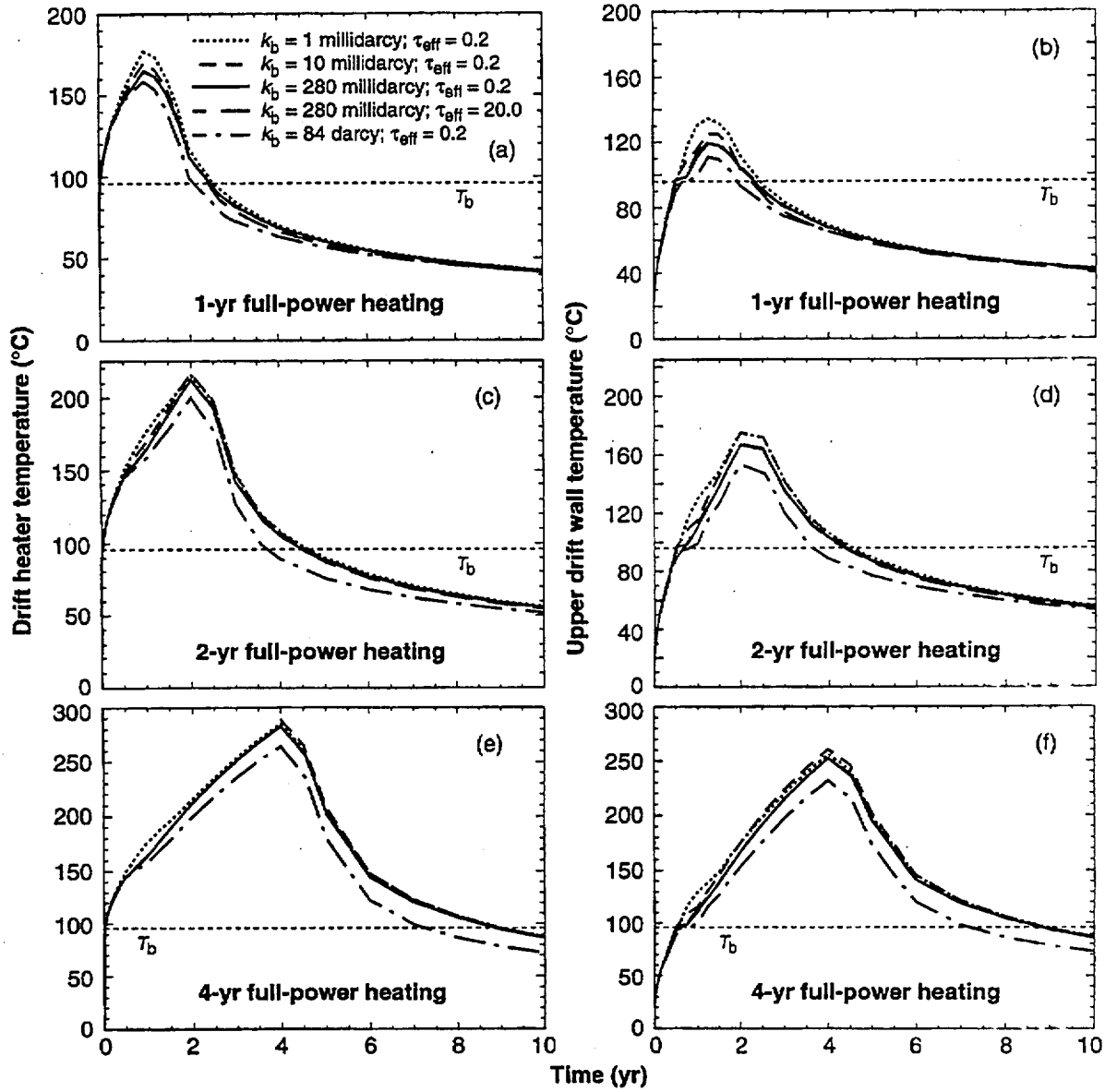

Figure 1.9-24. (a, c, e) Temperature history on drift heater and (b, d, f) temperature history on upper drift wall for a row of drift-emplaced, large-WP-sized heaters generating a lineal heat load of 0.8 kW/m and flanked by two horizontal-borehole-emplaced wing heater arrays. The heater arrays are generating an APD of 105 W/m^2 over the interval $4 < |x| < 9$ m and 157.5 W/m^2 over the interval $9 < |x| < 14$ m from the drift centerline. Bulk permeability k_b = 280 millidarcy, and vapor diffusion tortuosity factor $\tau_{eff} = 0.2$. Temperature histories are shown for three different periods of full-power heating. The full-power heating period is followed by a 1-yr linear-rampdown period to zero power.

TF (8-22-96) fig 1.9-24

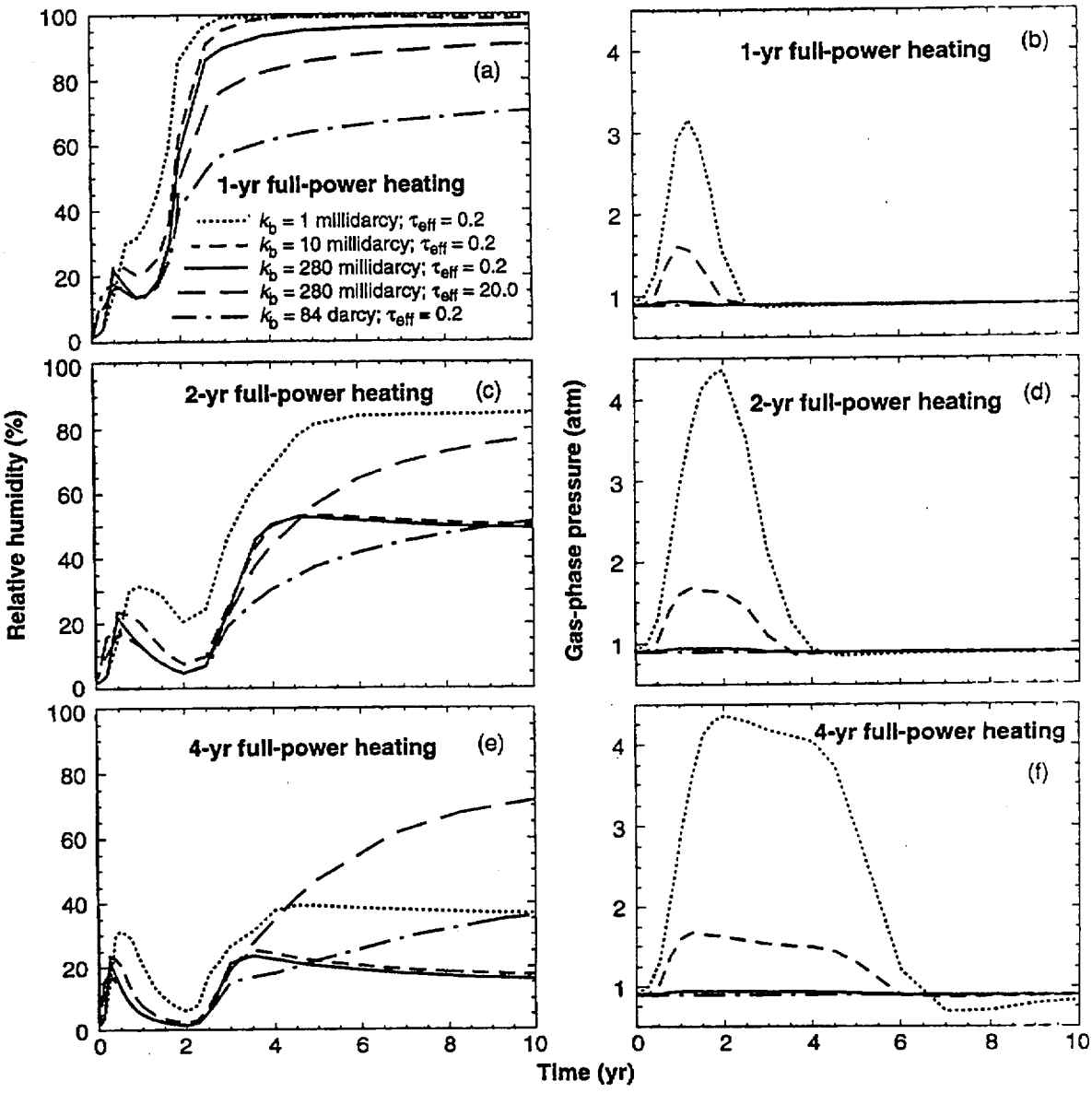

Figure 1.9-25. (a, c, e) Relative humidity on surface of drift heater and (b, d, f) gas-phase pressure in heater drift for a row of drift-emplaced, large-WP-sized heaters generating a lineal heat load of 0.8 kW/m and flanked by two horizontal-borehole-emplaced wing heater arrays. The heater arrays are generating an APD of 105 W/m^2 over the interval $4 < |x| < 9$ m and 157.5 W/m^2 over the interval $9 < |x| < 14$ m from the drift centerline. Bulk permeability k_b = 280 millidarcy, and vapor diffusion tortuosity factor τ_{eff} = 0.2. Relative humidity and gas-phase pressure histories are shown for three different periods of full-power heating. The full-power heating period is followed by a 1-yr linear-rampdown period to zero power.

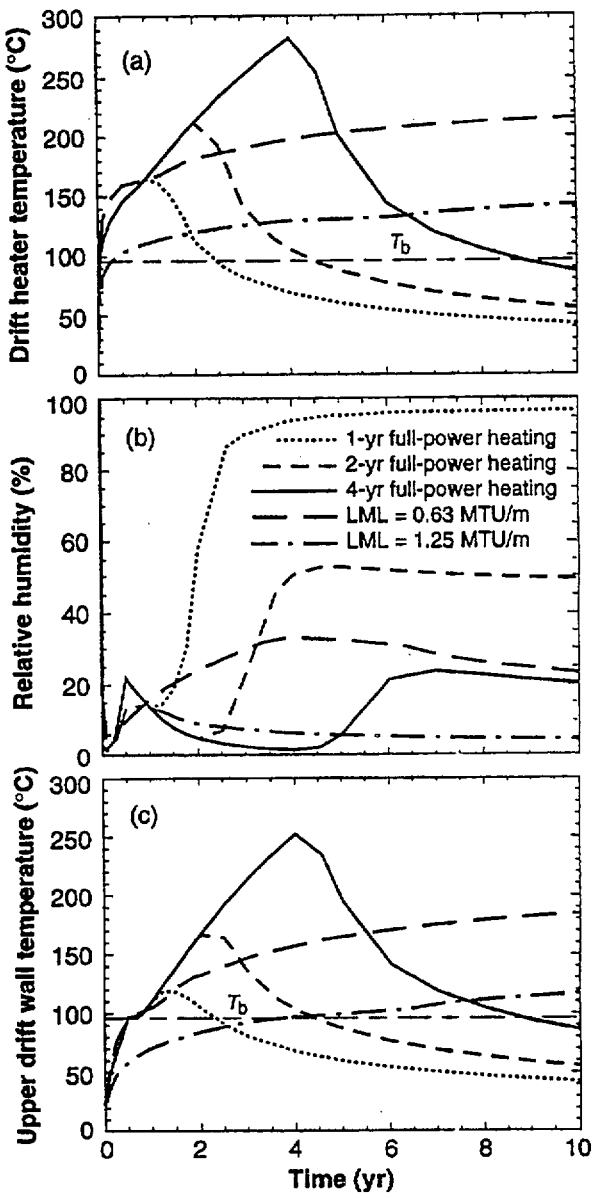

Figure 1.9-26. (a) Temperature and (b) relative humidity on drift heater and (c) temperature on upper drift wall for a row of drift-emplaced, large-WP-sized heaters generating a lineal heat load of 0.8 kW/m and flanked by two horizontal-borehole-emplaced wing heater arrays. The heater arrays are generating an APD of 105 W/m^2 over the interval $4 < |x| < 9$ m and 157.5 W/m^2 over the interval $9 < |x| < 14$ m from the drift centerline. Bulk permeability $k_b = 280$ millidarcy, and vapor diffusion tortuosity factor $\tau_{eff} = 0.2$. Curves are shown for three different periods of full-power heating. The full-power heating period is followed by a 1-yr linear-rampdown period to zero power. Curves are also shown for two 80-MTU/acre repositories with 26-yr-old (OFF) SNF and the following: (i) LML = 1.25 MTU/m, drift spacing = 60 m, and WP spacing = 6 m; and (ii) LML = 0.63 MTU/m, drift spacing = 30 m, and WP spacing = 12 m. Repository temperature and relative humidity values pertain to the WP surface.

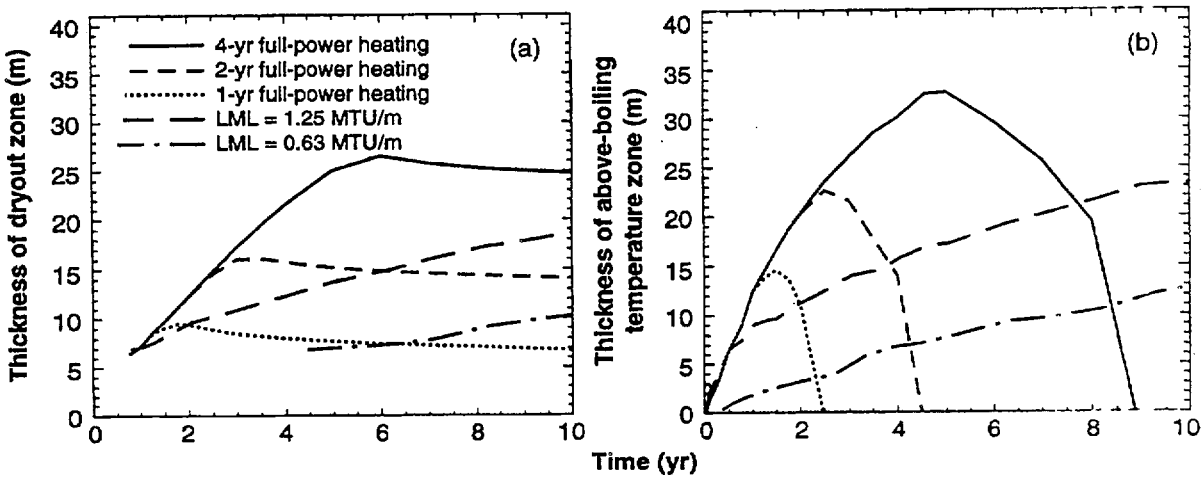

Figure 1.9-27. Vertical thickness of (a) dryout zone and (b) above-boiling temperature zone along the centerline of a row of drift-emplaced, large-WP-sized heaters generating a lineal heat load of 0.8 kW/m and flanked by two horizontal-borehole-emplaced wing heater arrays. The heater arrays are generating an APD of 105 W/m^2 over the interval $4 < |x| < 9$ m and 157.5 W/m^2 over the interval $9 < |x| < 14$ m from the drift centerline. Bulk permeability k_b = 280 millidarcy, and vapor diffusion tortuosity factor τ_{eff} = 0.2. Curves are shown for three different periods of full-power heating. The full-power heating period is followed by a 1-yr linear-rampdown period to zero power. Curves are also shown for two 80-MTU/acre repositories with 26-yr-old (OFF) SNF and the following: (i) LML = 1.25 MTU/m, drift spacing = 60 m, and WP spacing = 6 m; and (ii) LML = 0.63 MTU/m, drift spacing = 30 m, and WP spacing = 12 m.

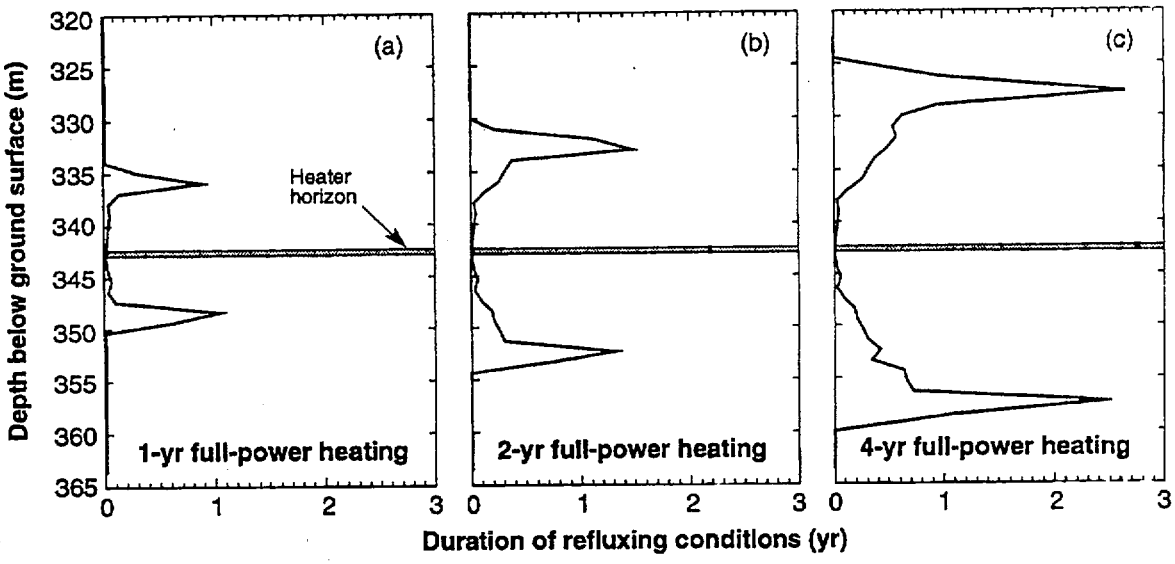

Figure 1.9-28. Duration of refluxing conditions (as given by the time between 95 and 97°C) vs depth along the centerline of a row of drift-emplaced, large-WP-sized heaters generating a lineal heat load of 0.8 kW/m and flanked by two horizontal-borehole-emplaced wing heater arrays. The heater arrays are generating an APD of 105 W/m^2 over the interval $4 < |x| < 9$ m and 157.5 W/m^2 over the interval $9 < |x| < 14$ m from the drift centerline. Bulk permeability $k_b = 280$ millidarcy, and vapor diffusion tortuosity factor $\tau_{eff} = 0.2$. Curves are shown for three different periods of full-power heating. The full-power heating period is followed by a 1-yr linear-rampdown period to zero power.

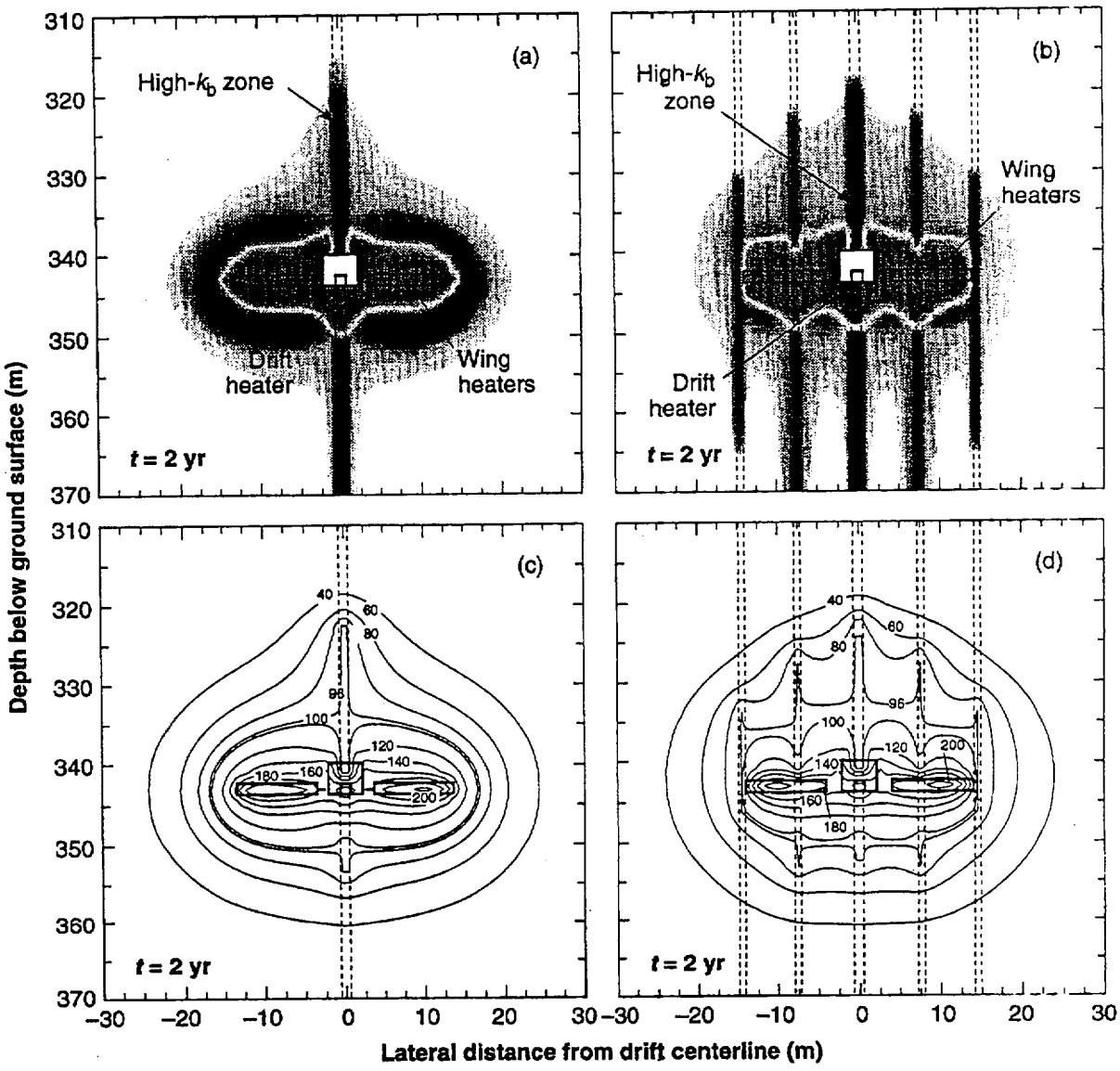

Figure 1.9-29. (a, b) Dimensionless liquid saturation distribution and (c, d) temperature distribution orthogonal to a row of drift-emplaced, large-WP-sized heaters generating a lineal heat load of 0.8 kW/m and flanked by two horizontal-borehole-emplaced wing heater arrays. The heater arrays are generating an APD of 105 W/m^2 over the interval $4 < |x| < 9$ m and 157.5 W/m^2 over the interval $9 < |x| < 14$ m from the drift centerline. The heterogeneous bulk permeability k_b distribution consists of 84-darcy high-k_b zones separated by 1-millidarcy nominal-k_b zones. Vapor diffusion tortuosity factor $\tau_{eff} = 0.2$. The medium-shaded area surrounding the heater array corresponds to regions that are drier than ambient liquid saturation (dryout zone). The dark-shaded areas correspond to regions that are wetter than ambient liquid saturation (condensation zone). The light shading surrounding the dark-shaded area corresponds to a small rise in liquid saturation (outer edges of the condensation zone). No shading indicates no change in liquid saturation.

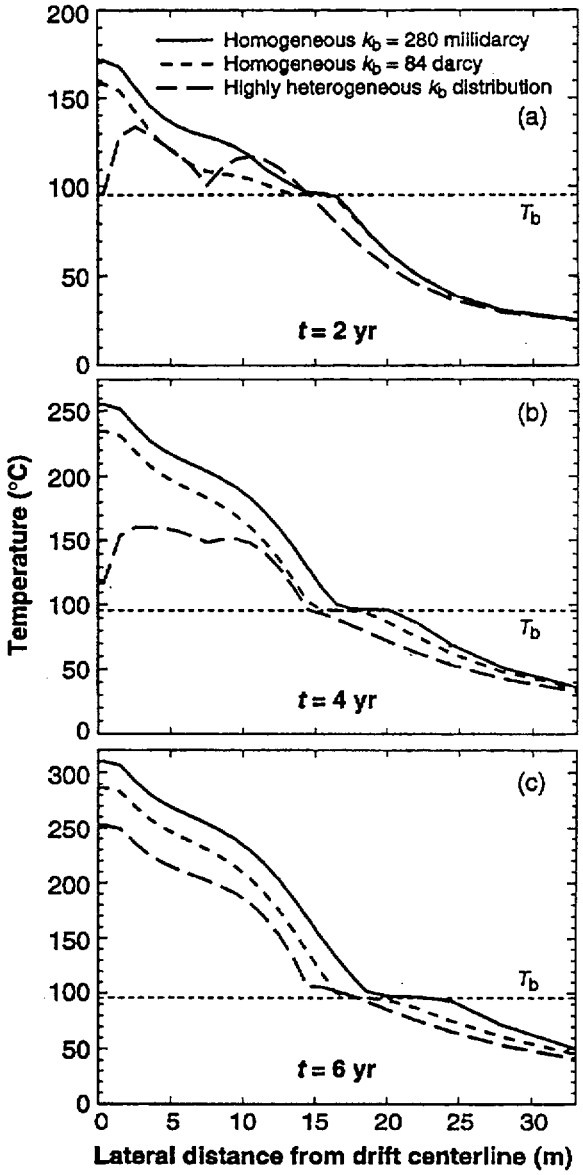

Figure 1.9-30. Horizontal temperature profile at the elevation of the upper drift wall (2.9 m above the top of the drift heaters) for a row of drift-emplaced, large-WP-sized heaters generating a lineal heat load of 0.8 kW/m and flanked by two horizontal-borehole-emplaced wing heater arrays. The heater arrays are generating an APD of 105 W/m^2 over the interval $4 < |x| < 9$ m and 157.5 W/m^2 over the interval $9 < |x| < 14$ m from the drift centerline. Bulk permeability k_b = 280 millidarcy, and vapor diffusion tortuosity factor τ_{eff} = 0.2. Temperature profiles are shown for three bulk permeability k_b distributions, including two homogeneous cases with k_b = 280 millidarcy and 84 darcy, and a highly heterogeneous case that consists of vertically oriented, narrow 84-darcy zones separated by 1-millidarcy zones (see Fig. 10).

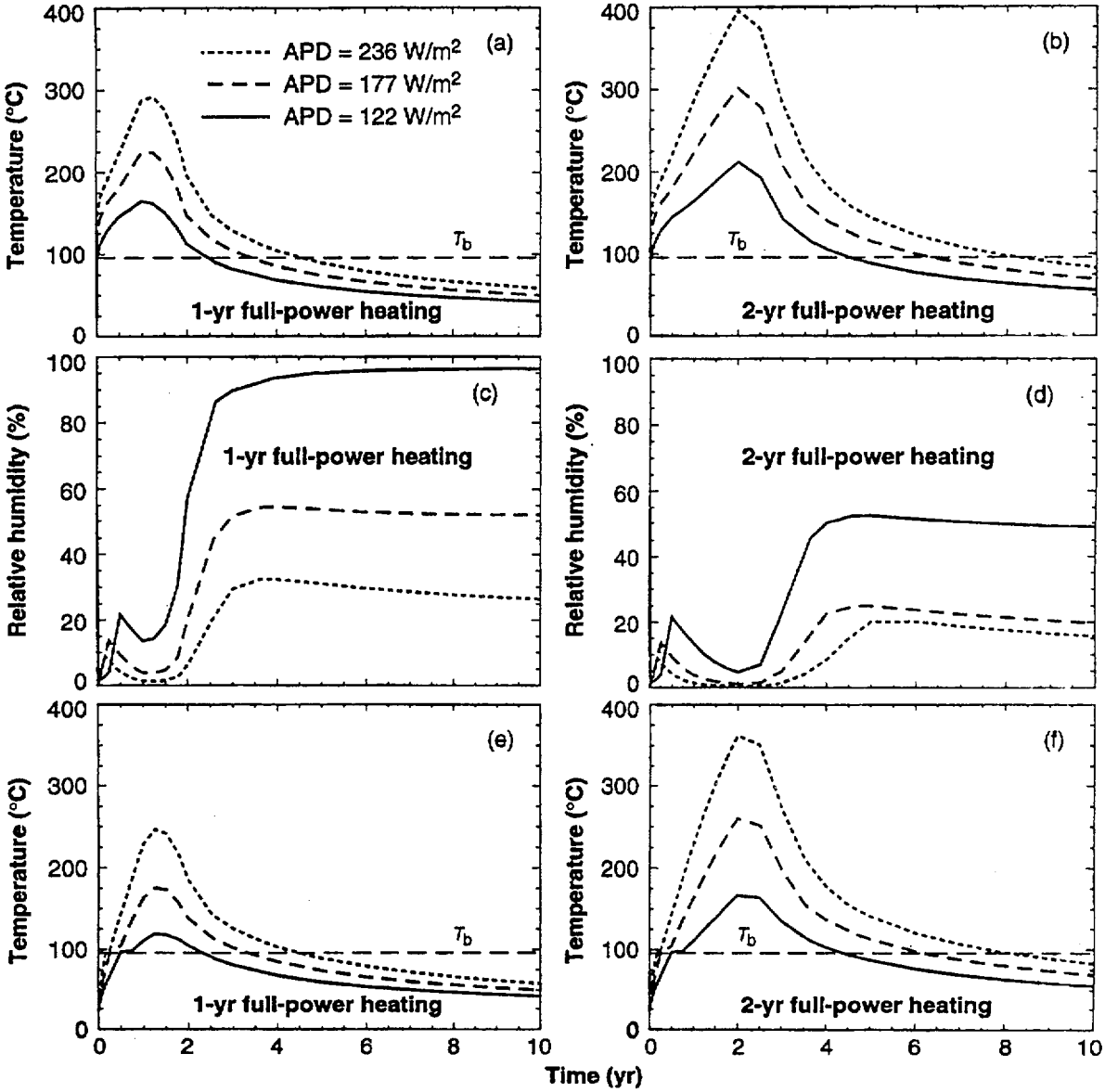

Figure 1.9-31. (a, b) Temperature and (c, d) relative humidity on drift heater and (e, f) temperature on upper drift wall for a row of drift-emplaced, large-WP-sized heaters generating, for the reference heating-rate case (APD = 122 W/m^2), a lineal heat load of 0.8 kW/m and flanked by two horizontal-borehole-emplaced wing heater arrays. The heater arrays are generating an APD of 105 W/m^2 over the interval $4 < |x| < 9$ m and 157.5 W/m^2 over the interval $9 < |x| < 14$ m from the drift centerline. Bulk permeability k_b = 280 millidarcy, and vapor diffusion tortuosity factor τ_{eff} = 0.2. Curves are shown (a, c, e) for a 1-yr full-power heating period and (b, d, f) for a 2-yr full-power heating period. The full-power heating period is followed by a 1-yr linear-rampdown period to zero power. Curves are shown for three different heating rates, including the reference case (APD = 122 W/m^2) and two accelerated-heating-rate cases (APD = 177 and 236 W/m^2).

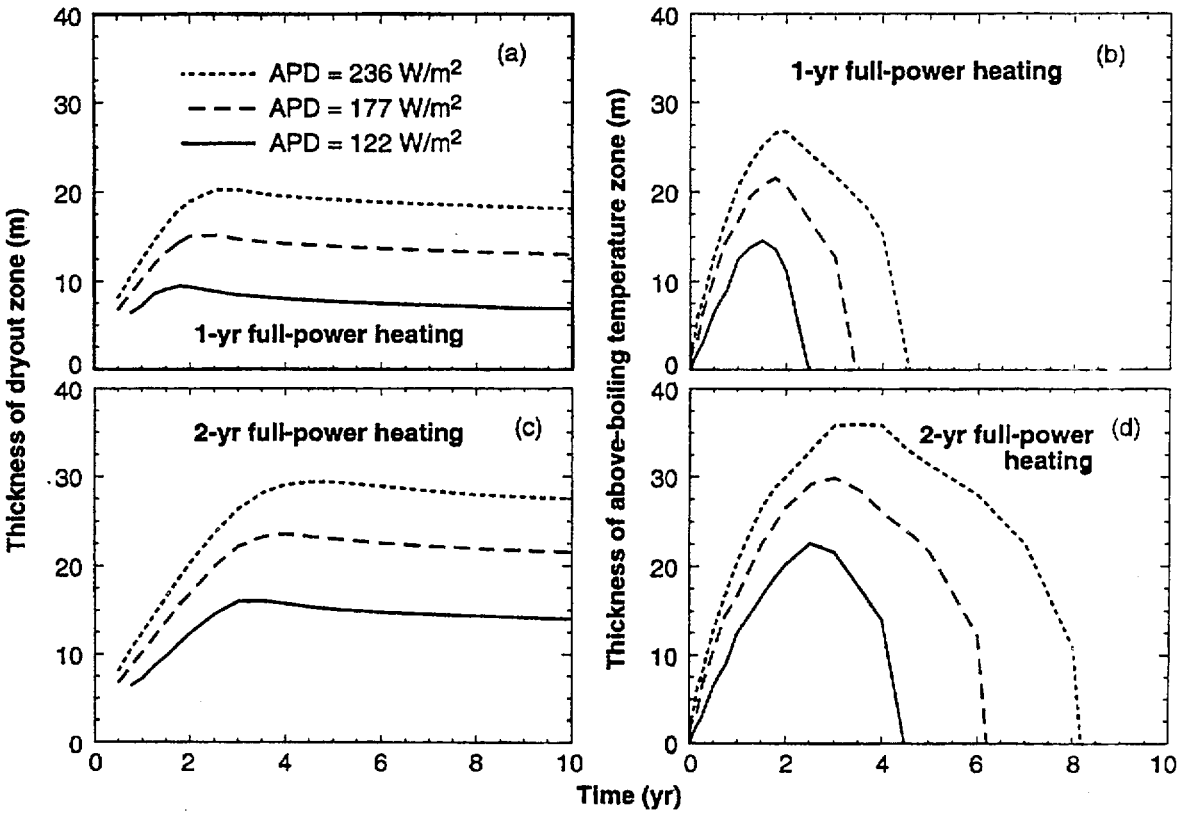

Figure 1.9-32. (a, c) Vertical thickness of dryout zone and (b, d) above-boiling temperature zone for a row of drift-emplaced, large-WP-sized heaters generating, for the reference heating-rate case (APD = 122 W/m^2), a lineal of heat load of 0.8 kW/m and flanked by two horizontal-borehole-emplaced wing heater arrays. The heater arrays are generating an APD 105 W/m^2 over the interval $4 < |x| < 9$ m and 157.5 W/m^2 over the interval $9 < |x| < 14$ m from the drift centerline. Bulk permeability k_b = 280 millidarcy, and vapor diffusion tortuosity factor τ_{eff} = 0.2. Curves are shown (a, b) for a 1-yr full-power heating period and (c, d) for a 2-yr full-power heating period. The full-power heating period is followed by a 1-yr linear-rampdown period to zero power. Curves are shown for three different heating rates, including the reference case (APD = 122 W/m^2) and two accelerated-heating-rate cases (APD = 177 and 236 W/m^2).